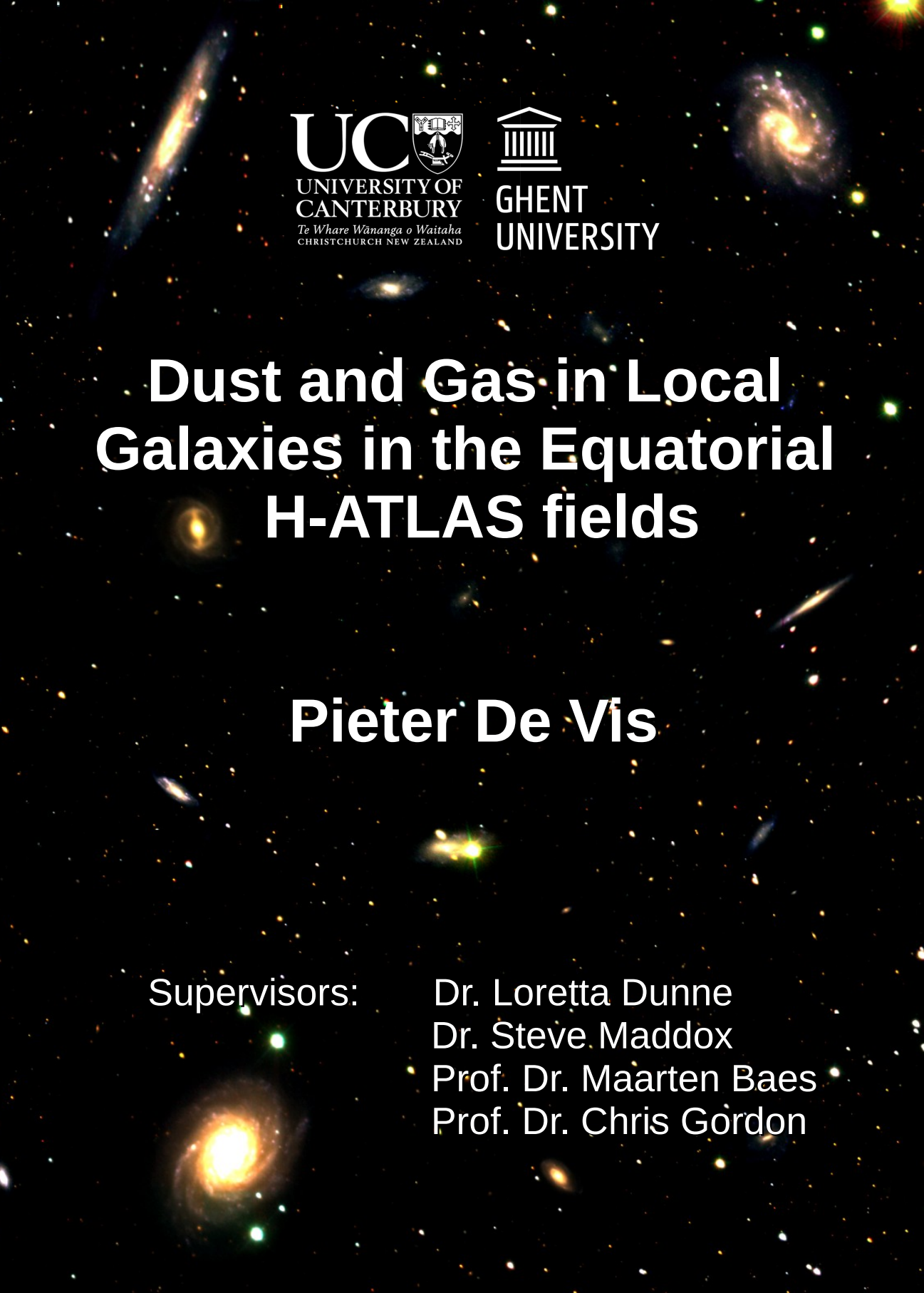

UNIVERSITY OF CANTERBURY
Te Whare Wānanga o Waitaha
CHRISTCHURCH NEW ZEALAND

GHENT UNIVERSITY

Dust and Gas in Local Galaxies in the Equatorial H-ATLAS fields

Pieter De Vis

Supervisors: Dr. Loretta Dunne
Dr. Steve Maddox
Prof. Dr. Maarten Baes
Prof. Dr. Chris Gordon

Faculty of sciences
Department of Physics and Astronomy

Dust and Gas in Local Galaxies in the Equatorial H-ATLAS Fields

Pieter De Vis

This dissertation is submitted for the joint degree of

Doctor of Philosophy in Astronomy	From the University of Canterbury
Doctor of Science: Astronomy	From Ghent University

Supervisors: Dr. Loretta Dunne, Dr. Steve Maddox,
Prof. Dr. Chris Gordon, Prof. Dr. Maarten Baes

December 2016

Supervisors

Dr. Loretta Dunne
School of Physics and Astronomy, Cardiff University
Institute for Astronomy, The University of Edinburgh
Department of Physics and Astronomy, Canterbury University

Dr. Steve Maddox
School of Physics and Astronomy, Cardiff University
Institute for Astronomy, The University of Edinburgh
Department of Physics and Astronomy, Canterbury University

Prof. Dr. Maarten Baes
Department of Physics and Astronomy, UGent

Prof. Dr. Chris Gordon
Department of Physics and Astronomy, Canterbury University

Other members of the examination committee

Prof. Dr. Sven De Rijcke (chair)
Department of Physics and Astronomy, UGent

Dr. Ilse De Looze
Department of Physics and Astronomy, UGent
Department of Physics and Astronomy, University College London

Dr. Suzanne Madden
Service d'Astrophysique, CEA, Saclay

Dr. Pierre Royer
Department of Physics and Astronomy, KU Leuven

ABOUT THE COVER

The cover shows a compilation three-colour image of all the HIGH galaxies, which are used in Chapters 2 – 6 to study the gas and dust content of nearby high gas fraction galaxies. The SDSS g-band is shown in blue, the SDSS i-band in green, and the VIKING Y-band in red. The locations and relative distances between the galaxies are strongly out of proportion. Individual multi-wavelength imagery for the HIGH galaxies is given in Chapter 2.

Acknowledgements

Writing a thesis is by no means a one-person feat. There are many people I would like to thank for their unwavering support and useful insights. I was fortunate to get the chance to start my PhD at Canterbury University in Christchurch (New Zealand), and finish it at Ghent University (Belgium), as well as work together with people in Cardiff (UK), Perth and Sydney (Australia). It has been an amazing adventure meeting everyone in each of these beautiful places.

First and foremost I would like to thank my supervisors. I was lucky to have a team of excellent supervisors from different places around the world. The research presented in this dissertation was conceived by my two main supervisors Loretta Dunne and Steve Maddox. To them I am deeply grateful for the opportunity to embark on this project, for their bright ideas, for the interesting in-depth scientific discussion and for all the time and energy spent on my supervision. I also wish to thank Maarten Baes, for giving me the fantastic opportunity to continue my research at Ghent University, for the warm welcome and atmosphere, and the invaluable comments on this dissertation. I am also grateful to Amanda Bauer, for the good advice and the chance to visit the AAO, and to Chris Gordon, for all the help in making my joint PhD possible. My heart-felt thanks also to Haley Gomez, for all the advice, support, and pleasant and interesting collaboration. I would also like to express my thanks to the members of the jury for their very insightful comments on this thesis, the interesting discussion during the closed defense, and their valuable suggestions.

Next I would like to thank everyone else who contributed to this work. This dissertation would not have been possible without the close collaboration with Chris Clark and Simon Schoffield, to whom I am very grateful for the interesting and productive discussions. I would also like to thank Jacinta Delhaize for the great help with HI-stacking. I also gratefully acknowledge the H-ATLAS team for making this project possible and the insightful comments; Martha Haynes, Riccardo Giovanelli, and the ALFALFA team for supplying the latest ALFALFA survey data; Suzanne Madden for providing the emission line tables for the Dwarf Galaxy Survey; Maritza Lara-López for emission lines in the GAMA fields; and Sébastien Viaene for compiling HRS photometry as well as the many interesting and pleasant discussions. I would also like to thank everyone who helped me administratively to make my (joint) PhD possible.

Next I would like to extend a special thanks to my colleagues (both in Christchurch and Ghent) for the support and for the very nice memories. In Christchurch I have very much enjoyed the casual chats, the outside-work excursions, the Friday cake days, and of course, the golden mile. The S9 group in Ghent I would like to thank for their friendly welcome, the nice atmosphere and the enjoyable lunches.

I have also had the luck to have the support of an amazing group of friends. To everyone in and around the Haast Eagle Academy, I will never forget the amazing times I had while there. You are a fantastic group of the most open-minded, friendly, and fun people I have ever had the pleasure to meet. Thanks also to the fysicasa crew for the support and fun times as well as all the amazing memories both in the last half year and during the bachelor and master years. A special shout out to Jelle for managing the challenging feat of staying in touch with me throughout my travels and even making it all the way across the world for a visit.

Last but not least, some very special people deserve a very big thanks. Moeke, Jan en Lukas, I am eternally grateful for your unwavering support, for encouraging me in all my endeavours, even if they take me to the other side of the world. Thank you for everything. Moeke, I cannot thank you enough for all the things you have ever done for me. You are the best. And then finally, I would like to thank Ariadna from the bottom of my heart, for all your love and daily support during both the highs and lows of this PhD. You are amazing and I would not have been able to do it without you.

Table of contents

Chapter 1

Introduction

1.1 Thesis overview

One of the main challenges for extragalactic astronomy is to understand how the baryonic components of galaxies evolve from simple clouds of unenriched atomic gas into complex systems consisting of stars, dust, heavy elements and the different gas phases we observe today. This transformation is driven by the ongoing star formation in galaxies, yet there are many other poorly understood interactions between the different constituents that strongly affect the evolution. The physical properties of the galaxy population have been observed to change over time. For example, the stellar mass is built up monotonically, and the star formation rate within galaxies has changed drastically over the past $\sim$ 10 billion years. The main challenge in galaxy evolution is to procure a more detailed understanding of the various physical and chemical processes responsible for the observed changes in the physical properties of galaxies.

Galaxies evolve over cosmic time, and thus much too slow to observe any changes directly. In order to study how the physical properties of a galaxy change, they need to be compared to the physical properties of galaxies at different evolutionary stages. There are two approaches to achieve this. The first one is to study the average change in the galaxy properties with redshift. Many studies (see next sections) have used this approach to study the redshift-evolution of various galaxy properties and these have dramatically changed our understanding of galaxy evolution. However, because of the difficulties of observing very distant objects, this method can only be used to study the evolution out to a given limiting redshift, which is determined by the used wavelength and telescope. Especially for atomic hydrogen (HI) gas, which has a hyperfine emission line at 21 cm, the current generation of telescopes strongly restricts the observations to the relatively nearby Universe. And since the HI gas is a key component in galaxy evolution, it is hard to get a detailed understanding of galaxy evolution beyond the local Universe.

One way to extract information for HI beyond the most nearby sources is to use a 'stacking' analysis technique. Stacking is the process of combining many low signal-to-noise observations of different individual objects in order to retrieve a high-significance statistical detection (e.g. Delhaize et al., 2013). This technique enables studies of the changes in average galaxy properties out to larger distances (and thus larger lookback times). Part III of this thesis describes the 'HI-stacking' analysis of dust-selected sources.

The second approach to study galaxy evolution is to investigate the differences in galaxy properties between galaxies at different evolutionary stages, rather than between galaxies at different times. In this context, the evolutionary stage of a galaxy can be defined by its gas fraction, i.e. by how much gas has been converted into stars. So as galaxies evolve, they move from high to low gas fractions and the changes in the physical galaxy properties are studied as a function of gas fraction rather than as a function of time. The rate at which galaxies evolve is determined by their star formation rate, which is in turn dependent on the galaxy's halo mass and environment. Galaxies span a wide range of halo masses and environments, and hence a correspondingly large range in star formation rates. By the current epoch, some galaxies have converted most of their gas into stars, whereas others still mainly consist of gas. Galaxies in the local Universe span a range of different evolutionary stages due to the differences in their star formation histories. Depending on how the sources are selected, a sample can consist of more evolved or more unevolved sources. In Part I of this thesis, we present a local HI-selected sample and compare to a local stellar mass selected and local dust-selected sample in order to study the changes in galaxy properties over as much of the evolutionary track as possible.

Galaxy evolution entails much more than the formation of stars from the available gas. As stars evolve, they synthesise metals (i.e. all elements except hydrogen and helium) in their cores, and subsequently expel them into the interstellar medium (ISM) at the end of the stars' lives. About half of these metals are locked up in dust grains (Whittet, 1992). This dust absorbs about 30 to 50% of the optical light emitted by galaxies (e.g. Driver et al., 2016; Viaene et al., 2016) and enshrouds some of the most interesting environments in these galaxies. It is therefore difficult to develop a thorough understanding of galaxy evolution without also understanding how dust affects the observations. In Part I of this thesis we will put additional focus on the dust content of galaxies selected by their HI, dust and stellar content. In Part II, we determine the metal content of the same galaxies and study how dust is formed and destroyed by comparing dust and chemical evolution models (that predict the build-up of dust, gas and metals) with observed galaxy properties.

This thesis describes three distinct, but closely related, research projects I conducted during the course of my PhD, all dealing with cosmic dust and HI gas in the context of galaxy evolution. This introductory chapter briefly summarises the current theoretical and

observational framework of galaxy evolution, with a focus on cosmic dust and HI gas. Chapter 2 explains how we have selected the HIGH sample (HI-selected Galaxies in H-ATLAS) and dealt with observational issues. Chapter 3 describes the pipeline that was developed to perform the photometry and the SED fitting code that was used to determine the galaxy properties. Chapter 4 details the scaling relations between the different galaxy properties and how the galaxy properties of HIGH compare to a stellar selected and dust-selected sample. Chapter 5 explains how metallicities have been derived using fibre optical spectroscopy. In Chapter 6, we study dust sources and sinks by comparing models of the build-up of dust, gas and metals with the observed properties of galaxies. Chapter 7 presents the HI-stacking methods and preliminary results. Finally, in Chapter 8 we summarise our conclusions and describe potential future work.

1.2 Galaxy evolution

The first stars and small galaxies started to form a few hundred million years after the Big Bang. Galaxy formation and evolution are best decribed within the framework of Λ-Cold Dark Matter Cosmology (ΛCDM; see review in Liddle, 2003). In this model, most of the energy in the Universe is in the form of dark energy (Λ), and quantum fluctuations shortly after the Big Bang lead to regions of over- and under-density (Starobinskii, 1978; Linde, 1982). As the Universe expanded and cooled, and more and more primordial gas (mainly hydrogen and helium) started to contract onto over-dense regions, the conditions for star formation were met. Not much is known about the first galaxies, since with current telescopes, these are only observed as faint 'blops' at best. However, this field is evolving rapidly, and several large extragalactic surveys have now resulted in the identification of a large number of galaxies at $z \sim 7-8$ (e.g. Schmidt et al., 2014; McLure et al., 2013; Finkelstein et al., 2015), and even some $z \sim 9-11$ candidates (e.g. Oesch et al., 2013; 2014; 2016; Ellis et al., 2013; Calvi et al., 2016). However, spectroscopic confirmations of these very high-redshift candidates remains very challenging, and only a few galaxies have confirmed redshifts (e.g. Shibuya et al., 2012; Zitrin et al., 2015). The James Web Space Telescope (JWST), scheduled to launch in October 2018, will provide the next leap forward in this field.

The main driver of galaxy evolution is the ongoing star formation in galaxies. Atomic gas cools and condenses into molecular clouds that then collapse in the formation of new stars. At the same time, the interstellar medium (ISM) is enriched by heavy elements that have been synthesised in stellar cores (nucleosynthesis) during the stars' lifetime and are then expelled into the galactic environment (see Thielemann et al., 2001 for a review). The rate at which the metallicity (relative abundance of heavy elements compared to hydrogen) of a galaxy changes

depends strongly on the initial mass function (IMF; the mass distribution of newly formed stars) and the star formation efficiency of the galaxy (e.g. Bastian et al., 2010). The more massive a star is, the hotter its core due to gravitational pressure, and the faster the nucleosynthesis (which is why massive stars are more short-lived). For relatively low mass stars, hydrogen is mainly fused into helium, yet other elements like carbon, nitrogen and oxygen are also present. Due to the higher temperture and pressure in their core, high mass stars go on to fuse heavier and heavier elements. For the most massive stars, the fusion finally produces iron, at which point no further energy can be gained from fusion and the thermal pressure in the core will start falling. As a result the core implodes and then explodes as a supernova, which produces even more heavy elements, and expels the produced metals into the ISM (Woosley & Weaver, 1995). All elements heavier than beryllium have been synthesised in stars and all natural elements heavier than iron in supernovae. Supernovae can also heat, compress and/or blow gas out of the galaxy in a 'galactic wind', and thus can both inhibit and enhance star formation in galaxies (Efstathiou, 2000).

As star formation went on as early galaxies evolved, the associated supernovae seeded the galaxies with the first heavy elements and heated the surrounding gas. This heating stabilised the contraction of the primordial gas and, due to conservation of momentum and the second law of thermodynamics, the gas settled slowly in a rotating disk (e.g. Fall & Efstathiou, 1980). In contrast to the abundant spiral and elliptical galaxies in the local Universe, the earliest galaxies still had very irregular morphologies, as not enough time had passed for the gas and stars to settle and because of the ongoing interactions between nearby galaxies. Many of these earliest galaxies merged with each other to form larger and larger galaxies as time went on. In Figure 1.1, we show an illustration of a timeline showing that in the early Universe, all galaxies started as irregular galaxies, whereas in the local Universe we find a mix of spiral, elliptical and irregular galaxies.

The two main reasons galaxies in the local Universe have different morphologies, are the different initial conditions of each galaxy and differences due to environmental processes. There is a strong observed dependence between a galaxy's mass and its evolutionary stage (and gas fraction), which is referred to as 'downsizing' (Cowie et al., 1996). The irregular galaxies in the local Universe typically have small masses, where the small gravitational potential was not enough for the components to settle in a more or less stable orbit. There are also more massive irregular galaxies that had a recent merger. Spiral galaxies have larger masses and their angular momentum was large enough for the components to settle into a stable thin disk. For elliptical galaxies the angular momentum is smaller (relative to the density) and the components settle in a more spherical distribution. The angular momentum for each galaxy is determined both by its

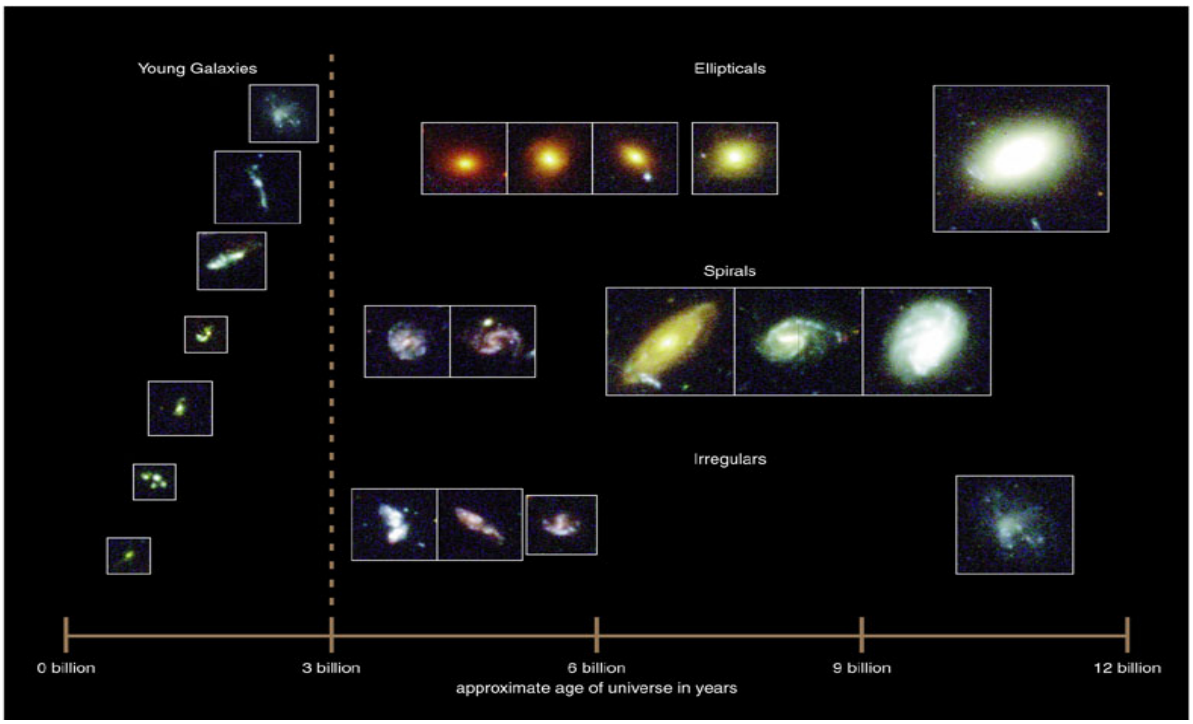

Figure 1.1: Timeline illustration of galaxies in the early and local Universe. Galaxies all started out as irregular galaxies, but then evolved into the different galaxy morphologies we observe today. Image credit: Pearson Education

initial conditions and the mergers (and other environmental processes) it has undergone since formation.

On average, elliptical galaxies are most evolved (most gas converted into stars), followed by spiral galaxies and then irregular galaxies. The classification in the Hubble sequence of ellipticals as Early Type Galaxies (ETGs) and spirals as Late Type Galaxies (LTG) is thus somewhat confusing. Our current understanding is that the massive ETGs seen in the modern Universe are the result of mergers in its history (e.g. Glazebrook, 2013), which are more common in dense regions of space like galaxy clusters. If a significant amount of gas is present, these mergers result in a period of intense star formation, also called 'starbust' (e.g. Mihos & Hernquist, 1996), and account for the peak in the star formation rate of the Universe seen at $2 < z < 3$ (Madau & Dickinson, 2014a). These periods of intense star formation rapidly exhaust the gas reservoir of the galaxies, and they are quenched thereafter, leaving behind the 'red and dead' ETGs seen today. Quenching can arise either because the increased SFR exhausts the whole gas reservoir (Barnes & Hernquist, 1992; Mihos & Hernquist, 1994) or because Active Galactic Nuclei (AGN) and supernovae blow the gas out of the galaxy (Springel et al., 2005; Croton et al., 2006). Galaxy clusters at higher redshift ($z > 0.2$) appear to contain more blue and spiral galaxies than their counterparts in the local Universe (Butcher & Oemler,

1978; Wirth et al., 1994). In isolated galaxies, star formation appears to have evolved more steadily, at a rate dependent on the mass.

1.3 Cosmic dust

1.3.1 Extinction and emission by dust

30 to 50% of the radiative energy produced by galaxies is absorbed by dust and thermally re-emitted in the Far-InfraRed (FIR) and submillimetre (submm) (Fixsen et al., 1996; Hauser & Dwek, 2001; Dole et al., 2006; Dale et al., 2007; Driver et al., 2007; Burgarella et al., 2013; Driver et al., 2016; Viaene et al., 2016). Dust thus not only significantly affects the UltraViolet (UV) and optical observations of galaxies, it also provides a window (FIR/submm) to study the ISM of galaxies. Many of the key processes that affect galaxy evolution happen in the ISM. During the last century, dust has thus gone from being a nuisance for optical and UV astronomy, to one of the most important tools to understand galaxy evolution.

By absorbing photons or scattering them from the line of sight, dust hides some of the most interesting environments in galaxies. Stars are formed in dense interstellar clouds, which are heavily obscured by dust. In order to study stars still in their stellar nurseries, one needs to correct the observations for extinction by dust. However, not all wavelengths are equally affected by dust. The Near-InfraRed (NIR) is only barely obscured by dust whereas the obscuration increases significantly towards shorter wavelengths, as shown in Figure 1.2. The light from massive stars, which have higher surface temperatures and thus emit light at shorter wavelengths, is therefore more heavily obscured than the light from lower mass stars. Because massive stars are short-lived, they are a good tracer of recent star formation. Star formation estimators are thus particularly sensitive to obscuration, and need well constrained obscuration corrections.

As the dust absorbs the stellar emission, it is heated and consequently, it thermally re-radiates this energy at longer (FIR/submm) wavelengths. By observing this longer-wavelength emission by dust, we can probe the galaxy environments that were previously hidden from view. A system in (quasi-) thermal equilibrium emits the same amount of energy it absorbs. Figure 1.3 shows the Spectral Energy Distribution (SED) for the evolved galaxy NGC4030 and for the more immature galaxy UGC09299. The black line shows the model SED from the MAGPHYS library that best fits the observations. The SEDs can be divided in two main parts: the stellar SED and the dust SED. The dust SED describes the re-radiated dust emission at wavelengths $\lambda \gtrsim 5$ μm. At shorter wavelengths, the emission is dominated by stellar radiation. Figure 1.3 also shows a blue curve, which is the stellar SED before obscuration. The difference

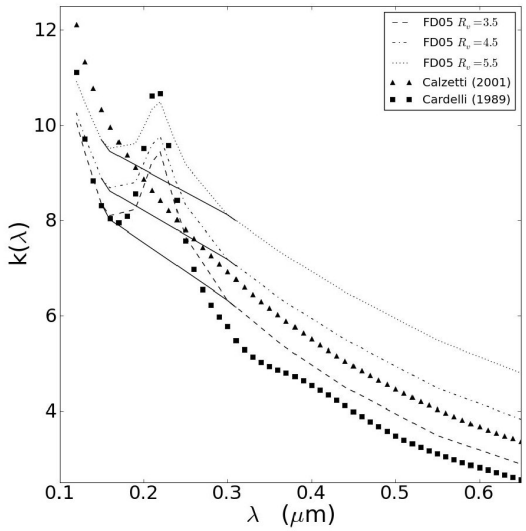

Figure 1.2: Obscuration curves showing how dust obscuration depends on wavelength. Short wavelengths (UV) are much more obscured than longer wavelengths (NIR). The shown obscuration curves are from Cardelli et al. (1989), Calzetti (2001) and Fischera & Dopita (2005), labelled as FD05 (Rv = 3.5, 4.5, 5.5). This figure was taken from Wijesinghe et al. (2011).

between the blue and black curve in the stellar part of the SED is the amount of energy that is absorbed by dust. Because of conservation of energy, this is equal to the energy under the black curve in the dust emission part of the SED. The obscuration for the evolved galaxy NGC4030 is clearly larger than the more immature galaxy UGC09299 (see also Chapter 4). By constraining the dust SED by FIR-submm observations, we can study the dust properties of galaxies and constrain the dust obscuration and are thus also able to determine better obscuration corrections to the UV-NIR observations.

1.3.2 LTE and NLTE dust emission

Dust is made up of grains with significantly different sizes. The precise size distribution is not well constrained (Jones et al., 1996) but ranges broadly from $\sim$ 10 nm to $\sim$ 10 μm (Kim et al., 1994). As a result of this, there are two emission regimes within the dust SED of a galaxy: local thermal equilibrium (LTE) and non-local thermal equilibrium (NLTE). The latter is for very small dust grains (or polycyclic aromatic hydrocarbon molecules; PAHs). For larger dust grains, the absorption of a single photon does not excite the grain to very high energy levels and the grains remain in thermal equilibrium with their environment. A blackbody emitter in thermal

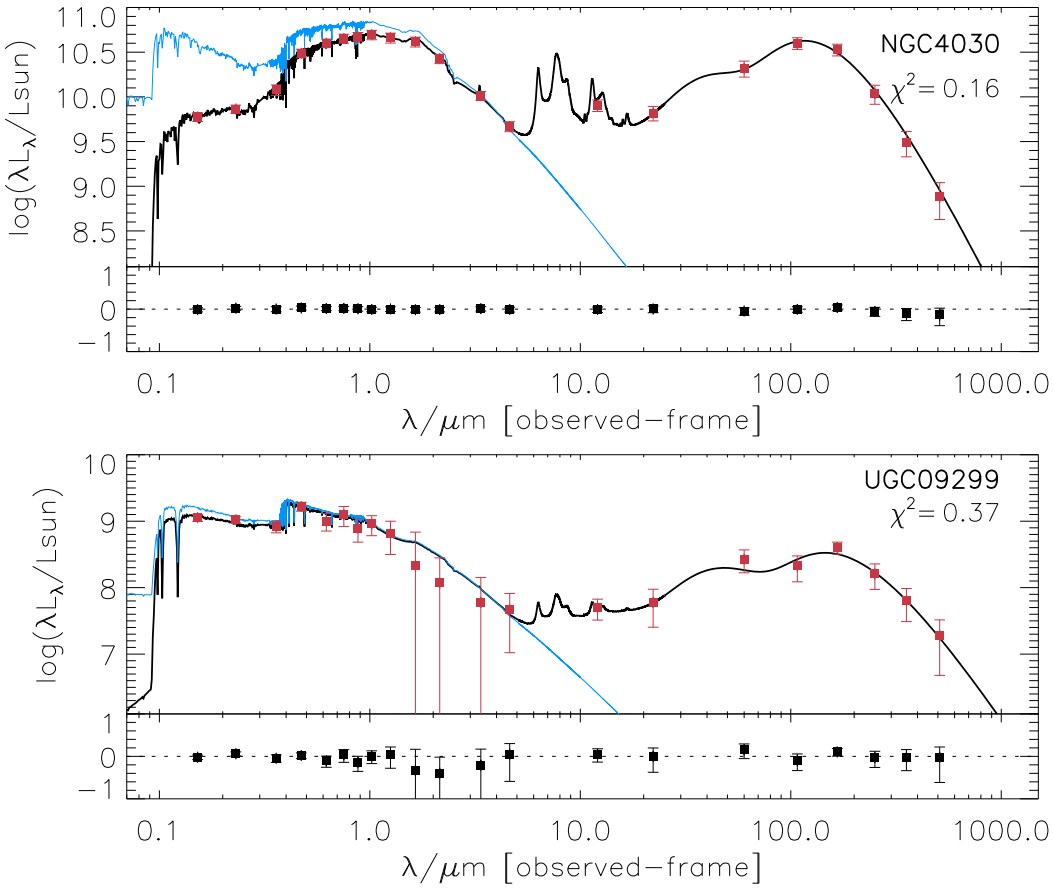

Figure 1.3: Spectral Energy Distributions for the evolved galaxy NGC4030 an for the more immature galaxy UGC09299. The best fitting model is compared to the observed fluxes. The black curve shows the best fit model SED to multiwavelength observations. The blue curve shows how the stellar SED would look without any obscuration.

equilibrium with its environment has a temperature T described by the Stefan-Boltzmann law:

$$T^4 = \frac{Uc}{4\sigma} \tag{1.1}$$

where U is the energy density of the local radiation field, c is the speed of light, and σ is the Stefan-Boltzmann constant. The spectrum for a blackbody at that temperature in function of frequency ν is given by the Plank function $B_\nu(T)$:

$$B_\nu(T) = \frac{2h\nu^3}{c^2}\frac{1}{e^{\frac{h\nu}{kT}} - 1} \tag{1.2}$$

where h is the Planck constant, and k is the Boltzmann constant. The fluxes S_ν of a source are proportional to mass of dust M_d, and inversely proportional to the distance squared D^2. For a

blackbody emitter, the spectrum will thus be given by:

$$S_\nu = \frac{\kappa_\nu M_d B_\nu(T)}{D^2} \tag{1.3}$$

where κ_ν is the dust mass absorption coefficient, which for a blackbody emitter is a constant and just describes the constant of proportionality. However dust is a not an ideal emitter and thus cannot be described with an ideal blackbody. Instead, the spectrum is modified to account for changes in the efficiency with which the object emits at different frequencies. This can be achieved by making κ_ν frequency dependent. In the FIR/submm regime, κ_ν can be described as:

$$\kappa_\nu \simeq \kappa_{\nu_0} \left(\frac{\nu}{\nu_0}\right)^\beta \tag{1.4}$$

where β is the emissivity index. It is possible to determine β by observing the dust emission SED, as it is the spectral index of the power-law slope of the Rayleigh-Jeans tail. There is observational (Dunne & Eales, 2001; Clemens et al., 2013; Smith et al., 2013) and experimental (Demyk et al., 2013) evidence that suggests $\beta = 2$ is an appropriate value for emissivity index for cold dust in local late type galaxies, though in general it is found to be $1 \leqslant \beta \leqslant 2$ for various types of dust. Large dust grains thus radiate as a modified blackbody with a spectrum described as:

$$S_\nu \propto \nu^\beta B_\nu(T) \tag{1.5}$$

and the dust mass is given by:

$$M_d = \frac{\nu_0^\beta S_\nu D^2}{\kappa_{\nu_0} \nu^\beta B_\nu(T)} \tag{1.6}$$

κ_{ν_0} is dependent on many poorly constrained variables like the dust grain size, density, shape, chemical composition, and so forth. The uncertainty on this value is generally thought to be about an order of magnitude (James et al., 2002). Two often used values are $\kappa_{850} = 0.077$ m^{2}kg^{-1} (Dunne et al., 2000; James et al., 2002) and $\kappa_{350} = 0.192$ m^{2}kg^{-1} (Draine, 2003). Though it is also possible that κ_ν varies from galaxy to galaxy, which would lead to potential significant offsets between the real and estimated dust masses of galaxies.

When very small grains absorb a single optical/UV photon, the internal energy of the grain is increased so much its temperature reaches a much higher temperature than the surrounding environment. Subsequently, the grain emits at shorter wavelengths (mid-infrared) and its emission spectrum varies over time. This NLTE emission is visible in Figure 1.3 as the peaks in the model SED between 5 μm $< \lambda <$ 20 μm. This process is called stochastic heating and is much harder to describe than LTE emission. We refer the reader to Camps et al. (2015) for a more detailed discussion.

Due to differences in the local radiation field experienced by different dust grains, the dust in any given galaxy (or even along any given line of sight within a galaxy) will not be at one uniform dust temperature, but instead at a range of different temperature. However since the limited amount of observational data, we cannot disentangle the modified blackbody spectra for all different temperatures. Instead, a common approach is to model the dust emission using a limited number of dust components. Often, the main components used are a cold ($10 < T < 30$ K) dust component, which makes up the bulk of the dust mass, and a warm ($30 < T < 60$ K) component, which despite a limited amount of dust mass can make up a significant fraction of the dust luminosity ($L_d \propto T^{4+\beta}$). Other typical dust components at shorter wavelength include hot dust and NLTE dust. These 4 different components have been used in the modelling of the dust SED in Figure 1.3 (see Section 3.4 for details).

1.3.3 Dust lifecycle

Dust is made up of heavy elements synthesised in the cores of stars. There are large uncertainties to the shape (nearly spherical or amorphous/'fluffy') and size distribution of dust grains. The chemical composition of dust grains is also not well known, though carbon and silicate are believed to be the most important constituents. By observing the gas phase of interstellar clouds with significant amounts of dust, one can determine which elements have been depleted in the formation in this dust[1]. It is found that dust mainly consists of Si, C, O, Mg, and Fe (Jenkins, 2009; 2013). The largest grains can have mantels of ice, formed by accretion of (gas phase) atoms and molecules of O, C, N, S along with hydrogen.

Dust is continuously produced and destroyed by means of several mechanisms. Figure 1.4 shows an illustration of the different main processes associated to the dust life cycle. Dust is formed in the winds of evolved low-to-intermediate mass stars (LIMS) as they reach the Asymptotic Giant Branch (AGB) phase of their lives (Ferrarotti & Gail, 2006; Sargent et al., 2010), and in core-collapse supernovae (SN) ejecta as massive, short-lived stars end their lives (e.g. Dunne et al., 2003; 2009; Barlow et al., 2010; Matsuura et al., 2011; Gomez et al., 2012b; Indebetouw et al., 2014; Gall et al., 2014). Some of the produced dust and metals will stay in the molecular clouds they were formed in, and some will dissipate into the diffuse ISM. As the molecular clouds collapse to form the next generation of stars, the newly formed dust will be consumed together with the gas as fuel for the stars. This form of dust destruction is called 'astration'. Supernovae shocks also destroy dust as high-energy ions 'sputter' atoms from the surface of dust grains (Barlow, 1978; Draine & Salpeter, 1979; Jones et al., 1994), and collisions between dust grains also break them up (Jones et al., 1996; Jones & Nuth,

[1] This also affects gas cooling since dust locks away some important gas coolants such as C^+ and Si^+ (Bekki, 2015; McKinnon et al., 2016).

2011). Additional processes such as thermal sputtering, and ionising destruction by cosmic rays, high-energy photons, and free elections further reduce the dust mass (see Jones, 2004 for a review). The predicted timescale for dust destruction in the ISM is of the order of 10^8 years. If this rapid destruction does occur, then the majority of the dust grains must be (re-)formed there (Jones & Nuth, 2011), and dust grain growth in the ISM is necessary.

There are strong indications for grain growth in the ISM as dust grains acquire additional mass from the gas phase by accretion (Mattsson et al., 2012; Asano et al., 2013a; Zhukovska, 2014). Recent studies require efficient dust production by supernovae, efficient grain growth and/or low efficiency of grain destruction by SN shocks to explain the quantities of dust observed in both high- and low-redshift galaxies (Morgan & Edmunds, 2003; Dwek et al., 2007; Michałowski et al., 2010; Matsuura et al., 2009; Gall et al., 2011a; Dunne et al., 2011; Rowlands et al., 2014b). Understanding the balance between these sources and sinks of dust, and their differing contributions in various phases of galaxy evolution, is a challenge, and remains an important ongoing area of research (e.g. Aoyama et al., 2016).

Another important role of dust is that it catalyses the formation of molecular hydrogen and other molecules[2] (Gould & Salpeter, 1963). The H_2 molecule is the main component of molecular clouds, and is thus the raw material out of which stars are formed. On top of this, dust shields the molecules in molecular clouds by absorbing the energetic radiation from young stars. This allows the clouds to cool further and enables them to collapse to form the next generation of stars. Dust thus facilitates one of the processes out of which it is born.

1.3.4 Herschel Space Observatory

Dust properties have been investigated for several decades using IR Space telescopes such as IRAS (Neugebauer et al., 1984), ISO (Kessler et al., 1996) and *Spitzer* (Werner et al., 2004) and ground based submillimetre instruments as SCUBA (Holland et al., 1999), SCUBA2 (Holland et al., 2013) and LABOCA (Siringo et al., 2009). However, with the advent of the *Herschel Space Observatory* (hereafter *Herschel*, Pilbratt et al., 2010) we have entered a new era for interstellar dust studies. The angle of the research in this thesis is that it combines HI observations with *Herschel* observations to study the interaction between gas and dust in the context of galaxy evolution. Given its importance, we describe *Herschel* in some detail in this section.

Herschel (illustrated in Figure 1.5 left) is one of the European Space Agency's (ESA) cornerstone missions and was succesfully launched on the 14$^{\text{th}}$ of May 2009. Due to its 3.5 m diameter, *Herschel* has superior angular resolution and sensitivity compared to previous FIR

[2]Dust is thus both a production site and reservoir for the more complex molecules that planets, and thus life, are made from.

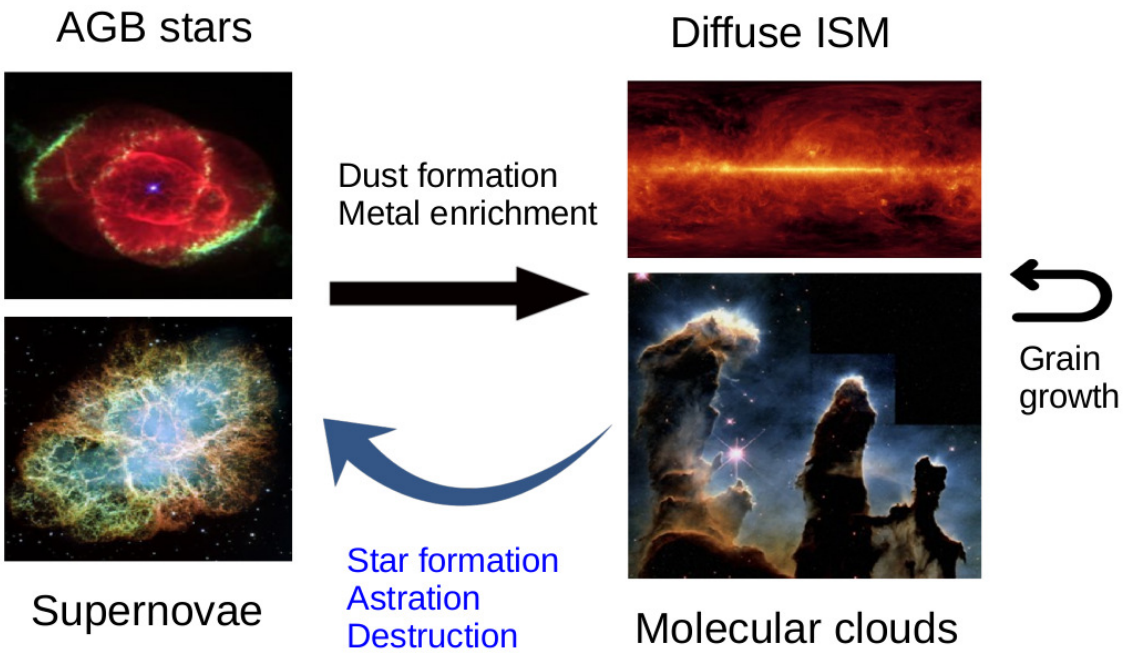

Figure 1.4: Illustration of the dust life cycle. Dust is produced in the winds of low-to-intermediate mass stars in the Asymptotic Giant Branch (AGB) phase and in core-collapse supernovae (SN) as massive, short-lived stars end their lives. As a result of the ongoing star formation in molecular clouds, destruction by SN shocks and astration removes dust and returns it to metals. Dust grains also acquire additional mass from grain growth.

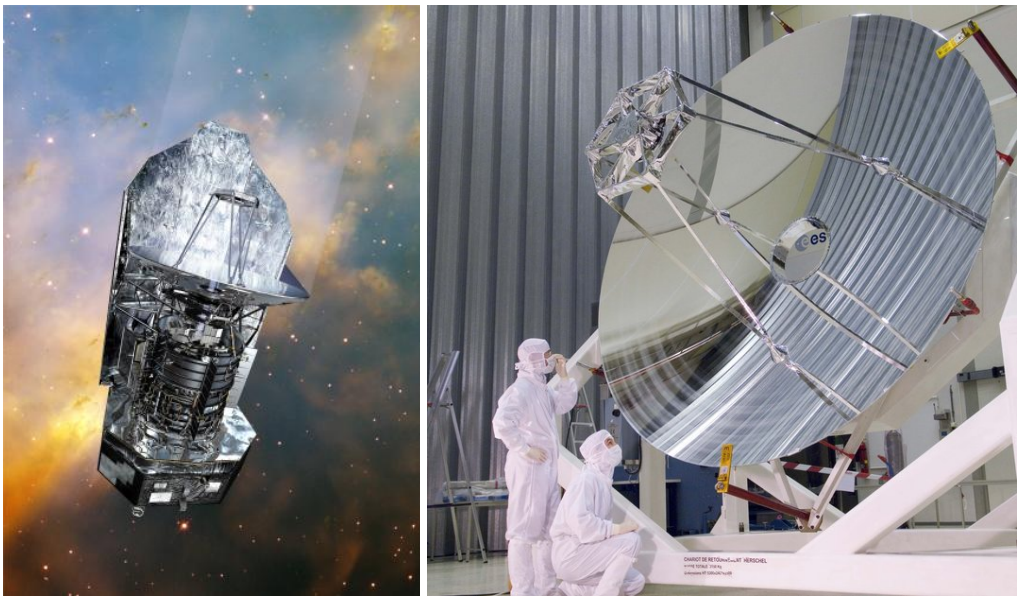

Figure 1.5: *Left:* Artist impression of the *Herschel* Space Observatory. Image Credit: UK *Herschel* outreach. *Right:* Herschel's 3.5 m primary mirror at ESTEC. Image credit: ESA

missions and it operates at longer wavelengths ($70-500\,\mu$m), making it sensitive to the diffuse cold ($T < 30$ K) dust component that dominates the dust mass in galaxies (Dunne & Eales, 2001; Draine et al., 2007; Law et al., 2011; Ford et al., 2013; Hughes et al., 2014).

The FIR and submm wavelengths are particularly hard to observe. The main reason is the opacity of the atmosphere at FIR and submm wavelengths, as illustrated in Figure 1.6. There are some atmospheric windows towards the long wavelength end of the submm, for which observations can be made from very arid high-altitude sites (e.g. ALMA operates from the Atacama Plateau). Even so, these submm observations remain affected by atmospheric absorption and background emission and in the FIR the opacity of the atmosphere is too high for any ground based observations. Therefore FIR/submm observations are primarily done from space.

The *Herschel* telescope is a classical Cassegrain telescope and has a primary mirror of 3.5 m (shown in Figure 1.5 right). This mirror is the largest ever deployed in space and is 4 times larger than that of any previous orbital telescope operating in this wavelength range. One of the main reasons a large mirror is vital for FIR and submm observations is the diffraction limit:

$$\theta \simeq 1.22\,\frac{\lambda}{D} \tag{1.7}$$

where θ is the resolution, λ is the wavelength and D the diameter of the primary mirror. The resolution at submm wavelengths will thus be ~ 1000 times worse than in the optical and a large mirror is key to get to obtain resolved observations (and to limit confusion[3]). Additionally, the large mirror is important for the sensitivity of the observations (scales with the squared radius of the primary mirror). The mirror for *Herschel* was the largest possible that would still fit inside the Ariane V rocket used to launch *Herschel* into orbit.

Another issue with FIR and submm observations, is the thermal emission of the telescope itself. *Herschel* emits light at the very same wavelengths it was designed to observe. In order to mitigate this, the *Herschel* instruments are placed in a cryostat and are cooled using liquid helium to a temperature of 1.6 K. The lifetime of Herschel's mission is limited by its reservoir of liquid helium. On 29$^{\text{th}}$ April 2013, almost 4 years after launch, the last of the helium boiled off. Due to the limited helium reservoir, it would be impossible to cool the telescope mirrors to the same temperature. Therefore both mirrors are passively cooled to the environmental temperature of about 85 K by the use of sunshields. Even with this shielding, the thermal emission from the primary mirror is still the primary source of instrumental noise during normal operation.

[3]When multiple unresolved sources (such as distant galaxies) are located with smaller angular separation than the resolution of the observations, it is not possible to determine how much of the flux originates from each source.

A final difficulty is the detection of photons at FIR and submm wavelengths. At shorter wavelengths, it is possible to use photoconductors, in which the photons excite electrons, which leads to measurable changes in the conductivity. However in order for photoconductors to achieve this, the photon's energy must be greater than the photoconductor's band gap. The energy of a FIR photon can just be enough to excite electrons past the band gap[4], yet the energy of a submm photon is insufficient for this to work. At wavelengths longer than the submm, it becomes possible to use antennae to detect incident radiation. However, for *Herschel* the best detectors for the photometers are bolometers. A bolometer is an electrical instrument that measures incoming radiation. It is typically a thermistor cooled to extremely low temperature, such that even when small amounts of low-energy radiation are absorbed by the thermistor, its temperature changes enough to produce a measurable difference in its resistive properties.

Herschel has three scientific instruments aboard – SPIRE, PACS, and HIFI. HIFI is the dedicated spectrometer and PACS and SPIRE contain both photometers and spectrometers. Together these provide full photometric and spectroscopic coverage of the $52-670$ μm wavelength range. Only the PACS and SPIRE photometers are used in this work and described in the following paragraphs.

PACS

The Photodetector Array Camera and Spectrometer (PACS; Poglitsch et al., 2010; PACS observers manual[5]) operates across the $60-210$ μm wavelength range. The PACS photometer observes in three photometric bands, centred at wavelengths of 70, 100 and 160 μm respectively. The transmission profiles of the three bands are shown in Figure 1.7 (left). However, PACS only has two filled arrays of bolometers. In one run, one can only observe one of the two shorter wavelength bands (together with the 160 μm band). The shorter wavelength bands are observed by a 2048 element array and 160 μm band by a 512 element array. The FOV for both is $3.5' \times 1.75'$.

PACS can conduct mapping in several different scanning modes. The standard mapping mode is the scan mapping mode with a speed of $20''$ s^{-1}, yet a faster mapping speed of $60''$ s^{-1} is also available. The latter leads to an increase in the ellipticity and Full-Width Half-Maximum (FWHM) of the Point Spread Function (PSF), particularly for the shorter wavelength band.There is also a mini-scan mapping mode, which produces a $3'$ region of full coverage. Mapping is typically done with orthogonal sets of scans. This permit the isolation of time-variant instrumental noise, and also reduces the ellipticity of the PSF when using fast scan mode.

[4]By stressing the photoconductors, it is possible to decrease the band gap to allow the use of photoconductors up to wavelengths of 210 μm.

[5]http://herschel.esac.esa.int/Docs/PACS/pdf/pacs_om.pdf

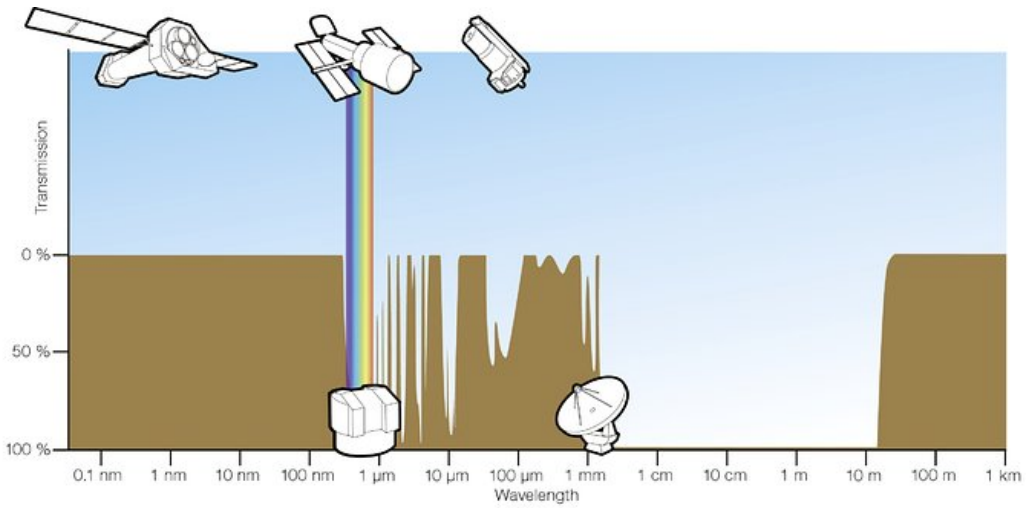

Figure 1.6: In this graph, the level of the brown curve represents how opaque the atmosphere is at the given wavelength. Ground-based astronomy is mostly confined to the visible and radio atmospheric windows, wavelength ranges in which the atmosphere is nearly transparent. ALMA operates in a borderline region, where the opacity depends strongly on how high and dry the site is. Space telescopes are necessary to observe the FIR (and most of the submm). Image Credit: ESA/Hubble (F. Granato)

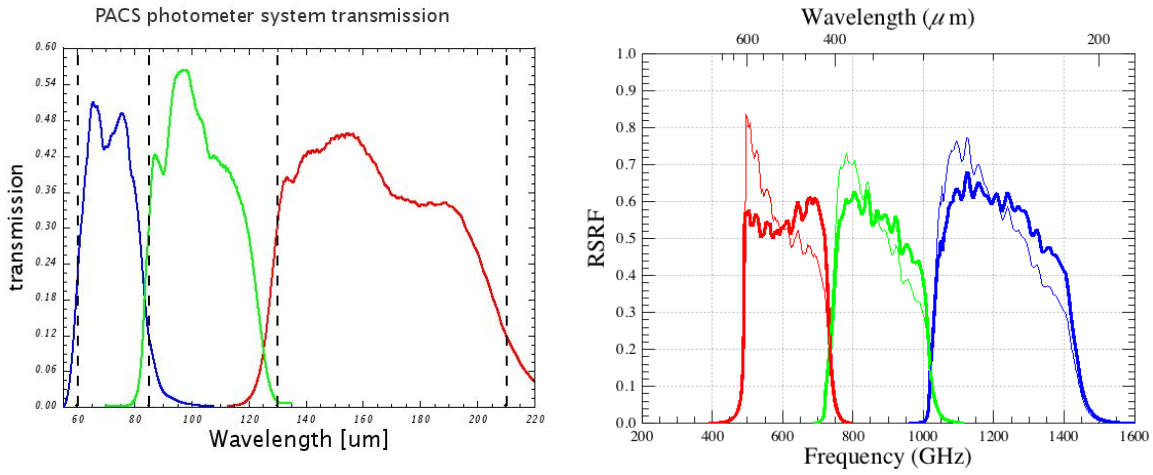

Figure 1.7: *Left:* Filter response in function of wavelength for the 70μm (blue), 100μm (green) and 160 μm (red) PACS bands. Image taken from the PACS observers manual. *Right:* Filter response as a function of frequency for the 250μm (blue), 350μm (green) and 500μm (red) SPIRE bands. Image credit: NASA *Herschel* science center.

SPIRE

The Spectral and Photometric Imaging Receiver (SPIRE; Griffin et al., 2010; SPIRE handbook[6]) contains a photometer and a low-resolution spectrometer covering 194 to 672 μm. This wavelength range is particularly important for constraining the temperatures of cold dust, which often dominates the dust mass. SPIRE has a photometer with a FOV of $4' \times 8'$ that simultaneously images three photometric broad bands centred around 250, 350, and 500 μm, observed with arrays of 139, 88, and 45 bolometers respectively. The response function of the three SPIRE bands are shown in Figure 1.7 (right). A full sampling of the FOV requires the instrument to scan across the target area, continuously taking observations.

SPIRE can also conduct mapping in several different scanning modes. The large map mode can provide maps for arbitrarily-sized regions of sky and has two scan speeds. The normal scan speed is $30''$ s^{-1}, yet a faster mapping speed of $60''$ s^{-1} is also possible. As for PACS, mapping is typically done with orthogonal sets of scans, which permits the isolation of time-variant instrumental noise. The SPIRE small map mode is set up for individual point or small extended sources. This mode provides coverage of a a $5'$ region of sky and always uses a scan speed of $30''$ s^{-1}.

The PACS photometer can also be operated in parallel with the SPIRE photometer at speeds of either $20''$ s^{-1}, or $60''$ s^{-1}. The scan direction is optimised for SPIRE, which leads to a small further degradation of the PACS PSF. When observing large areas of sky, parallel mode achieves larger observational depths in a given amount of time than would be possible using one instrument, then the other.

1.4 Neutral atomic hydrogen

1.4.1 The importance of HI

Neutral atomic hydrogen (HI) gas is one of the most fundamental components of a galaxy. As previously mentioned in Section 1.2, HI makes up most of the primordial gas out of which galaxies are formed. As it cools, HI is converted into H_2, and condenses into molecular clouds. It is within these clouds that gravity can compress the gas to high enough pressures and temperatures to allow for the formation of stars. HI thus provides the fuel that is indirectly responsible for star formation, and thus for the evolution of a galaxy. The gas fraction is a good measure for how much of the available gas mass has been converted into stellar mass M_*. Throughout this thesis, we define the gas fraction as $f_g = \frac{M_g}{M_* + M_g}$, where $M_g = 1.32\, M_{\rm HI}$ to

[6] http://herschel.esac.esa.int/Docs/SPIRE/spire_handbook.pdf

take into account the mass of neutral helium[7]. Due to the difficulty in obtaining reliable H_2 masses for the different samples in this work, particularly for low stellar mass sources, we do not take into account any molecular component. We do estimate the effect including H_2 has on our results and find it does not change our conclusions.

Throughout this work we define the evolution of a galaxy as the transition from high gas fraction to low gas fraction and assume that this transition is dominated by the process of star formation converting gas mass to stellar mass. Another (equivalent) proxy for evolutionary stage is the HI-to-stellar mass ratio $M_{\rm HI}/M_*$. There are a few caveats associated with the use of the gas fraction or $M_{\rm HI}/M_*$ as a proxy of evolution. The most important one is that galaxies are not closed-box systems where there is just a gradual conversion of gas into stars. Gas can be gained and lost by galaxies through gas infall, outflows and merging (e.g. Tinsley, 1980; Jaskot et al., 2015). Additionally we are implicitly assuming that the extended reservoir of HI is a good measure of the fuel available for future star formation (e.g. Stroe et al., 2015). Despite these caveats, the current gas fraction is still a good indicator of the evolutionary state of a galaxy, as regardless of how or when the gas was gained or removed, it is still a snapshot of how much future star formation could be sustained relative to the stars already formed.

In the early Universe HI gas was the dominant (baryonic) component but currently it makes up less then 1% of the (baryon) mass (Prochaska & Wolfe, 2009). There thus has been significant evolution in the HI density of the Universe (and thus also for the average galaxy). The majority of that HI has not been converted to heavier elements, but instead is locked up in stars or exists as hot gas. Since star formation is what consumes the HI, the Star Formation History (SFH) of galaxies is intimately linked to the evolution of the HI density. The SFH of the Universe peaks at a redshift $2 < z < 3$ (Driver et al., 2013; Madau & Dickinson, 2014a, ; and references therein), which is thus also the epoch at which most of the HI was consumed. However, tracing the consumption of HI over cosmic time is a challenge.

There are multiple ways HI is observed in galaxies. At high redshifts, one can study Damped Lyman α (DLA) systems, concentrations of neutral hydrogen gas detected in absorption in the spectra of quasars, to study the cosmic HI density (e.g. Prochaska et al., 2005; Rao et al., 2006; Prochaska & Wolfe, 2009). At low redshift, HI is observed using the neutral hydrogen 21 cm hyperfine emission line. In the nearby Universe, this can be done by direct detection of the HI line. However, the detection of HI becomes increasingly difficult beyond the local Universe using the current generation of telescopes. Nevertheless there have recently been a number of studies that detect HI for a small sample of galaxies beyond $z = 0.1$. The current highest redshift HI detection is at $z = 0.376$ (Fernández et al., 2016). However, because it does not require individual detections, HI-stacking can be used to extract information on the HI content

[7]The primordial gas contains, by mass, 24% helium (Walker et al., 1991).

of large samples of galaxies out to larger redshifts. By combining undetected HI signals of many different sources, identified using external redshift catalogues, it is possible to obtain a statistical detection for the average galaxy (e.g. Fabello et al., 2011a; Delhaize et al., 2013).

The gas content (or gas fraction) of galaxies does not only vary with cosmic time, but also with other galaxy properties such as stellar mass, environment, colour, morphology and so forth. Cluster galaxies are characterized by a significantly lower atomic gas content than similar stellar mass galaxies in the field (e.g. Haynes et al., 1984; Cortese et al., 2011). As previously mentioned in Section 1.2, there is also a strong observed dependence between a galaxy's mass and its evolutionary stage (and gas fraction), which is referred to as 'downsizing' (Cowie et al., 1996). Both mass and environment are important drivers of the rate at which a galaxy evolves from high to low gas fraction. Because of this, different galaxies will have reached different stages of evolution by the current epoch of the Universe. By comparing how other galaxy parameters such as metallicity, dust mass, dust temperature, and obscuration, scale with changes in gas fraction, we are able to study how these parameters change throughout the different stages of a galaxy's evolution.

1.4.2 21 cm observations

Neutral atomic hydrogen in its ground state has two hyperfine energy states, for which the quantum spins of its electron and proton are either parallel or anti-parallel. The parallel state has a slightly higher energy than the anti-parallel state. When the transition from the higher to the lower energy state occurs, the released energy corresponds to the emission of a photon at a wavelength of 21.105 cm (1420.4058 MHz). The mean lifetime in the parallel state is $\sim 10^7$ years, which is much longer than the collision rates between atoms which maintain the relative populations of the two energy levels. There is thus a constant relation between the HI mass $M_{\rm HI}$ of a galaxy and the 21 cm emission it produces:

$$M_{\rm HI} = 2.36 \times 10^5 D^2 \int S(v_{\rm rad})\, dv_{\rm rad} \tag{1.8}$$

where $M_{\rm HI}$ is given in $M_\odot$, D is the distance in Mpc, and $S(v_{\rm rad})$ is the flux density in Jy and $v_{\rm rad}$ the radial velocity in $\mathrm{km\,s^{-1}}$. The integrated flux is thus in units of $\mathrm{Jy\,km\,s^{-1}}$. Here we have to integrate over the galaxy's HI profile because of the rotational velocity of the galaxy and the velocity dispersion of the gas shifting the line in frequency (the intrinsic spread in the frequency of the emitted photons is negligible). Due to differences in the radial distribution of the HI, and in the rotational profile of galaxies, there are large differences between the HI profiles of galaxies, with many galaxies having a 'double-horned' HI profile. We show two examples in Figure 1.8 (same sources as the SEDs in Figure 1.3).

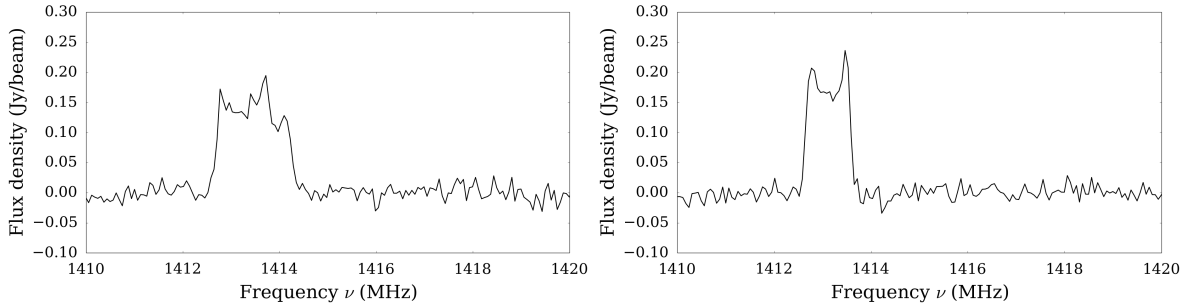

Figure 1.8: HI profile of NGC4030 (*left*), and UGC09299 (*right*). The HI profiles are from the HIPASS survey (Meyer et al., 2004).

Due to the long wavelength of the observations, radio telescopes need very large diameters in order to get decent resolution. Even so, single dish telescopes with large diameters, such as the 64 m Parkes telescope in Australia or the 305 m Arecibo Observatory in Puerto Rico, still have limited resolution compared to telescopes at other wavelengths. The Parkes beamsize at 21 cm is $15.5'$, the velocity resolution is 18 $\mathrm{km\,s^{-1}}$ and the rms noise is 13 $\mathrm{mJy\ beam^{-1}}$. With a beamsize of $\sim 3.5'$ and rms noise of 2 $\mathrm{mJy\ beam^{-1}}$, Arecibo outperforms Parkes in both sensitivity and resolution, yet it can still not resolve the most extended local galaxies used in this work. Both Parkes and Arecibo were fitted with multibeam receivers to drastically increase their instantaneous field of view. This made it possible to scan large areas of sky, instead of pointed observations of known sources. By performing blind large area surveys, one can obtain large numbers of HI sources that have been selected on their HI content alone. In contrast to pointed surveys, no HI-bright galaxies are missed because they are not bright enough in other parts of the spectrum to be selected.

The HI Parkes All Sky Survey (HIPASS; Barnes et al., 2001) was the first survey to perform a blind all-sky survey of atomic gas. The entire sky south of $DEC < +25^\circ$ was mapped out to $z = 0.0423$. This lead to the detection of 5,317 galaxies, for which the HI properties can be found in the HIPASS catalogue (HICAT; Meyer et al., 2004; Wong et al., 2006). This survey provided key insights on the HI content of galaxies in the local universe. HIPASS also allowed for a more accurate determination of the HI mass function in the local universe (Zwaan et al., 2005), as shown in Figure 1.9.

The Arecibo L-band Feed Array (ALFA) 7 beam receiver that was installed on Arecibo in 2004 also has a wide field of view and excellent frequency resolution. This instrument facilitated the Arecibo Legacy Fast ALFA (ALFALFA; Giovanelli et al., 2005; Haynes et al., 2011) HI survey, which is currently ongoing. The full ALFALFA survey is intended to cover 7000 $\mathrm{deg^2}$ of sky in two regions of high Galactic latitude and $0^\circ < DEC < +36^\circ$. Due to the large dish diameter, ALFALFA has better sensitivity and resolution than HIPASS and can thus

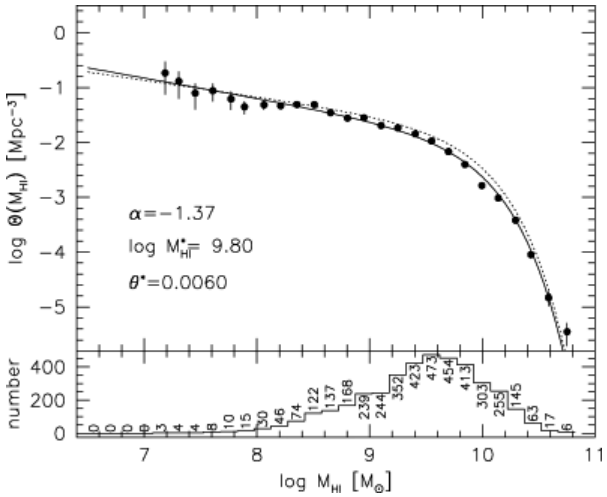

Figure 1.9: The HIPASS HI mass function for galaxies in the local universe. The number of galaxies contributing to each point is shown in the bottom panel. This figure was taken from Zwaan et al. (2005).

detect a larger number of sources, and out to larger redshifts ($z \sim 0.06$). A source catalogue of 40% of the final survey area was presented in Haynes et al. (2011) and contains 15,855 sources.

One complication that arises from the use of poor resolution telescopes, is that often there are multiple galaxies within the same beam of the observation. If these galaxies also have the same radial velocity (i.e. same distance), then it is impossible to distinguish the HI signal from the different sources. Such sources are labelled 'confused' (see also Section 2.3.2). Radio interferometers (e.g. the Karl G. Jansky Very Large Array or JVLA) can obtain better resolution due to the long baselines used, yet are not practical for large area blind surveys, such as the ones used in this work.

1.5 Observing galaxy evolution

1.5.1 Multiwavelength surveys of galaxy evolution

As we have discussed in the previous sections, each different component of a galaxy plays a different role in its evolution. Young, massive stars emit the bulk of their energy in the UV-optical part of the spectrum, and trace star formation. Lower mass stars emit at optical-NIR wavelengths and trace the total stellar mass. The stellar light is attenuated and thermally re-emitted in the FIR/submm by dust. HI can be observed using the 21 cm line, and the warm ionised gas and gas phase metallicities can be inferred from Hα and other optical emission lines. The molecular H_2 cannot be observed directly and is instead inferred from observations of the CO line. Hot ionised gas is the dominant baryonic component in the current Universe

and can be observed by its X-ray emission. Dark matter can by definition not be observed directly, yet can be inferred from galaxy rotation curves, and makes up most of the mass in galaxies. In order to get the best possible understanding of galaxies, it is important to study the interplay between as many of these different components as possible. In order to get a unified picture of galaxy evolution, it is necessary to obtain multiwavelength observations by combining observations from different telescopes.

There are many surveys that provide essential information over a limited range of wavelengths. For example, the Sloan Digital Sky Survey (SDSS; York et al., 2000) has observed millions of galaxies in 5 optical bands as well as provided spectroscopy that can be used to determine redshifts. However because of the importance of dust, the number of surveys that can be used to get a multiwavelength picture of galaxy evolution is limited by the availability of *Herschel* observations, which is essential for reliable dust estimates. Some of the main surveys with *Herschel* coverage are: HeViCS (Davies et al., 2010), the Herschel Reference Survey (Boselli et al., 2010b), the *Herschel*-ATLAS (Eales et al., 2010), KINGFISH (Kennicutt et al., 2011), HerMES (Oliver et al., 2012), and the Dwarf Galaxy Survey (Madden et al., 2013).

The *Herschel* Astrophysical Terahertz Large Area Survey (*Herschel*-ATLAS or simply H-ATLAS) is the largest extragalactic submm survey covering ~ 600 deg^2 (1/80$^{\text{th}}$ of the entire sky) in 5 bands from 100-500 μm. The H-ATLAS is the largest *Herschel* open time Key Project, with 600 hours of observations carried out in fast parallel mode using the PACS and SPIRE instruments. Detailed descriptions of the H-ATLAS data reduction can be found in Valiante et al. (2016). In this work we use the H-ATLAS Phase 1 public data release (Valiante et al., 2016; Bourne et al., 2016). H-ATLAS have developed their own program to find unresolved sources on Herschel images: the Multi-band Algorithm for source Detection and eXtraction (hereafter MADX; Maddox et al., *in prep.*). MADX creates variance maps including instumental and confusion noise and then produces a list of potential sources by finding all peaks in the maps with signal-to-noise > 2.5. The photometry is then performed at these positions and only sources with a measured flux density $> 4\sigma$ in at least one of the three SPIRE wavelengths (250, 350 and 500 μm) are included in the H-ATLAS catalogue (Valiante et al., 2016).

In the three equatorial fields alone (together ~ 160 deg^2) H-ATLAS detected 120230 sources. H-ATLAS provides us with a blind, large-area sample of both nearby and high-redshift galaxies, with resolution and sensitivity hitherto only found in targeted dust surveys. Optical counterparts to H-ATLAS sources were found by direct comparison with the SDSS DR7 (Abazajian et al., 2009) and DR9 (Ahn et al., 2012), and provide spectroscopic redshifts where available. The matching was performed using a likelihood ratio technique, where only SDSS sources with a reliability $R > 0.8$ are considered to be likely matches to the H-ATLAS sources (Smith et al., 2011; Bourne et al., 2016). H-ATLAS only provides FIR/submm coverage for its

sources, and thus needs to be combined with ancillary surveys to obtain an overall picture of galaxy evolution. The three equatorial H-ATLAS fields coincide with the Galaxy and Mass Assembly (GAMA; Driver et al., 2011) survey.

GAMA provides a repository of multiwavelength information for thousands of galaxies. By working together with different surveys such as H-ATLAS, GAMA have compiled excellent ancillary data from UV-submm, along with spectroscopic redshifts for more than 250,000 galaxies. The optical spectroscopy is provided by the AAOmega spectrograph on the Anglo-Australian Telescope, and combined with spectroscopy from previous redshift surveys such as SDSS, 2 Degree Field Galaxy Redshift Survey (2dFRGS, Colless et al., 2003), and the Millenium Galaxy Catalogue (MGC, Driver et al., 2005), to provide redshift coverage complete down to a magnitude limit of $r < 19.4$. GAMA performed supplementary reductions of ultraviolet (UV) GALEX (Morrissey et al., 2007), optical SDSS DR6 (Adelman-McCarthy et al., 2008), Near-InfraRed (NIR) VISTA VIKING (Sutherland, 2012) and Mid-InfraRed (MIR) WISE (Wright et al., 2010; Cluver et al., 2014) data. Details for these reprocessed maps can be found in Driver et al. (2016).

1.5.2 Part I of this thesis - Scaling relations

In Part I of this thesis we use multiwavelength photometry to determine the dust, stellar and gas content of galaxies. In order to better understand the dust and gas content of galaxies, the first step is to quantify how the dust and gas content of galaxies varies with galaxy properties such as stellar mass, colour, star formation rate (SFR), and so forth. By using gas fraction as a proxy for the evolutionary stage of a galaxy, we reveal the evolution of the dust, gas and stellar content of galaxies in the local Universe. These scaling relations provide important insights into the interplay of dust, gas and the star formation cycle, and give better understanding of the physical processes regulating galaxy evolution (e.g. Dunne et al., 2011; Cortese et al., 2012b; Rémy-Ruyer et al., 2015).

Before *Herschel*, the main dust scaling relations studied were the global relations between dust, gas and stellar masses (e.g. Devereux & Young, 1990; Sanders et al., 1991; Dunne et al., 2000; Driver et al., 2007) and the evolution of the dust-to-gas ratio with stellar mass and metallicity (e.g. Issa et al., 1990; Lisenfeld & Ferrara, 1998; James et al., 2002; Draine et al., 2007). These studies showed that there is a strong correlation between dust and gas mass, and they found an increase of the dust-to-gas mass ratio as a function of stellar mass and metallicity, though there is often disagreement in the exact slope of the relationships. da Cunha et al. (2010) used *IRAS* data to show that the dust-to-stellar mass ratio strongly correlates with specific star formation rate (SSFR), as predicted by chemical evolution models. This result has since been

supported by further *Herschel* studies (Smith et al., 2012; Sandstrom et al., 2013; Rowlands et al., 2014a).

Since then, *Herschel* has expanded on these studies by including the cold dust component and explored a much wider range of galaxy types and luminosities, and far greater numbers, than was possible with previous telescopes. The *Herschel* Reference Survey (HRS, Boselli et al., 2010b) is a quasi stellar mass selected sample of 323 local galaxies. Various HRS studies have derived scaling relations between the gas, dust and star formation properties as well as trends with FIR/submm and UV colours, stellar mass, morphology and environment. Apart from providing benchmark scaling relations, these works showed that cluster galaxies are characterized by a significantly lower atomic, molecular, and dust mass content than similar stellar mass galaxies in the field (Cortese et al., 2011; 2012b;a; 2014; 2016; Boselli et al., 2012; 2013; 2014b; 2015). Dust scaling relations in H-ATLAS have been studied by Bourne et al. (2012) through stacking $\sim$ 80000 optically selected galaxies, and also by Smith et al. (2011) who used fits to the UV-FIR photometry of 1402 250 μm-selected sources. More recently H-ATLAS has produced a local volume limited sample, and Clark et al. (2015, hereafter C15) used it to study the dust properties of one of the first true dust mass selected sample of galaxies in the local Universe.

C15 show that stellar mass selected samples are biased towards galaxies that have converted a lot of their gas into stars, i.e. towards more evolved galaxies, and thus under-represent immature high gas fraction sources. Dust selection produces a more uniform range of gas fractions but preferentially samples galaxies near the peak of their dust content. In Part I of this thesis we compare a local, HI-selected sample from the H-ATLAS equatorial fields to these stellar and dust mass selected samples. We will highlight scaling relations concerning dust properties as these have not been studied before for HI-selected samples. Since HI selection preferentially selects galaxies with high gas fractions, we can populate the scaling relations for these hitherto missing immature galaxies and, for the first time, study their dust properties. This is particularly important given the relevance of immature, unevolved sources as analogues for the first galaxies. By comparing the three samples selected by stellar, dust and atomic gas content, we span a large range of gas fractions and can study the relationship of dust, gas and stars across as wide a range of evolutionary status as possible.

1.5.3 Part II of this thesis - Chemical evolution models

The scaling relation from Part I can also be used to set strong constraints on chemical evolution models (e.g. Rowlands et al., 2014b). One can learn about dust sources and sinks by comparing models that predict the build-up of dust and gas with the observed properties of galaxies. Metallicity information provides further constrains and allows to discriminate between different

chemical evolution models. In Part II of this thesis we add additional metallicity information to the results from Part I and use chemical evolution models to interpret the interplay between dust, gas and metals in galaxies.

Understanding the dust evolution of galaxies has been the focus of many numerical modelling studies (Dwek, 1998; Lisenfeld & Ferrara, 1998; Hirashita & Ferrara, 2002; Inoue, 2003; Morgan & Edmunds, 2003; Valiante et al., 2009; Asano et al., 2013b; Rowlands et al., 2014b; Zhukovska, 2014; Feldmann, 2015). These models study the changing balance between the dust sources and sinks, and include processes such as the formation of dust in stellar winds and supernovae, dust growth and destruction in the ISM, and radiation field effects. Not all models include all of these processes, yet many require efficient dust production by supernovae, efficient grain growth and/or low efficiency of grain destruction by SN shocks (Morgan & Edmunds, 2003; Dwek et al., 2007; Michałowski et al., 2010; Rowlands et al., 2014b).

Most of these models are one-zone models, meaning they study the integrated properties of galaxies without spatial resolution. Recently smoothed-particle hydrodynamical simulations resolving local dust variations have been developed (Bekki, 2013; 2015; Aoyama et al., 2016), as well cosmological simulations including dust evolution of Milky Way-sized galaxies (McKinnon et al., 2016). One big advantage over one-zone models is that these 3D models can be used to make predictions about the distribution of dust within a galaxy.

C15 attempted to model the HRS and HAPLESS galaxies using a simple one-zone closed box chemical evolution model and suggested the following: as galaxies evolve, their dust content first rises steeply, then levels off and reaches its peak about half way through their evolution. The dust content starts declining towards lower gas fractions as more dust is destroyed/consumed than produced. C15 provided further evidence that significant quantities of supernovae dust (as well as dust from LIMS) must be included otherwise the model cannot account for the dust scaling relations in the dust-selected sample (as also seen in e.g. Morgan & Edmunds, 2003; Matsuura et al., 2009; Dunne et al., 2011; Gall et al., 2011b; Rowlands et al., 2014b).

In Part I of this thesis we find that our HI-selected sample, particularly the low stellar mass sources, are offset from the simple evolutionary scenario put forward in C15, with lower dust-to-gas ratios than predicted by the chemical models for the same gas fractions. Assuming that the gas fraction can be a proxy for how evolved a galaxy is, this provides an opportunity to model the evolution of dust, metals, stars and gas content as galaxies consume their gas into stars and evolve from gas-rich to gas-poor.

Combining dust-to-gas observations with metallicity information can also provide a way to discriminate between different chemical evolution models and dust sources (e.g. Edmunds, 2001; Dwek, 1998). The dust-to-gas ratio of Milky Way-like, metal-rich galaxies, appears to

scale linearly with metallicity (e.g. Dwek, 1998), suggesting a constant dust-to-metal ratio in galaxies. Various literature studies quote values of 0.5 ± 0.1 (see Clark et al., 2016 and references therein). At low metallicities, there are hints that the dust-to-gas ratios are lower than expected from this linear relationship (Lisenfeld & Ferrara, 1998; Galliano et al., 2011; Rémy-Ruyer et al., 2013; 2015), though sample sizes are often small in this regime. Zhukovska (2014) used a chemical evolution model similar to C15 to show that the observed variation in dust-to-gas ratio and metallicity in local star-forming dwarfs can be explained using models with bursty star formation histories, low dust yields from core-collapse SNe and additional grain growth in the ISM.

In Part II of this thesis, we apply a one-zone chemical evolution model to interpret the data from Part I, combined with metallicity information. In order to study the sources and sinks of dust, we relax the closed box model assumption from C15 and add inflows and outflows, use different SFHs, and allow for dust grain growth in the ISM and dust destruction.

1.5.4 Part III of this thesis - HI-stacking

In Part I of this thesis, we use direct detection of the HI line to determine the HI masses of nearby galaxies ($z \lesssim 0.04$) in the equatorial H-ATLAS fields. Unfortunately the limited sensitivity of the current generation of telescopes does not allow us to obtain large samples of galaxies with HI-detections past the nearby Universe. However, by performing an HI-stacking analysis in Part III of this thesis, we derive average HI properties for dust-selected galaxies out to $z \sim 0.1$. There are 1325 dust-selected galaxies available for stacking in the equatorial H-ATLAS fields between $0.04 \lesssim z \lesssim 0.1$.

The HI observations over the equatorial H-ATLAS fields were made using the Parkes telescope. The large Parkes $15.5'$ beam means that the HI signal of a target galaxy will be indistinguishable from that of multiple other galaxies in its proximity. At the redshifts used, the HI signal of each galaxy will be confused with 5 other galaxies on average. In order to deal with this, we derive correction factors to account for the estimated fraction of the HI signal coming from the target source. These correction factors are derived using HI scaling relations for nearby galaxies, and locations of the confused galaxies compared to the target location.

The validity of the stacking technique was first demonstrated by Zwaan (2000), who stacked 45 undetected galaxies at $z = 0.18$ to achieve a 2.5σ detection, and later also by Chengalur et al. (2001) and Lah et al. (2007), to study the influence of the environment on HI properties of cluster galaxies out to $z = 0.37$. Fabello et al. (2011a;b; 2012) succesfully used stacking to study the impact of bulge presence and AGN activity on the HI content of galaxies, and found strong average detections were possible when stacking large samples. It is also possible to

study the scaling relations of gas fraction with stellar mass, stellar surface density and colour using stacking (Fabello et al., 2011a; Brown et al., 2015).

Delhaize et al. (2013) and Delhaize (2014) stacked HI-signals observed with the Parkes telescope. We follow their stacking technique in Part III of this thesis to obtain HI information on dust-selected galaxies out to $z \simeq 0.1$. Delhaize et al. (2013) studied 3,277 optically selected galaxies from the 2dFGRS optical catalogue at $0.04 < z < 0.13$, using new observations near the south Galactic pole, and 15,093 2dFGRS galaxies at $z < 0.04$ observed by HIPASS. They achieve 35σ and 12σ for the low- and high-redshift samples respectively and average HI masses of $(6.93 \pm 0.17) \times 10^9$ and $(1.48 \pm 0.03) \times 10^9\, h^{-2}\, \mathrm{M}_\odot$. After accounting for source confusion, they find a cosmic HI mass density of $\Omega_{HI} = 3.19^{+0.43}_{-0.59} \times 10^{-4}\, h^{-1}$ for the high-redshift sample and $\Omega_{HI} = 2.82^{+0.30}_{-0.59} \times 10^{-4}\, h^{-1}$ for the low-redshift sample.

In Part III of this thesis, we report our progress on an HI-stacking analysis of low SNR HI signals from 1325 dust-selected sources between $0.04 \lesssim z \lesssim 0.1$. We correct the HI signals for confusion using correction factors based on local scaling relations. We compare our preliminary results for dust-selected sources to results from stacking the HI signals of stellar mass selected sources using the same method. We also compare to results from Delhaize (2014), who stacked optically selected galaxies over the same fields, and performed their own deconfusion method. HI scaling relations with stellar mass and galaxy colours are also studied by dividing the sample in several sub-samples (e.g. using bins of stellar mass) and stacking the HI signal of the galaxies in each sub-sample.

Part I

HI and Dust Scaling Relations in an HI-Selected Sample

Chapter 2

The HIGH sample

2.1 Introduction

Multiwavelength photometry is one of the most useful tools astronomers have at their disposal. Combining observations at different wavelengths allows the study of the various components of galaxies and their interactions. By providing submillimetre observations, the *Herschel* telescope has opened an important section of the spectral energy distribution of galaxies. Many surveys have used *Herschel* data with the aim of understanding dust in nearby galaxies, including H-ATLAS (Eales et al., 2010), HRS (Boselli et al., 2010b), HeViCS (Davies et al., 2010), KINGFISH (Kennicutt et al., 2011), ... However, there has not previously been a survey of dust in local galaxies selected on their atomic gas (HI) content. This chapter explains in detail how we selected the HIGH ('HI-selected Galaxies in H-ATLAS') sample. HIGH is the first HI-selected sample of galaxies that uses *Herschel* observations to enable the study of the galaxies' dust properties. Since HI-selected samples consist typically of young and immature galaxies, we are able to probe the dust content of galaxies at the earliest stages of their evolution.

2.2 Observations

In order to obtain a sample of galaxies with sufficient multiwavelength information to determine the stellar, dust and atomic gas (HI) content, it is necessary to select an area of sky that has been surveyed in the optical, the submillimetre (submm) and at 21 cm. The ideal fields with the necessary multiwavelength data are the three equatorial fields ($\sim$160 deg^2) of the *Herschel*-ATLAS (H-ATLAS; Eales et al., 2010), which have excellent multiwavelength ancillary data and overlap with the Galaxy And Mass Assembly spectroscopic survey (GAMA; Driver et al., 2009). The HI Parkes All-Sky Survey (HIPASS; Barnes et al., 2001), supplemented by the

Arecibo Legacy Fast ALFA Survey (ALFALFA; Giovanelli et al., 2005) is used to determine the atomic gas properties. The different used surveys are discussed in Sections 1.4.2 and 1.5.1. Here we summarise the catalogues we have used for selecting our sample and determining submm and optical counterparts.

The HI Parkes All Sky Survey (HIPASS; Barnes et al., 2001; Meyer et al., 2004) provides 21 cm coverage over the equatorial H-ATLAS/GAMA fields. The Parkes beamsize is $15.5'$, the velocity resolution is 18 $\mathrm{km\,s^{-1}}$ and the rms noise is 13 $\mathrm{mJy\,beam^{-1}}$ in a channel of this width. The HIPASS catalogue (HICAT, Meyer et al., 2004; Zwaan et al., 2004; Wong et al., 2006) is used to identify our sources and extract the basic HI-parameters.

The HIPASS data are supplemented by observations from the Arecibo Legacy Fast ALFA Survey (ALFALFA, Giovanelli et al., 2005; Haynes et al., 2011; Haynes, *priv comm.*). With a beamsize of $\sim 3.5'$ and rms noise of ~ 2 $\mathrm{mJy\,beam^{-1}}$ (for 11 $\mathrm{km\,s^{-1}}$ channels), ALFALFA outperforms HIPASS in both sensitivity and resolution. It does not, however, have full coverage over the three equatorial H-ATLAS/GAMA fields in this study. For this reason we use HIPASS data supplemented with ALFALFA where available.

The uniqueness and strength of this HI-selected sample is that it makes use of the H-ATLAS - the largest extragalactic submm survey covering ~ 600 $\mathrm{deg^2}$ in 5 bands from 100-500 μm. This work makes use of the H-ATLAS Phase 1 public data release, hereafter 'DR1' (Valiante et al., 2016; Bourne et al., 2016). To determine submm counterparts to our HI-selected sources (see next section), we use the DR1 catalogue of 4σ detections in any of the SPIRE bands (Valiante et al., 2016) produced using the MAD-X algorithm (Maddox et al., *in prep.*). Optical counterparts (which provide spectroscopic redshifts) to H-ATLAS sources were found by direct comparison with SDSS DR7 (Abazajian et al., 2009) and DR9 (Ahn et al., 2012).

The SDSS DR9 catalogue and the GAMA version-25 specObj catalogue have been used to determine any further potential optical counterparts to our HI-selected sources. By identifying the GAMA counterparts to our sources, we have access to a wealth of information through the use of the different GAMA data products (e.g. spectroscopy).

2.3 Sample selection

The HIGH sample consists of the 32 sources in the HIPASS catalogue (HICAT) that overlap with the H-ATLAS/GAMA footprints. These HI sources are then cross-matched to the H-ATLAS DR1 catalogue to determine the submm counterparts, and to the SDSS DR9 catalogue (Ahn et al., 2012) and the GAMA version-25 specObj catalogue to determine the optical counterparts. The matching is done by determining all sources that lie within the $15.5'$ Parkes

beam (centred on the HI position) and have a spectroscopic redshift within the redshift range[1] of the HIPASS profile. To be accepted, optical matches need to have a reliable redshift from GAMA (redshift quality NQ > 2) or SDSS ("zwarning" flag = 0) and the H-ATLAS matches need to have a reliable SDSS counterpart ($R > 0.8$, Bourne et al., 2016). Duplicate matches occur as most SDSS objects are also included in the GAMA catalogue and since H-ATLAS has SDSS counterparts. These duplicate matches are combined into a single listing for each source. Figure 2.1 shows the 3 equatorial H-ATLAS fields and the locations of each HIPASS source in our sample with each of its (combined) counterparts.

GAMA has more spectra available than SDSS and includes the majority of the SDSS objects within the equatorial H-ATLAS fields that we are studying. However, there are a few SDSS matches in our sample that did not make it into the GAMA catalogue, which is why we need to match to both GAMA and SDSS. UM 501 and UGC07531 are two sources that lie inside the H-ATLAS footprint, yet just outside the GAMA footprint, as can be seen on the left of the G12 panel of Figure 2.1. The SDSS matches are used instead for these sources. The mismatch between the GAMA and H-ATLAS footprint is due to the constraints on the scanning direction of *Herschel*. In order to completely cover the GAMA footprint, the H-ATLAS needed a larger footprint.

We identified two additional sources by checking the literature[2] for bright HI sources that are located in the H-ATLAS fields, but that are not found by our matching technique. Both UGC0700 and NGC5746 are bright enough to be detected by HIPASS, yet lie just outside the beam of the closest HIPASS source (separation of about $20'$). The close proximity to another, bigger HIPASS source likely caused these sources to be missed. However they are still bright enough to meet our selection[3] and both these sources are added to our sample (labelled 'c' in Table 2.1 and Table 2.4).

[1] This redshift range is computed from the upper and lower radial velocity bound on the HI profile (manually specified), as given in HICAT.

[2] We used positional searches in de HYPERLEDA database (Paturel et al., 2003). The search radii were set to be large enough to cover the whole equatorial H-ATLAS fields.

[3] Without the close proximity to another HIPASS source, both these sources would have been included in the HIPASS sample.

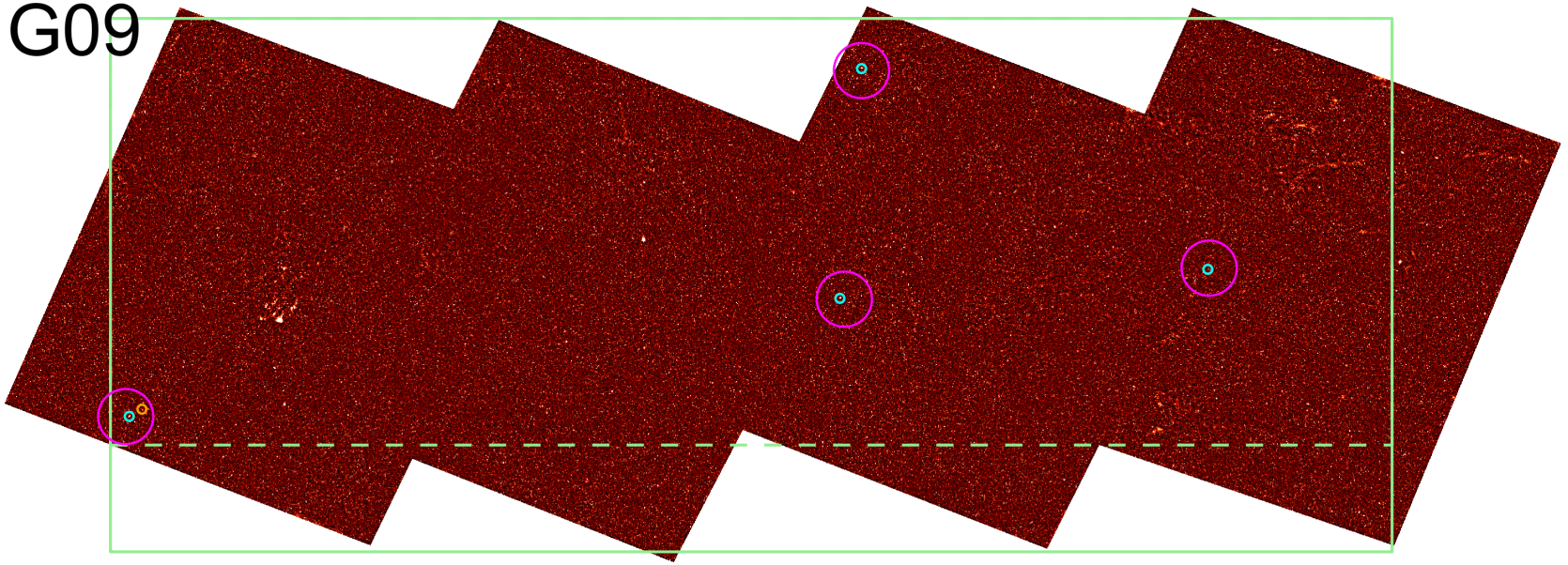

Figure 2.1: The three equatorial H-ATLAS fields are shown with the locations of the HIGH sources. The images are the 250 μm DR1 H-ATLAS maps. The GAMA footprint is plotted in green (Solid line for GAMA II data release (Liske et al., 2015), dashed line for GAMA I (Baldry et al., 2012)). The locations of the HIPASS sources used for the selection of our sample are shown in magenta (the radius is the FWHM of 15.5′). The sources in HIGH only include unconfused sources and are shown in cyan. The confused sources that have no higher resolution detections available are shown in orange.

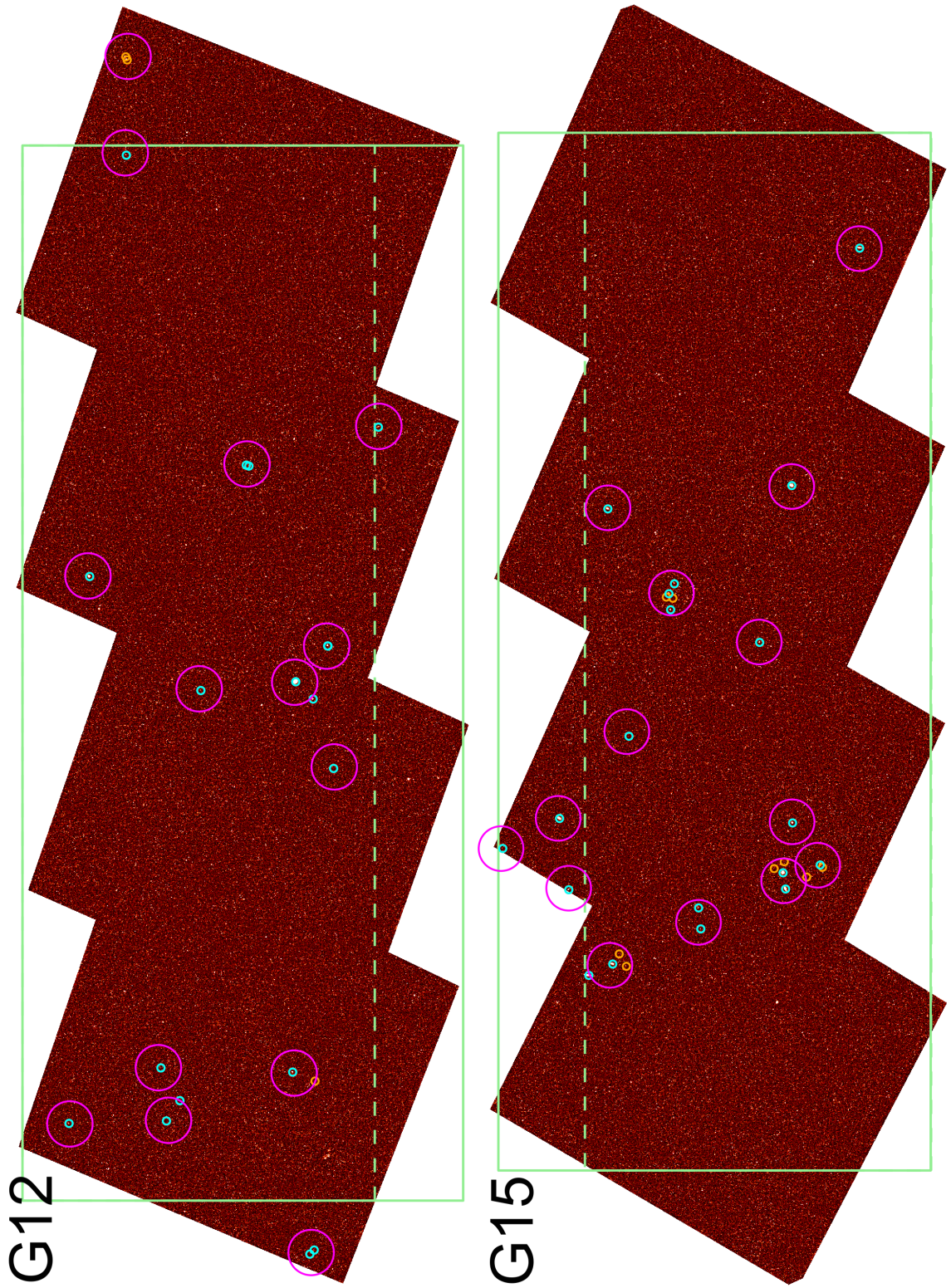

Figure 2.1: - *Continued*

2.3.1 Shredding

Multiple optical matches are found for most of the HIPASS sources due to two different issues. The first is that the SExtractor source detection used by SDSS and GAMA was not optimised for the very extended local sources in our sample (semi-major axis up to $3'$). Moreover, most of the sources in our sample have clumpy optical distributions, which together with their large angular sizes, leads to SExtractor 'shredding' galaxies into several components. When this happens, there are multiple matches in very near proximity of each other which, upon visual inspection, are found to lie within the same galaxy. This is not due to different redshift surveys included in GAMA, as when there are duplicate spectra, the specObj catalogue only lists the best quality object. The separate matches within the same galaxy still differ in position, with typically one central match, and other surrounding matches corresponding to bright and clumpy star formation regions within the galaxy. 71% of the sources in our sample are affected by this shredding. For these sources we determine the correct central position manually (based on the best fitting aperture) and reject the spurious listings. We have shown an example of the shredding issue in Figure 2.2.

2.3.2 HI-Confused sources

After correcting the shredding issue, there are still a number of HIPASS sources that have multiple distinct galaxies matched to the HI source. These galaxies are 'confused' in the large HI beam and there is no sure way of determining how much of the HI signal corresponds to each of the sources without obtaining additional observations with higher angular resolution. We have shown two confused galaxies in Figure 2.3. Their separation ($8.4'$) is significantly smaller than the $15.5'$ Parkes beam. The galaxies for which the HIPASS signal is confused are labelled 'a' in Table 2.1 and Table 2.4. The projected physical distance between these confused galaxies is relatively small (order of ~ 100 kpc) and they form groups (the largest group in our sample consists of 5 members). In total, there are 49 matches to the 32 HIPASS sources in our sample, as shown in Figure 2.1.

In order to better determine the HI properties for these confused sources, we have supplemented our HIPASS data with ALFALFA data where available ($3.5'$ resolution). ALFALFA only covers the more northern sources in our sample (dec $> -0.05^\circ$) and we find 23 detections, 16 of which are for not confused sources. Because of its higher sensitivity, we use the ALFALFA HI measurements for all sources that lie in its footprint. The ALFALFA data deblend 3 of the confused HIPASS sources (from a total of 9) into 7 separate HI sources, each with its own optical counterpart. We are then left with 6 confused HIPASS sources, containing 14 optical matches between them. For these we have searched the literature for the highest

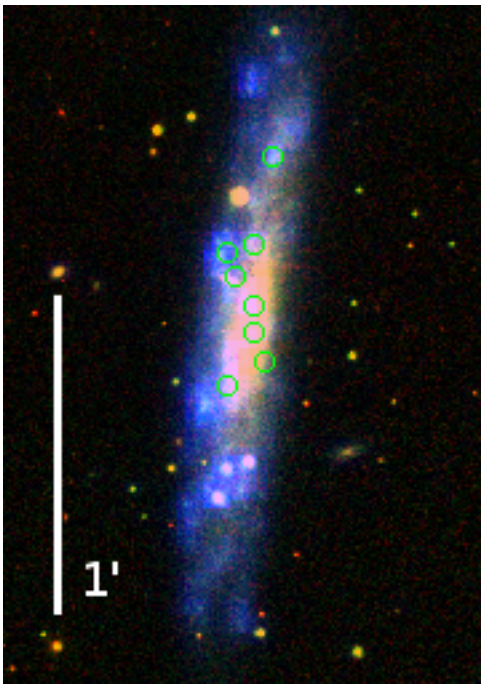

Figure 2.2: NUV/*r*/Z image of NGC 5496 showing the positions of the different shredded GAMA objects associated with this galaxy overlaid as green circles. A scale bar of $1'$ is shown in white.

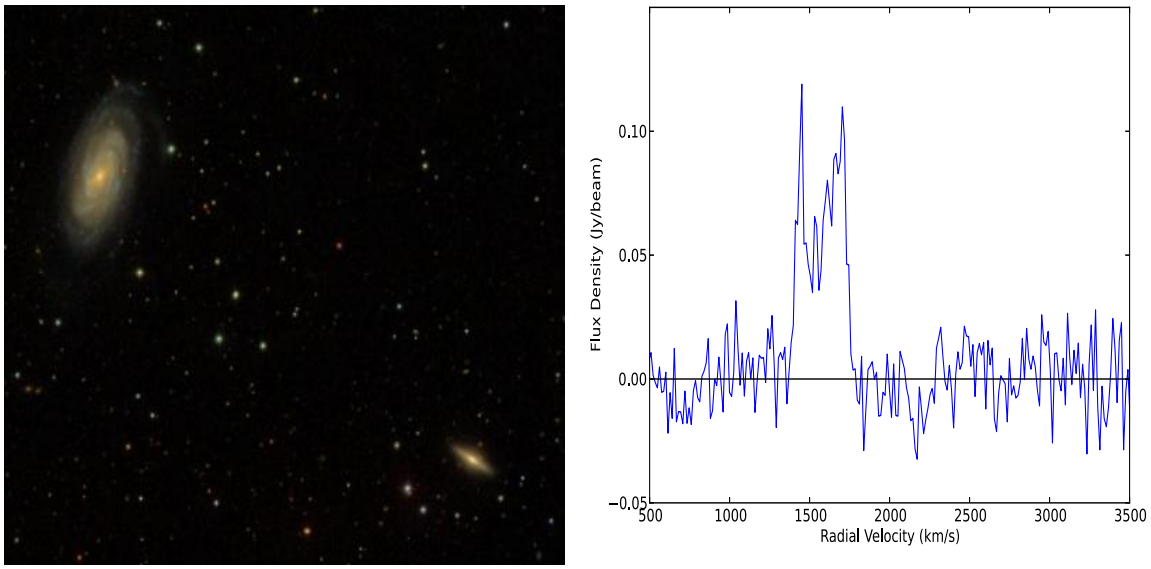

Figure 2.3: The confused sources NGC 5738 and NGC 5740 both lie within the beam and HI profile of HIPASS J1444+01. *Left: g*/*r*/*i* image with a size of $10'$, centred on the HI position of HIPASS J1444+01, is shown. *Right:* The HI profile of HIPASS J1444+01 includes HI contributions from both sources. Considering galaxies can have a double-horned HI profile, it is impossible to separate the contributions from the individual galaxies.

Table 2.1: Different identifiers for the 40 sources in HIGH. Throughout the tables in this work we will list properties in the same order, using the ID in the first column as the identifier. For sources with multiple shredded GAMA matches, only the GAMA CATAID for the most central match is given. The HAPLESS ID (C15) is given for sources that overlap with the HAPLESS sample.

#	Common name	HIPASS ID	H-ATLAS IAU ID	GAMA CATAID	HAPLESS-ID
1	SDSSJ084258.35+003838.5	HIPASSJ0842+00	HATLASJ084258.4+003838	622084	
2	UGC04673	HIPASSJ0855+02	HATLASJ085552.3+023125	517868	
3	UGC04684	HIPASSJ0856+00	HATLASJ085640.5+002229	600168	39
4[a,b]	UGC04996	HIPASSJ0923-00	HATLASJ092315.6-004342	198771	
5	UGC06578	HIPASSJ1136+00b	HATLASJ113636.7+004901	6821	41
6	UGC06780	HIPASSJ1148-02	HATLASJ114850.4-020156	177588	19
7[a]	UM456	HIPASSJ1150-00		559584	17
8[a]	UM456A	HIPASSJ1150-00	HATLASJ115033.8-003213	559609	24
9	UGC06903	HIPASSJ1155+01	HATLASJ115536.9+011417	22741	31
10	UGC06970	HIPASSJ1158-01		185266	
11	NGC4030b	HIPASSJ1200-00		584731	
12	NGC4030	HIPASSJ1200-01	HATLASJ120023.7-010553	31520	6
13	UGC07053	HIPASSJ1204-01		185622	
14	UGC07332	HIPASSJ1217+00		85878	
15[a]	NGC4202	HIPASSJ1218-01	HATLASJ121808.4-010350	32362	
16[a]	FGC1412	HIPASSJ1220+00		611446	
17[a]	CGCG014-010	HIPASSJ1220+00		611520	
18	UGC07394	HIPASSJ1220+01	HATLASJ122027.6+012812	221194	11
19[a]	UGC07531	HIPASSJ1226-01	HATLASJ122611.1-011813	-99	34
20[a]	UM501	HIPASSJ1226-01		-99	
21	NGC5496	HIPASSJ1411-01	HATLASJ141137.7-010928	496978	7
22	NGC5584	HIPASSJ1422-00	HATLASJ142223.4-002313	63349	14
23	UGC09215	HIPASSJ1423+01	HATLASJ142327.2+014335	238952	3
24[a]	2MASXJ14265308+0057462	HIPASSJ1427+00	HATLASJ142653.0+005745	106616	
25[a]	IC1011	HIPASSJ1427+00	HATLASJ142804.4+010023	106717	
26[a]	IC1010	HIPASSJ1427+00	HATLASJ142720.5+010132	106640	
27	UGC09299	HIPASSJ1429-00	HATLASJ142934.8-000105	593645	9
28	SDSSJ143353.30+012905.6	HIPASSJ1433+01		239634	
29	NGC5690	HIPASSJ1437+02	HATLASJ143740.9+021729	262444	23
30	NGC5691	HIPASSJ1437-00	HATLASJ143753.3-002354	64553	28
31	UGC09432	HIPASSJ1439+02		367146	
32[a]	NGC5705	HIPASSJ1439-00	HATLASJ143949.5-004305	49167	26
33	NGC5725	HIPASSJ1440+02		343415	
34[a]	NGC5713	HIPASSJ1440-00	HATLASJ144011.1-001725	64771	29
35[a]	NGC5719	HIPASSJ1440-00	HATLASJ144056.2-001906	64804	20
36[a]	UGC09482	HIPASSJ1442+00	HATLASJ144247.1+003942	16863	
37[a]	UGC09470	HIPASSJ1442+00	HATLASJ144148.7+004121	16828	30
38[a]	NGC5740	HIPASSJ1444+01	HATLASJ144424.3+014046	321075	10
39[c]	UGC07000		HATLASJ120110.4-011750	144491	8
40[c]	NGC5746		HATLASJ144455.9+015719	251941	21

[a] The HIPASS signal for this source is confused. Higher resolution HI data from ALFALFA or literature was supplemented to resolve confusion. Note that only unconfused counterparts are listed in this table.
[b] Based on the colour, stellar mass and offsets in position, we identified this galaxy as the most likely source of most of the HI flux in HIPASSJ0923-00.
[c] UGC0700 and NGC5746 are both sources that are bright enough to make it into HIPASS and our sample, yet they were missed in HIPASS due to their close proximity to other, brighter HIPASS sources.

Table 2.2: Offsets in optical position and best redshift, together with stellar masses and NUV-r for UGC 04996 and GAMA 198763. The bottom row shows the estimated HI mass based on the scaling relation between $M_{\rm HI}/M_*$ and NUV-r in Chapter 4 (see Table 4.1). UGC 04996 is clearly the dominant source.

	UGC 04996	GAMA 198763
$\Delta\theta$	$1.9'$	$9.9'$
Δz	0.00016	0.00033
log M_* [$M_\odot$]	9.3	7.0
NUV-r [mag]	1.7	0.9
log $M_{\rm HI,estimated}$ [$M_\odot$]	9.7	7.9

resolution 21 cm observations available, leading to the deconfusion of 5 HIPASS sources into 8 separate HI sources with optical counterparts.

This leaves us with 1 HIPASS source (HIPASSJ0923-00) for which there are two optical matches (UGC 04996 and GAMA 198763). For this source, it is possible to estimate which of the two counterparts is responsible for the vast majority of the HI signal. This dominant source was found by comparing the stellar mass, the NUV-r colour and the offsets in optical position and best redshift between HIPASS and the optical counterparts. We show this comparison in Table 2.2 and estimate the HI mass for each counterpart using scaling relations we derive in Chapter 4. We are confident that one counterpart (labelled 'b' in Table 2.1 and Table 2.4) has nearly all the HI mass and the other one is a small satellite galaxy that can be discarded.

Finally we arrive at a sample of 40 unconfused HI-selected sources that make up the HIGH sample, 22 of which overlap with the C15 dust-selected sample (HAPLESS ID given in Table 2.1). The unconfused sources in the HIGH sample are indicated as cyan circles in Figure 2.1, confused counterpart without higher resolution HI detections as orange circles. Note that there are more HIGH sources than the original number of HIPASS sources due to the additional ALFALFA and literature data for the confused sources. Multiwavelength imagery of the HIGH galaxies is shown in Figure 2.4.

2.3.3 Selection bias due to better resolved observations

Adding in higher resolution HI data for known HIPASS detections could affect our HI selection. Although we have found ALFALFA counterparts to each of our HIPASS sources in the common region, we cannot be confident that these individual counterparts would have made the HIPASS detection limit by itself. We aim to use the same blind HI selection as HIPASS for each of our individual sources. However the HIPASS source selection is somewhat complex and therefore it is not straightforward to determine one selection limit and to determine the potential bias due to the addition of higher resolution data. The HIPASS selection happens in 3 stages: first,

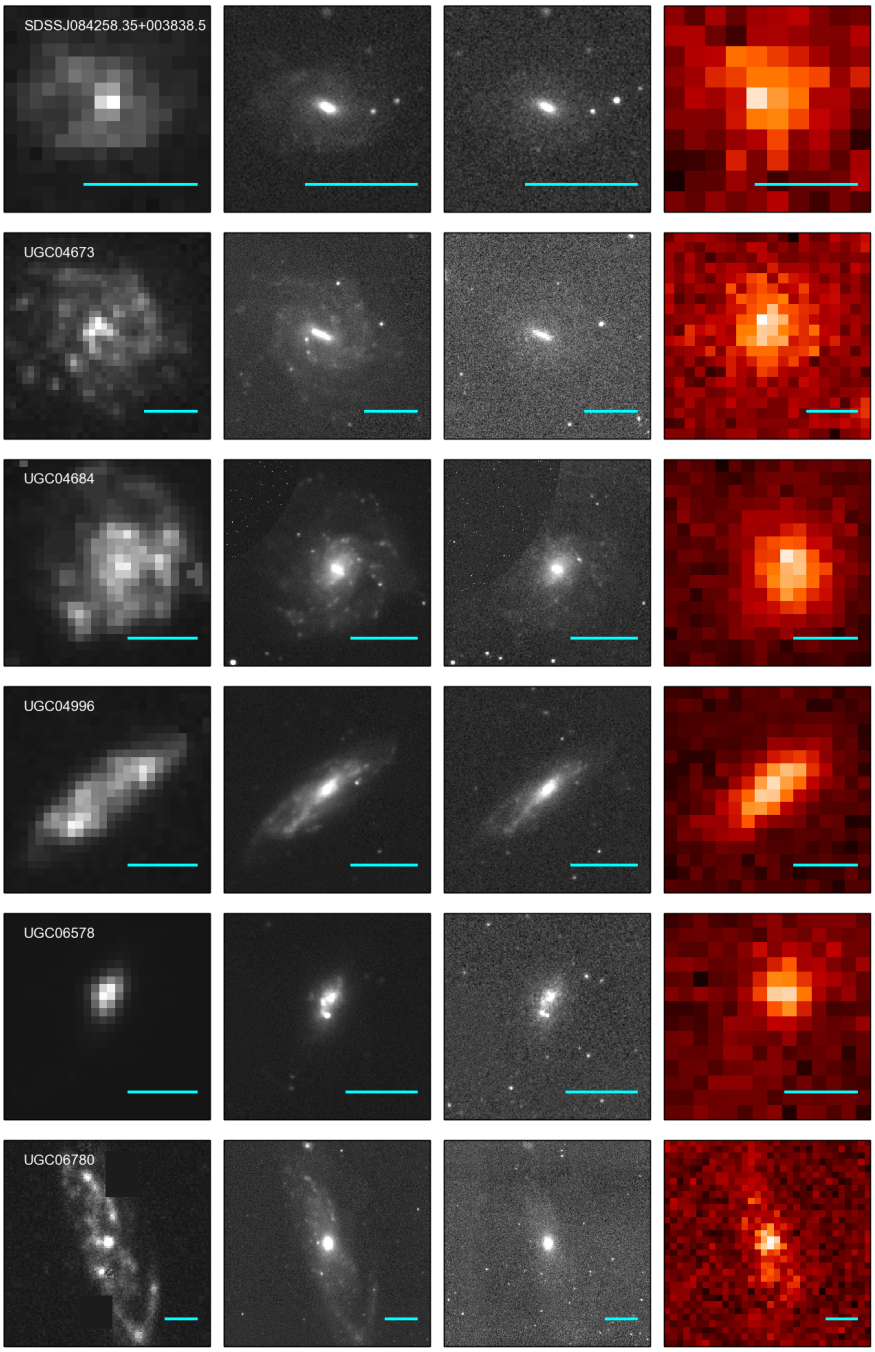

Figure 2.4: Multiwavelength images for the sources in HIGH. The brightest foreground stars and background galaxies have been subtracted and replaced by adjacent pixels. The bands displayed, from left-to-right, are: GALEX FUV, SDSS *r*-band, VIKING K_s-band, and *Herschel* 250 μm. The size of each cutout is 1.5 times the semi-major axis and a scale bar with a length of 30" is shown on each image in cyan.

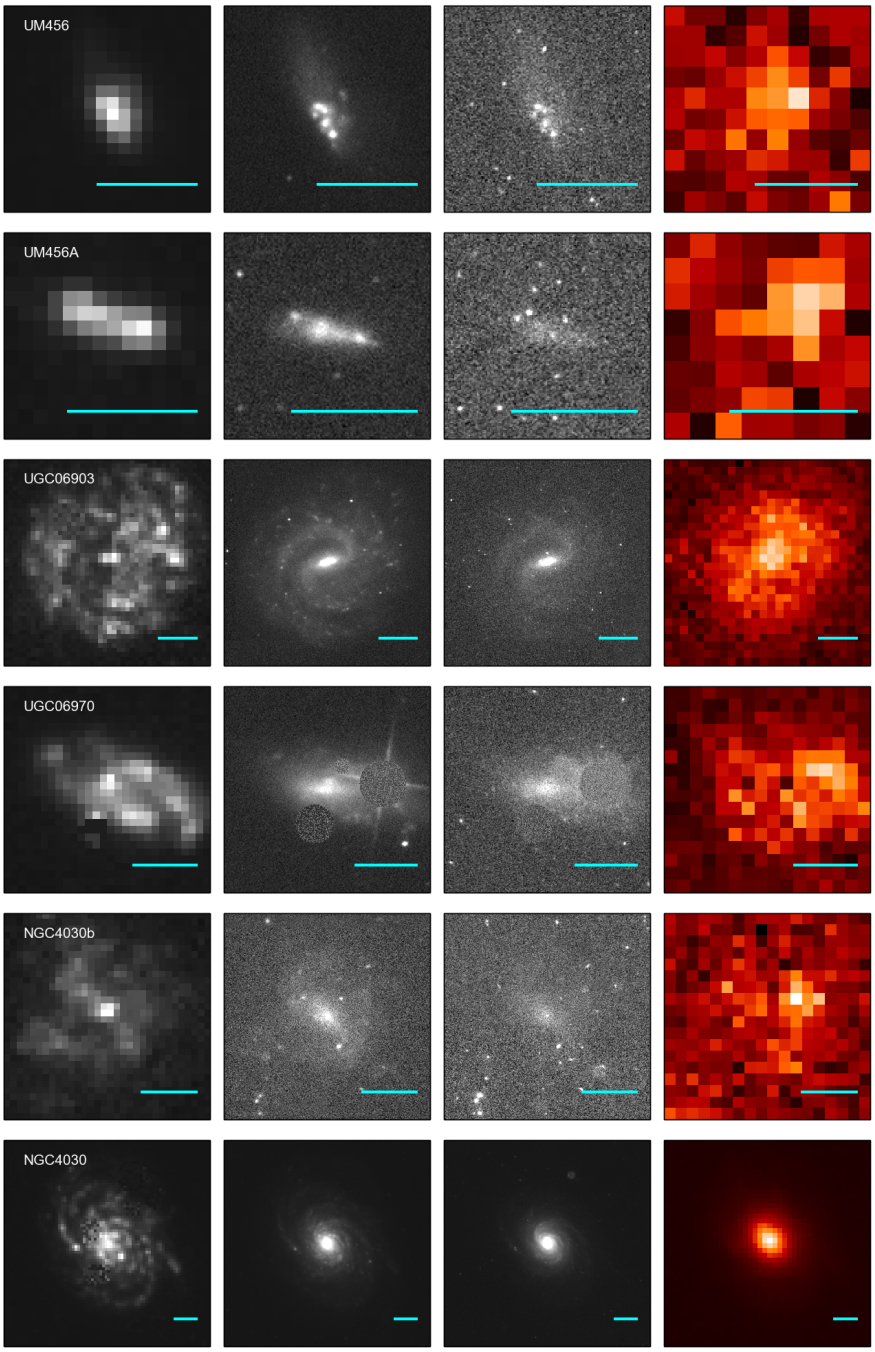

Figure 2.4: - *Continued*

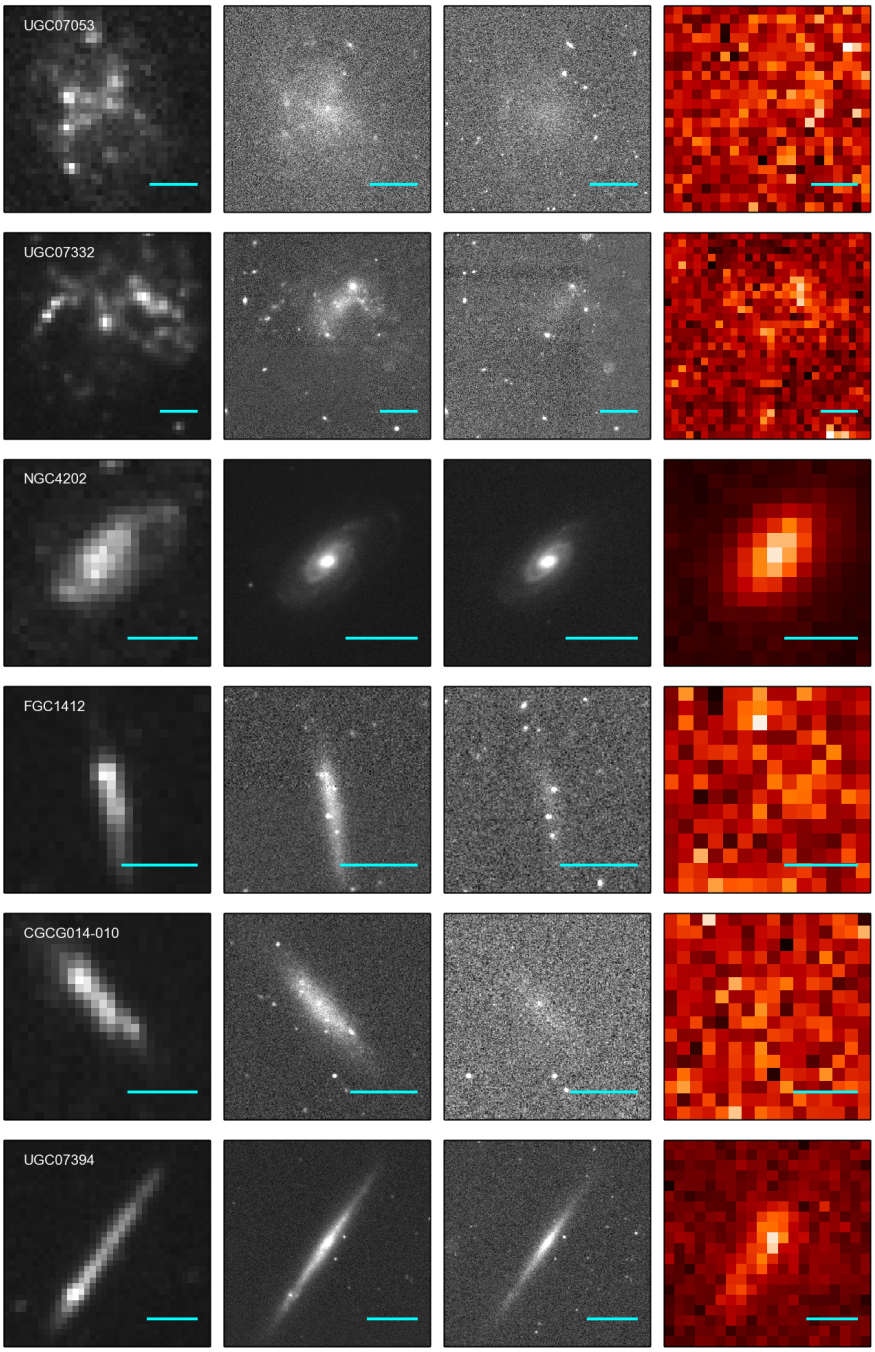

Figure 2.4: - *Continued*

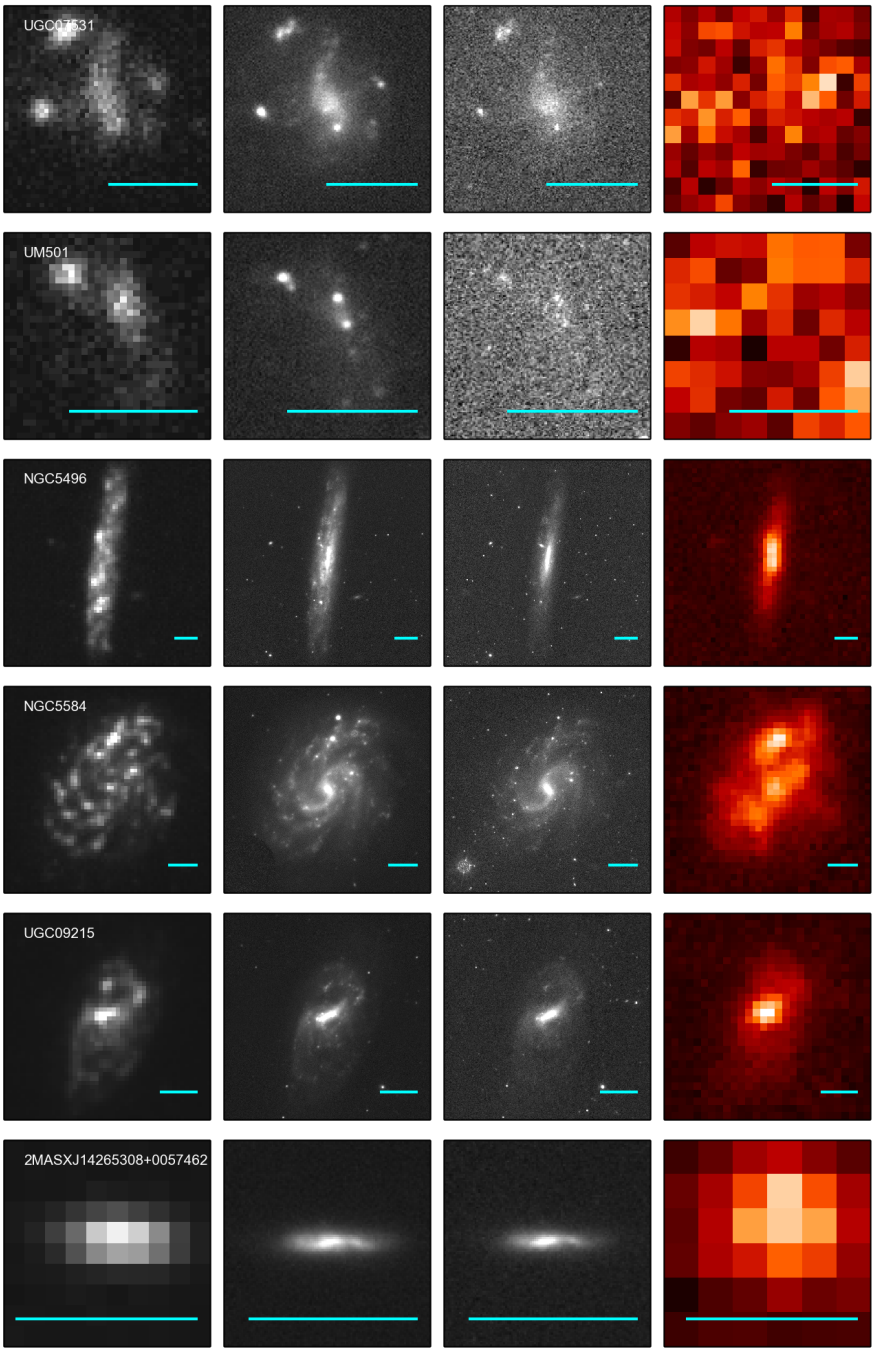

Figure 2.4: - *Continued*

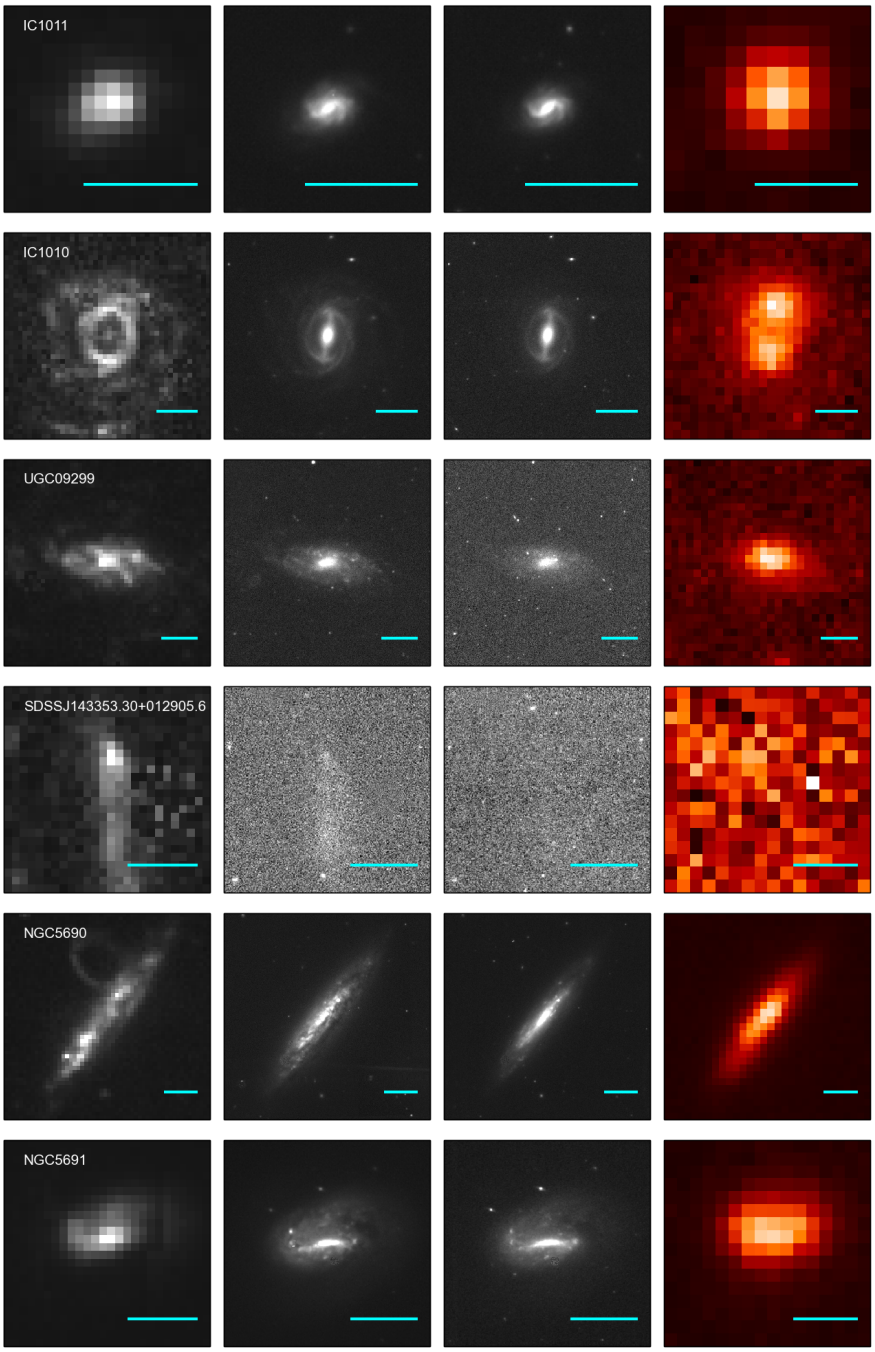

Figure 2.4: - *Continued*

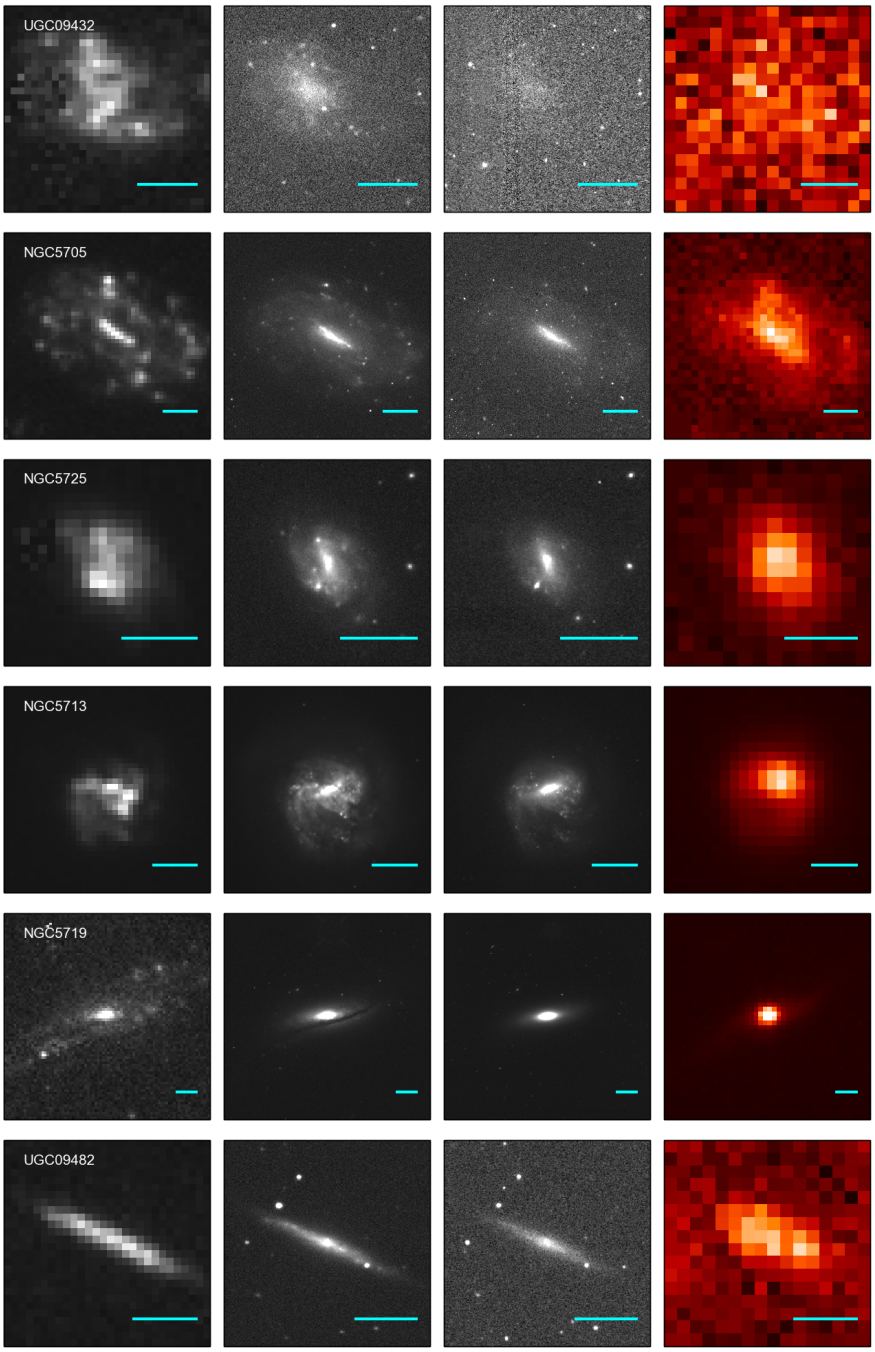

Figure 2.4: - *Continued*

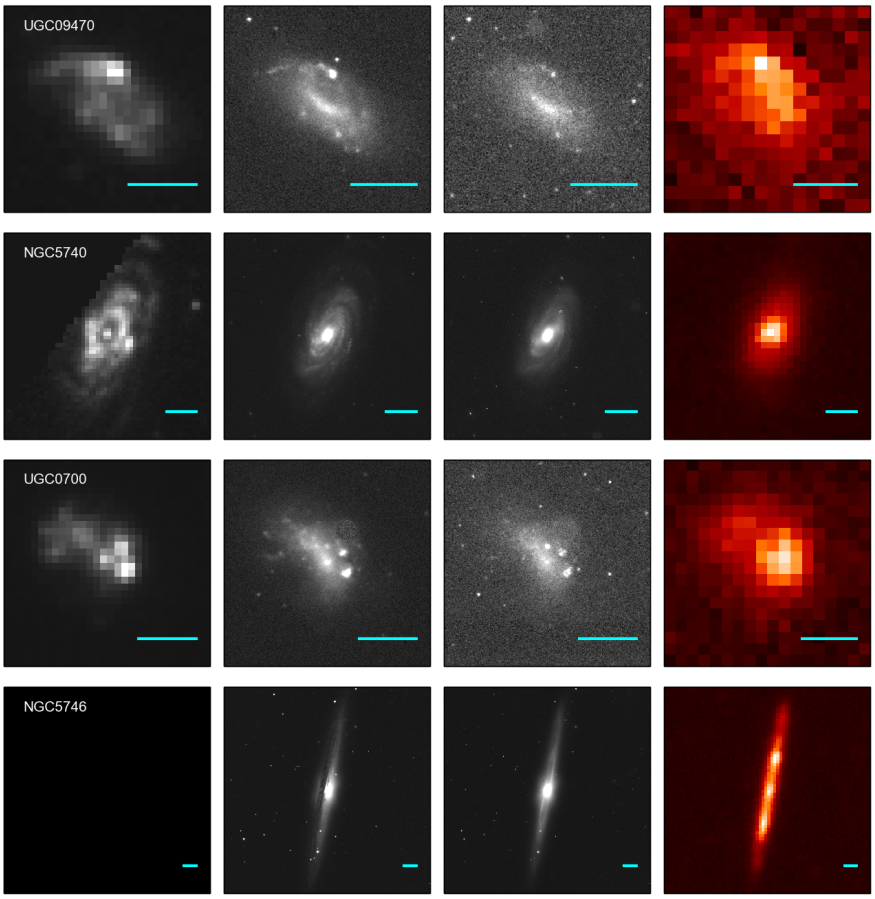

Figure 2.4: - *Continued*

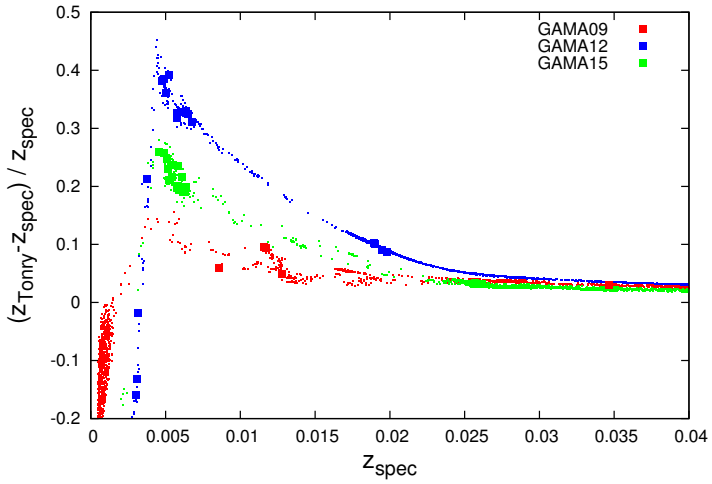

Figure 2.5: Normalised difference between the spectroscopic redshift $z_{\rm spec}$ and the Hubble flow (Tonry et al., 2000) corrected redshifts $z_{\rm tonry}$. The correction is applied to account for the motion of the Local Group relative to the Cosmic Microwave Background. GAMA12 is most affected due to gravitational interaction with the nearby Virgo Cluster.

candidate sources are selected using either local 4σ detections ($\langle 4\sigma \rangle = 52$ mJy/beam) in one channel, or using a tophat search for emission on a variety of velocity width scales between 1 and 40 channels. For the southern HIPASS catalogue this leads to 137060 candidates from the former method (4σ) and 17232 candidates from the latter method, though many of these candidates will correspond to a single source. In a second stage, 81000 candidates are rejected by either visually inspecting the full HIPASS spectrum or preliminary removal of multiple detections of the same object and remaining RFI. Additionally, 56961 candidates are removed after examination in spectral, position and position-velocity space by one of three observers. The final catalogue contains 4315 sources, with the faintest sources having a peak flux of ~ 25 mJy/beam (less then $\langle 4\sigma \rangle$) and an integrated flux of ~ 1.3 Jy km s^{-1}. None of the better resolved sources in our sample are fainter than the faintest HIPASS source. There is no formal HIPASS flux limit, though for sources below 5 Jy km s^{-1}, we cannot be entirely sure they will be included in the HIPASS catalogue. There are unconfused HIPASS sources in our sample with fluxes as low as 3 Jy km s^{-1}. Below 3 Jy km s^{-1}, we only find sources which are confused in HIPASS and where better resolved observations allowed the detection of the individual faint galaxy.

There are 3 (HIPASS-confused) sources have unconfused integrated fluxes between 1.3 and 2.0 Jy km s^{-1} from ALFALFA or literature, which could have easily not made it into the HIPASS catalogue by themselves. These are labelled 'd' in Table 2.4 and we ignore these when we discuss selection effects later. Including these sources would not affect our conclusions in any way (these rather distant sources follow the scaling relations for more nearby sources). There are an additional 3 HIPASS-confused sources with unconfused integrated fluxes between 2 and 3 Jy km s^{-1} from ALFALFA or literature. All three of these sources are very gas rich, and we do not believe they are atypical for an HI-selected sample. We thus suspect these do not bias our results. In any case, excluding these sources does not change any of our conclusions in Chapters 4 and 6.

2.3.4 Distances

All sources in our sample have spectroscopic redshifts available from GAMA. These heliocentric redshifts are corrected by GAMA (Baldry et al., 2012) to account for bulk deviations from Hubble flow (Tonry et al., 2000)[4]. This is necessary to account for the motion of the Local Group relative to the Cosmic Microwave Background due to the gravitation from the Virgo Cluster and the Great Attractor. In Figure 2.5 we show how big this correction is for the sources in our sample. To give a more complete picture of the resulting corrections in the H-ATLAS

[4]For the two sources outside the GAMA footprint, we used corrected redshifts using the same model (Baldry, *priv comm.*).

equatorial fields, we have also included the relative corrections for the GAMA objects[5] in the same redshift range for each of the fields. It can be seen that this correction is strongest for sources with $z \sim 0.006$ (distance ~ 25 Mpc) in the GAMA12 field (up to 40% difference), closely followed by the GAMA15 field. This is due to the close proximity of these sources to the Virgo Cluster. Throughout this work we adopt the cosmology of Planck Collaboration et al. (2013), specifically $H_0 = 67.30\,\mathrm{km\,s^{-1}\,Mpc^{-1}}$, $\Omega_m = 0.315$, and $\Omega_\Lambda = 0.685$.

Distances are then calculated using the corrected redshifts and $D = v/H_0 = c\,z_{\mathrm{corr}}/H_0$. After correcting the redshifts, we find our HIGH sample spans a distance range from 11–159 Mpc. For NGC 5584, there is a redshift-independent distance that is available from measurements of Cepheid variables (Riess et al., 2011). However, there is some scatter in redshift-independent distance estimates for NGC5584, and we have opted to use the same method as for the other sources in our sample for consistency.

Table 2.1 lists the common names and catalogue identifiers for all the sources in HIGH. In Table 2.3, we present some key characteristics, such as positions, redshifts (before and after Hubble flow correction), distances and sizes. The HI-derived properties for our sample are listed in Table 2.4.

2.4 Subdivisions of the HIGH sample

2.4.1 HIGH-high and HIGH-low

The HIGH sample consists mainly of very blue, low surface brightness gas-rich sources with irregular or flocculent morphologies, and active star formation. As we will show in Chapter 4, a significant fraction of the HIGH sources have a lower dust content than expected from extrapolating scaling relations from other (less gas-rich) samples. There is thus a transition from a more dust-poor to a more dust-rich population of galaxies. In order to highlight these different populations we have divided our sample in two.

We found that using a stellar mass cut at $M_* \sim 10^9\,\mathrm{M_\odot}$ provides a good separation between the dust-rich and dust-poor subsamples. We will use this criterion to split the HIGH sample into HIGH-low (for $M_* < 10^9\,M_\odot$) and HIGH-high (for $M_* > 10^9\,M_\odot$) throughout the rest of this work. HIGH-low makes up 40% (16 sources) of the HIGH sample.

The criterion used to separate the samples is somewhat arbitrary, since there is a transition zone between the two populations. However for our purposes, it is sufficient to identify a cut so that all the enigmatic dust-poor sources are contained within the subsample. The new

[5]Here we have used all objects in the GAMA DistanceMeasuresv14 catalogue with reliable redshift (NQ>2) that lie within the equatorial fields.

Table 2.3: Positional characteristics of the HIGH sample. z_{corr}, velocities and distances are corrected for bulk deviation from Hubble flow (Tonry et al., 2000; Baldry et al., 2012). Semi major axes were calculated using the photometry pipeline detailed in Section 3.2.

#	RA (J200 deg)	DEC (J200 deg)	z (helio)	z_{corr} (Tonry)	velocity ($km\,s^{-1}$)	Distance (Mpc)	Semi-maj (")
1	130.74318	0.64408	0.03464	0.03565	10696	158.90	36.60
2	133.967	2.52426	0.01277	0.0134	4020	59.70	77.30
3	134.17066	0.37591	0.00859	0.0091	2730	40.60	61.00
4	140.81604	-0.72945	0.01174	0.01284	3852	57.30	61.00
5	174.153	0.81678	0.00378	0.00458	1374	20.4	56.90
6	177.20993	-2.03249	0.00578	0.00766	2298	34.2	126.00
7	177.65105	-0.56613	0.00574	0.00757	2270	33.7	40.60
8	177.6415	-0.53795	0.006	0.00797	2391	35.50	32.40
9	178.9025	1.23817	0.00635	0.00845	2534	37.7	105.70
10	179.69101	-1.46169	0.005	0.0068	2040	30.30	65.1
11	180.19873	-0.02333	0.0065	0.00861	2581	38.40	73.20
12	180.09841	-1.10033	0.00477	0.00659	1978	29.40	170.80
13	181.0863	-1.53071	0.00488	0.00676	2028	30.10	85.40
14	184.48653	0.43491	0.00318	0.00312	936	13.90	109.80
15	184.53574	-1.06413	0.019	0.02091	6272	93.20	56.90
16	184.85783	0.21197	0.00302	0.00254	761	11.30	52.80
17	185.08868	0.36769	0.00306	0.00266	796	11.80	61.00
18	185.11652	1.46789	0.00526	0.00732	2197	32.60	81.30
19	186.55054	-1.30325	0.00675	0.00885	2654	39.40	45.00
20	186.59463	-1.2534	0.00676	0.00886	2658	39.50	31.60
21	212.9082	-1.15909	0.00488	0.00614	1840	27.40	210.00
22	215.59857	-0.3869	0.00548	0.00678	2033	30.20	138.3
23	215.86342	1.7243	0.00457	0.00575	1726	25.60	109.80
24	216.72078	0.96285	0.02618	0.027	8099	120.40	24.20
25	217.01885	1.00607	0.02564	0.02646	7938	118.00	36.50
26	216.83483	1.02589	0.02566	0.02651	7954	118.20	97.60
27	217.39393	-0.01906	0.00516	0.00635	1904	28.30	113.90
28	218.47167	1.48543	0.00609	0.0074	2220	33.00	61.00
29	219.42	2.29162	0.00583	0.0072	2160	32.10	122.00
30	219.47216	-0.39846	0.00626	0.00748	2244	33.40	61.00
31	219.766	2.94708	0.00513	0.0064	1920	28.50	69.1
32	219.95623	-0.71874	0.00589	0.00703	2110	31.40	117.90
33	220.24298	2.18655	0.00543	0.0066	1980	29.40	52.80
34	220.04759	-0.28933	0.00633	0.00754	2260	33.60	89.50
35	220.23393	-0.31856	0.00575	0.00689	2067	30.70	185.00
36	220.69539	0.66151	0.00606	0.00727	2179	32.40	65.1
37	220.45274	0.68756	0.00637	0.00763	2290	34.00	61.00
38	221.10171	1.68019	0.0052	0.0063	1890	28.10	126.10
39	180.295	-1.29751	0.00501	0.0069	2070	30.80	69.1
40	221.23292	1.955	0.00575	0.0069	2070	30.80	276.6

Table 2.4: HI-Properties for all the sources in our HI-selected HIGH sample. The gas fraction does not include molecular gas (i.e. $f_g = M_{\rm HI}/(M_{\rm HI}+M_*)$. The $M_{\rm HI}/M_*$ and $M_d/M_{\rm HI}$ ratios use MAGPHYS derived stellar and dust masses (see Table 3.4).

#	common name	$S_{\rm int}$ (Jy)	log $M_{\rm HI}$ ($M_\odot$)	gas fraction	log $M_{\rm HI}/M_*$	log $M_d/M_{\rm HI}$	HI origin
1[d]	SDSSJ084258.35+003838.5	1.56	9.97	0.58	0.14	-2.81	ALFALFA
2	UGC04673	7.18	9.78	0.82	0.67	-2.41	ALFALFA
3	UGC04684	9.72	9.58	0.63	0.23	-2.91	ALFALFA
4[a,b]	UGC04996	9.00	9.84	0.75	0.48	-2.71	HIPASS
5	UGC06578	6.72	8.82	0.86	0.8	-3.11	ALFALFA
6	UGC06780	26.90	9.87	0.88	0.87	-2.94	HIPASS
7[a]	UM456	2.86	8.89	0.8	0.6	-3.93	Taylor et al. (1995)
8[a]	UM456A	2.86	8.93	0.92	1.05	-4.06	Taylor et al. (1995)
9	UGC06903	14.11	9.68	0.38	-0.21	-2.53	ALFALFA
10	UGC06970	5.20	9.05	0.31	-0.34	-2.56	HIPASS
11	NGC4030b	6.61	9.36	0.78	0.55	-3.76	ALFALFA
12	NGC4030	72.00	10.17	0.16	-0.71	-2.27	HIPASS
13	UGC07053	8.30	9.25	0.92	1.06	-4.46	HIPASS
14	UGC07332	19.61	8.95	0.95	1.25	-4.65	ALFALFA
15[a]	NGC4202	12.56	10.41	0.56	0.11	-2.97	Richer et al. (1987)
16[a]	FGC1412	2.35	7.85	0.89	0.92	-4.02	ALFALFA
17[a]	CGCG014-010	4.87	8.21	0.89	0.93	-4.74	ALFALFA
18	UGC07394	6.86	9.24	0.67	0.31	-2.4	ALFALFA
19[a]	UGC07531	3.05	9.05	0.74	0.45	-2.58	Taylor et al. (1995)
20[a]	UM501	6.60	9.39	0.97	1.49	-4.31	Taylor et al. (1995)
21	NGC5496	60.90	10.03	0.79	0.58	-2.95	HIPASS
22	NGC5584	27.10	9.76	0.38	0.76	-2.3	HIPASS
23	UGC09215	23.18	9.56	0.64	0.25	-2.64	ALFALFA
24[a,d]	SDSSJ142653.06+005746.2	1.23	9.62	0.52	0.03	-2.4	ALFALFA
25[a,d]	IC1011	1.62	9.73	0.27	-0.43	-2.34	ALFALFA
26[a]	IC1010	10.80	10.55	0.36	-0.26	-2.65	ALFALFA
27	UGC09299	45.54	9.94	0.95	1.32	-3.57	ALFALFA
28	SDSSJ143353.30+012905.6	3.42	8.94	0.94	1.18	-4.43	ALFALFA
29	NGC5690	32.97	9.9	0.25	-0.48	-2.33	ALFALFA
30	NGC5691	5.50	9.16	0.12	-0.85	-2.33	HIPASS
31	UGC09432	8.03	9.19	0.91	1.0	-4.8	ALFALFA
32[a]	NGC5705	25.30	9.77	0.73	0.44	-2.46	Fisher et al. (1981)
33	NGC5725	4.20	8.93	0.39	-0.2	-2.53	ALFALFA
34[a]	NGC5713	42.79	10.06	0.24	-0.5	-2.55	Schneider et al. (1986)
35[a]	NGC5719	52.45	10.07	0.16	-0.72	-2.67	Schneider et al. (1986)
36[a]	UGC09482	5.86	9.16	0.74	0.45	-3.1	ALFALFA
37[a]	UGC09470	4.84	9.12	0.62	0.22	-2.94	ALFALFA
38[a]	NGC5740	29.23	9.74	0.22	-0.54	-2.61	ALFALFA
39[c]	UGC0700	5.7	9.1	0.5	-0.01	-2.7	Sulentic et al. (1983)
40[c]	NGC5746	30.7	9.84	0.03	-1.47	-1.87	Popping et al. (2011)
Mean		16.25	9.46	0.61	0.28	-3.05	
$M_* < 10^9$		9.72	9.07	0.87	0.87	-3.74	
$M_* > 10^9$		21.33	9.76	0.44	-0.09	-2.56	

[a] The HIPASS signal for this source is confused. Higher resolution HI data from ALFALFA or the literature were supplemented to resolve confusion. Note that only unconfused counterparts are listed in this table.
[b] Based on its colour, stellar mass and position, we identified this galaxy as the likely source of most of the HI flux in HIPASSJ0923-00.
[c] UGC0700 and NGC5746 are both sources that are bright enough to make it into HIPASS and our sample, yet they were missed in HIPASS due to their close proximity to other, brighter HIPASS sources.
[d] The individual HI-flux is lower than HIPASS detection limit.

population of dust-poor sources all have stellar masses smaller than $10^9 M_\odot$ and are thus included in HIGH-low. It would also have been possible to use gas fraction to separate the samples, without affecting the conclusions of this work.

2.4.2 BADGRS - Blue and dust-rich

C15 identified an enigmatic population of very blue, dust-and-gas-rich galaxies dubbed 'Blue And Dusty, Gas Rich Sources' (hereafter BADGRS). The BADGRS are low-intermediate stellar mass ($10^8 - 10^{10} M_\odot$) objects with irregular or flocculent morphologies and, in some cases, extended UV disks. Surprisingly, these galaxies have high specific dust masses (M_d/M_*) and cold (15 K) dust temperatures, contrary to what might naively have been expected from their blue colours and high specific star formation rates. C15 defined this population as having $\mathrm{FUV} - \mathrm{K_s} < 3.5$ (or $u - \mathrm{K_s} < 1.76$ for the sources without GALEX coverage). Of the 42 galaxies in the C15 sample (HAPLESS), 27 (64%) satisfy this criterion and 25 (93%) of these exhibit irregular and/or highly flocculent morphology.

When we look for BADGRS in HIGH, we find 30 galaxies (75%) bluer than $\mathrm{FUV} - \mathrm{K_s} = 3.5$. However, not all of these are dusty like the population in C15: the dust-poor sources in HIGH-low also have $\mathrm{FUV} - \mathrm{K_s} < 3.5$ and would be classified as BADGRS if this were the only criterion. By using an additional criterion, $M_d/M_* > 10^{-2.7}$, we select only the dust-rich sources. The BADGRs are thus defined by both their colour and dust-richness and there are 18 (45%) of these sources in HIGH.

The BADGRs are gas-rich sources and thus have not yet converted much gas into stars. They are at a relatively early stage in their evolution (see Chapter 4 and 6). However, the dust-poor blue galaxies in HIGH-low are even more gas-rich (highest gas fractions), suggesting these are in the earliest stages of evolution, and thus even more immature than galaxies in the BADGRS and HIGH-high samples.

There is some overlap between the BADGRS and HIGH-low (and between the BADGRS and HIGH-high) samples if we strictly follow their selection criteria. However, there is a significant contrast between the samples in terms of their dust content as we will see in Chapter 4. The BADGRS are not highlighted as separate subsample, but will be discussed throughout the text.

Chapter 3

Determining galaxy properties for the HIGH sample

3.1 Introduction

In order to study galaxies, we need to reliably determine their properties, such as the masses of the different components, the star formation rate, dust temperature, and so forth. Even though this is the basis of observational astronomy, it remains a challenging task to do consistently. In this work, we use the MAGPHYS code of da Cunha et al. (2008) to determine galaxy properties from the observed SEDs. MAGPHYS has been shown to be reliable (e.g. Michałowski et al., 2014; Hayward & Smith, 2015; Smith & Hayward, 2015) and is presented in Section 3.4. However, to obtain well constrained galaxy properties, it is necessary to use accurate well-determined photometry (including uncertainties) across the entire UV-to-submm wavelength range. This is the reason why we have selected the HIGH sources in the equatorial H-ATLAS/GAMA fields.

The H-ATLAS and GAMA consortia (see also Section 1.5.1) provide photometric catalogues containing a large number of galaxies (including most of the HIGH sources as can be seen from the IDs in Table 2.1). H-ATLAS provides PACS and SPIRE photometry (Valiante et al., 2016, hereafter 'V16') and GAMA carried out their own reductions of GALEX, SDSS, UKIDSS-LAS, VIKING, and WISE observations, to ensure that their photometry is performed consistently across all wavelengths (Driver et al., 2016). However, H-ATLAS and GAMA primarily focus on galaxies beyond the nearby Universe, and consequently their photometry process is optimised for making accurate measurements of distant galaxies, which have small angular sizes. As mentioned in Chapter 2, a large fraction of the HIGH galaxies have highly irregular and flocculent morphologies, and large angular scales. It is very challenging to make a

pipeline that is able to cope with both distant and nearby irregular and flocculent galaxies. The SExtractor (Bertin & Arnouts, 1996) pipeline used by GAMA, is set up for distant galaxies, which for local flocculent galaxies leads to multiple seperate 'shredded' objects within the same galaxy, as discussed in Section 2.3.1.

Therefore, to study the extended galaxies in HIGH in a consistent way across 21 bands ranging from FUV to 500 μm, we determine an aperture that encompasses all galaxy emission and consider the same physical area for each wavelength. With this aim, a pipeline was developed to perform accurate and consistent aperture photometry, using a diverse multiwavelength dataset. The initial pipeline was made by Chris Clark in order to study the dust-selected HAPLESS sample. We helped with the development and testing of the pipeline, and added major contributions to the contaminant removal and uncertainty determination. For the *Herschel* bands, the photometry is performed analogously to the H-ATLAS photometry process. In this chapter, we perform photometry and derive galaxy properties for the HIGH sample. The photometry pipeline is presented in C15 and discussed in Section 3.2. We have performed tests to confirm that the obtained photometry is reliable in Section 3.3. Finally, in Section 3.4 we show how we have determined galaxy properties with MAGPHYS.

3.2 Extended-source photometry

3.2.1 Overview of the photometry pipeline

The bespoke pipeline performs aperture-matched photometry across the entire UV-to-submm wavelength range, with exceptions for the IRAS 60 μm measurements and for the aperture fitting and contaminant masking for the *Herschel* bands. The exceptions are described in Sections 3.2.5 and 3.2.3 respectively. For all other wavelengths, the photometry is performed consistently and tailored to the different angular sizes (ranging from $0.5-3'$) and morphologies for the galaxies in our sample. The aperture matched photometry uses 20 photometric bands: GALEX FUV and NUV; SDSS *ugri*; VIKING ZYJHK$_s$; WISE 3.4, 4.6, 12 and 22 μm; *Herschel*-PACS 100 and 160 μm and *Herschel*-SPIRE 250, 350 and 500 μm.

For ultraviolet, optical and near-infrared data, we use images compiled by the Galaxy And Mass Assembly spectroscopic survey (GAMA; Driver et al., 2011; Hopkins et al., 2013; Liske et al., 2015). GAMA provides spectroscopic redshifts, along with supplementary reductions of ultraviolet (UV) GALEX (Morrissey et al., 2007; Seibert et al., 2012), optical SDSS DR6 (Adelman-McCarthy et al., 2008), Near-InfraRed (NIR) VISTA VIKING (Sutherland, 2012) and Mid-InfraRed (MIR) WISE (Wright et al., 2010; Cluver et al., 2014) data. Details of these

reprocessed maps can be found in Driver et al. (2016). The *Herschel* photometry is performed on H-ATLAS DR1 maps (V16; Bourne et al., 2016).

In summary, the first stage of the photometry process consists of determining the appropriate aperture for each source. The optimal shape and size of the aperture are automatically determined in each band spanning FUV-MIR. The largest aperture is selected as the definitive photometric aperture, which was subsequently used to perform matched photometry across all bands. An illustration from C15 showing the different steps is shown in Figure 3.1.

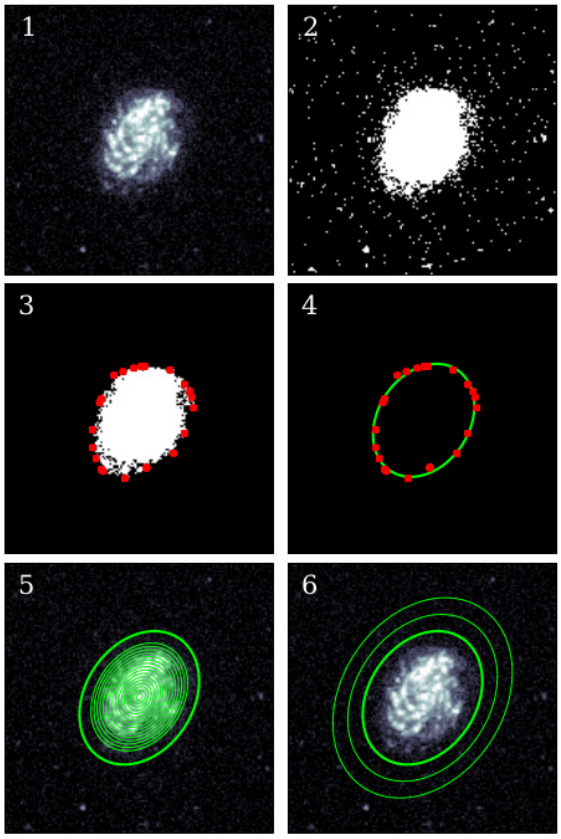

Figure 3.1: Illustration of the stages of the aperture-fitting process, using GALEX FUV imagery of galaxy NGC 5584 as an example. Panel 1 shows the inner $500'' \times 500''$ portion of the cutout centred upon the target source. Panel 2 shows all of the pixels in the cutout with SNR > 3. Panel 3 shows the significant pixels of the target source, contained within their convex hull (red points). Panel 4 shows an ellipse fitted to the convex hull; this ellipse provides the position angle and axial ratio of the source aperture. Panel 5 depicts the incremental annuli used to establish the semi-major axis at which annular flux falls to SNR < 2 (thin concentric lines); 1.2 times this distance is then used as the semi-major axis of the source aperture (thick line). Panel 6 demonstrates the final source aperture (thick line) and sky annulus (thin lines). The apertures at all bands for a given sources are then compared to select the largest, which is then employed for all bands. Figure and caption taken from C15.

In more detail, the first stage of the process consists of determining the appropriate aperture for each source in each band spanning FUV-MIR[1]. We first cut-out a $2000'' \times 2000''$ region centred on the target source in each band and remove foreground stars and background galaxies (see Section 3.2.2). Then a preliminary estimate is made of the per-pixel noise (after clipping the pixel values to get rid of contaminants, as in Section 3.2.6). In order to determine the position angle and axial ratio of the aperture, we start by identifying all the pixels with a $SNR > 3$ (panel 2 of Figure 3.1). By determining the vertices of their corresponding convex hull[2] (panel 3 of Figure 3.1), it is possible to find a best fitting ellipse which corresponds to the best available shape of the aperture and provides us with the position angle and axial ratio (panel 4 of Figure 3.1).

Once the shape is found, the semi-major axis is determined by placing concentric elliptical annuli (with the already determined position angle and axial ratio) on the target, while increasing the semi-major axes in increments of one pixel-width (panel 5 of Figure 3.1). Starting at the smallest annulus and continuing to larger sizes, the mean SNR in each annulus is calculated until an annulus is found for which the $SNR < 2$. Because there is a gradual decrease in brightness towards the edges of a galaxies' emission (e.g. Sersic profile), there is always a fraction of the source flux that falls beyond the edge of any practical SNR cutoff[3]. Therefore, the fitted aperture was multiplied by a factor of 1.2. This factor is large enough to be sure the aperture encompasses nearly all the flux, while small enough to minimise aperture noise. Comparing to the result for larger apertures, tests upon simulated sources, and visual inspection, all indicate that the factor of 1.2 used here achieves this well. This then defines the size of the source aperture. The aperture is determined for all bands spanning FUV-MIR. The semi-major and semi-minor axes are corrected to account for the beam-size in each band, and the largest aperture is selected as the definitive photometric aperture. This aperture will be employed for every band for a given source. GALEX FUV and NUV served as the band defining the aperture (i.e. largest surface area) in all but one of the sources in our sample. The obtained semi-major axes are listed in Table 2.3.

In the second stage of the process the aperture matched photometry is performed in each band (after convolving the aperture size by the beam-size in that band) and the uncertainties are determined. For the FUV-MIR, we subtracted the background using a sky annulus with inner and outer semi-major axes of 1.25 and 1.5 times the semi-major axis of the source. For the *Herschel* bands we subtract the average of randomly placed background apertures on nebulised

[1]MIR-submm bands were not used to define the aperture size due to low signal to noise ratios for some sources and the high levels of confusion noise for SPIRE.

[2]The convex hull is the tightest polygon that can enclose a given set of points.

[3]This is also true for a curve-of-growth approach (Overcast, 2010) and the SDSS Petrosian method (Blanton et al., 2001).

maps (see Section 3.3.4). The photometry from the FUV to K_s-band was corrected for Galactic extinction in line with the GAMA method described in Adelman-McCarthy et al. (2008).

3.2.2 Foreground stars and background galaxies

Before determining the aperture and conducting the photometry, it is necessary to remove bright foreground stars and background galaxies. The SDSS DR9 (Ahn et al., 2012) catalogue was used to identify the locations of the brightest $\sim 20\%$ of stars in the maps and we used a curve-of-growth technique to determine the stars' contamination radius. All the pixels within this contamination radius were replaced by uncontaminated pixels randomly drawn from an annulus adjacent to the masked area (inner radius equal to the found stellar radius and outer radius equal to 1.5 times this radius). An example of this is shown in Figure 3.2. By drawing pixels from a surrounding aperture, the star is replaced by the local background or by the appropriate galaxy emission if the star was in front of the galaxy we are studying, and by randomly drawing pixels instead of taking the average, the noise in the stellar aperture is the same as the surrounding area. As a result, for stars that are not overlapping a galaxy, there is nearly no evidence of the original star after it has been subtracted (Figure 3.2).

The curve-of-growth technique to determine the contamination radius was fine-tuned for each wavelength and for a range of different stars. By increasing the radius by increments of 1 pixel and comparing the fluxes in consecutive apertures, we are able to determine the radius where the stellar radial profile levels off. We then apply an empirical correction so that the aperture contains almost all of the stellar emission, yet is not unnecessarily big. This empirical correction is dependent on wavelength and was determined by visual inspection for stars with a large range of radii. In some cases, the curve-of-growth technique failed due to saturated pixels close to the central position of bright stars. These pixels showed a false level off, yet were still very bright. Therefore we added an additional constraint that the brightness at the final radius needs to be below a wavelength dependent limit that was chosen to be much fainter than the saturated pixels, yet still significantly brighter than any galaxy emission.

The pipeline automatically identifies the locations of the brightest $\sim 20\%$ of stars using the SDSS DR9 catalogue. This proved to provide a good first identification of the brightest stars in all necessary bands (UV-NIR), but not all contaminating stars were identified (especially for the fainter galaxies). Using more than the brightest $\sim 20\%$ of the catalogue proved to be problematic for the brighter galaxies as spurious listings overlapping the galaxy would corrupt our subtraction process (our curve-of-growth technique does not work without a central peak in the brightness profile). Instead we manually determined the location of the remaining bright stars in the neighbourhood of the source. Even with all this fine-tuning, our method is still far from perfect, and there are some stars for which the radius is not determined properly in some

bands. In particular, some stars showed no clear level off in their brightness. For the handful of stars for which this happened, we determined the radius manually and replaced the pixels as for the other stars.

A similar technique was used to remove resolved background galaxies. For the FUV-MIR bands, the aperture for these contaminating galaxies was determined manually and all pixels in the aperture replaced by pixels in the surrounding annulus. The *Herschel* bands are not affected by foreground stars, yet both the PACS and SPIRE cutouts are also contaminated by extended background galaxies. In order to perform an appropriate noise estimation (as explained in the Section 3.2.6), it is necessary to mask these extended sources for both PACS and SPIRE. All extended sources within the H-ATLAS catalogue are masked using the catalogued aperture. The brightest point sources in the PACS and SPIRE cutouts were also masked manually.

C15 only removed the automatically identified brightest $\sim 20\%$ of stars in the maps and removed them using the same curve-of-growth technique. The additions outlined in this section were necessary for our sample as many of the HI-richest sources are low surface brightness and more susceptible to the effects of contaminating sources in the apertures.

3.2.3 *Herschel* photometry

For PACS we use cut-outs generated from the H-ATLAS DR1 PACS maps. In the standard H-ATLAS PACS 100 and 160 μm data reduction (V16), NEBULISER[4] was used to flatten the maps after they were run through SCANAMORPHOS[5]. The filtering applied to the maps could lead to a localised negative background for very extended sources (V16). In Section 3.3.2 we have tested whether using nebulised maps leads to an underestimation of the flux of very extended sources (NEBULISER has a filter with a scale of $90''$). We find that there are no significant systematic differences in the fluxes obtained when either using a larger aperture or when the raw SCANAMORPHOS maps are used instead. Even though we find no offset above the noise, the filtering applied to the maps could lead to (a small) systematic bias for very extended sources. By limiting the PACS aperture to the obvious extent of the dust emission we are minimising the effects of these large scale background issues and increasing the accuracy and reliability of the flux measurements. As long as all the emission at these wavelengths is included, using a smaller aperture will not bias our photometry and it will in fact lead to smaller uncertainties (since the error scales with aperture size).

Therefore we define our PACS apertures separately, using apertures which contain the visible 250 μm flux for each source, as these are reliable indicators of where dust emission is present. However, we do not always have strong enough 250 μm detections to do this

[4] NEBULISER is an algorithm to remove the background emission; Irwin, 2010; see also Section 3.3.2.
[5] SCANAMORPHOS deals with 1/f noise on the maps; Roussel, 2013.

Table 3.1: The FWHM (in $''$) of the beam for each of the bands used in this work.

Band	FHWM ($''$)	Band	FHWM ($''$)	Band	FHWM ($''$)
GALEX FUV	4.0	VIKING Y	0.8	WISE 22μm	12.0
GALEX NUV	5.6	VIKING J	0.8	IRAS 60μm	240.0
SDSS *u*	1.5	VIKING H	0.8	PACS 100μm	11.4
SDSS *g*	1.5	VIKING K_s	0.8	PACS 160μm	13.7
SDSS *r*	1.5	WISE 3.4μm	6.1	SPIRE 250μm	18.0
SDSS *i*	1.5	WISE 4.6μm	6.4	SPIRE 350μm	25.0
VIKING Z	0.8	WISE 12μm	6.5	SPIRE 500μm	36.0

reliably. If $SNR_{250} < 5$, the definitive (largest) aperture size from the other bands is scaled by a factor of 0.8 and this aperture used instead. The factor of 0.8 was determined as the average fraction of the 250 μm aperture size over the largest aperture size for the sources for which the $SNR_{250} > 5$.

For SPIRE the 250 μm-defined aperture misses a fraction of the flux for some sources (Section 3.3.1), and we use the the standard aperture from the FUV-MIR bands instead. The cutouts for SPIRE are extracted from the H-ATLAS DR1 SPIRE maps. These maps are in units of Jy/beam, and are converted to Jy/pixel using the nominal beam areas given in the SPIRE handbook[6]. For the 250, 350 and 500 μm bands we respectively use beam areas of 469, 831 and 1804$''$ for maps with pixel sizes of 6, 8 and 12$''$.

3.2.4 Point spread function

A point source in any image gets spread over the map according to a Point Spread Function (PSF). The typical PSF is a more or less circular Gaussian beam[7], which is defined by the Full Width at Half Maximum (FWHM) of the beam. The FWHM of the beams for the different bands used throughout this work are listed in Table 3.1. Telescopes with poorer resolution have beams with larger FWHM. Since our extended sources also get spread over the beam, we correct the aperture sizes in each band for their beam by adding half the FWHM of the beam in quadrature to the semi-major and semi-minor axes of the aperture[8]. By doing this, most of the galaxy emission is included in the aperture.

However for sources with large beams, such as the *Herschel* bands, there will still be a non-negligible fraction of the source emission that falls outside of the aperture. The Enclosed Energy Fraction (EEF) shown in Figure 3.3 for PACS and SPIRE, shows the fraction of the flux

[6]http://herschel.esac.esa.int/Docs/SPIRE/spire_handbook.pdf

[7]Though for many bands the PSF is not completely circular (e.g. Bocchio et al., 2016 for PACS), the assumption of a circular PSF has little effect on our results.

[8]When we are determining the largest aperture we subtract half the FWHM of the beam in quadrature from the semi-major and semi-minor axes of the aperture for each band before determining the definitive aperture.

that is enclosed within an apertures of a given size. Using the H-ATLAS EEF (V16), we correct our *Herschel* photometry for the fraction of flux outside the aperture using the (beam-corrected) aperture size for each source. We need to divide our *Herschel* fluxes by a factor between 0.83–0.97. We note that these EEF corrections are determined for a point source and thus are somewhat underestimated for our extended sources.

3.2.5 IRAS SCANPI photometry

Even though our aperture photometry spans a wide range of bands, there is a sizeable gap in the wavelength coverage between the WISE 22 μm and PACS 100 μm. In order to get information on this regime, we used the Scan Processing and Integration Tool (SCANPI[9]), following the procedure by Sanders et al. (2003) to measure 60 μm IRAS fluxes for our sources. For a third of the sources in our sample, no reliable detection could be found at the location of the source. For these sources the scans were inspected manually and an upper limit was defined for the flux as 3 times the local rms where necessary.

3.2.6 Aperture noise

3.2.6.1 FUV-MIR

In order to estimate the aperture noise for the FUV-MIR bands, we randomly place 100 apertures with the same size of the aperture in the $2000'' \times 2000''$ cutout centred on the source and determine the standard deviation between them. It is necessary to first get rid of stellar contamination. In the source aperture and background annuli we have used the curve-of-growth technique described in Section 3.2.2 to remove stars. However, this same technique is not practical for the whole cutout as it is not able to find an appropriate radius for each star and thus requires manual checking and adjusting. This would be a very time consuming process since there are much more stars in the $2000'' \times 2000''$ cutouts than just within the source aperture and background annulus. Instead we remove the stellar contaminating in an automated way by clipping pixels that are much brighter than their surroundings (outside 3σ). This clipping method could not be used in the source aperture as we want to be sure not to remove any galaxy emission.

In order to get rid of stellar contamination in the $2000'' \times 2000''$ cutout, we first 3σ-clipped the pixels, while excluding the source aperture from the clipping process and the associated noise determination. The clipped pixels are masked and are not taken into account when determining the aperture noise. Circular apertures with the same area as the source apertures

[9]Provided by the NASA/IPAC Infrared Science Archive: http://irsa.ipac.caltech.edu/applications/Scanpi/

were then randomly placed on the map and background subtracted[10]. If either the circular aperture or its background annulus overlapped with the source aperture, the circular aperture was discarded. The pixel values in each of these randomly placed apertures were then inspected and the aperture was only accepted if fewer then 20%[11] of the pixels were clipped. To determine the flux in the accepted apertures, the clipped pixels ($< 20\%$) in the aperture are replaced by the average of the non-clipped pixels. This process was repeated until 100 apertures were accepted and the aperture noise was determined from the standard deviation of the flux in these apertures. Clipping the pixels within the circular apertures effectively removes the bulk of the stellar emission. However, for the brightest foreground stars, there is a considerable area around the star that will be contaminated enough to affect the flux in the circular aperture, yet not enough to be clipped. This is why we did not accept apertures that were very contaminated by foreground stars ($> 20\%$ of pixels clipped).

We have performed tests to check that this clipping results in a equivalent subtraction of the stellar emission to our curve-of-growth stellar subtraction that is applied within the source aperture, where clipping is not possible. In the background annulus both methods are available and we can compare them. First we checked how the pixel values (converted to flux) for the two subtraction methods compare. We have shown an example of the histogram of the pixel values in the background annulus in Figure 3.4. Compared to the original unsubtracted maps, clipping removes all the pixels above a certain value (i.e. all the pixels dominated by contaminating stellar emission). When we compare this to our curve-of-growth stellar subtraction, we find that this method also removes nearly all the pixels above the clipping value, which is encouraging. However, it also removes a number of pixels around the star and replaces them with other pixels. This effectively removes pixels that are only moderately contaminated by stars (not enough to be clipped), yet it also replaces uncontaminated pixels with other random uncontaminated pixels. This leads to the minor differences between both subtraction methods in Figure 3.4.

The moderately contaminated pixels generally only make up a small fraction of the flux. However around bright stars, there are so many of them that their contribution becomes significant and clipping (which does not remove these pixels) does not perform well enough. For this reason, apertures with more than 20% of pixels clipped were rejected. However, there are not many apertures for which more than 20% of pixels were clipped, especially for the optical bands. Even when there is a significant number of bight stars, the majority of the apertures is accepted, even when there is definitive evidence of remaining stellar emission (e.g.

[10]The background subtraction is performed using a sky annulus with inner and outer semi-major axes of 1.25 and 1.5 times the semi-major axis of the randomly placed aperture, in the same way as for the source aperture.

[11]To be accepted, 20% is the absolute limit for the fraction of pixels clipped. Often we use a smaller limit to reject the apertures that are outliers in terms of their fraction of clipped pixels as will be explained later in this section.

the total clipped flux in that aperture is much higher than the flux in apertures without big stars). It is more appropriate to determine a smaller rejection limit depending on the band and source (harder to limit noisy sources). In order to do this we studied the distribution of the fraction of clipped pixels in each randomly placed aperture. When there is a bright star within a particular aperture, we find an outlying number of clipped pixels for this aperture. In order to select these spurious apertures, we determine the outliers in the histogram as the ones for which the fraction of clipped pixels is more than twice the standard deviation higher than the average fraction of clipped pixels. This effectively removes the most contaminated apertures.

In Figure 3.5 we show an example of the histograms of the fraction of non-clipped pixels and the corresponding total aperture flux in 100 randomly placed apertures. By rejecting the apertures with the lowest fractions of non-clipped pixels, we have also removed apertures which had significant stellar contamination remaining (i.e. strong outliers with respect to the more or less Gaussian distribution of the total flux in the apertures). It is possible a few of the rejected listings were not overly contaminated, but just contained a larger fraction of randomly outlying pixels. Even though these apertures would not have introduced any offsets, replacing them with another randomly placed aperture should not make a difference.

3.2.6.2 *Herschel* bands

For the *Herschel* bands we also use randomly placed apertures to determine the noise. However the process for removing contaminating emission is different. In the UV-MIR, foreground stars are easily removed by clipping as the UV-MIR maps have good resolution and sensitivity, and stars are many times brighter than their surroundings. Yet this is not the case for contaminating galaxies in the FIR. The pixel values of background galaxies are much closer to the noise than stellar pixels are in the optical. This means we cannot just clip the pixels in each randomly placed aperture for the PACS and SPIRE bands. Instead, we mask the contaminating galaxies, including both extended sources and a few point sources (Section 3.2.2). In addition we also mask the source galaxy and any pixels which are within $40''$ of an edge of the H-ATLAS maps. The randomly placed apertures for the noise determination are only accepted if they do not contain any masked pixels. The aperture noise is then determined by taking the standard deviation in 1000 accepted apertures[12].

[12]Here we use 1000 apertures instead of 100 to be consistent with the H-ATLAS aperture noise determination. For the FUV-IR bands, using 1000 apertures would make the photometry process very time consuming (due to the large number of pixels contained within the apertures).

3.2.7 Contaminant removal uncertainty

Another limitation of our method comes from the subtraction of foreground stars and background galaxies. To quantify the uncertainty due to this contaminant removal, we have repeated the photometry for subtractions using a stellar/galaxy radius that differs by $\pm 10\%$ to that found by the curve-of-growth. We calculate the resulting error as the average relative difference between the new photometry and original photometry for each source and each band. For most sources this uncertainty is very small ($< 1\%$) but for the few sources with high contamination this error needs to be added to account for the uncertainty in removing all the stellar radiation properly.

In UGC 04684, a bright foreground star overlapped with a significant fraction of the galaxy. In UGC 06970 there is an overlapping extended background galaxy and an overlapping bright star. For both these sources, the contaminated area was replaced by adjacent pixels for all affected bands (including FIR/submm for UGC 06970), as described in Section 3.2.2. For the WISE bands the contamination is so large that these bands cannot be used. The method for estimating the uncertainty associated with the contaminant removal by changing the radius of the removed area, is insufficient for these sources.

Instead, we estimate the uncertainty associated with the contaminant subtraction for these two sources by manually placing apertures over the contaminated areas and measuring the flux within these apertures (after the subtraction has been performed). In order to determine the uncertainty on the flux in the contaminated aperture, we take the sensible range for this flux to be between zero (all the emission in the aperture originates from the contaminant) and twice the measured flux in the contaminated aperture (the subtraction method has removed too much flux). We then determine the variation assuming a uniform distribution[13] of fluxes between these extreme cases:

$$\Delta F = (2F_{\rm cont} - 0)/\sqrt{12} = F_{\rm cont}/\sqrt{3} \tag{3.1}$$

where ΔF is the uncertainty and $F_{\rm cont}$ is the measured flux in the contaminating aperture, after the stellar subtraction had been applied. This gives us a conservative estimate of the uncertainty in each band, which varies between 5 and 13 % of the source flux. We still use the measured flux in the source aperture so this approach will not bias the flux towards missing any galaxy emission. We have only increased the uncertainty for these two sources.

[13] Note that this distribution is symmetric around the measured flux in the source aperture.

3.2.8 Calibration and SED fitting uncertainties

The contaminant removal uncertainties are added in quadrature to the aperture noise and the resulting uncertainty is given in Table 3.2 together with the fluxes for all sources. Before fitting SEDs (see Section 3.4), we apply an additional term of uncertainty to account for the calibration uncertainty, model uncertainties in our SED fitting and uncertanities in any contributions from spectral lines. For this additional term we use either 10% or the calibration error, whichever is larger. The calibration errors (as given by Morrissey et al. (2007) for *GALEX*, the SDSS DR9 Data Release Supplement[14] for SDSS, Edge & Sutherland (2013) for VIKING, the WISE All-Sky Data Release Explanatory Supplement[15] for WISE, V16 for PACS and SPIRE) are smaller than 10% for all bands except WISE 12 and 22 μm, for which they are 10.7 and 15.4 % respectively.

For the IRAS 60 μm photometry acquired with SCANPI, the reported flux uncertainty is added in quadrature to a 20% calibration uncertainty (Sauvage, 2011) to provide the total photometric uncertainty for each source. The UV to submm photometry for our HIGH sample can be found in Table 3.2.

3.3 Testing the photometry pipeline

3.3.1 Aperture size for *Herschel* photometry

For the UV-MIR bands, we have used an aperture defined by the band with the most extended emission. This is done to ensure all the stellar emission is included in each band. However it is not a priori clear that the dust is distributed in the same way (e.g. Smith et al., 2016), or whether it is more appropriate to define an aperture based on the FIR emission and use this aperture for all *Herschel* bands. In the FIR, we have the best SNR for the 250 μm band and we will use this band to determine the aperture for the dust emission, using the same method as for the UV-MIR bands, including multiplying the found aperture by a factor of 1.2. However, we do not always have strong enough 250 μm detections to determine the aperture reliably. If $SNR_{250} < 5$, the definitive (largest) aperture size from the other bands was scaled by a factor of 0.8 and this aperture used instead. The factor of 0.8 was determined as the average fraction of the 250 μm aperture size over the largest aperture size for the sources for which the $SNR_{250} > 5$.

In Figure 3.6 we compare the *Herschel* photometry using 250 μm determined apertures to *Herschel* photometry using the aperture from the UV-MIR bands. For PACS we find no offset above the scatter, and we can thus use the smaller 250 μm apertures. This serves mainly to

[14] http://www.SDSS3.org/dr9/
[15] http://wise2.ipac.caltech.edu/docs/release/allsky/expsup/

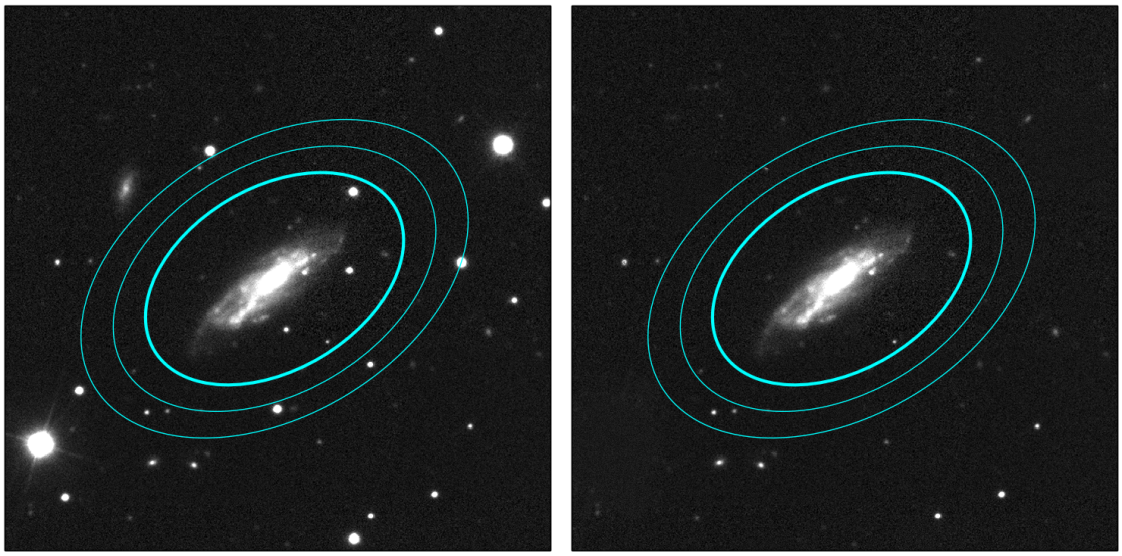

Figure 3.2: SDSS *r*-band image for source UGC 04996 before (*left*) and after (*right*) bright stars and background galaxies have been subtracted. The source aperture and inner and outer boundaries of the background annulus are shown in cyan.

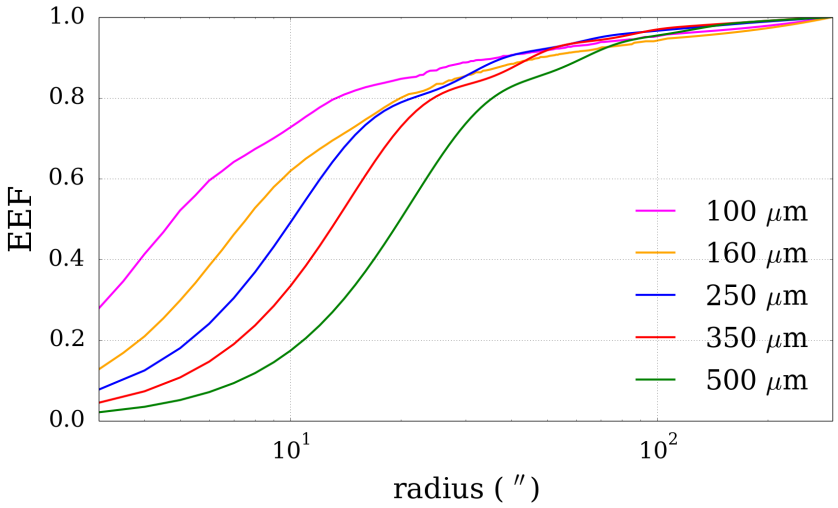

Figure 3.3: Enclosed Energy Fraction (EEF) from H-ATLAS (V16) against radius for the five *Herschel* bands.

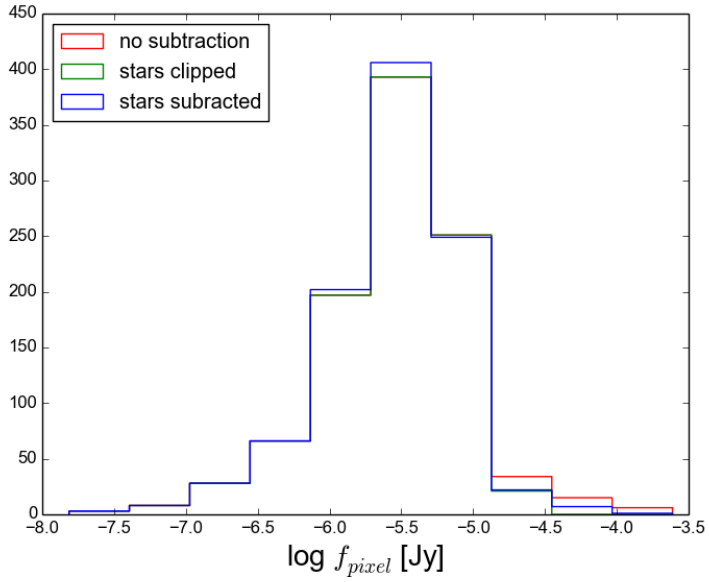

Figure 3.4: Histogram showing the pixel values (converted to flux) within the background annulus of the WISE 4.6μm band of UGC07332 before and after both stellar subtraction methods. The histograms before (red) and after (green) clipping overlap except for a cut-off above the clipping limit. The curve-of-growth method also gets rid of the high pixel value tail and replaces some other pixels within its aperture randomly.

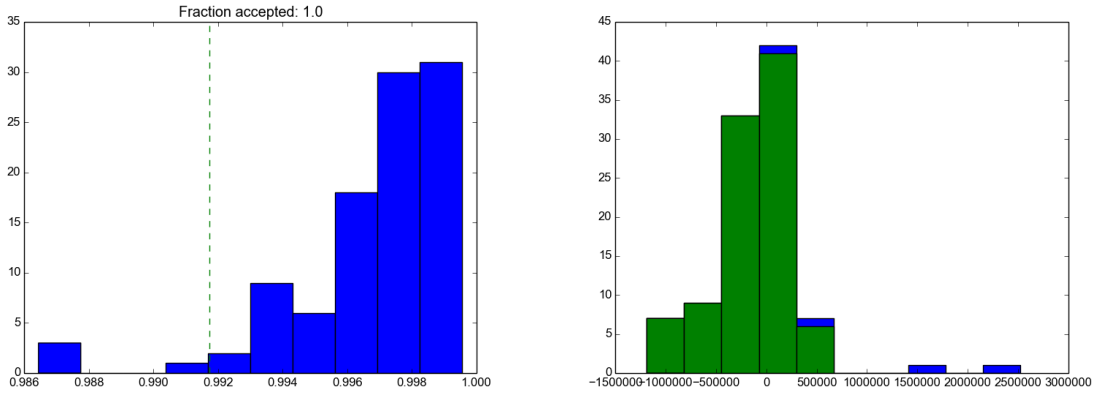

Figure 3.5: Histograms showing the distribution in fraction of non-clipped pixels (*left*) and the sum of the pixel values (*right*) for the same 100 randomly placed apertures for the Y band for UGC07053. For this source all randomly placed apertures are accepted based on the $< 20\%$ of pixels clipped criterion, yet there are some deviantly bright apertures. Instead the limit of fraction of pixels accepted is set based on the standard deviation in the distribution and is shown as a dashed line. The accepted apertures are shown in green in the right panel and rejected apertures in blue.

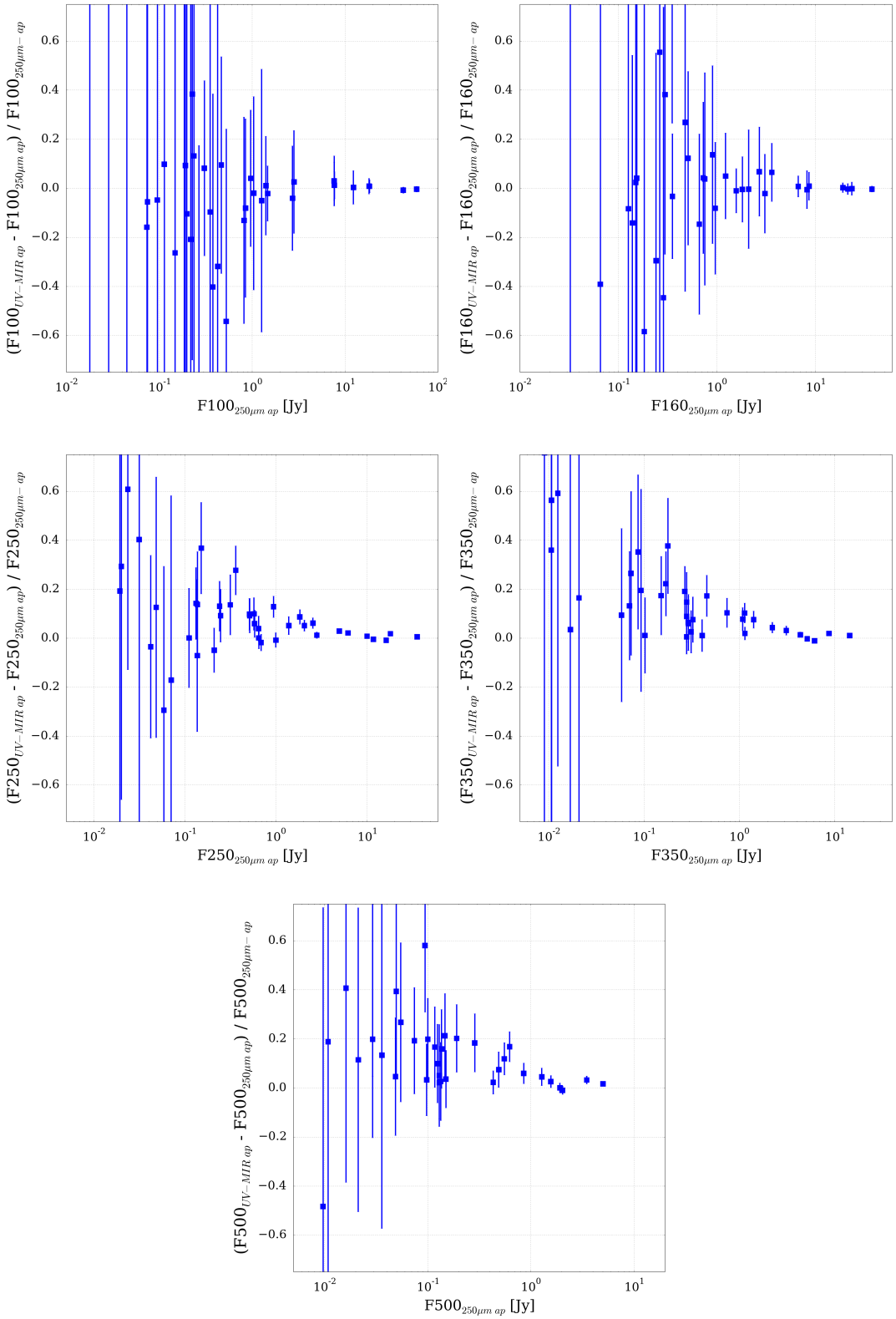

Figure 3.6: The relative offsets between the *Herschel* photometry using 250 μm defined apertures and using the aperture from the UV-MIR bands against the flux in the 250 μm defined apertures. Some flux is missed when using the 250 μm defined apertures.

Table 3.2: Photometry for our HI-selected sample. UV-IR photometry has been corrected for Galactic extinction in line with Adelman-McCarthy et al. (2008). The *Herschel*-SPIRE fluxes were measured using maps reduced for extended sources, but have not been colour-corrected. The semi-major axis of the aperture is denoted by a, the position angle by θ and the axial ratio by a/b.

#	Common name	Aperture dimensions			GALEX (mJy)				SDSS (mJy)							
		$a(''$)	θ (deg)	a/b	FUV	ΔFUV	NUV	ΔNUV	u	Δu	g	Δg	r	Δr	u	Δu
1	SDSSJ084258.35+003838.5	36.39	2.91	1.33	0.21	0.01	0.26	0.02	0.59	0.1	1.37	0.07	1.97	0.11	2.63	0.25
2	UGC04673	77.19	-10.73	1.2	1.06	0.04	1.39	0.04	0.47	0.58	4.86	0.4	5.94	0.7	6.76	2.06
3	UGC04684	62.38	104.22	1.08	1.91	0.22	2.51	0.29	3.74	0.67	8.89	1.41	11.83	2.12	13.13	2.7
4	UGC04996	72.62	21.87	1.73	1.3	0.05	1.87	0.05	3.05	0.31	7.12	0.29	9.26	0.45	10.26	0.96
5	UGC06578	56.81	47.37	1.21	1.81	0.08	2.07	0.05	2.75	0.64	5.08	0.23	5.8	0.32	6.33	0.65
6	UGC06780	134.99	103.96	3.25			2.79	0.08	4.99	0.65	11.98	0.61	14.36	0.87	17.04	1.63
7	UM456	40.29	101.21	1.29	0.97	0.04	1.18	0.03	1.75	0.16	3.34	0.24	3.87	0.29	3.93	0.46
8	UM456A	32.06	-13.84	1.93	0.29	0.01	0.32	0.01	0.48	0.06	0.94	0.05	1.16	0.08	1.17	0.25
9	UGC06903	109.43	24.7	1.2	2.88	0.13	3.02	0.09	4.38	0.89	19.49	1.3	27.99	2.09	34.11	3.64
10	UGC06970	72.62	-5.58	1.59	1.05	0.15	1.47	0.21	3.44	1.25	7.99	1.38	12.97	2.36	21.8	4.15
11	NGC4030b	73.11	18.44	1.14	0.64	0.03	0.78	0.03	0.98	0.72	3.66	0.26	5.4	0.57	6.59	0.97
12	NGC4030	180.68	132.02	1.31	11.98	0.51	22.33	0.58	56.81	4.51	191.95	7.65	327.86	14.54	447.53	24.54
13	UGC07053	85.33	100.18	1.56	0.61	0.03	0.81	0.02	1.72	0.69	3.09	0.22	3.66	0.69	4.07	1.09
14	UGC07332	109.76	16.85	1.09	1.68	0.07	1.98	0.05	3.06	0.52	6.62	0.59	4.35	1.04	8.35	1.74
15	NGC4202	62.38	46.12	1.17	0.28	0.01	0.75	0.02	2.55	0.2	7.46	0.29	12.9	0.57	17.03	0.95
16	FGC1412	48.49	99.14	3.27	0.19	0.01	0.24	0.01	0.41	0.04	0.86	0.04	1.01	0.06	1.14	0.1
17	CGCG014-010	60.89	-42.33	2.76	0.42	0.02	0.55	0.02	0.85	0.09	1.79	0.11	1.94	0.12	2.31	0.23
18	UGC07394	81.17	54.57	1.75	0.41	0.02	0.7	0.02	1.98	0.22	5.04	0.5	7.18	0.43	8.17	0.94
19	UGC07531	32.51	-44.26	1.24	1.99	0.09	2.15	0.06	3.26	0.33	6.1	0.44	6.87	0.5	7.16	0.86
20	UM501	32.51	-44.26	1.24	0.5	0.02	0.4	0.02	0.79	0.15	1.36	0.13	1.39	0.12	1.34	0.17
21	NGC5496	174.83	83.07	3.15	5.26	0.18	7.99	0.17	13.31	3.66	34.04	1.34	46.23	2.18	55.42	3.37
22	NGC5584	154.25	71.46	1.41	9.92	0.38	13.54	0.32	26.67	2.76	64.37	2.93	93.92	4.8	105.32	7.92
23	UGC09215	124.5	68.88	1.67	5.77	0.23	7.45	0.2	13.63	1.74	29.34	1.87	38.34	2.49	45.71	4.54
24	2MASXJ14265308+0057462	62.38	6.92	2.08	0.18	0.01	0.26	0.01	0.6	0.05	1.64	0.07	2.27	0.11	2.49	0.15
25	IC1011	62.35	80.85	1.44	0.69	0.03	1.11	0.03	2.33	0.19	5.35	0.21	7.95	0.37	9.86	0.59
26	IC1010	93.48	95.59	1.13	1.16	0.05	1.52	0.06	3.28	0.65	12.54	0.77	22.47	1.31	28.48	2.94
27	UGC09299	113.83	-19.59	1.5	2.44	0.09	3.47	0.1	4.3	0.75	11.25	1.29	8.92	2.43	13.38	4.23
28	SDSSJ143353.30+012905.6	60.89	98.24	3.0	0.15	0.01	0.2	0.01	0.2	0.14	0.67	0.11	0.82	0.15	0.97	0.49
29	NGC5690	154.25	55.04	1.84	2.0	0.08	3.82	0.12	13.17	1.99	42.83	2.28	71.55	4.75	98.47	5.73
30	NGC5691	78.54	-38.92	1.06	2.08	0.08	3.28	0.08	14.31	1.11	36.52	1.39	53.98	2.34	65.5	3.57
31	UGC09432	69.04	123.87	1.26	0.89	0.04	1.04	0.04	1.87	0.47	3.81	0.34	4.29	0.41	4.2	0.97
32	NGC5705	117.84	-20.27	1.38	4.21	0.16	5.32	0.13	5.72	1.37	23.73	1.15	36.26	2.11	44.33	3.09
33	NGC5725	52.73	117.69	1.14	1.57	0.06	2.22	0.05	4.27	0.42	9.59	0.37	13.37	0.62	15.66	0.92
34	NGC5713	124.5	52.7	1.18	4.67	0.18	9.65	0.23	33.5	2.64	95.45	3.54	157.65	6.81	201.45	10.86
35	NGC5719	170.98	30.67	2.77	0.33	0.02	0.69	0.03	8.04	0.82	37.02	1.4	86.33	3.77	134.29	7.31
36	UGC09482	64.96	-22.6	2.23	0.41	0.02	0.63	0.02	1.47	0.11	3.36	0.13	4.72	0.21	5.6	0.31
37	UGC09470	60.89	-42.57	1.35	1.24	0.05	1.58	0.04	2.99	0.29	6.12	0.29	8.31	0.4	9.37	1.09
38	NGC5740	139.43	78.2	2.17	3.15	0.12	4.98	0.12	11.58	2.91	47.28	1.89	84.11	3.86	112.24	6.08

Table 3.2: - *continued*

#	VIKING (mJy)										WISE (mJy)							
	Z	ΔZ	Y	ΔY	J	ΔJ	H	ΔH	K_S	ΔK_S	3.4μm	Δ3.4μm	4.6μm	Δ4.6μm	12μm	Δ12μm	22μm	Δ22μm
1	2.77	0.34	3.2	0.62	3.33	0.49	3.56	1.19	2.76	0.54	1.6	0.24	1.04	0.22	2.19	0.66	3.8	2.27
2	6.87	1.82	6.47	2.65	6.29	2.22	2.57	5.72	4.79	2.7	4.59	0.84	3.06	0.75	4.44	1.67	13.5	5.46
3	12.07	3.98	10.58	4.27	13.62	3.7	13.43	3.29	11.26	2.72	12.32	2.9	6.96	1.73	11.9	3.11	2.73	3.79
4	11.38	0.86	12.7	0.97	13.24	1.17	11.71	2.3	11.47	0.89	4.99	0.5	3.46	0.46	9.25	1.3	18.13	5.32
5	7.22	0.67	6.18	0.75	6.71	1.16	2.58	1.44	2.98	1.37	3.86	0.59	2.3	0.41	8.66	1.43	42.85	7.53
6	16.0	1.72	13.48	1.72	19.54	2.04	18.49	4.03	11.61	2.8	9.8	1.44	5.2	1.06	5.12	1.62	21.01	7.15
7	4.18	0.62	4.39	0.71	4.35	0.98	4.28	2.31	3.12	1.78	1.35	0.64	0.87	0.47	1.31	0.75	14.26	3.66
8	1.23	0.2	1.23	0.28	1.37	0.26	1.32	0.35	1.3	0.36	0.56	0.36	0.18	0.19	0.36	0.38	3.82	1.87
9	44.42	7.23	47.33	10.33	49.93	8.32	51.89	8.29	40.11	6.84	23.05	4.6	14.65	2.87	31.27	3.91	25.52	9.5
10	21.52	4.25	23.66	4.77	25.1	5.22	24.92	5.29	22.57	4.73	20.47	4.23	12.78	2.74	15.41	3.65	24.77	7.56
11	6.17	0.7	6.79	0.79	6.7	0.88	6.76	1.37	6.2	1.95	3.82	0.83	2.53	0.63	2.62	1.55	3.95	7.8
12	543.79	34.29	667.78	44.27	759.13	56.02	900.17	61.03	759.53	44.85	457.94	25.73	285.11	21.48	1283.61	137.51	1935.21	298.45
13	2.66	1.21	2.41	1.75	4.16	2.03	3.19	4.03	2.73	1.6	2.21	0.56	1.95	0.6	-0.74	1.32	11.07	6.22
14	6.16	1.7	6.43	2.64	11.32	3.45	-	-	1.05	4.78	2.62	1.63	3.51	2.52	9.8	13.35	-63.51	32.42
15	20.19	1.36	24.48	1.65	27.05	2.18	30.77	2.17	26.63	1.69	14.33	0.82	8.7	0.73	32.55	3.76	43.22	7.96
16	1.37	0.12	1.46	0.15	1.41	0.18	0.59	1.46	1.14	0.43	0.51	0.14	0.21	0.19	0.37	0.74	8.01	3.12
17	2.71	0.2	2.77	0.23	2.79	0.28	-	-	2.18	0.7	1.22	0.2	0.39	0.29	0.19	1.79	-2.72	3.75
18	10.08	0.83	11.07	1.06	11.44	1.11	17.29	3.33	9.46	1.17	5.22	0.85	3.07	0.7	4.58	1.29	11.94	4.08
19	7.12	0.93	7.3	0.98	7.26	0.84	7.25	0.75	5.77	0.65	2.92	0.5	1.79	0.45	3.71	0.99	14.55	4.04
20	1.33	0.15	1.35	0.18	1.28	0.26	1.23	0.23	0.97	0.19	0.69	0.13	0.31	0.12	0.35	0.44	10.28	2.45
21	-	-	-	-	59.95	5.11	76.25	7.8	49.32	4.05	36.91	2.21	23.05	1.85	43.46	5.07	77.61	14.03
22	121.55	9.79	130.23	11.15	129.63	12.22	131.07	11.37	117.31	9.89	72.97	5.42	45.19	4.57	159.4	17.96	330.48	52.1
23	49.25	4.98	53.22	6.89	55.49	5.4	54.48	5.67	38.67	5.07	28.18	2.55	17.91	2.69	51.16	5.74	117.3	18.91
24	3.33	0.28	3.83	0.33	4.13	0.38	4.18	0.34	3.98	0.4	1.96	0.21	1.26	0.19	5.7	0.71	10.99	2.06
25	11.89	0.79	13.82	1.0	15.35	1.16	17.54	1.25	14.3	0.92	9.12	0.54	5.86	0.5	33.85	3.65	55.37	8.78
26	24.03	3.13	39.34	4.25	40.05	4.04	52.51	6.16	37.98	4.24	24.32	2.91	13.65	1.91	24.24	3.05	26.02	6.4
27	9.89	3.68	13.22	4.08	11.74	5.98	5.05	11.01	3.63	4.97	2.88	3.96	3.04	2.31	8.59	2.7	19.0	10.76
28	1.1	0.48	1.16	0.46	1.18	0.5	1.08	0.76	1.62	1.39	0.4	0.28	-0.17	0.24	0.32	0.5	-0.97	2.06
29	125.6	8.42	157.19	10.58	179.43	13.83	220.96	15.9	190.36	13.22	120.91	6.89	78.68	5.99	399.25	42.82	608.7	93.85
30	76.51	4.78	86.42	5.74	92.99	6.84	102.02	6.94	80.4	5.11	47.57	2.71	30.42	2.3	130.53	13.99	303.01	46.76
31	4.52	0.87	3.34	1.15	4.95	1.32	-10.55	2.46	3.73	2.18	1.97	0.9	0.51	0.57	0.39	1.04	1.26	3.71
32	43.51	3.05	44.15	3.37	42.96	3.48	36.88	2.93	34.33	4.8	26.25	1.73	15.42	1.48	27.06	3.31	32.67	8.18
33	17.5	1.15	19.14	1.41	20.55	1.58	23.72	1.89	17.09	1.24	10.36	0.7	6.27	0.61	17.67	2.0	24.54	4.67
34	241.55	15.0	288.91	19.0	325.85	23.83	370.05	24.72	312.08	19.6	190.36	10.67	129.9	9.73	914.36	97.85	2359.95	363.48
35	180.95	11.4	243.54	16.0	306.64	22.46	390.96	26.14	340.42	20.17	182.85	10.28	111.22	8.4	353.33	37.83	650.23	100.22
36	6.17	0.4	6.6	0.48	6.8	0.53	7.15	0.6	5.58	0.54	2.55	0.21	1.55	0.21	1.64	0.49	5.11	1.99
37	10.15	0.68	10.29	0.78	10.33	1.04	9.97	1.19	8.7	0.86	5.09	0.46	2.72	0.37	2.8	0.7	13.3	3.04
38	143.51	8.95	173.27	11.39	196.99	14.4	228.0	15.31	178.16	10.48	101.87	5.79	58.8	4.48	182.09	19.53	326.8	50.51

Table 3.2: - *continued*

#	IRAS SCANPI (mJy)		*Herschel*-PACS (mJy)				*Herschel*-SPIRE (mJy)					
	60 μm	Δ60 μm	100 μm	Δ100 μm	160 μm	Δ160 μm	250 μm	Δ250 μm	350 μm	Δ350 μm	500 μm	Δ500 μm
1	140.0	-38.74	199.69	72.57	187.12	69.55	99.41	86.56	51.19	50.53	24.86	25.41
2	60.0	60.05	240.4	129.02	263.09	121.03	390.56	136.42	265.57	100.22	154.48	68.77
3	350.0	129.64	1118.35	226.06	869.99	172.89	633.67	263.15	312.04	165.37	163.01	104.83
4	340.0	111.75	763.93	153.22	576.21	138.17	561.17	268.49	319.89	174.63	138.37	102.27
5	380.0	132.62	280.53	74.69	296.86	83.64	218.55	132.95	130.13	83.09	69.17	54.86
6	160.0	85.4	50.31	158.63	528.81	164.6	452.22	217.31	298.13	194.37	176.77	120.88
7	110.0	67.79	35.84	86.1	55.5	72.57	54.08	58.97	32.03	33.39	8.49	14.6
8	350.0	-99.78	4.46	49.43	88.67	47.56	44.75	40.11	25.03	22.59	9.01	10.3
9	310.0	111.05	604.76	320.66	2509.41	487.12	1491.37	252.42	827.47	182.4	331.08	136.53
10	280.0	119.17	701.13	399.42	618.93	358.91	630.01	455.14	303.38	226.68	141.52	112.0
11	190.0	-57.52	410.45	314.36	209.63	254.58	128.57	77.95	112.23	59.35	44.42	29.5
12	16550.0	3376.36	56594.71	8405.6	74154.97	11095.96	36030.36	8660.74	14600.39	4614.27	5119.09	2260.28
13	141.3	-47.1	146.05	220.25	138.35	191.2	49.12	47.3	5.36	38.9	0.41	19.87
14	140.0	77.51	801.12	492.3	499.9	420.53	59.53	108.15	45.07	80.78	86.0	53.83
15	290.0	124.05	1508.56	266.54	1765.52	300.4	1006.33	594.38	421.25	308.31	154.19	135.61
16	156.87	-52.29	-45.16	57.33	-37.23	48.21	22.08	19.44	5.81	11.61	19.06	10.93
17	160.11	-53.37	44.83	66.17	-55.83	67.83	-1.59	21.9	10.57	17.25	-4.78	11.58
18	-99000.0	-99000.0	78.72	93.33	148.64	72.52	261.73	130.94	191.7	112.68	116.44	89.63
19	260.0	68.0	219.64	119.32	126.47	114.21	183.87	92.17	105.05	63.59	74.54	50.73
20	-99000.0	-99000.0	50.9	46.33	26.71	38.32	44.45	14.39	20.13	10.02	10.71	6.43
21	1000.0	268.79	2552.48	459.94	3215.4	551.13	2762.98	688.23	1560.02	494.86	732.64	310.92
22	2345.0	519.91	7837.31	1302.46	9479.87	1530.4	6405.07	1290.58	3262.83	842.49	1346.56	537.62
23	1420.0	327.92	3224.24	549.87	3368.8	564.56	2186.05	622.94	1233.58	392.05	513.24	243.16
24	210.0	81.61	581.06	127.58	345.87	99.2	194.98	198.12	100.72	105.08	53.53	49.8
25	780.0	208.25	1733.93	285.51	1577.0	265.15	688.41	591.03	292.77	258.54	113.57	103.69
26	310.0	-50.56	1091.86	260.49	1194.22	275.53	1102.18	450.98	566.46	265.19	249.89	131.87
27	230.0	86.61	323.99	136.7	951.47	195.38	574.67	238.12	323.17	167.11	136.46	101.67
28	184.83	-61.61	6.88	86.17	-2.91	74.06	12.56	18.82	5.64	16.11	4.95	11.41
29	6460.0	1336.34	18568.49	2763.53	22069.54	3313.53	11791.91	3678.21	5179.55	1944.26	1922.29	984.16
30	3480.0	796.25	7871.32	1182.49	7527.21	1137.41	2861.88	1478.02	1163.1	767.76	450.82	361.79
31	159.39	-53.13	295.09	267.74	67.18	302.08	76.09	40.15	9.18	16.16	-6.61	6.28
32	440.0	129.63	1125.18	340.74	2140.65	442.6	2006.32	460.83	1186.69	370.75	623.19	301.37
33	430.0	125.97	-110264.9	110264.9	-112753.95	112753.95	663.25	414.7	322.59	250.26	140.72	111.32
34	21290.0	4326.29	41941.45	6185.42	41609.18	6229.08	16222.05	6713.8	6105.52	3109.81	1978.87	1316.57
35	8535.0	1747.16	18218.84	2736.83	20238.91	3051.3	9454.79	5549.59	4032.37	2455.35	1426.28	967.52
36	430.68	-143.56	45.26	62.37	160.37	64.7	155.66	87.7	83.58	55.59	39.72	27.71
37	170.0	68.84	299.65	124.55	469.86	128.62	280.46	115.61	182.41	92.46	94.37	59.85
38	3170.0	711.04	7135.59	1102.94	8706.24	1346.78	5160.67	1698.97	2315.92	882.45	913.38	454.16

minimise any potential underestimation of the flux due to NEBULISER removing large scale emission (Section 3.2.3). Additionally this will also reduce the aperture noise for the PACS bands. For SPIRE, however, there is a systematic offset in Figure 3.6. Some flux is thus missed in the SPIRE bands when using 250 μm determined apertures, and it is thus better to use the larger, UV-MIR defined apertures. The larger apertures will result in more noisy photometry, but there will be no underestimation of the flux. We note that for the brightest sources, there is very little difference between the fluxes for the two methods of aperture determination. These sources are bright enough to have almost all of their emission included in the aperture with a radius for which the annulus has a $SNR < 2$ (multiplied by factor of 1.2, as for other apertures in this work).

3.3.2 Nebulised PACS maps vs RAW PACS maps

We have performed our PACS photometry on nebulised DR1 H-ATLAS maps. The NEBULISER algorithm removes emission from Galactic dust by removing a filtered background value from each pixel. This background value is determined by taking the median[16] of the pixel values in a square of $180'' \times 180''$. A box-car mean filtering, with box size chosen to be $90'' \times 90''$ is then applied to the background values.

In Section 3.2.3 we have discussed that this could lead to a localised negative background for very extended sources and thus an underestimation of the PACS fluxes, which is why we use the smaller 250 μm-determined apertures for PACS. Since the HIGH sample contains sources larger than the above scales, we test if there are any systematic biases between the photometry on nebulised and non-nebulised (hereafter RAW) maps. The H-ATLAS team have done their own tests and found there is no loss of flux discernible in these maps. Yet, because we have such a large fraction of very extended sources, and to justify our difference of method compared to C15[17], we here confirm that there is no offset for our sources.

Figure 3.7 shows the difference between the photometry on nebulised and RAW maps for 100 and 160 μm as a function of the radius. We note that the acquired fluxes include a background subtraction from the average of randomly placed apertures (see Section 3.3.4). The background subtraction significantly affects the photometry the RAW maps but not for the nebulised maps. If NEBULISER caused an underestimation of the PACS fluxes at large scales, we would see that the offset in Figure 3.7 would be systematically positive for large radii. This is not the case, and thus NEBULISER does not remove significant emission from our sources. We can thus safely use nebulised maps for all sources in our sample.

[16] Pixel values that are 10σ smaller or 3σ higher than the median are rejected.

[17] C15 use RAW maps for sources with semi-major axis $> 75''$, since the filter scale used in their PACS maps was only $30''$.

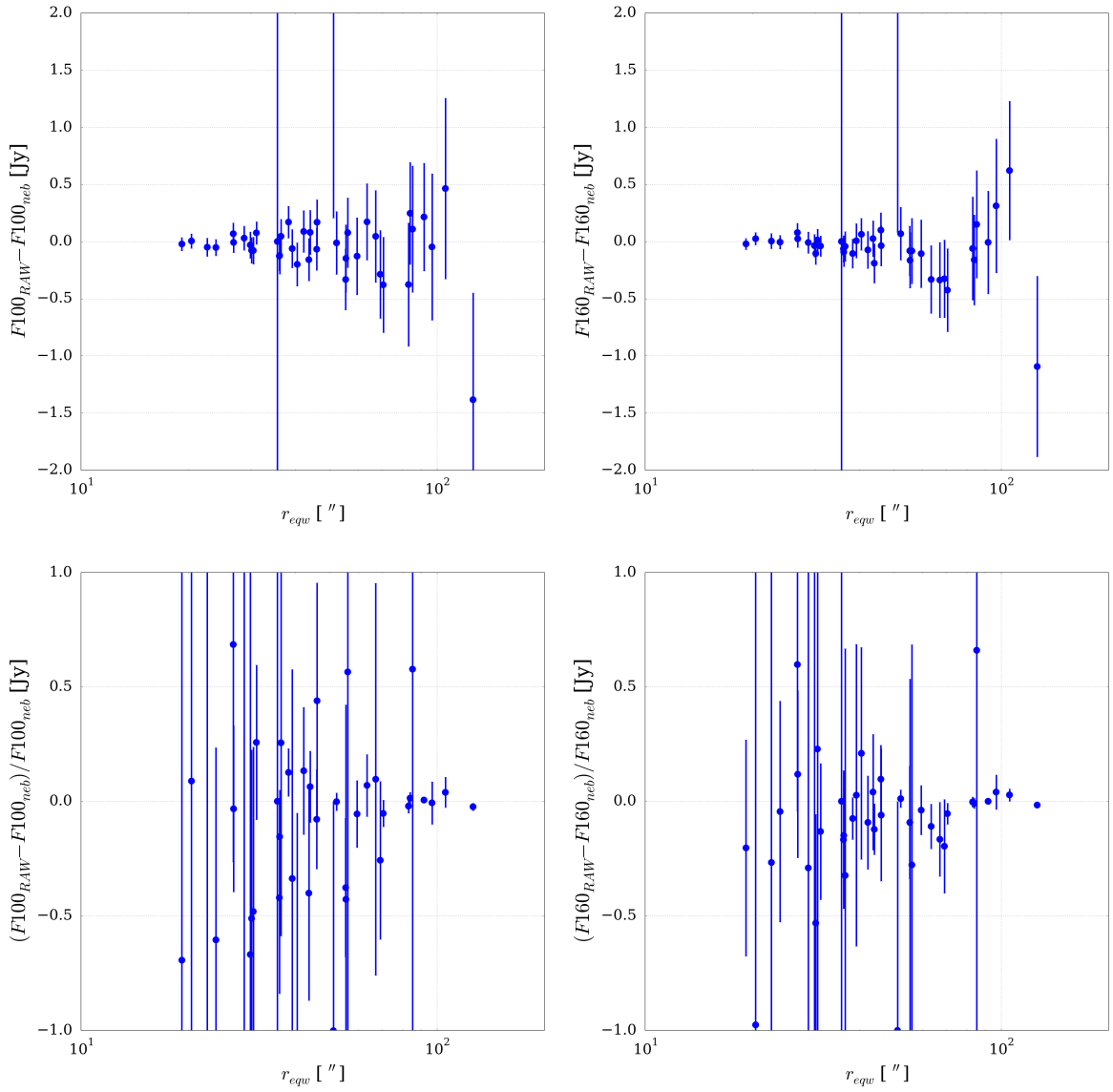

Figure 3.7: Linear (*top*) and relative (*bottom*) offset between the PACS fluxes using nebulised and RAW maps vs the equivalent aperture radius ($r_{\rm eqw} = \sqrt{r_{\rm maj} * r_{\rm min}}$ where $r_{\rm maj}$ and $r_{\rm min}$ are the semi-major and semi-minor axis respectively) for 100 and 160 μm. There is no systematic bias for large radii and we can thus use nebulised maps for all sources in our sample.

3.3.3 Photometry on residual SPIRE maps

The *Herschel* bands are not affected by foreground stars, yet there are still many contaminating background sources in the maps (in part due to the negative k-correction[18]). Due to the low dust content of many of the HIGH galaxies, contaminating background sources can significantly

[18]Even though naively the apparent brightness of an object decreases with the inverse square of its distance, the brightness for SPIRE sources does not decease as much because a different part of the SED is sampled. As one

affect the SPIRE photometry, even if they are quite faint. To test how much our photometry is affected by this issue, we have repeated our SPIRE photometry using residual maps, where all the H-ATLAS 5σ-detected point-sources were PSF-subtracted from the SPIRE maps. These maps were provided by Maddox (*priv. comm.*) and are for the Phase 1 Version 3 data release. Unfortunately these maps were not available for DR1[19]. The PSF subtraction is done both within the source aperture and in the rest of the image. Since point sources are also subtracted within the source aperture, we need to add some of the removed point source fluxes to the extracted photometry in order to get the total flux for a source. Each of the PSF-subtracted sources within the aperture is inspected manually to judge whether it is part of the source we are trying to measure or not.

About 25% of our sources contain no point-sources bright enough to make it into the H-ATLAS catalogue within the aperture. The fluxes for these sources were not affected by the PSF-subtraction of point sources. Another $\sim$ 50% of the HIGH sources only has one, centrally located, point source within the aperture. This point source flux is added to the aperture flux for these sources. For the remaining $\sim$ 25% there are multiple catalogued point sources within the aperture. For each of these we need to judge whether or not they are part of the source we are trying to measure. Figure 3.8 shows NGC5584, a typical example of a source with multiple point sources within the aperture. We inspect each of the point sources and check whether the point source location coincides with UV/optical/NIR emission of the galaxy. If this is the case, and the source is blended with the extended emission of the galaxy, we consider this point source part of the galaxy, and its flux is added to the aperture flux. This is the case for two of the point sources within the aperture of NGC5584. The other three do not have any UV/optical/NIR detection at the location of the point source, nor are they blended with the extended FIR emission (they are separate point sources with size of the beam). These sources are not added to the flux within the aperture. This process effectively removes point sources that contaminate our SPIRE cutouts, which results in a more correct flux measurement of the source and a reduced noise in the rest of the image.

PACS is much less affected by these contaminating point sources and it is not necessary to perform a PSF subtraction of the point sources. However, both the PACS and SPIRE cutouts are also contaminated by extended galaxies. In order to perform an appropriate aperture noise estimation, it is necessary to mask these extended sources for both PACS and SPIRE. This is again done by masking all extended sources in H-ATLAS using their aperture. The reason

moves to more distant objects, the redshift causes the SPIRE bands to sample a progressively more luminous part of the SED (closer to the peak) for a typical source.

[19]For the comparison in this section we use the DR1 beam areas for the conversion of Jy/beam to Jy/pixel for both sets of SPIRE maps to allow for a more consistent comparison. Using the Phase 1 Version 3 recommended beam areas leads to an offset of $\sim$ 10% (see also Section 3.4.6.1).

Table 3.3: The average (per pixel) background surface brightness for both subtraction methods, as measured on the nebulised maps, together with the standard deviation of the background surface brightness between the different sources. Average values (in μJy/pixel) are computed using all HIGH sources. The sky annulus method estimates the background from an annulus around the source and the sky apertures method from 1000 randomly placed apertures.

Band [μJy/pixel]	PACS 100	PACS 160	SPIRE 250	SPIRE 350	SPIRE 500
sky annulus average	-15	1.3	83	90	42
sky apertures average	-2.1	-7.2	3.7	3.4	5.3
sky annulus std	90	155	145	164	161
sky apertures std	10	21	9.4	10	14

this is necessary for SPIRE even though all 5σ sources are PSF subtracted, is that the PSF subtraction assumes these sources are point sources rather than extended. The PSF subtraction thus removes the flux of the whole extended galaxy as if it was a point source, which results in a negative centre and positive fluxes at larger radii. An example of this is shown in Figure 3.9, where it can be seen that the PSF-subtraction successfully removes point sources (green) but not extended sources, which instead have a point source removed from their centre. The pixels within the magenta apertures will be masked. By masking the whole galaxy, we do not need to worry that background apertures partially overlapping the subtracted source will be biased. The differences to the photometry due to using residual maps are discussed in Section 3.3.5. The use of residual maps also affects the background subtraction, as discussed in the following section.

3.3.4 Background subtraction on nebulised maps

We use nebulised (i.e. background subtracted) maps for all our *Herschel* photometry. Here we compare the results of performing photometry without additional background subtraction to results with further background subtraction using two methods. We perform either a local background subtraction in a sky annulus around the source, or subtract the average from the randomly placed apertures for the noise determination. The sky annulus subtraction is done using an annulus with inner and outer semi-major axes of 1.5 and 2 times the source semi-major axis. The annulus thus spans an area 1.75 times as big as the source aperture. The flux in the annulus is scaled to the aperture size of the source and subtracted from the source flux. We also measure the average flux in the 1000 randomly placed apertures for the noise determination (hereafter referred to as sky apertures method). The aperture size is the same as for the source aperture and no apertures with masked pixels are accepted.

We then look at the offset between the photometry using no background subtraction (other than NEBULISER) and the photometry with background subtraction for both proposed methods.

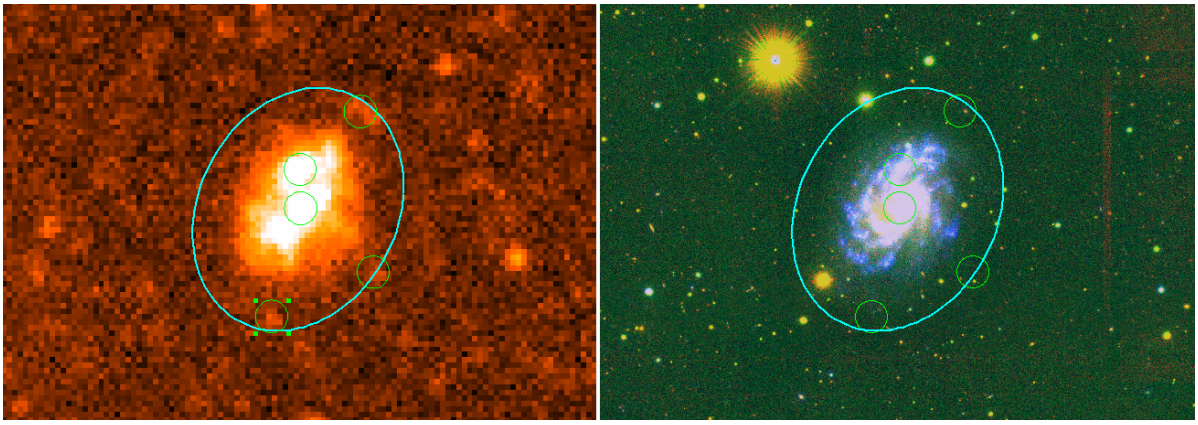

Figure 3.8: *Left:* 250 μm image (before PSF subtraction) of NGC 5584. The source aperture is shown in cyan and the locations of the different point sources in green. *Right:* NUV/*i*/H image of NGC5584 with the same aperture and locations of *Herschel* point sources. Only the two central point sources are associated with the galaxy.

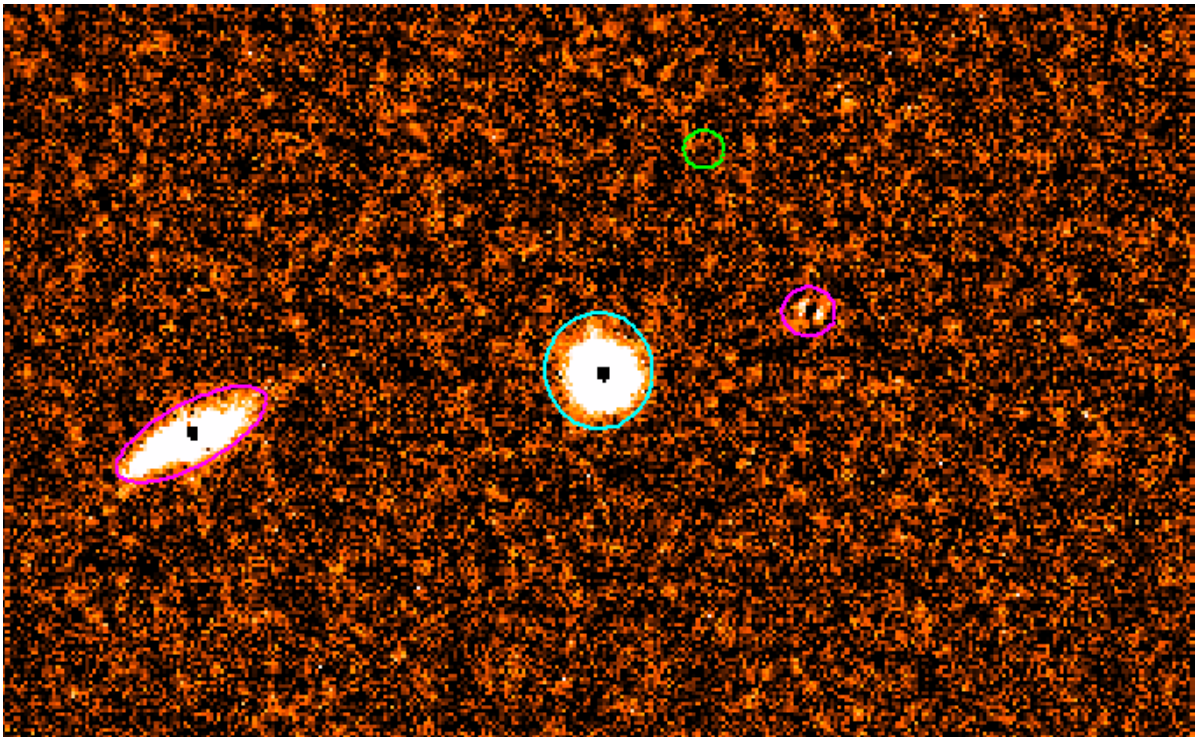

Figure 3.9: 250 μm image (after PSF subtraction) of NGC 5713. The source aperture is shown in cyan and two contaminating extended galaxies in magenta. The green circles shows the position where a point source used to be before the PSF subtraction. It can be seen that the PSF-subtraction successfully removes point sources (green) but not extended sources, which instead have a point source removed from their centre. The pixels within the magenta apertures will be masked so the noise estimation is not affected.

The average per pixel offsets (compared to nebulised maps) and the standard deviation in the offset are given in Table 3.3. We find the average surface brightness (flux per pixel) in the randomly placed background apertures is closer to zero (i.e. more similar to nebulised maps) and shows less scatter than the sky annulus subtraction. We note that even for the sky annulus, the deviation from the nebulised maps is smaller than the 1σ errors for nearly all sources.

We also plot the total background flux (in the source aperture; not per pixel) relative to the aperture error without further background subtraction against aperture size in Figure 3.10 . As the aperture size we take the radius of a circle with the same area as the elliptical aperture ($r_{\rm eqw} = \sqrt{r_{\rm maj}\, r_{\rm min}}$ where $r_{\rm maj}$ and $r_{\rm min}$ are the semi-major and semi-minor axis respectively). We again find the sky annulus method leads to more scatter than the sky apertures method. It is not surprising this method shows more scatter as it based on a much smaller number of pixels and thus is more noisy. In summary, the sky annulus method provides a less accurate estimate of the background and we will not use it further for the *Herschel* maps. For PACS the scatter in the background from sky apertures is small and around zero. For PACS it thus does not really matter whether we use the sky apertures subtraction or not.

However for the SPIRE maps, there are systematic offsets depending on which method is used. For the masked DR1 maps used throughout this work, there is a small offset towards a positive average of the sky, which increases with the size of the aperture. In Figure 3.10, we have also shown the offset for nebulised DR1 maps without any masking. Here there is a clear positive offset. This is because the maps have been nebulised using clipping of contaminated pixels (flux$> 3\sigma$), which effectively removes contaminating (point) sources. If the contaminating point sources are not masked in our photometry, this significantly affects the background estimation. Because the number of contaminants and thus the total background flux in the aperture scales quadratically with radius, and the aperture error scales linearly with radius, there is an increase with $r_{\rm eqw}$ in Figure 3.10. We have masked extended souces and the brightest point sources for the SPIRE maps used throughout this work. However there is still a small offset with the nebulised maps, because more contaminating emission has been removed by NEBULISER's clipping than by our masking.

For extended sources[20], there will be statistically as many contaminating point sources in the source aperture as in any other part of the sky. To get the most reliable estimate of the flux, it is thus important that the background estimate to be subtracted contains a similar amount of contaminating emission as the source we are studying. To achieve this, we automatically mask extended sources and manually mask the brightest point sources in the maps (both inside and outside the source aperture), and use the average of the fluxes in the randomly

[20]Contrary to for extended sources, it is best to use nebulised maps without further background subtraction for point-source photometry, since it can be assumed there are no contaminants overlapping with the source.

placed apertures to estimate the background (thus including moderate contaminating point sources). Using this method to estimate the background only leads to negligible differences to the galaxy parameters derived in Section 3.4, compared to using nebulised maps without further background subtraction. The largest differences compared to the aperture noise, are for sources with large apertures, for which the signal-to-noise ratio is typically high and the differences to the measured flux is typically of the order of a few per cent or less.

For comparison we have also added to Figure 3.10 the offsets between the photometry using no background subtraction and the photometry using the average of the randomly placed background apertures on residual SPIRE maps. Here it can be seen that the local randomly placed background apertures have a negative average. The used PSF subtraction has removed more contaminants than NEBULISER did. Since we have applied the same process within the source aperture, we again opt to estimate the background from the average of randomly placed apertures in the residual maps (for the same reason as for non-residual maps). Compared to no further background subtraction, this will not make a big difference as the effect of this subtraction is on average only 11%, 25% and 36% of the 1σ errors for the SPIRE 250, 350 and 500 μm bands respectively and thus only a very small fraction of the total flux for most sources.

3.3.5 Comparison to H-ATLAS photometry

In this section we compare our photometry, which we label 'DV16' to results from the DR1 H-ATLAS catalogue (V16) for both PACS and SPIRE. For SPIRE we also compare our photometry on non-PSF subtracted maps ('DV16') to the photometry performed on the residual maps described in Section 3.3.3 ('DV16 residual'). In Figure 3.11 we show how the aperture noise (as discussed in Section 3.2.6) scales with the equivalent radius $r_{\rm eqw} = \sqrt{r_{\rm maj}\, r_{\rm min}}$. The noise estimates scale well with the radius for all *Herschel* bands. For both PACS and SPIRE, the errors for DV16 scale consistently with the H-ATLAS catalogue from V16. This is not surprising as the photometry is performed on the same maps, while using very similar methods[21]. The errors for the PSF-subtracted DV16 residual maps, are significantly reduced (by about $\sim 40\%$). This is not surprising as we have removed many of the contaminants that in part determine the error (confusion noise).

In Figure 3.12 and 3.13 we show how the H-ATLAS catalogue fluxes from V16 compare to our results. We plot the differences (linear and relative) between the H-ATLAS catalogue and our DV16 method, performed on the same nebulised DR1 maps for each *Herschel* band.

[21] Both methods mask all extended sources in H-ATLAS and determine the aperture noise using 1000 randomly placed apertures without any masked pixels. We note that our photometry process was tailored to be in line with H-ATLAS.

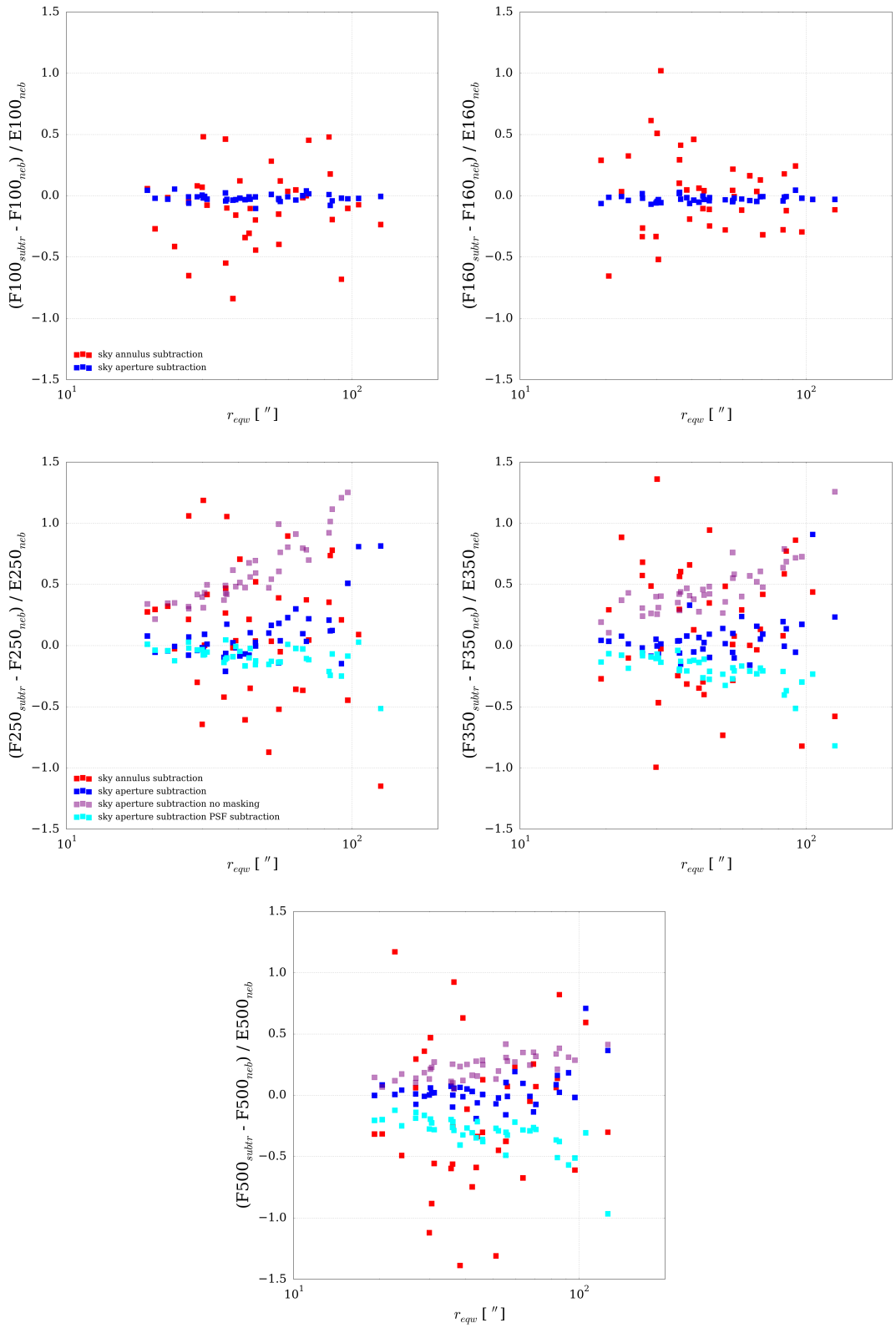

Figure 3.10: The offsets between the photometry using no background subtraction and the photometry with background subtraction, relative to the error with no background subtraction are plotted against the equivalent aperture radius ($r_{\rm eqw} = \sqrt{r_{\rm maj}\, r_{\rm min}}$ where $r_{\rm maj}$ and $r_{\rm min}$ are the semi-major and semi-minor axis respectively) for each of the *Herschel* bands.

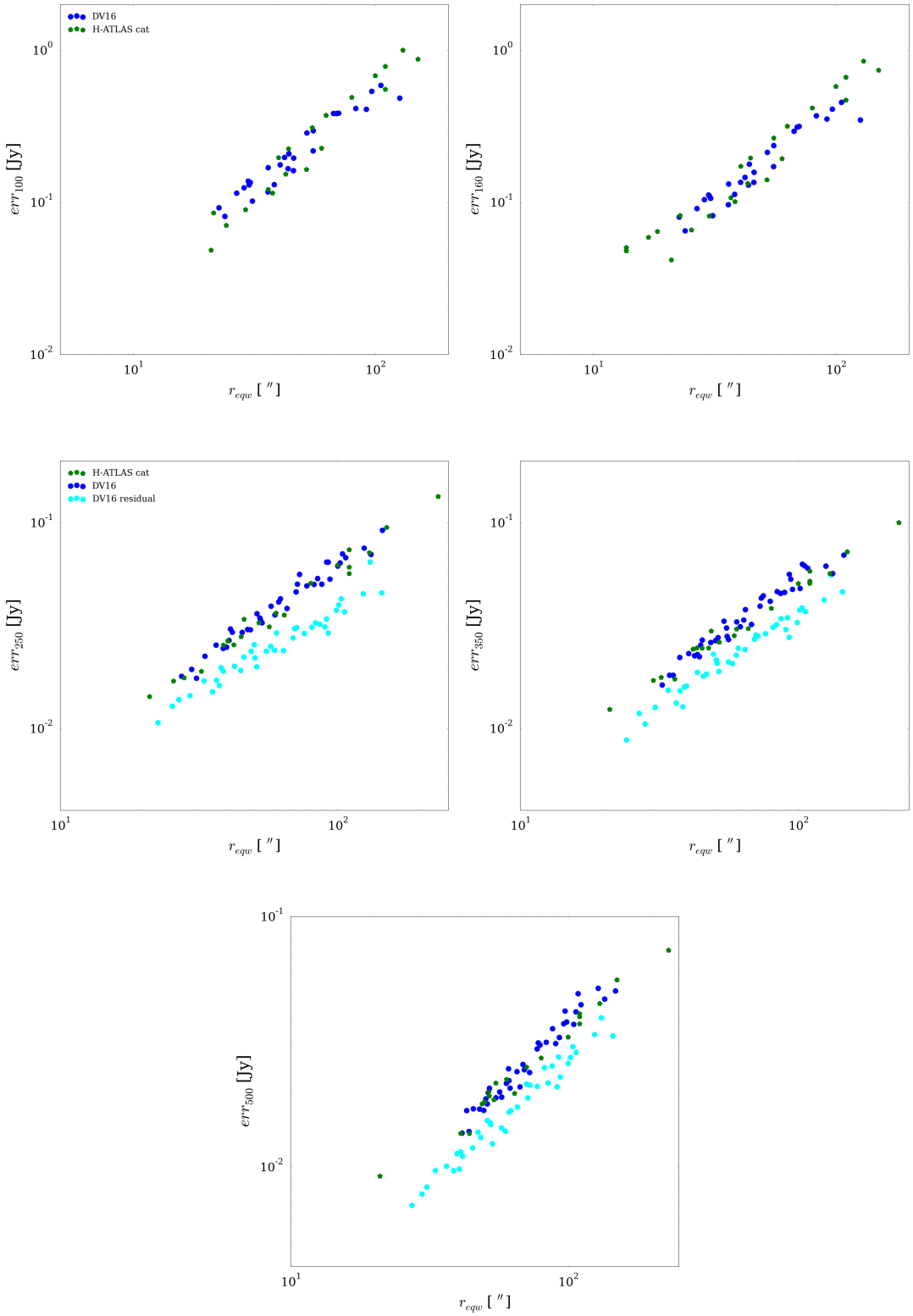

Figure 3.11: These figures show how the aperture noise scales with the equivalent aperture radius ($r_{\rm eqw} = \sqrt{r_{\rm maj}\, r_{\rm min}}$ where $r_{\rm maj}$ and $r_{\rm min}$ are the semi-major and semi-minor axis respectively) for each of the *Herschel* bands. The DV16 method used in this wok is consistent with H-ATLAS and the residual maps unsurprisingly have smaller errors at the same radius.

We find that there is overall good agreement between our method and H-ATLAS, though with a few outliers. There are some outliers towards small fluxes (left side of the plot) and one bright outlier. Upon closer inspection, the two faint outliers (UGC07000 and UGC04673) were classified as point sources in the DR1 H-ATLAS catalogue, and thus missed some of the FIR/submm emission for these moderately extended sources. The bright outlier is NGC5746, a notorious edge-on spiral galaxy. For this source the offset is again due to the H-ATLAS aperture not encapsulating all the emission of the source, as shown in Figure 3.14.

We also find that the results for the residual maps are slightly offset towards lower fluxes compared to the results for our DV16 method, yet the differences between the methods are small and both methods give more or less consistent results with H-ATLAS. The different fluxes for the residual (PSF-subtracted) maps are at least in part due to the subtraction of contaminating sources within the aperture, as explained in Section 3.3.3. There are also small differences because the residual map has been created from Phase 1 Version 3 maps rather than the more up-to-date DR1 maps (as 5σ PSF-subtrated DR1 maps have not been made).

3.3.6 Comparison to the LAMBDAR pipeline

As a further test of our method, we compare our photometry to results by LAMBDAR (Lambda Adaptive Multi-Band Deblending Algorithm in R), a photometry pipeline presented in Wright et al. (2016). Just as our method, LAMBDAR performs matched aperture photometry across non-uniform multiwavelength images. LAMBDAR uses prior aperture definitions derived from high resolution *r*-band imaging by SExtractor. Wright et al. (2016) perform checks to automatically detect poor aperture definitions and correct them manually. However, as we will see later in this section, not all poor apertures are detected using this method. The LAMBDAR pipeline includes key features such as the propagation of apertures to images with arbitrary resolution, local background estimation, aperture normalisation, uncertainty determination and propagation, and object deblending. LAMBDAR has been applied to the 21-band photometric dataset from the GAMA Panchromatic Data Release from Driver et al. (2016), and provides more accurate photometry than was previously available. The resulting catalogue contains 220395 sources, including 37 HIGH galaxies.

In Figure 3.17, we have plotted the relative differences in flux between this method and our DV16 method against the DV16 fluxes, for all used bands. We find a large number of sources where the LAMBDAR fluxes are significantly lower than our fluxes. This is largely due to LAMBDAR having smaller apertures and deblending some of the emission in the apertures. In part due to its *r*-band aperture selection, the apertures are smaller than for our method (the UV emission is more extended than the optical emission for our sources), and it is thus possible that a portion of the galaxy emission is missed in some bands. In Figure 3.16, we have plotted the

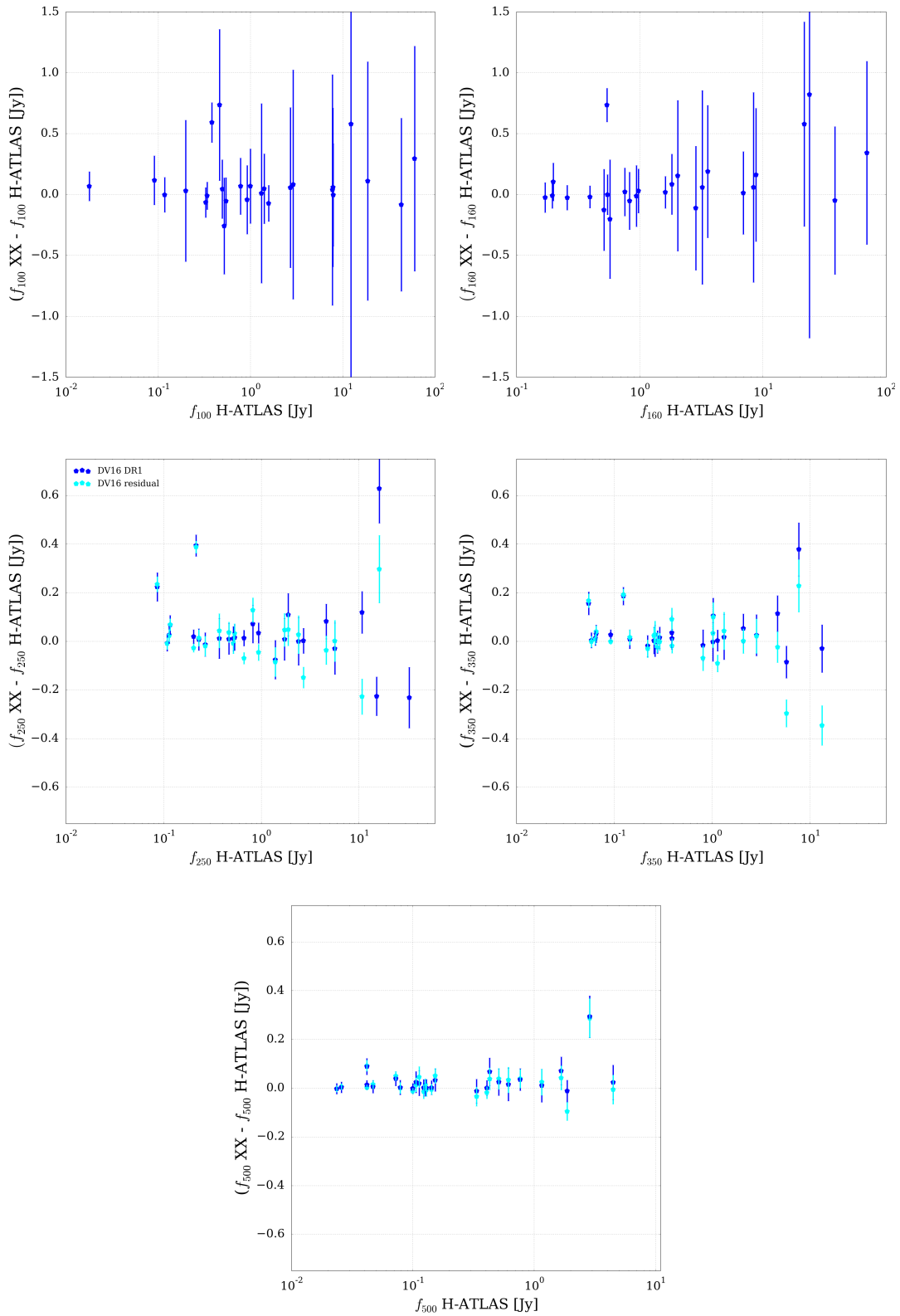

Figure 3.12: The H-ATLAS catalogue flux versus the offset between this flux and the flux from our DV16 method on DR1 maps (blue). For SPIRE, results are also shown for photometry on PSF-subtracted maps (cyan). We find overall good agreement, with a few outliers.

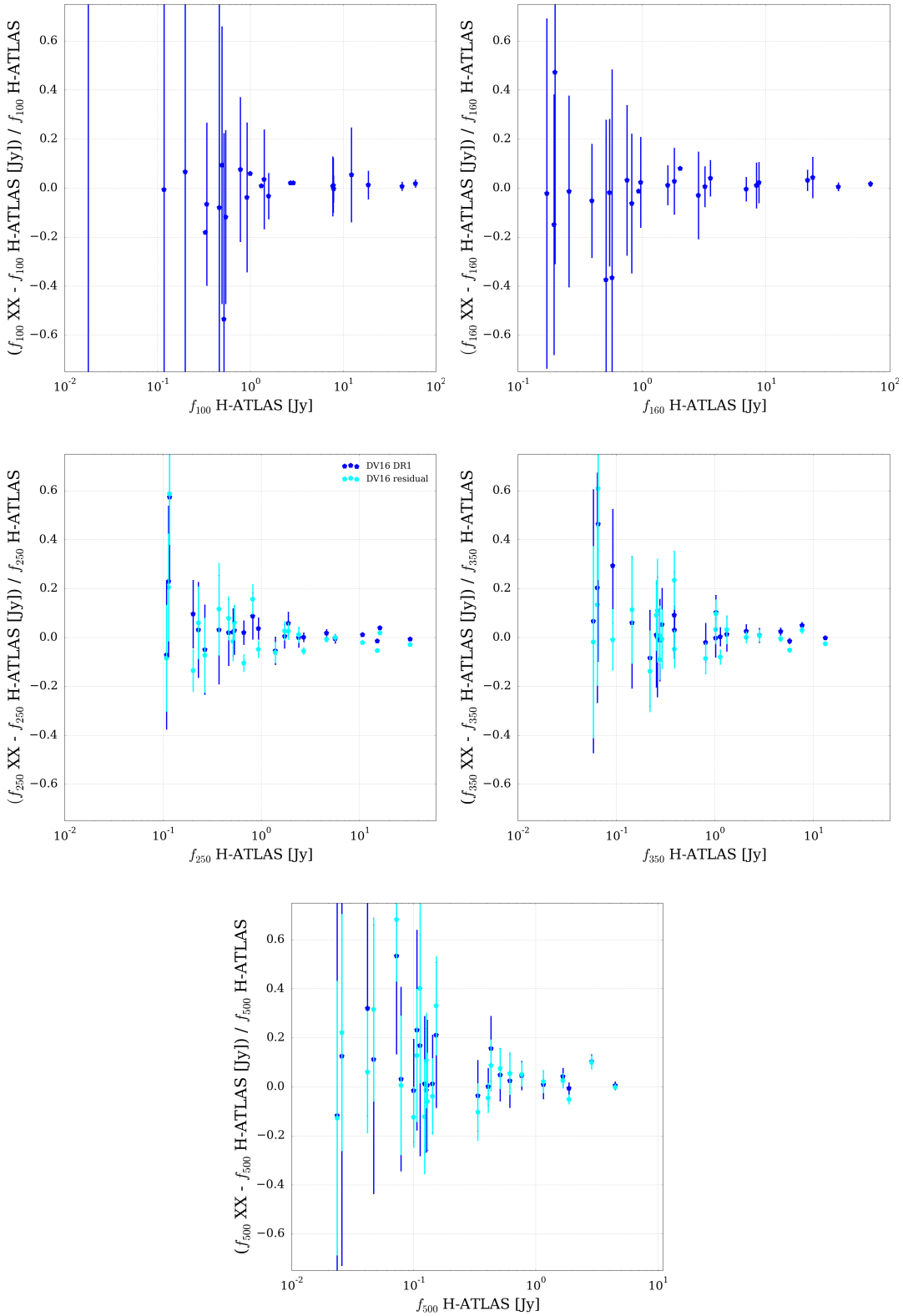

Figure 3.13: Analogue to Figure 3.12, yet showing relative (to the H-ATLAS flux) rather than linear offsets. We find the offsets are small relative to the source flux.

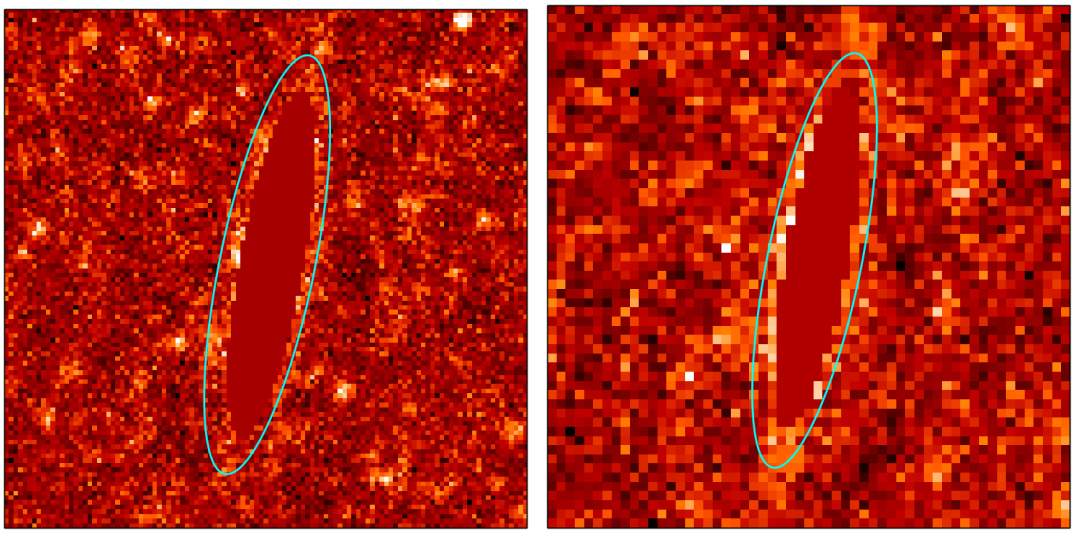

Figure 3.14: Zoomed in image of the 250 (*left*) and 500 μm (*right*) maps for NGC5746. The DV16 aperture is shown in cyan and the pixels within the H-ATLAS apertures have been set to zero. There is significant emission within the DV16 aperture that is not encompassed within the H-ATLAS aperture, which leads to the offset between both methods for this source.

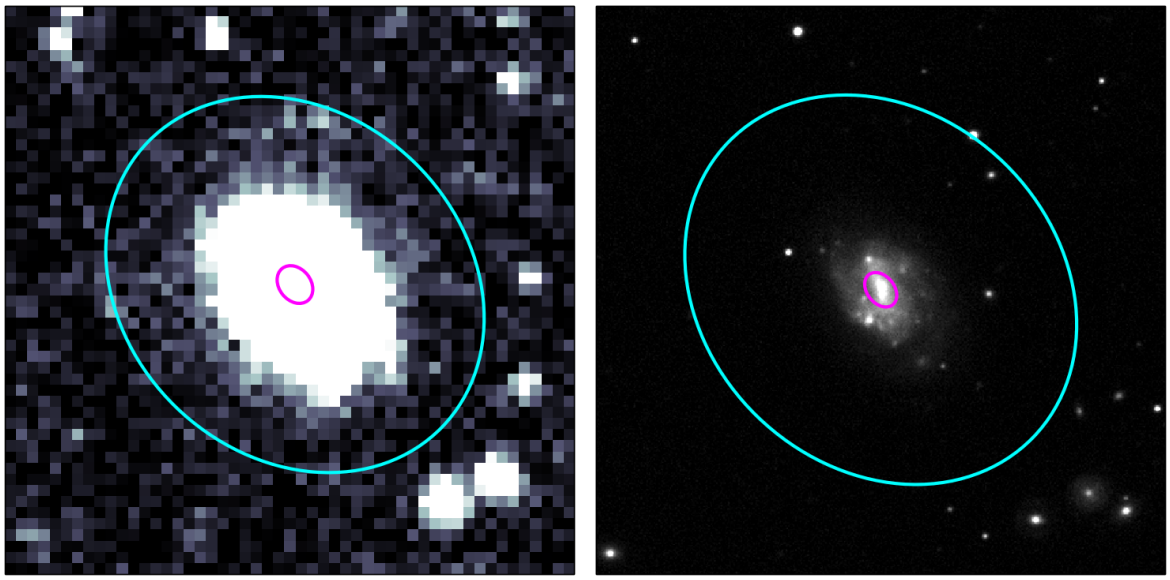

Figure 3.15: Zoomed in image of the NUV (*left*) and *r* (*right*) maps for NGC5725. The DV16 aperture is shown in cyan and the LAMBDAR one in magenta. The LAMBDAR aperture misses significant emission of the source, even in the *r*-band which was used to define its aperture.

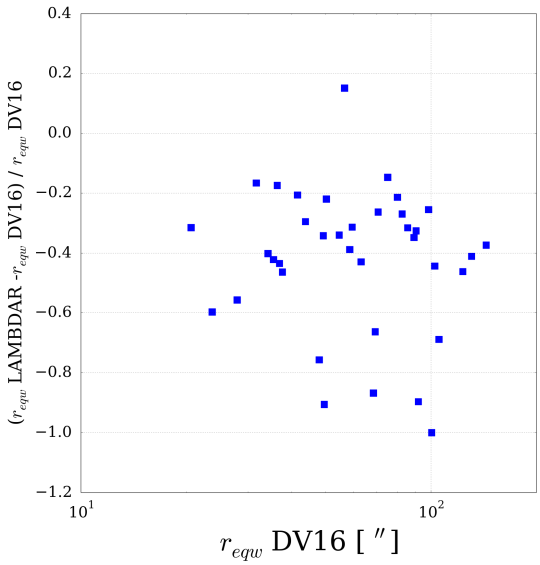

Figure 3.16: Relative differences between the equivalent radius ($r_{\rm eqw} = \sqrt{r_{\rm maj}\, r_{\rm min}}$ where $r_{\rm maj}$ and $r_{\rm min}$ are the semi-major and semi-minor axis respectively) for LAMBDAR (r-band) and DV16 apertures (for the largest band, after the beam has been subtracted quadratically from the aperture size). The LAMBDAR apertures are significantly smaller.

relative difference between the LAMBDAR and DV16 aperture sizes against radius. Due to the r-band selection, the apertures are typically about 10–50% smaller than for DV16. However, there are also some sources (e.g. NGC5725) for which the LAMBDAR aperture is much too small (less than half the DV16 aperture). For these sources the aperture is even too small for the r-band. An exampe of this is shown in Figure 3.15. Here SEXTRACTOR has defined a too small aperture and missed a large fraction of the low surface brightness emission. As mentioned previously, SEXTRACTOR is not set up for the flocculent, extended, low surface brightness sources present in HIGH.

To test how much flux was missed due to using the smaller LAMBDAR apertures, we reran our photometry using the LAMBDAR apertures (we add half the beam in quadrature for each band rather than actually convolving the aperture as LAMBDAR does). We have shown the differences between the resulting photometry and LAMBDAR in magenta in Figure 3.17. When using the LAMBDAR apertures, our fluxes for some sources are significantly lower and the match with the LAMBDAR photometry is much better. This shows that in these cases significant galaxy emission falls outside the r-defined apertures.

Even when using the same apertures, there are still significant differences for some sources in some bands. There are a few positive outliers where the fluxes in the r-defined apertures are smaller for DV16 than for the LAMBDAR method. All of these sources are heavily contaminated by stars (and background galaxies) within the source aperture and DV16 has removed more

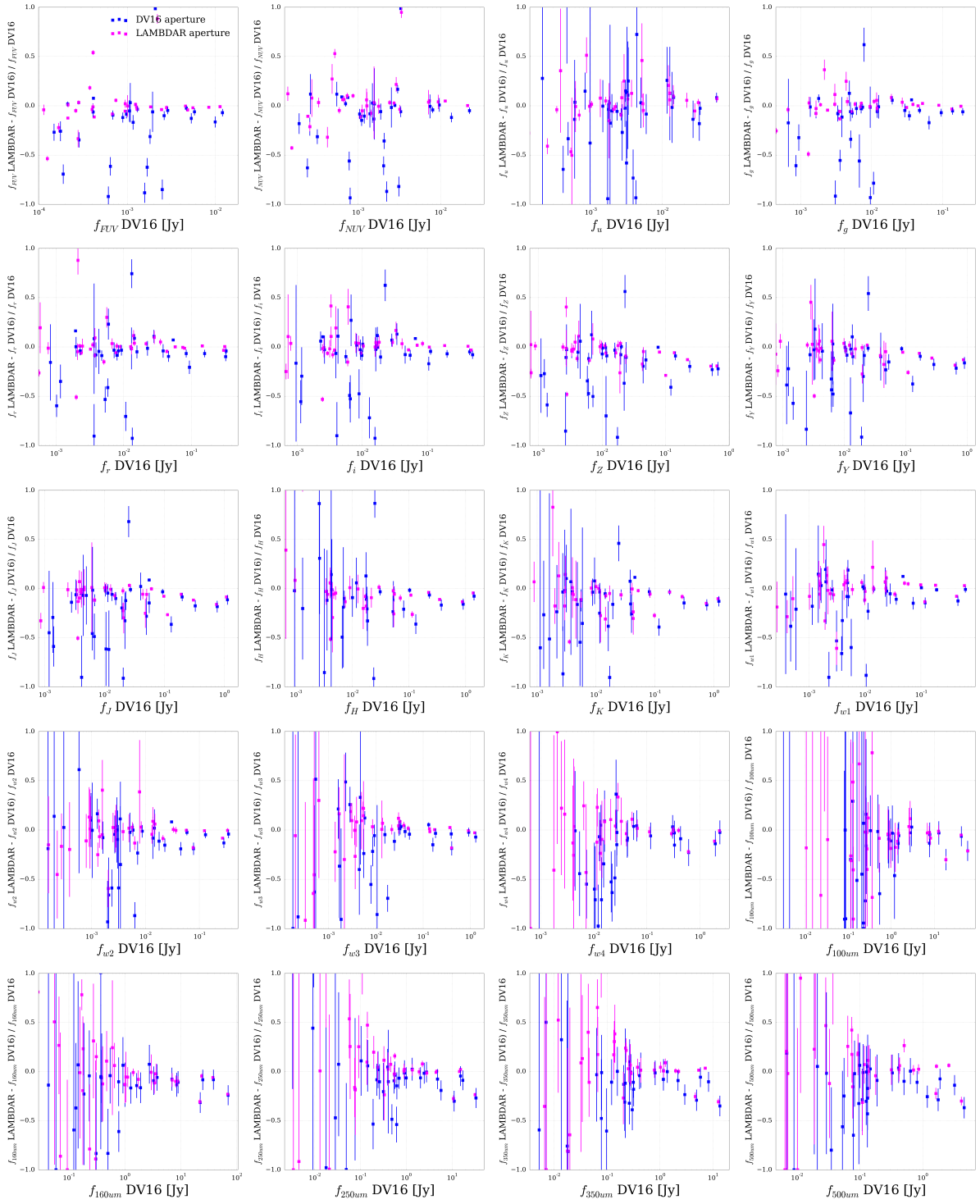

Figure 3.17: The H-ATLAS catalogue source flux using our pipeline versus the relative offset between the LAMBDAR flux and the flux from our method. Since LAMBDAR has smaller apertures, we have run our pipeline both using our apertures (blue) and using the LAMBDAR apertures (magenta). The LAMBDAR apertures contain significantly less flux for a number of sources.

contaminants than LAMBDAR. LAMBDAR masks contaminating sources, but due to the large number of sources, there is no manual inspection and further subtraction that we have applied to the low surface brightness galaxies in our sample (Section 3.2.2).

Additionally, LAMBDAR deblends the emission from overlapping galaxies. Only one source in our sample (UGC06970) is significantly blended with another relatively bright galaxy[22]. For this source we have replaced the contaminated flux by adjacent pixels and estimated the uncertainty, as described in Section 3.2.7. For UGC06970, our method has removed more flux than the automated deblending in LAMBDAR, which leads to the strongest outlier for the stellar bands in Figure 3.17. There are other cases where LAMBDAR deblends some of the emission, whereas upon inspection, there is no visible evidence for a need to deblend. This leads to some of the LAMBDAR fluxes being underestimated and thus negative outliers. A good example of this is NGC4030, the brightest *Herschel* source in our HIGH sample, which erroneously has significant flux removed (e.g. 7.05 Jy at 250 μm) to account for blending, yet there are no contaminating sources within the aperture that could possibly account for such a large offset.

Except for these few outliers, the GALEX, SDSS, WISE and SPIRE bands show good agreement with LAMBDAR when the smaller apertures are used. For PACS and bright VIKING sources however, there is a small systematic offset, with LAMBDAR fluxes being lower than for our photometry. It is currently unclear where these offsets are coming from. For PACS our results agree with H-ATLAS, thus it would be surprising if these were wrong. For VIKING, further comparison of both pipelines is necessary to determine where the offset for bright sources is coming from. These findings have been passed along to Angus Wright, the author of LAMBDAR.

In summary, our pipeline performs well and contains all the emission associated with the extended sources in our sample. In contrast, using an *r*-band defined aperture as for LAMBDAR misses some of the galaxy emission of these low surface brightness extended sources. This is not surprising as our pipeline was specifically designed to perform the photometry on extended galaxies, and we were able to inspect the results for each galaxy due to the limited number of sources, whereas LAMBDAR is set up to do the photometry on a much larger sample and out to higher redshift. Our fluxes are higher on average since the LAMBDAR apertures are in some cases significantly smaller than the DV16 apertures. Yet it is reassuring for the consistency of our method that we can more or less reproduce the LAMBDAR photometry within the scatter if we assume their aperture. The remaining outliers occur mainly due to differences in the contaminant removal.

[22] We have visually checked all the other sources for which our fluxes and the LAMBDAR fluxes are not within the 1σ errors manually, and none show evidence of significant blending of galaxies to the extend that it could cause the offset.

3.4 SED fitting

3.4.1 MAGPHYS

To interpret the resulting panchromatic SEDs of the galaxies in our HIGH sample in terms of their physical properties, we use the MAGPHYS code of da Cunha et al. (2008)[23]. MAGPHYS uses libraries of physically motivated optical and infrared models to describe the stellar and dust emission respectively. The stellar and dust models are combined so that the energy balance between the attenuation of starlight at ultraviolet, optical and near-infrared wavelengths and the dust emission at mid/far-infrared and submillimetre wavelengths is maintained. Since MAGPHYS is able to incorporate multiwavelength information in a self-consistent way, it is an ideal tool to interpret the observations available for this sample of galaxies as they span 21 wavelengths from FUV to submm. Here we briefly summarize the main features; for more details we refer to da Cunha et al. (2008).

The unattenuated stellar emission from ultraviolet to near-infrared is computed by assuming a Chabrier (2003) initial mass function (IMF) and using the Bruzual & Charlot (2003) stellar population synthesis models. The star formation histories are a combination of continuous star formation (exponentially declining with time) and superimposed random bursts. The attenuation by dust follows the prescription of Charlot & Fall (2000) and includes attenuation in the birth clouds (i.e. molecular clouds where stars form) and in the ambient (i.e. diffuse) interstellar medium (ISM). The dust emission is made up of four different components. In the birth clouds the components are: polycyclic aromatic hydrocarbons (PAHs), hot mid-infrared continuum from small stochastically heated grains and warm dust in thermal equilibrium with the radiation field ($T_w = 30 - 60$ K). The dust emission in the ambient ISM includes the same components plus an additional cold dust component in thermal equilibrium with the interstellar radiation field and $T_c = 10 - 30$ K[24]. The PAHs are modelled using a fixed template based on observations of the star-forming region M17, and the hot dust using the sum of two modified blackbodies of temperatures $T = 130$ and 250 K to mimic the radiation from stochastically heated small grains. The warm and cold components are described using modified blackbody spectra with emissivity index $\beta = 1.5$ and 2.0 for the warm and cold components respectively, and the dust mass absorption coefficient $\kappa_\lambda \propto \lambda^{-\beta}$ has a normalisation of $\kappa_{850} = 0.077$ m^{2}kg^{-1} (Dunne et al., 2000; James et al., 2002).

[23]The user friendly MAGPHYS package containing the models of da Cunha et al. (2008) is publicly available at: www.iap.fr/MAGPHYS

[24]The standard MAGPHYS infrared library contains models in the range of 15 - 30 K. This range needed to be extended due to very cold dust temperatures in the galaxies in our sample.

MAGPHYS produces libraries of $\sim$ 50000 optical and $\sim$ 50000 infrared models at the redshift of each galaxy in the sample. Each of these models has a parameter $f_\mu = \frac{L_{\rm dust,ISM}}{L_{\rm dust,Tot}}$ associated with it, which represents the fraction of the total dust luminosity originating in the diffuse ISM. For the optical models the dust is responsible for attenuation, whereas it is the source of emission for the infrared model. To maintain the energy balance in both components (ISM + birth clouds), the f_μ parameter has to be the same for both the optical and infrared models (within a tolerance of 15%) and the total dust luminosity is scaled to match between both models. A large number of templates (combination of optical and infrared models) is found for which the energy balance is maintained.

The MAGPHYS models contain both the attenuated and unattenuated SEDs as well as the physical properties related to the star formation history and dust components corresponding to these SEDs. For each template, the model SED is compared to the observed galaxy SED at the appropriate wavelengths and a goodness-of-fit χ^2 calculated. By running over each template that satisfies the energy balance criterion, probability density functions (PDF) can be made for any of the model physical parameters by weighting the value of that parameter by the probability $e^{\frac{-\chi^2}{2}}$ corresponding to that template. Our best estimate for each parameter is taken to be the median value of its PDF and the corresponding uncertainties as the $16^{\rm th}$ and $84^{\rm th}$ percentiles of the PDF.

We made some adaptations to MAGPHYS in order to tailor it to our sample. These include:

- The cold dust temperature range needed to be extended to 10 - 30 K (instead of the standard 15 - 25 K) in order to fit some of the dusty sources in our sample.

- Some HIGH sources have bands with low SNR, and in some cases the measured fluxes in the FIR are negative, though with errors that are consistent with a zero or positive flux at the 1σ level. The standard MAGPHYS version does not deal with negative fluxes, yet we have incorporated them in our χ^2 calculation, as they still give statistical constraints.

- Additionally we added a routine that allows to include IRAS 60 μm upper limits (necessary for a third of our sample). For these upper limits, we only add a contribution to χ^2 if the model fluxes are higher than the upper limit flux.

- We have generated a PDF for the dust attenuation in the FUV (A_{FUV}) by comparing the attenuated and unattenuated model FUV fluxes for each model.

- Additional PDFs have been produced for some of the parameters in the libraries, such as dust-to-stellar mass ratio (M_d/M_*), age parameters, the fraction of stars produced in the last burst and the stellar metallicity.

3.4.2 Photometry corrections

In order to compare aperture photometry to model SEDs (i.e. to fit SEDs), we need to apply two corrections to the *Herschel* photometry. The first correction is the $K_{\rm beam}$ correction and applies to SPIRE only. The conversion from Jy/beam to Jy/pixel requires the beam area. To obtain our aperture photometry, we have used the nominal beam areas given in the SPIRE handbook. However, the real beam area is SED dependent, and we need to apply a correction to the SPIRE photometry to account for this. We have applied the $K_{\rm beam}$ corrections from an interpolation of Table 5.5 in the SPIRE handbook, based on the uncorrected MAGPHYS median temperature (e.g. for 15 K, the $K_{\rm beam}$ correction factors are: 1.0221, 1.0363 and 1.0802 for 250, 350 and 500 μm respectively).

The second correction one needs to apply is the colour correction. The *Herschel* photometry is obtained using broad-band filters. Therefore it is not correct to compare our photometry to the SED at a single effective wavelength of the filter. We need to take into account the fluxes at a range of wavelengths the receiver is sensitive to. For each band, MAGPHYS calculates the fluxes for each model SED by integrating the SED using the filter response function, which effectively weights the fluxes at each wavelength proportional to how sensitive the receiver is to these wavelengths. These colour corrections for MAGPHYS (internally implemented) are slightly different than the $K_{\rm colP}$ colour corrections from the SPIRE handbook. In future work, we aim to use updated MAGPHYS filter response functions that are consistent with $K_{\rm colP}$.

Before fitting SEDs to the fluxes in Table 3.2, we thus correct the SPIRE fluxes for $K_{\rm beam}$ and apply the additional uncertainty term to all bands (see Section 3.2.8). MAGPHYS intrinsically applies colour corrections to all fluxes, so the $K_{\rm colP}$ colour corrections from the SPIRE handbook do not need to be applied.

3.4.3 Results

The MAGPHYS results for the 40 sources in the HIGH sample are presented in Table 3.4 and the MAGPHYS fits to the SEDs of the HIGH sources are shown in Figure 3.19. Additionally, we have shown an example of the PDFs (together with the associated best fitting SED) in Figure 3.18 for an evolved galaxy (NGC4030) and an unevolved galaxy (UGC09299).

3.4.4 Unreliable MAGPHYS SFR for sources with a recent burst

The SFR estimate from MAGPHYS averages the SFH over the last 10^8 years. The model SFHs include randomly imposed bursts, for which the SFR is strongly elevated (and constant) between a discrete start and end time. Some of the blue sources in our sample have a stellar

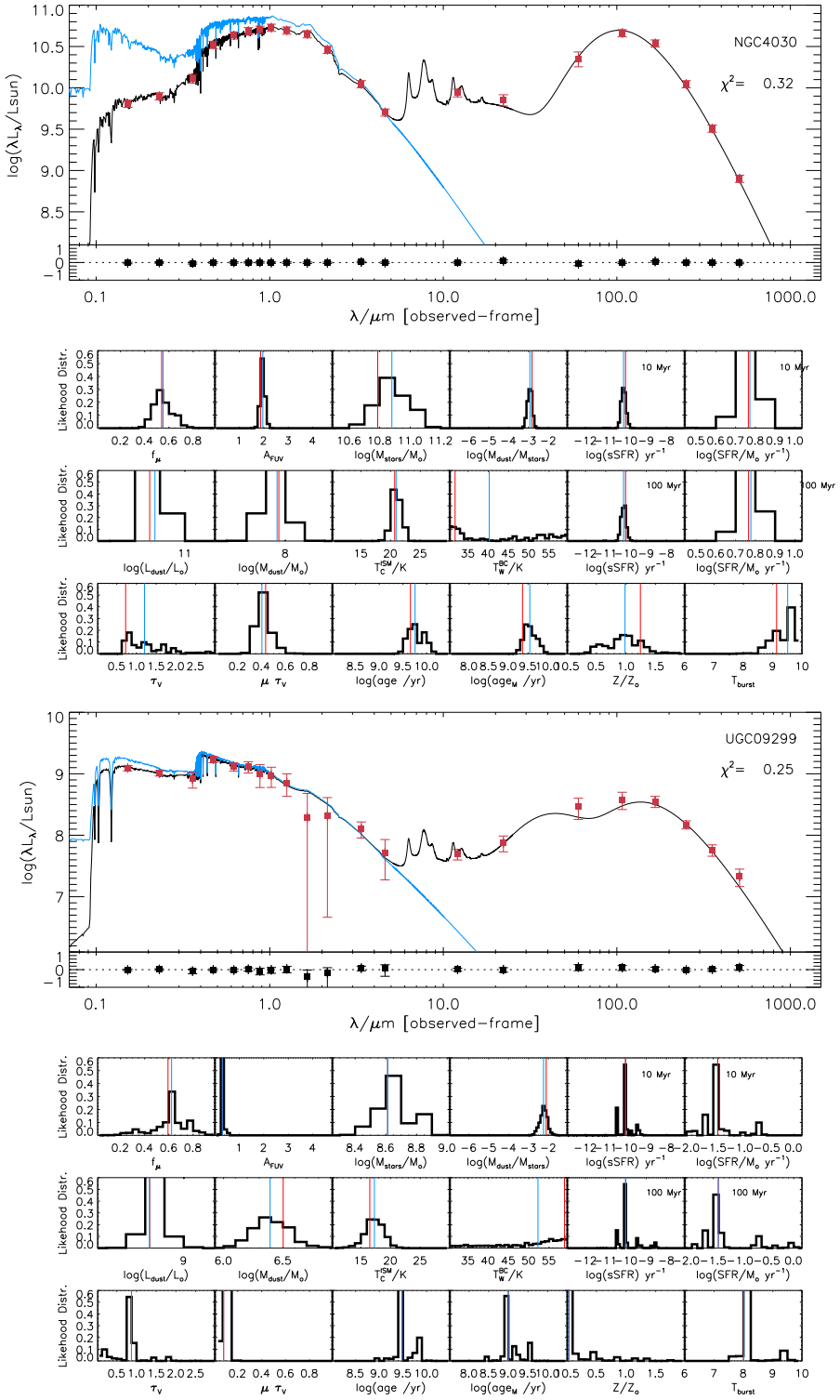

Figure 3.18: MAGPHYS SED and PDFs for the evolved galaxy NGC4030 an for the more immature galaxy UGC09299. The best fitting model is compared to the observed fluxes. The black curve shows the best fit model SED to multiwavelength observations. The blue curve shows how the stellar SED would look without any obscuration. The PDF show a blue line for the median and a red line for the parameter values of the best bit.

Table 3.4: Properties of the 40 HIGH sources derived with MAGPHYS SED fitting. The columns are (from left to right): Index, galaxy name, stellar mass, dust luminosity, dust mass, dust-to-stellar mass ratio, temperature of the cold dust component, star formation rate (SFR) averaged over the last 10^8 years, specific star formation rate (SSFR) averaged over the last 10^8 years, f_μ (the fraction of the total dust luminosity contributed by the diffuse ISM), and the FUV attenuation by dust. Uncertainties are indicated by the 84^{th}-16^{th} percentile range from each of the individual PDF.

#	Name	$\log M_*$ ($M_\odot$)	$\log L_d$ ($L_\odot$)	$\log M_d$ ($M_\odot$)	$\log M_d/M_*$	T_c (K)	$\log SFR$ ($M_\odot\,\mathrm{yr}^{-1}$)	$\log SSFR$ (yr^{-1})	A_{FUV} (mag)	f_μ
1	SDSSJ08...	$9.84^{+0.13}_{-0.13}$	$9.80^{+0.12}_{-0.15}$	$7.21^{+0.40}_{-0.41}$	$-2.63^{+0.42}_{-0.43}$	$16.1^{+4.2}_{-3.3}$	$-0.03^{+0.10}_{-0.13}$	$-9.88^{+0.16}_{-0.18}$	$0.81^{+0.20}_{-0.23}$	$0.29^{+0.19}_{-0.14}$
2[a]	UGC04673	$9.12^{+0.20}_{-0.17}$	$9.15^{+0.10}_{-0.14}$	$7.40^{+0.23}_{-0.27}$	$-1.74^{+0.28}_{-0.29}$	$12.5^{+2.1}_{-1.4}$	$-0.24^{+0.04}_{-0.05}$	$-9.36^{+0.18}_{-0.21}$	$0.34^{+0.07}_{-0.07}$	$0.49^{+0.37}_{-0.21}$
3	UGC04684	$9.35^{+0.14}_{-0.15}$	$9.40^{+0.07}_{-0.10}$	$6.70^{+0.16}_{-0.14}$	$-2.64^{+0.22}_{-0.21}$	$17.5^{+1.9}_{-2.0}$	$-0.36^{+0.10}_{-0.12}$	$-9.72^{+0.18}_{-0.19}$	$0.61^{+0.17}_{-0.13}$	$0.36^{+0.19}_{-0.13}$
4	UGC04996	$9.36^{+0.12}_{-0.10}$	$9.61^{+0.05}_{-0.06}$	$7.18^{+0.21}_{-0.19}$	$-2.18^{+0.25}_{-0.24}$	$14.8^{+2.5}_{-2.1}$	$-0.17^{+0.06}_{-0.06}$	$-9.53^{+0.12}_{-0.13}$	$0.69^{+0.07}_{-0.10}$	$0.23^{+0.16}_{-0.14}$
5	UGC06578	$8.02^{+0.10}_{-0.06}$	$8.68^{+0.04}_{-0.07}$	$5.72^{+0.32}_{-0.29}$	$-2.31^{+0.30}_{-0.32}$	$16.1^{+2.9}_{-2.5}$	$-1.02^{+0.03}_{-0.04}$	$-9.04^{+0.06}_{-0.11}$	$0.51^{+0.07}_{-0.07}$	$0.16^{+0.12}_{-0.05}$
6[a]	UGC06780	$9.00^{+0.18}_{-0.12}$	$8.85^{+0.04}_{-0.06}$	$6.97^{+0.20}_{-0.23}$	$-2.06^{+0.20}_{-0.24}$	$12.8^{+1.7}_{-1.2}$	$-0.36^{+0.11}_{-0.11}$	$-9.36^{+0.16}_{-0.21}$	$0.24^{+0.05}_{-0.00}$	$0.41^{+0.10}_{-0.10}$
7[a]	UM456	$8.28^{+0.15}_{-0.15}$	$8.64^{+0.10}_{-0.12}$	$4.96^{+0.59}_{-0.45}$	$-3.33^{+0.60}_{-0.46}$	$22.4^{+5.0}_{-5.8}$	$-0.76^{+0.04}_{-0.04}$	$-9.04^{+0.15}_{-0.16}$	$0.34^{+0.07}_{-0.07}$	$0.18^{+0.06}_{-0.14}$
8	UM456A	$7.88^{+0.11}_{-0.13}$	$8.30^{+0.21}_{-0.33}$	$4.89^{+0.65}_{-0.55}$	$-2.98^{+0.65}_{-0.56}$	$20.7^{+6.0}_{-5.8}$	$-1.32^{+0.12}_{-0.09}$	$-9.19^{+0.17}_{-0.14}$	$0.49^{+0.23}_{-0.25}$	$0.19^{+0.13}_{-0.12}$
9[a]	UGC06903	$9.89^{+0.09}_{-0.15}$	$9.48^{+0.04}_{-0.03}$	$7.17^{+0.10}_{-0.09}$	$-2.68^{+0.17}_{-0.14}$	$16.4^{+1.0}_{-1.1}$	$-0.24^{+0.04}_{-0.04}$	$-10.13^{+0.16}_{-0.10}$	$0.56^{+0.03}_{-0.03}$	$0.58^{+0.23}_{-0.11}$
10	UGC06970	$9.39^{+0.12}_{-0.15}$	$8.89^{+0.14}_{-0.18}$	$6.52^{+0.35}_{-0.51}$	$-2.86^{+0.39}_{-0.54}$	$14.6^{+3.6}_{-2.5}$	$-0.86^{+0.10}_{-0.12}$	$-10.26^{+0.18}_{-0.16}$	$0.56^{+0.25}_{-0.20}$	$0.32^{+0.14}_{-0.16}$
11	NGC4030b	$8.85^{+0.16}_{-0.14}$	$8.63^{+0.13}_{-0.20}$	$5.64^{+0.53}_{-0.44}$	$-3.22^{+0.55}_{-0.47}$	$19.9^{+5.6}_{-5.6}$	$-0.98^{+0.09}_{-0.32}$	$-9.83^{+0.16}_{-0.35}$	$0.39^{+0.13}_{-0.15}$	$0.32^{+0.41}_{-0.17}$
12	NGC4030	$10.88^{+0.12}_{-0.09}$	$10.88^{+0.03}_{-0.02}$	$7.96^{+0.04}_{-0.08}$	$-2.93^{+0.10}_{-0.14}$	$20.9^{+0.8}_{-0.5}$	$0.78^{+0.04}_{-0.05}$	$-10.10^{+0.10}_{-0.13}$	$1.96^{+0.10}_{-0.10}$	$0.55^{+0.04}_{-0.05}$
13[a]	UGC07053	$8.19^{+0.18}_{-0.10}$	$7.98^{+0.33}_{-0.34}$	$4.80^{+0.56}_{-0.54}$	$-3.41^{+0.58}_{-0.57}$	$23.2^{+4.5}_{-6.3}$	$-1.03^{+0.06}_{-0.07}$	$-9.22^{+0.12}_{-0.19}$	$0.19^{+0.15}_{-0.10}$	$0.71^{+0.23}_{-0.54}$
14[a]	UGC07332	$7.70^{+0.14}_{-0.13}$	$7.78^{+0.18}_{-0.28}$	$4.31^{+0.48}_{-0.40}$	$-3.40^{+0.50}_{-0.42}$	$24.1^{+4.2}_{-6.5}$	$-1.39^{+0.04}_{-0.04}$	$-9.09^{+0.13}_{-0.15}$	$0.19^{+0.07}_{-0.07}$	$0.27^{+0.66}_{-0.13}$
15	NGC4202	$10.30^{+0.11}_{-0.10}$	$10.29^{+0.03}_{-0.03}$	$7.46^{+0.07}_{-0.06}$	$-2.81^{+0.11}_{-0.14}$	$20.3^{+0.8}_{-0.8}$	$0.05^{+0.06}_{-0.17}$	$-10.25^{+0.11}_{-0.20}$	$1.74^{+0.10}_{-0.07}$	$0.67^{+0.11}_{-0.05}$
16	FGC1412	$6.94^{+0.13}_{-0.10}$	$7.33^{+0.20}_{-0.41}$	$3.84^{+0.78}_{-0.53}$	$-3.11^{+0.78}_{-0.55}$	$21.3^{+6.0}_{-7.3}$	$-2.43^{+0.14}_{-0.17}$	$-9.37^{+0.17}_{-0.21}$	$0.69^{+0.25}_{-0.38}$	$0.18^{+0.21}_{-0.10}$
17[a]	CGCG014-010	$7.29^{+0.13}_{-0.12}$	$6.88^{+0.34}_{-0.23}$	$3.48^{+0.45}_{-0.40}$	$-3.82^{+0.47}_{-0.39}$	$25.0^{+3.5}_{-5.8}$	$-2.14^{+0.04}_{-0.04}$	$-9.42^{+0.12}_{-0.14}$	$0.14^{+0.13}_{-0.05}$	$0.57^{+0.30}_{-0.48}$
18	UGC07394	$8.93^{+0.14}_{-0.12}$	$8.70^{+0.17}_{-0.13}$	$6.87^{+0.21}_{-0.23}$	$-2.07^{+0.24}_{-0.27}$	$12.2^{+1.7}_{-1.3}$	$-1.22^{+0.17}_{-0.34}$	$-10.15^{+0.21}_{-0.36}$	$0.69^{+0.28}_{-0.17}$	$0.39^{+0.23}_{-0.19}$
19[a]	UGC07531	$8.60^{+0.15}_{-0.08}$	$8.98^{+0.09}_{-0.18}$	$6.49^{+0.39}_{-0.39}$	$-2.13^{+0.41}_{-0.42}$	$13.7^{+3.5}_{-2.6}$	$-0.38^{+0.04}_{-0.04}$	$-8.97^{+0.09}_{-0.16}$	$0.26^{+0.07}_{-0.07}$	$0.16^{+0.16}_{-0.05}$
20	UM501	$7.90^{+0.10}_{-0.10}$	$8.65^{+0.24}_{-0.09}$	$5.10^{+0.71}_{-0.54}$	$-2.80^{+0.72}_{-0.53}$	$19.4^{+6.9}_{-5.6}$	$-1.06^{+0.12}_{-0.04}$	$-8.95^{+0.15}_{-0.11}$	$0.54^{+0.28}_{-0.07}$	$0.10^{+0.09}_{-0.04}$

[a] For these sources, we use SFR and SSFR estimates using the same method for SFR as C15 since the MAGPHYS SFR and SSFR PDFs show two peaks.

Table 3.4: *Continued*

#	Name	log M_* ($M_\odot$)	log L_d ($L_\odot$)	log M_d ($M_\odot$)	log M_d/M_*	T_c (K)	log SFR ($M_\odot\,\mathrm{yr}^{-1}$)	log $SSFR$ (yr^{-1})	A_{FUV} (mag)	f_μ
21[a]	NGC5496	$9.46^{+0.14}_{-0.05}$	$9.51^{+0.04}_{-0.04}$	$7.12^{+0.14}_{-0.11}$	$-2.35^{+0.13}_{-0.14}$	$16.9^{+1.3}_{-2.0}$	$-0.23^{+0.04}_{-0.04}$	$-9.69^{+0.06}_{-0.14}$	$0.61^{+0.00}_{-0.10}$	$0.66^{+0.00}_{-0.37}$
22[a]	NGC5584	$9.97^{+0.09}_{-0.16}$	$10.04^{+0.04}_{-0.02}$	$7.51^{+0.07}_{-0.10}$	$-2.45^{+0.14}_{-0.15}$	$17.0^{+1.5}_{-1.2}$	$0.26^{+0.04}_{-0.04}$	$-9.71^{+0.16}_{-0.10}$	$0.79^{+0.13}_{-0.03}$	$0.39^{+0.40}_{-0.13}$
23	UGC09215	$9.31^{+0.14}_{-0.04}$	$9.57^{+0.02}_{-0.05}$	$6.95^{+0.09}_{-0.10}$	$-2.38^{+0.12}_{-0.16}$	$17.4^{+0.9}_{-1.5}$	$-0.24^{+0.02}_{-0.06}$	$-9.55^{+0.04}_{-0.15}$	$0.66^{+0.07}_{-0.05}$	$0.37^{+0.08}_{-0.06}$
24	2MASXJ14...	$9.60^{+0.13}_{-0.07}$	$9.98^{+0.07}_{-0.08}$	$7.26^{+0.18}_{-0.15}$	$-2.36^{+0.21}_{-0.19}$	$17.7^{+1.7}_{-2.1}$	$-0.03^{+0.07}_{-0.07}$	$-9.63^{+0.11}_{-0.14}$	$1.54^{+0.17}_{-0.15}$	$0.36^{+0.07}_{-0.06}$
25	IC1011	$10.16^{+0.13}_{-0.07}$	$10.59^{+0.04}_{-0.05}$	$7.41^{+0.08}_{-0.09}$	$-2.77^{+0.13}_{-0.14}$	$21.9^{+1.3}_{-1.2}$	$0.60^{+0.06}_{-0.04}$	$-9.56^{+0.09}_{-0.14}$	$1.66^{+0.13}_{-0.15}$	$0.40^{+0.10}_{-0.07}$
26	IC1010	$10.82^{+0.08}_{-0.25}$	$10.29^{+0.04}_{-0.02}$	$7.93^{+0.12}_{-0.13}$	$-2.85^{+0.21}_{-0.20}$	$16.1^{+1.4}_{-0.9}$	$0.44^{+0.04}_{-0.06}$	$-10.38^{+0.25}_{-0.10}$	$0.69^{+0.10}_{-0.07}$	$0.52^{+0.05}_{-0.15}$
27[a]	UGC09299	$8.61^{+0.19}_{-0.04}$	$8.82^{+0.03}_{-0.01}$	$6.39^{+0.15}_{-0.14}$	$-2.24^{+0.18}_{-0.20}$	$17.3^{+1.4}_{-1.4}$	$-0.55^{+0.04}_{-0.04}$	$-9.16^{+0.05}_{-0.20}$	$0.31^{+0.03}_{-0.00}$	$0.62^{+0.14}_{-0.04}$
28[a]	SDSSJ14...	$7.77^{+0.19}_{-0.18}$	$7.66^{+0.35}_{-0.41}$	$4.52^{+0.73}_{-0.63}$	$-3.24^{+0.76}_{-0.68}$	$21.3^{+5.9}_{-6.9}$	$-1.69^{+0.04}_{-0.04}$	$-9.46^{+0.19}_{-0.19}$	$0.26^{+0.28}_{-0.15}$	$0.31^{+0.54}_{-0.19}$
29	NGC5690	$10.38^{+0.11}_{-0.09}$	$10.48^{+0.03}_{-0.02}$	$7.61^{+0.05}_{-0.05}$	$-2.78^{+0.12}_{-0.12}$	$20.5^{+0.6}_{-0.8}$	$0.31^{+0.05}_{-0.04}$	$-10.07^{+0.10}_{-0.12}$	$2.59^{+0.10}_{-0.10}$	$0.59^{+0.05}_{-0.03}$
30	NGC5691	$10.01^{+0.10}_{-0.17}$	$10.15^{+0.03}_{-0.04}$	$6.85^{+0.07}_{-0.04}$	$-3.15^{+0.17}_{-0.14}$	$24.1^{+0.4}_{-1.2}$	$-0.06^{+0.06}_{-0.05}$	$-10.07^{+0.18}_{-0.11}$	$1.76^{+0.13}_{-0.10}$	$0.60^{+0.03}_{-0.04}$
31[a]	UGC09432	$8.19^{+0.02}_{-0.14}$	$7.76^{+0.17}_{-0.94}$	$4.40^{+0.48}_{-0.51}$	$-3.76^{+0.51}_{-0.53}$	$24.4^{+3.9}_{-6.0}$	$-1.06^{+0.05}_{-0.06}$	$-9.24^{+0.15}_{-0.06}$	$0.09^{+0.05}_{-0.07}$	$0.58^{+0.20}_{-0.50}$
32[a]	NGC5705	$9.33^{+0.08}_{-0.12}$	$9.34^{+0.01}_{-0.03}$	$7.35^{+0.12}_{-0.13}$	$-1.98^{+0.17}_{-0.15}$	$14.3^{+1.1}_{-1.3}$	$-0.24^{+0.04}_{-0.04}$	$-9.58^{+0.12}_{-0.09}$	$0.41^{+0.03}_{-0.03}$	$0.54^{+0.23}_{-0.16}$
33	NGC5725	$9.13^{+0.08}_{-0.13}$	$9.14^{+0.07}_{-0.09}$	$6.45^{+0.19}_{-0.19}$	$-2.68^{+0.21}_{-0.20}$	$17.3^{+2.6}_{-2.2}$	$-0.65^{+0.07}_{-0.07}$	$-9.78^{+0.14}_{-0.10}$	$0.71^{+0.10}_{-0.15}$	$0.32^{+0.14}_{-0.11}$
34	NGC5713	$10.56^{+0.14}_{-0.11}$	$10.94^{+0.03}_{-0.03}$	$7.54^{+0.05}_{-0.05}$	$-3.02^{+0.12}_{-0.14}$	$24.8^{+0.6}_{-0.9}$	$0.72^{+0.06}_{-0.05}$	$-9.84^{+0.12}_{-0.15}$	$2.71^{+0.10}_{-0.13}$	$0.57^{+0.04}_{-0.03}$
35	NGC5719	$10.79^{+0.09}_{-0.08}$	$10.45^{+0.03}_{-0.04}$	$7.43^{+0.07}_{-0.06}$	$-3.36^{+0.12}_{-0.11}$	$22.0^{+0.8}_{-1.0}$	$-0.17^{+0.04}_{-0.06}$	$-10.96^{+0.09}_{-0.11}$	$3.06^{+0.10}_{-0.17}$	$0.78^{+0.02}_{-0.02}$
36	UGC09482	$8.72^{+0.10}_{-0.14}$	$8.55^{+0.12}_{-0.15}$	$6.09^{+0.31}_{-0.27}$	$-2.62^{+0.32}_{-0.29}$	$15.5^{+2.6}_{-2.6}$	$-1.30^{+0.14}_{-0.18}$	$-10.02^{+0.19}_{-0.21}$	$0.56^{+0.17}_{-0.13}$	$0.29^{+0.31}_{-0.12}$
37[a]	UGC09470	$8.90^{+0.07}_{-0.13}$	$8.86^{+0.03}_{-0.03}$	$6.22^{+0.17}_{-0.19}$	$-2.65^{+0.16}_{-0.17}$	$18.2^{+2.3}_{-1.8}$	$-0.68^{+0.04}_{-0.04}$	$-9.58^{+0.13}_{-0.09}$	$0.39^{+0.07}_{-0.03}$	$0.50^{+0.16}_{-0.24}$
38	NGC5740	$10.28^{+0.11}_{-0.07}$	$10.03^{+0.04}_{-0.04}$	$7.16^{+0.07}_{-0.07}$	$-3.13^{+0.12}_{-0.10}$	$19.9^{+0.8}_{-0.9}$	$-0.05^{+0.04}_{-0.04}$	$-10.33^{+0.08}_{-0.12}$	$1.54^{+0.10}_{-0.13}$	$0.50^{+0.11}_{-0.05}$
39[a]	UGC07000	$9.11^{+0.08}_{-0.16}$	$9.15^{+0.07}_{-0.04}$	$6.43^{+0.12}_{-0.11}$	$-2.67^{+0.17}_{-0.14}$	$18.6^{+1.8}_{-1.5}$	$-0.45^{+0.04}_{-0.04}$	$-9.56^{+0.16}_{-0.09}$	$0.49^{+0.07}_{-0.13}$	$0.48^{+0.20}_{-0.25}$
40	NGC5746	$11.31^{+0.07}_{-0.10}$	$10.34^{+0.02}_{-0.01}$	$8.00^{+0.07}_{-0.07}$	$-3.30^{+0.10}_{-0.10}$	$17.1^{+0.4}_{-0.5}$	$-0.41^{+0.36}_{-0.70}$	$-11.72^{+0.37}_{-0.71}$	$1.46^{+0.10}_{-0.38}$	$0.87^{+0.08}_{-0.12}$
Mean		9.20	9.22	6.40	−2.80	18.9	−0.51	−9.71	0.86	0.43
$M_* < 10^9$		8.17	8.27	5.21	−2.96	19.8	−1.18	−9.35	0.38	0.38
$M_* > 10^9$		9.89	9.85	7.19	−2.69	18.3	−0.07	−9.95	1.18	0.50

[a] For these sources, we use SFR and SSFR estimates using the same method for SFR as C15 since the MAGPHYS SFR and SSFR PDFs show two peaks.

SED consistent with a burst around 10^8 years ago. An issue arises for these sources, as there is a nearly equally good fit to the SED for models with random burst ending just before or just after 10^8 years ago. However, the model SFR (averaged over the last 10^8 years) will be quite different if it includes a burst, compared to if the burst ended before 10^8 years ago. This results in a bimodal PDF for the SFR (see Figure 3.20 for an example), for which the median will not be a good representation of the true SFR. For the 16 sources for which this issue arises, we determine the SFR from the FUV and 22 μm fluxes as in C15 (Hirashita et al., 2003; Buat et al., 2011; Jarrett et al., 2013). These sources are labelled 'a' in Table 3.4. Schofield et al., (*in prep.*) will explore this issue in more detail. We note that the C15 SFR estimates would be biased when the SSFR is small and the dust luminosity has a large contribution from heating by old stars (Boquien et al., 2016; see also next section). This is not the case for these galaxies with a relatively recent burst.

3.4.5 MAGPHYS HRS results in other work

Viaene et al. (2016) has used MAGPHYS results in order to study the bolometric and UV attenuation in normal spiral galaxies in the HRS sample. The HRS sample will also be used throughout this work as a comparative sample (Section 4.2), and we thus derived MAGPHYS properties in the same manner as for the HIGH galaxies. Our results are slightly different to the MAGPHYS HRS results in Viaene et al. (2016) because they did not apply any corrections for Galactic extinction and $K_{\rm beam}$, and used smaller uncertainties. Eales et al. (*accepted*) uses the same MAGPHYS HRS results as derived in this work.

3.4.6 Comparing MAGPHYS to C15

As a sanity check, we compare MAGPHYS results to different techniques in the literature. C15, a companion paper to our work, used a combination of different techniques at different wavelengths for the HAPLESS and the HRS samples. These samples are used as comparative samples throughout this work, and we refer to Section 4.2 for a more complete description. We have derived consistent MAGPHYS results for both samples, which can thus be compared to the results published in C15.

3.4.6.1 Dust mass and temperature

The C15 dust masses and temperatures were determined using a two component modified blackbody SED fit to data at 60-500 μm. The MAGPHYS cold dust temperatures for HAPLESS are, on average, 3 K warmer and the dust masses smaller by 0.25 dex than the results in C15,

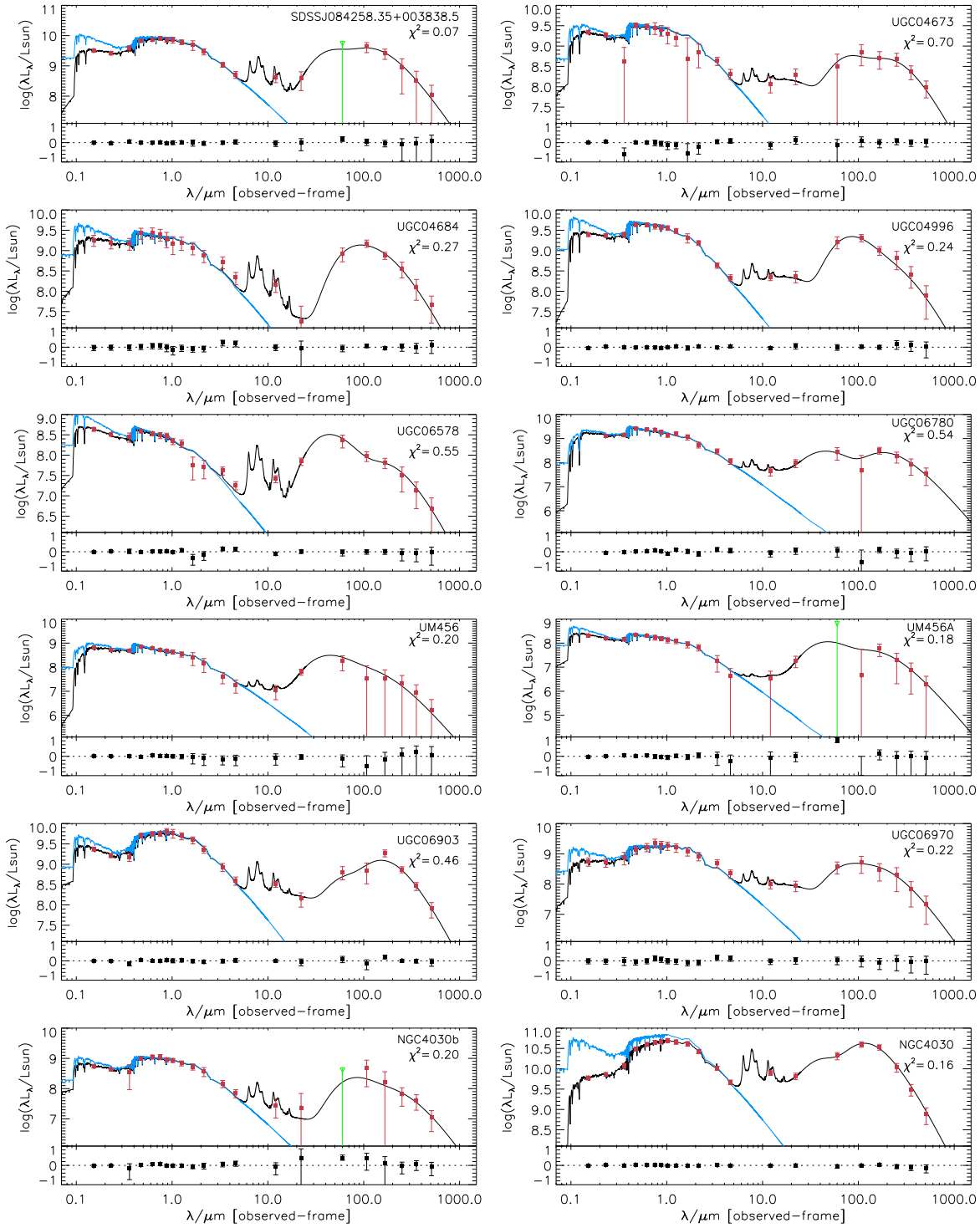

Figure 3.19: Multiwavelength SEDs of the HIGH sources, with observed photometry (red points) from FUV to the submillimetre. The photometry process (including errors) is described in Section 3.2. IRAS60 3σ-upper limits are shown as green triangles. Since negative fluxes cannot be plotted on a logarithmic scale, we have plotted the 1σ upper limits as orange triangles. The solid black line is the best-fit model SED and the solid blue line is the unattenuated optical model. The residuals of the fit are shown in the panel below each SED.

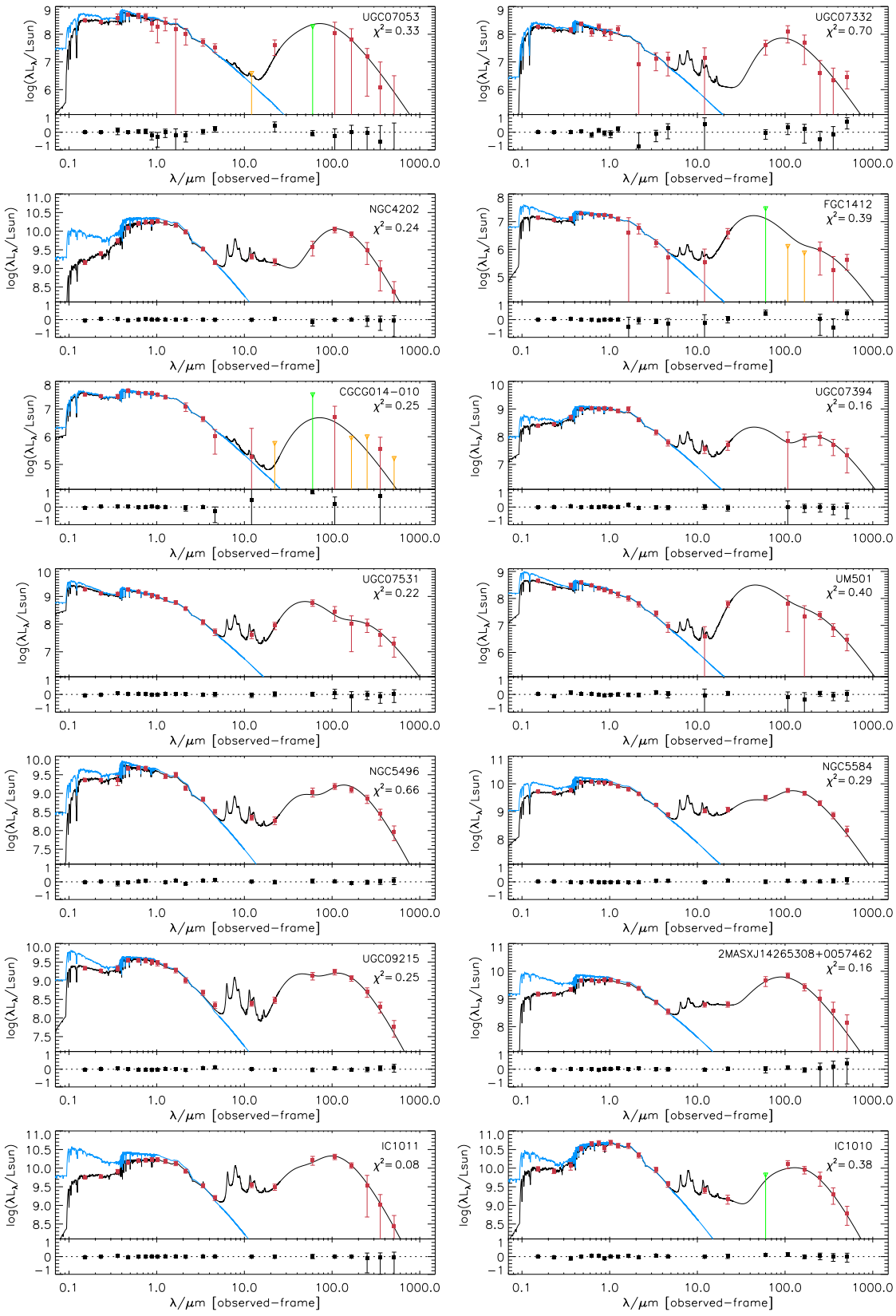

Figure 3.19: - *continued*

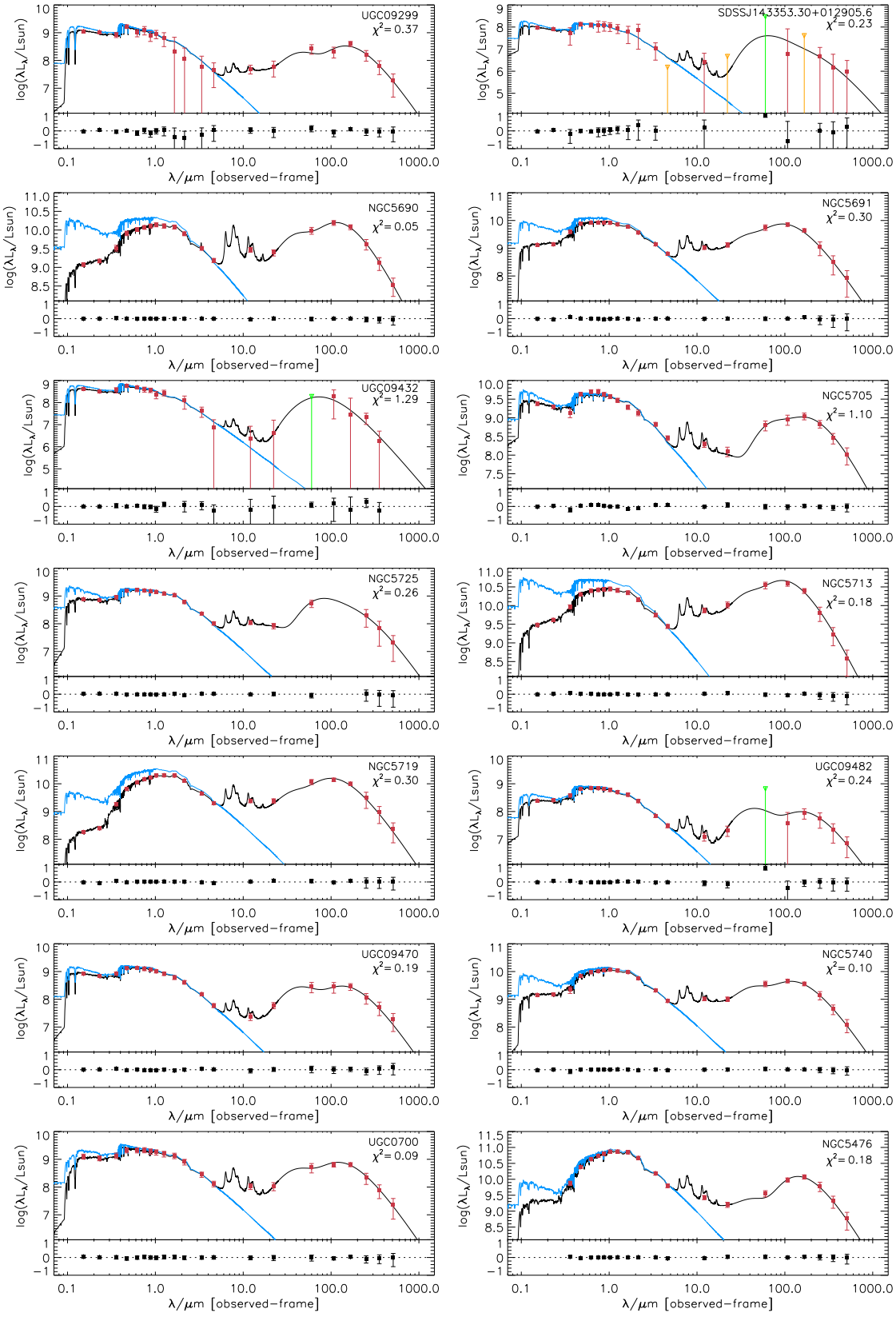

Figure 3.19: - *continued*

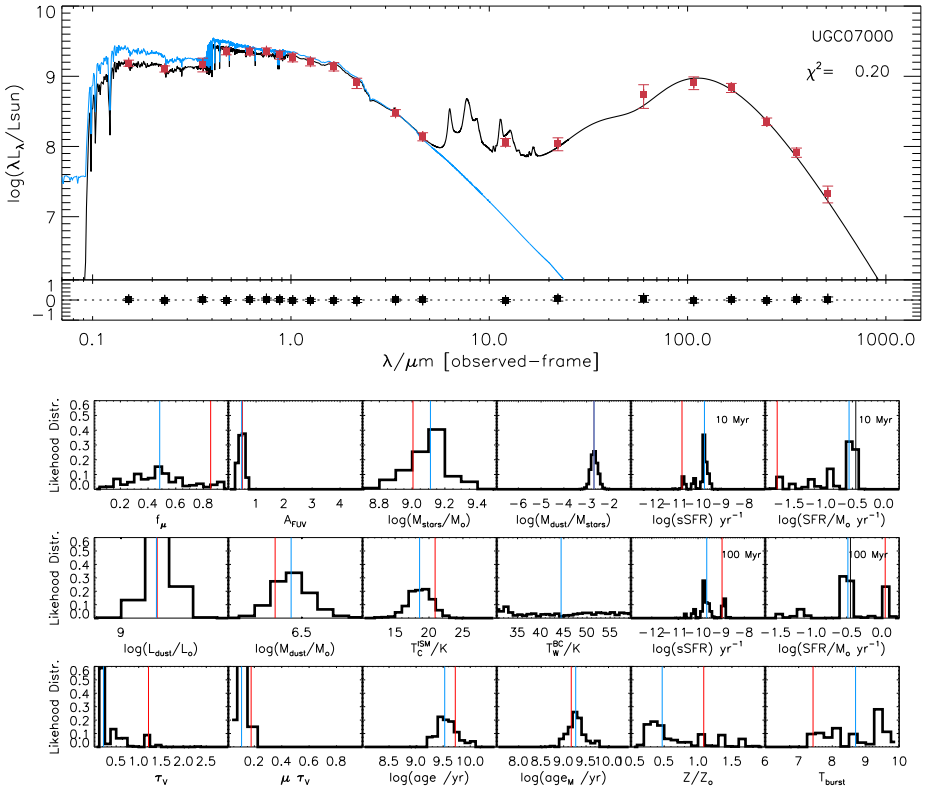

Figure 3.20: MAGPHYS SED and PDFs for UGC07000. Plotted lines are the same as in Figure 3.18, with an added gray line to indicate the C15 SFR in the PDFs for SFR. Note that the PDF for the SFR averaged over the last 100 Myr (second row; last column) has a bimodal distribution and there was a burst around 10 Myr ago (third row; last column).

and the offset is largest for sources with cold ($T_c < 15$ K) dust temperatures in C15. The differences originate in part from differences in the SED fitting technique and in part from changes to the *Herschel* photometry due to using the H-ATLAS DR1 data release instead of Phase 1 Version 3. The largest difference between the DR1 and Phase 1 version 3 photometry is the use of different beam areas for SPIRE, which leads to a flux difference of about $\sim 10\%$ for these bands[25]. Therefore the method from C15 was repeated using our more up-to-date photometry (Clark, *priv. comm.*). Using the more up-to-date photometry, there is still an offset of 2.5 K to T_c and 0.16 dex to M_d due to differences in the SED fitting. As can be seen in Figure 3.21, there is no offset for the sources with cold dust temperatures $T_c > 15$ K (as fitted by the C15 method). However, the difference between both methods increases as the C15 method fits colder and colder temperatures. Note, however, that there are also a number of sources for which both the C15 method and MAGPHYS have very low cold dust temperatures

[25] Additionally, in contrast to C15, we do not apply the k4e/k4p correction factors for extended-source photometry, as these are not recommended any more in the latest version of the SPIRE handbook.

and there is no offset; temperatures as low as 10 K in C15 are thus not necessarily unrealistic. The offset for some of the cold sources is due to several reasons.

In contrast to modified blackbody fits in C15, MAGPHYS limits the warm dust to $30 < T_w < 60$ K[26], and at least half of the dust luminosity in the diffuse ISM must originate from the cold dust component. Therefore MAGPHYS assigns low probabilities to poorly constrained cold dust components that make up a tiny fraction of the total luminosity but peak at the longest wavelengths, therefore making up the bulk of the dust mass. An example of this is shown in Figure 3.22. For a galaxy with an SED that is well-fitted by a single-component model, the C15 method is free to assign negligible luminosity (yet not necessarily negligible mass) to one of the dust components, or fit two identical-temperature components, whereas for MAGPHYS this is not the case. Note the different y-axis for the two panels in Figure 3.22 (C15 in Jy and MAGPHYS in W), without which the best fit SEDs would look more similar[27].

Additionally, MAGPHYS uses the median T_c from the PDF whereas C15 used the best fit to the data; when comparing C15 with the best-fit MAGPHYS result, we find overall a better agreement between the two estimates (see e.g. Figure 3.23). Though the parameter values for the best fitting SED have their benefit, we believe the median gives a more reliable estimation that is less dependent on random fluctuations due to the noise. By weighting each of the models that we deem reliable (e.g. $T_c > 10$ K) by their probability, we get robust estimates of the parameter values and associated uncertainties.

These two differences account for the strongly offset sources. However there are other differences between the methods that can affect the results, such as:

- The effect f_μ has on the MAGPHYS fit (the stellar SED affects the dust SED).
- Different colour corrections (Section 3.4.2) for MAGPHYS (internally implemented) and C15 (K_{colP} colour corrections from the SPIRE handbook).
- The warm dust component for MAGPHYS has a different emissivity index ($\beta = 2$ for C15; $\beta = 1.5$ for MAGPHYS) and is limited to $30 < T_w < 60$ K. Though we have tested the effect of this by also running the C15 method with a $\beta = 1.5$ and $30 < T_w < 60$ K for the warm dust in C15. The resulting differences have a minor effect, though do lead to a slightly better match.

[26]The cold dust for both methods is limited $T_c > 10$ K. For the C15 this means that some of the best fits will have parameters at the boundary of the allowed value (i.e. 10 K), which would otherwise have been fitted by even colder temperatures (which would have resulted in an even large offset).

[27]The MAGPHYS SED shows the observed fluxes before the intrinsic (SED dependent) colour correction has been applied, yet for C15 the correction has been applied to the plotted fluxes. For a more realistic comparison it is better to look at the residuals for MAGPHYS, where colour corrections were applied.

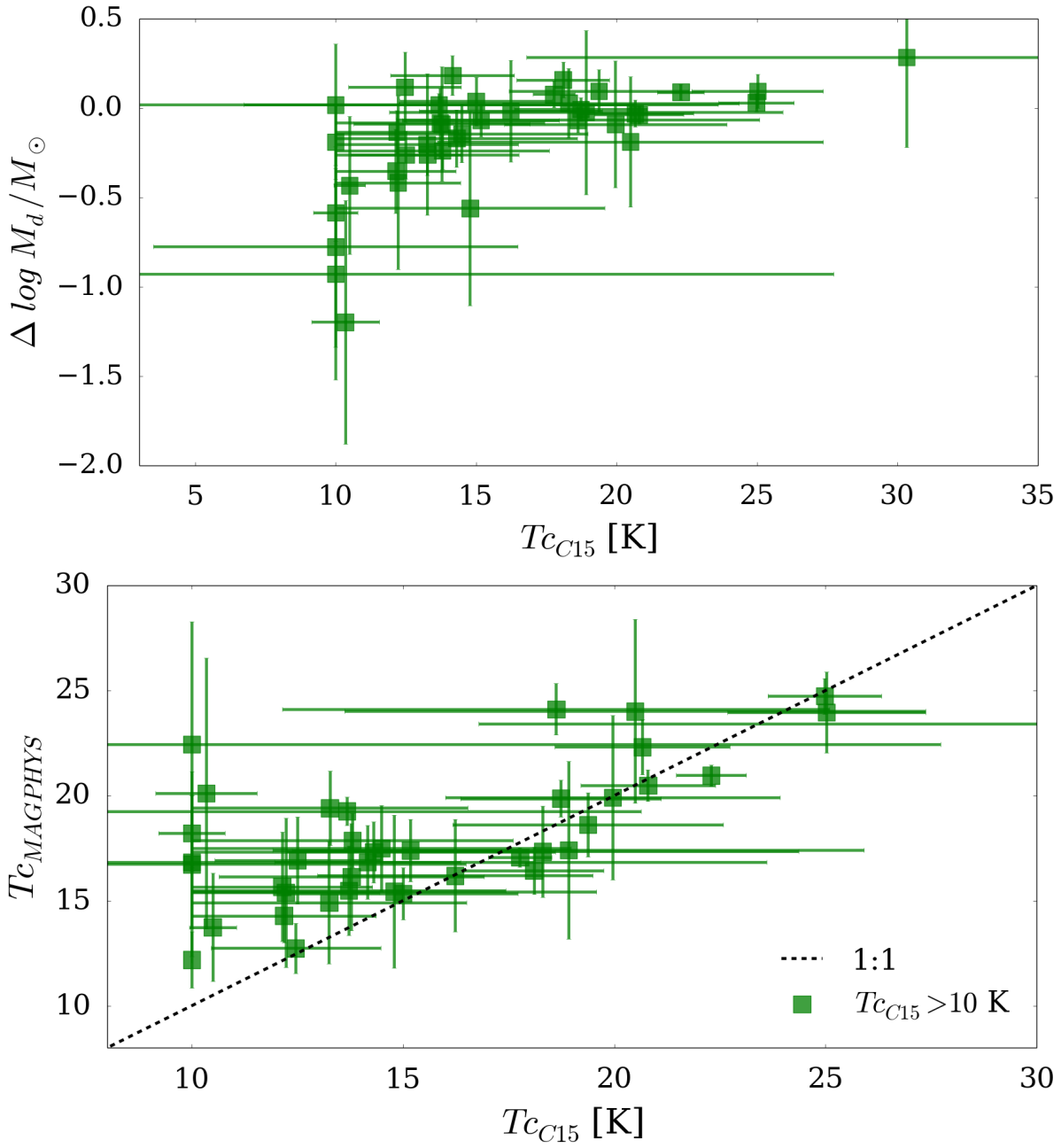

Figure 3.21: *Top:* Difference in dust mass between the C15 technique and MAGPHYS against the cold dust temperature fitted by the C15 technique for all HAPLESS sources. *Bottom:* MAGPHYS dust temperature is plotted in function of the cold dust temperature fitted by the C15 technique for all HAPLESS sources. The C15 estimates are often colder than MAGPHYS.

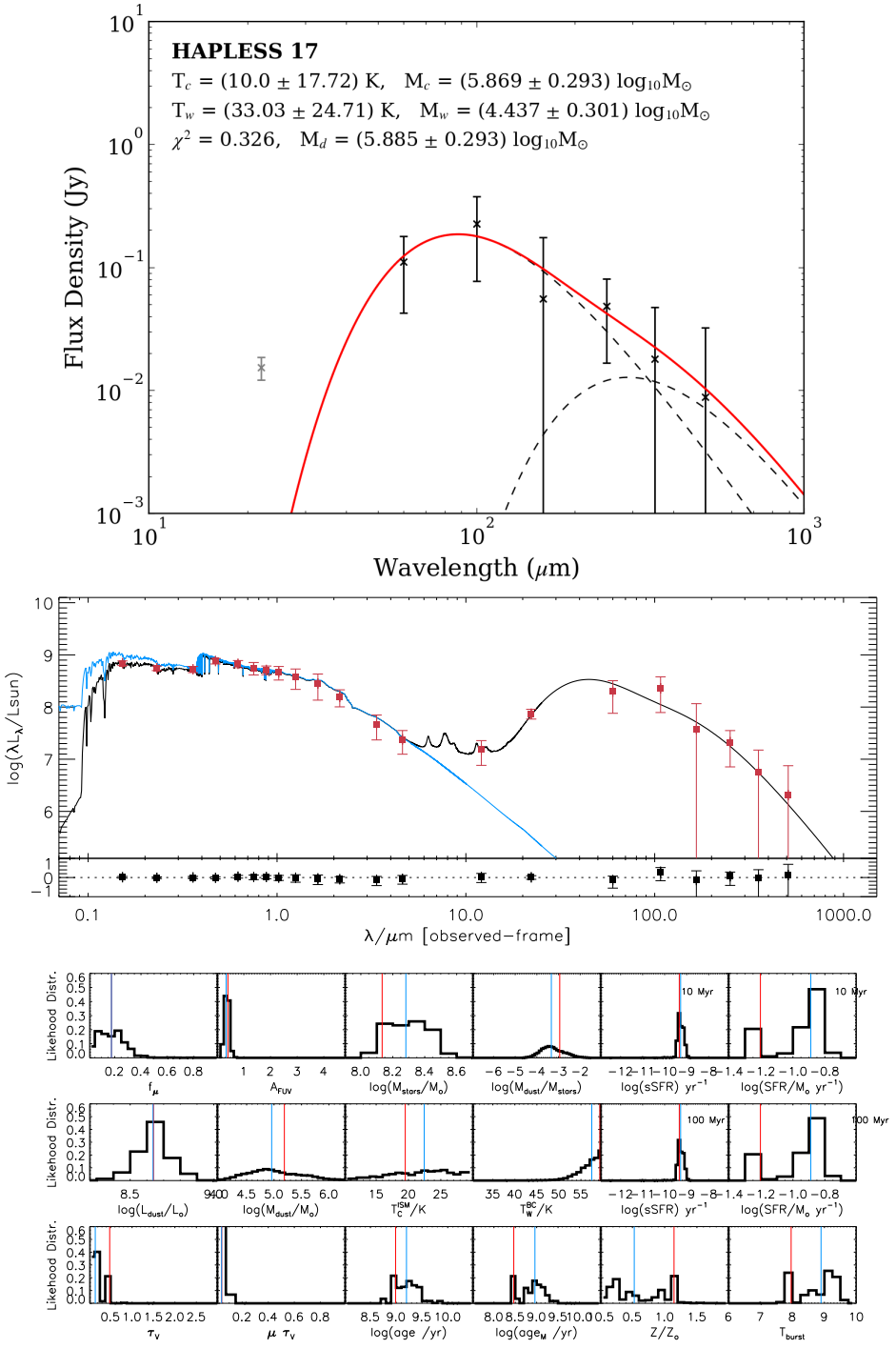

Figure 3.22: C15 technique SED (*top*) and MAGPHYS best-fit SED and PDFs (*bottom*) for UM456. The C15 techniques fits a very cold (indeed the bottom limit of $T_c = 10$ K) dust component, which takes only a fraction of the dust luminosity, yet the bulk of the dust mass. In MAGPHYS, this model is not allowed as at least half of the dust luminosity in the diffuse ISM must originate from the cold dust component, and f_μ for this source is low (and thus most dust luminosity comes from the diffuse ISM).

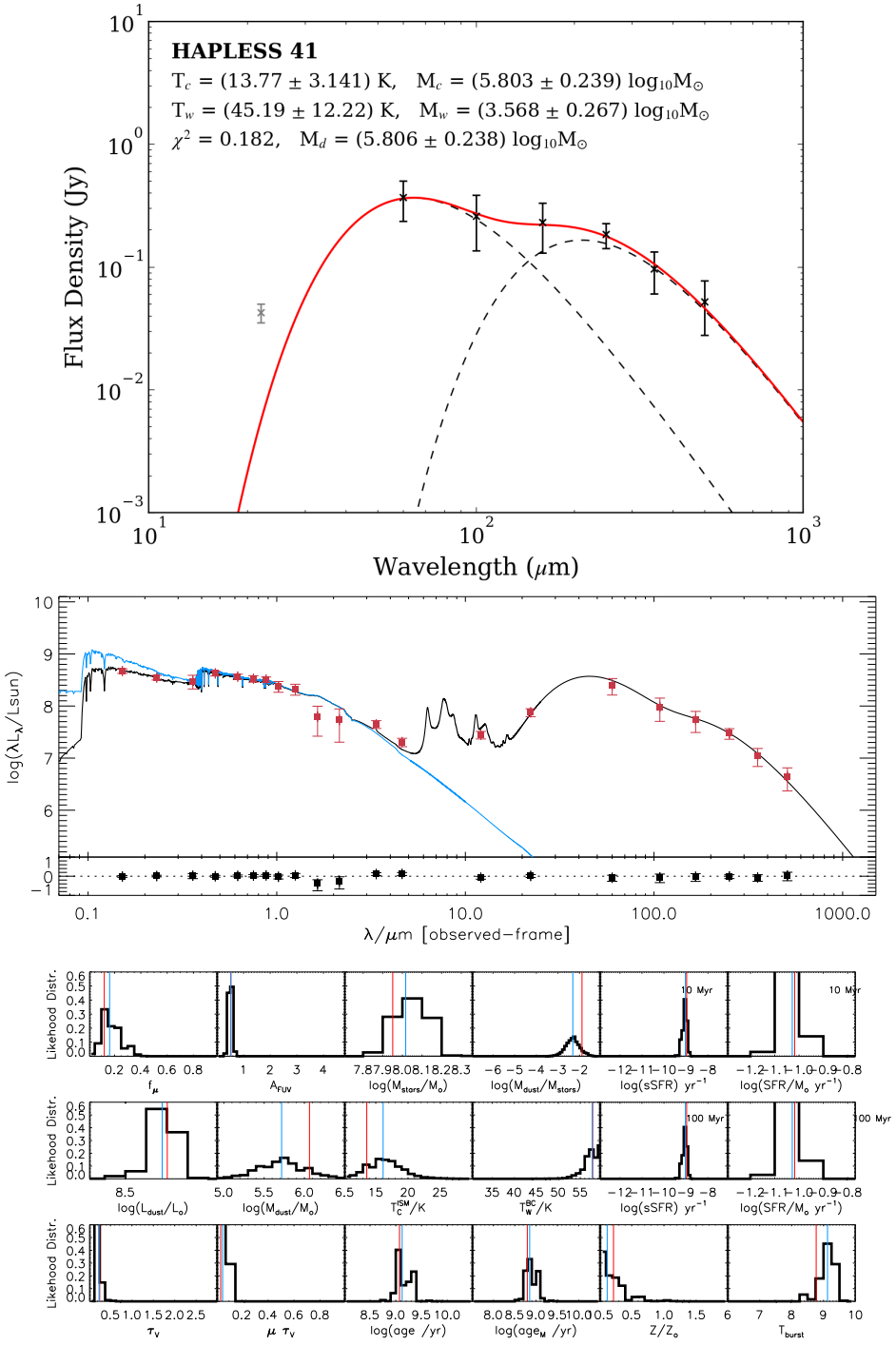

Figure 3.23: C15 technique SED (*top*) and MAGPHYS SED and PDFs (*bottom*) for UM456. For this sources we find the best fit from C15 and the best fit from MAGPHYS give similar results (note the different y-axis of the SED, with C15 in Jy and MAGPHYS in W). However for this source the best fit MAGPHYS parameter values are offset from the median values. We deem the latter more reliable.

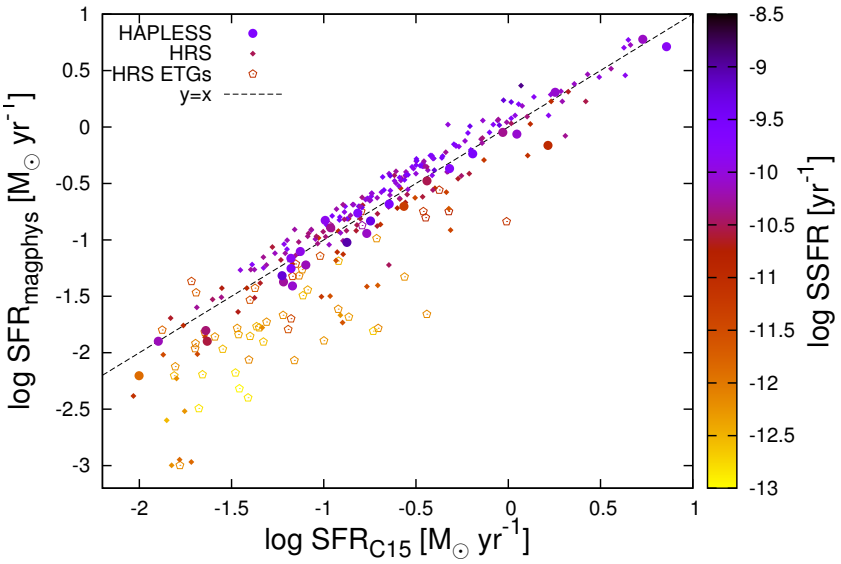

Figure 3.24: Comparison of the C15 and MAGPHYS estimates for the total (obscured + unobscured) SFR. To determine the obscured SFR, C15 uses WISE 22 μm measurements. In some cases the 22 μm flux has a significant contribution from stellar continuum radiation or dust heated by old stars, which biases the obscured SFR. This offset is strongest for quiescent sources. The 22 μm flux should not be used to estimate the obscured SFR for ETGs and quiescent sources without correcting for the stellar emission and dust heated by old stars.

3.4.6.2 Stellar mass and star formation rates

For stellar masses, C15 used the method of Zibetti et al. (2009) using *i*-band luminosity and *g*-*i* colour. This method was found to be in excellent agreement with the MAGPHYS stellar masses. For SFR, the agreement is not as good, especially for quiescent sources. When the non-bimodal MAGPHYS SFR are compared to C15, we find $\sim 20\%$ of the sources are outliers (Figure 3.24). The total (obscured + unobscured) SFR for C15 was derived from a combination of *GALEX* FUV and WISE 22 μm measurements following Hirashita et al. (2003). C15 did not account for the stellar continuum contribution to the WISE 22 μm flux by the (old) stars, nor for the contribution to the 22 μm emission from dust heated by AGB stars rather than star forming regions.

For a significant fraction of the HRS sources ($\sim 20\%$), the above contributions are not small compared to the dust emission at 22 μm from dust heated by newly formed stars. This causes the obscured SFR estimate for C15 to be overestimated by $0.4-1.3$ dex for these sources. The MAGPHYS SFR estimate takes into account the stellar continuum, and the energy balance accounts for dust heated by the older stellar population. For 80% of the sources, the stellar continuum contribution is small compared to the dust emission at 22 μm and there is a good match between the MAGPHYS and C15 SFR estimate. The average offset between the C15 and

MAGPHYS SFR for actively star forming sources (excluding those with bimodal SFR) is 0.029 dex (factor of 1.07). The C15 SFR estimates we use throughout this work for sources with a bimodal SFR (Table 3.4) have been scaled by this offset in order for a consistent comparison with MAGPHYS SFR.

As can be seen in Figure 3.24, the offset is largest for quiescent sources (low SSFR), where the stellar radiation dominates the 22 μm flux and the obscured SFR is small. The limitations of using UV+IR SFR tracers for quiescent sources have been recognised in the literature (Kennicutt, 1998; Hirashita et al., 2003; Calzetti et al., 2007; Kennicutt et al., 2009; Hao et al., 2011), yet this SFR tracer is still used for quiescent sources in several recent papers (e.g. Davis et al., 2014; C15). *We strongly recommend not using a 22 μm based estimate to determine the obscured SFR for ETGs and other quiescent sources without taking into account the stellar continuum emission and dust heated from the older stellar population directly, or using a hybrid SFR estimator that accounts for the (naturally variable) impact of dust heated by evolved stellar populations (e.g. Boquien et al., 2016).*

Chapter 4

HIGH compared to other Surveys

4.1 Introduction

To study the dust and gas content of galaxies in a evolutionary context, the first logical step is to quantify how the dust and gas content of galaxies varies with galaxy properties such as stellar mass, colour, gas content, star formation rate (SFR), etc. These scaling relations provide vital information on the interplay of dust, gas and the star formation cycle, which can then in turn provide us with important insights into the physical processes regulating galaxy evolution (e.g. Dunne et al., 2011) and set strong constraints on chemical evolution models (e.g. Rowlands et al., 2014b). In order to get a full picture of the chemical evolution of galaxies, one also needs to study how the gas phase of the ISM changes as a result of star formation and how this relates to the dust scaling relations. For example, it is important to quantify the link between the dust and the gas components of the ISM to trace how dusty galaxies are in different phases during their stellar mass build-up. In this chapter we will study scaling relation for our HIGH sample and compare them to differently selected samples. The work presented in this chapter is published in De Vis et al. (*accepted*).

4.2 Comparison samples

4.2.1 Dust-selected sample

The best comparative dust-selected sample is the *Herschel*-ATLAS Phase-1 Limited-Extent Spatial Survey (HAPLESS) described in a companion paper to our work (C15). HAPLESS is a volume limited sample consisting of 42 H-ATLAS galaxies detected at 250 μm in the equatorial H-ATLAS fields with $0.0035 < z < 0.01$. Throughout the rest of this work we will refer to HAPLESS as a dust-selected sample to indicate this 250 μm flux selection. Previous

blind surveys of dust emission in the local Universe were not sensitive to the cold dust that dominates dust mass, hence many cold galaxies were missed (Vlahakis et al., 2005, Dunne et al., 2011, C15). HAPLESS revealed the enigmatic population of BADGRS. These blue, dust- and gas-rich galaxies make up $\sim 65\%$ of the sample, and are briefly discussed in Section 2.4.2.

HAPLESS has 22 sources in common with HIGH and the photometry was performed using the same pipeline. For consistency, we have redetermined the *Herschel* photometry for HAPLESS using the H-ATLAS DR1 maps that have since become available. Additionally we redetermined the galaxy properties for HAPLESS using MAGPHYS instead of the combination of different techniques at different wavelengths used by C15. As discussed in Section 3.4.6, the MAGPHYS cold dust temperatures are, on average, 3 K warmer and the dust masses smaller by 0.25 dex than the results in C15, and the offset is largest for sources with cold ($T_c < 15$ K) dust temperature in C15. These differences due not affect the conclusions reached in this work, and originate in part from differences in the SED fitting technique and in part from changes to the *Herschel* photometry due to using the H-ATLAS DR1 data release instead of Phase 1 Version 3. C15 compiled literature atomic gas masses, including HIPASS (Meyer et al., 2004) and ALFALFA (Haynes, *priv. comm.)*.

4.2.2 Stellar mass selected sample

For a stellar mass selected sample we use the *Herschel* Reference Survey (HRS, Boselli et al., 2010b) which targeted 323 local galaxies. The HRS is a volume-limited sample (between 15 and 25 Mpc) and uses K_s-band selection because this band is only marginally affected by extinction and is known to be a good proxy for stellar mass (e.g. Gavazzi & Scodeggio, 1996); throughout the rest of this work, we will refer to the HRS as a stellar mass selected sample. For late type galaxies, an apparent magnitude limit of $K_s \leq 12$ was used. The HRS also contains numerous (75) Early Type Galaxies (ETGs) due to its stellar mass selection and an extensive overlap with the Virgo cluster. The ETGs were selected using a brighter flux limit of $K_s \leq 8.7$ to avoid having them dominating the sample. The ETGs mostly reside in clusters, are in the latest stages of their evolution, and their dust and gas content is often related to recent merger activity (Kaviraj et al., 2009; 2011; Davis et al., 2015). We will not include ETGs when determining best fit relations and correlations. Instead we highlight them as a separate sub-sample in the plots.

Again, for consistency, we derived properties for HRS galaxies using MAGPHYS. We take HRS photometry from the literature in 21 bands spanning GALEX (Cortese et al., 2012a), SDSS (Cortese et al., 2012a), 2MASS (Skrutskie et al., 2006), *Spitzer*/IRAC (Sheth et al., 2010), WISE (Ciesla et al., 2014), *Spitzer*/MIPS (Bendo et al., 2012b), *Herschel*/PACS (Cortese et al., 2014) and *Herschel*/SPIRE (Ciesla et al., 2012). Four HRS ETGs were discarded as

their SEDs were poorly matched, either because a considerable fraction of dust heating by AGN activity or the hot X-ray halo that is often present in ETGs[1] (and is not accounted for in MAGPHYS, which leads to an offset between the stellar and dust f_μ and thus a poorer match), or because synchrotron radiation contaminated the FIR fluxes.

Our results are slightly different to the MAGPHYS HRS results in Viaene et al. (2016) because they did not apply any corrections for Galactic extinction and $K_{\rm beam}$, and used smaller uncertainties. For the HI masses of the HRS galaxies, we used the unconfused results from Boselli et al. (2014a). For HRS, CO based H_2 masses are presented in Boselli et al. (2014a) and can be relatively large compared to their HI. However, they are still small compared to the total baryon mass and using total (HI+H_2) gas masses instead of HI masses only gives small differences to the overall scaling relations for HRS in this work (see also Appendix A).

4.3 Dust, gas and stars

4.3.1 Dust, HI and stellar masses

We first investigate the extend of the parameter space occupied by the 3 samples. Figure 4.1 shows the dust, stellar and HI mass distributions of our sample compared to the HRS and HAPLESS. It should be noted when comparing the HAPLESS and HIGH samples that the differences are solely due to from the non-overlapping halves of each sample. The left panel of Figure 4.1 shows that both the HAPLESS and HIGH samples have, on average, lower stellar masses than the HRS, as could be expected from the HRS stellar mass selection. From the central panel, we find that our HIGH sample has dust masses as high as HAPLESS, but also extends to sources with lower dust masses that would not have met the HAPLESS selection limit. For the HI mass distributions, we find that the HRS has the lowest atomic gas masses, followed by HAPLESS and then our HIGH sample. Dust-selected sources contain more gas on average than stellar mass selected sources. Selecting on HI mass and on dust mass produce broadly similar samples, which is not that surprising as dust is believed to be a good tracer of the total gas mass (Eales et al., 2010; Planck Collaboration et al., 2011a; Scoville et al., 2014). And although we do not know the molecular gas content, we do expect a natural correlation between the atomic gas mass and the total gas mass.

Next we investigate the distribution of the relative masses of stars, dust and atomic gas. The distribution of the gas fractions ($\frac{1.32M_{\rm HI}}{M_*+1.32M_{\rm HI}}$) in the top-left panel of Figure 4.2 shows important differences between the samples. The HIGH sample is more gas-rich than the HRS, while the HAPLESS gas fractions are relatively uniformly distributed. In this work, we define the

[1] The affected sources are known AGN and X-ray sources.

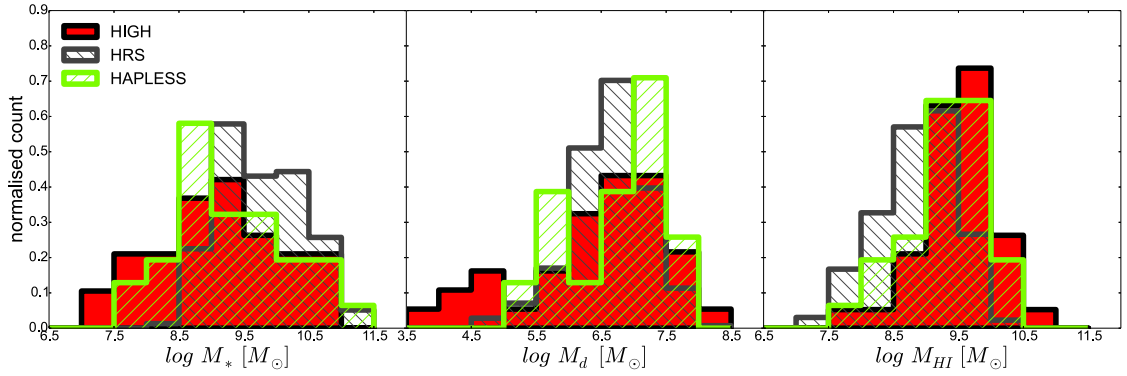

Figure 4.1: *From left to right:* Histograms showing the stellar, dust and HI mass distributions for our HIGH sample (in red), HAPLESS (in green) and HRS (in grey). The effects of dust mass selection (HAPLESS) and HI mass selection are similar and both are different to stellar mass selection (HRS).

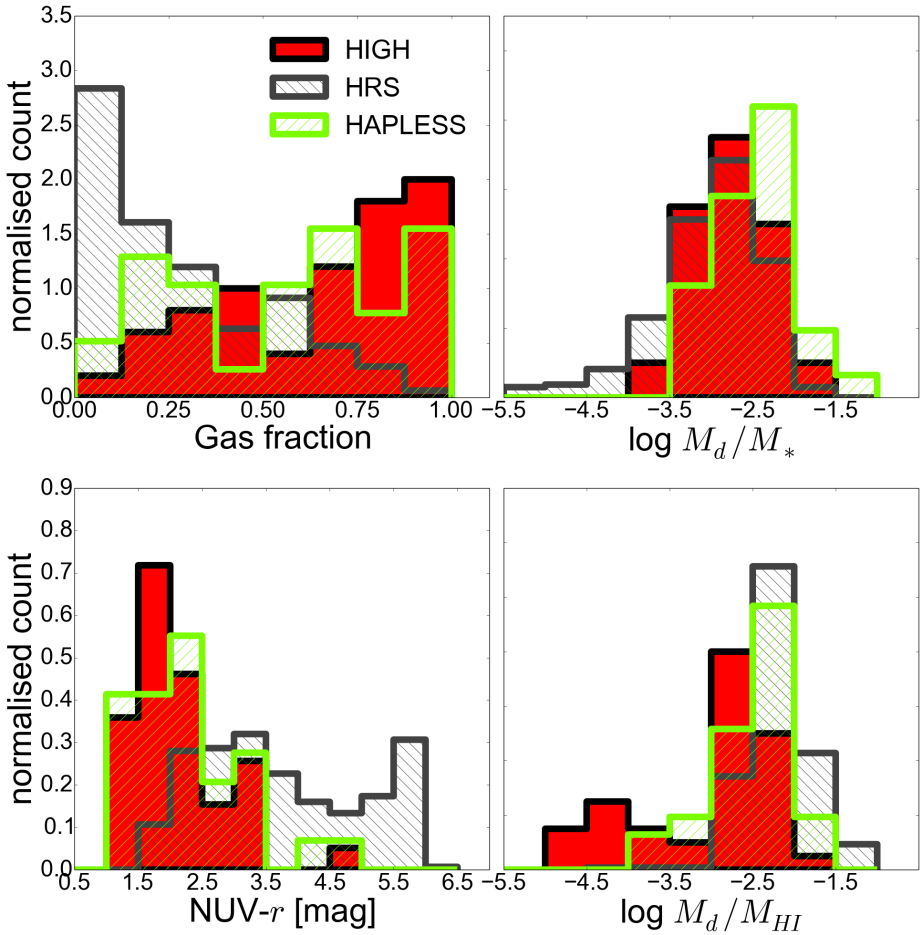

Figure 4.2: Histogram showing the distribution of gas fraction ($\frac{1.32M_{\rm HI}}{M_*+1.32M_{\rm HI}}$; *top-left*), specific dust mass (*top-right*), NUV-*r* colour (proxy for specific star formation rate; *bottom-left*) and dust-to-HI ratio (*bottom-right*) for the HIGH sample, HAPLESS and HRS.

evolutionary status of a galaxy using its gas fraction as a measure of how much of the available gas reservoir has been converted into stars[2]. A galaxy's gas fraction is equivalently defined by its HI-to-stellar mass ratio $M_{\rm HI}/M_*$. The latter is more useful in terms of determining linear scaling relations with other parameters, though we often refer to high HI-to-stellar mass ratio sources as high gas fraction sources for convenience, and because this term is more commonly used throughout literature. HRS then consists mainly of evolved sources, HAPLESS consists of galaxies at a range of stages of evolution and *the HIGH sample consists mainly of relatively unevolved sources*. Our HI selection therefore gives us vital insights into the 'youthful'[3] sources, which were previously under-represented in stellar mass selected samples like HRS.

The top-right panel of Figure 4.2 shows that the specific dust mass (M_d/M_*) is highest for HAPLESS, followed by HIGH and then HRS. When we look at the distribution of dust-to-HI ratio (bottom-right panel) we now find that HIGH has the lowest $M_d/M_{\rm HI}$, followed by HAPLESS and then HRS. Finally we show the NUV-r colour distribution in the bottom-left panel of Figure 4.2. This colour is closely related to the specific star formation rate (see Section 4.3.2) and we find that both the HAPLESS and HIGH samples are much bluer and thus more actively forming stars than HRS. The large tail of red sources in HRS is due to that sample containing a larger fraction of more evolved, passive sources.

As discussed in Section 2.4, the HAPLESS sample revealed a population of Blue And Dusty Gas-Rich Sources (BADGRS), which are also present in the HIGH sample (part of the overlap). Our HI selection reveals an additional population of blue, extremely gas-rich (gas fraction > 0.8) sources that, in contrast to the BADGRS, have a much smaller dust content. Both the populations revealed by HAPLESS and HIGH consist of very blue, highly irregular/flocculent sources with low stellar masses. The dust-poor population revealed by the HI selection has the highest gas fractions, suggesting these are at an earlier stage in their evolution compared to the BADGRS and the rest of HAPLESS and the HRS. To highlight these dust-poor sources, we have divided the HIGH sample in HIGH-high and HIGH-low, using a stellar mass cut of $M_* < 10^9 M_\odot$ (see Section 2.4).

In Figure 4.3 we show the stellar, dust and HI mass scaling relations. In the top-left panel we find a strong correlation between dust and stellar mass for both HIGH (Spearman rank correlation coefficient $r = 0.93$) and HAPLESS ($r = 0.81$). For HRS there is a strong correlation ($r = 0.88$) for the Late Type Galaxies (LTGs), yet the correlation weakens significantly ($r = 0.30$) if the ETGs are included. These ETGs have high stellar masses but very low dust

[2]The most important caveat to this method is that we do not take into account interactions like inflows, outflows and merging.

[3]These sources are not necessarily young in terms of the elapsed time since their formation. They can also be sources that have evolved at a much slower pace.

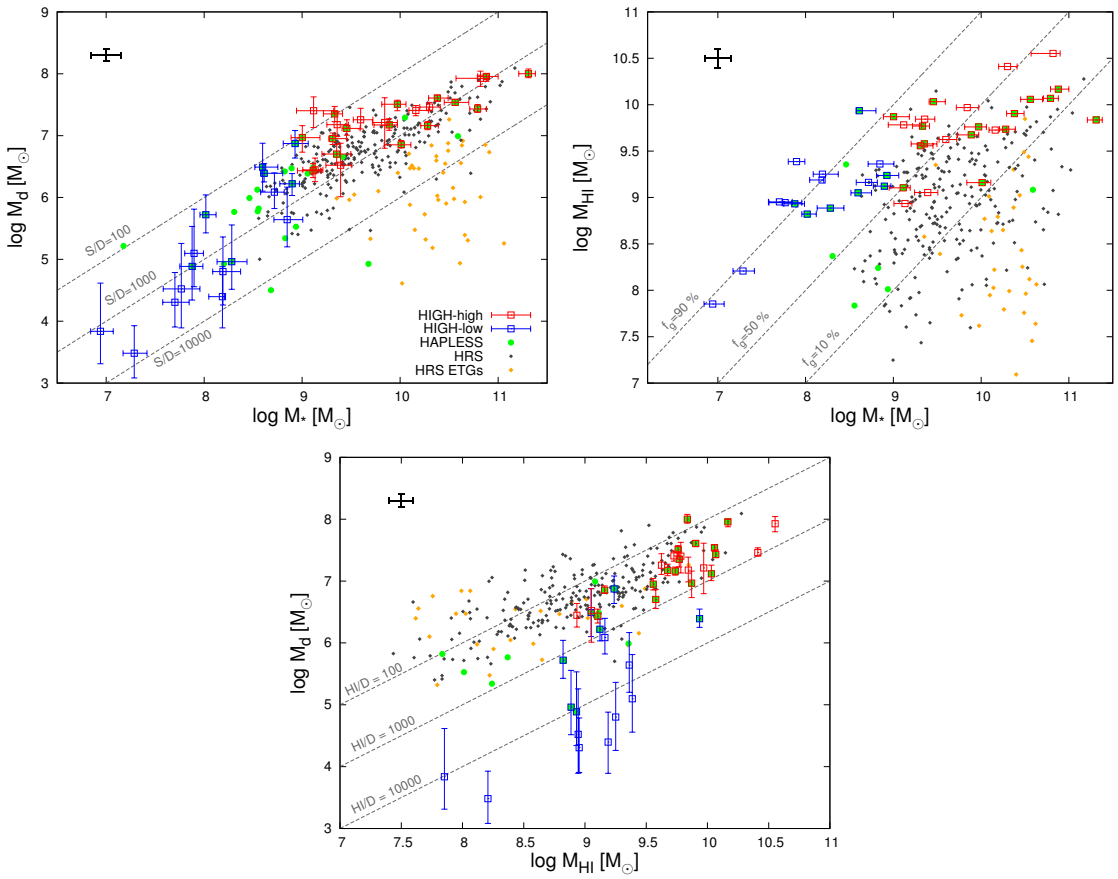

Figure 4.3: Scaling relations showing how the stellar, dust, and gas masses depend on each other for HIGH-low (blue squares), HIGH-high (red squares), HAPLESS (green circles) and HRS, which was divided in late type galaxies (grey dots) and early type galaxies (orange dots). A representative error bar for HRS is shown in the upper-left corner. Lines of constant M_*/M_d (S/D), gas fraction (f_g) and $M_{\rm HI}/M_d$ (HI/D) are shown in grey. Note the selection effects towards higher dust and gas masses for the HI-selected HIGH and dust-selected HAPLESS samples, compared to the stellar mass selected HRS sample.

masses, and are common ($15-25\%$ of the sources) in stellar mass selected samples[4] but not in selections based on ISM content like HAPLESS and HIGH. We note that HAPLESS would have been able to detect sources like those in the bottom-right corner had they been present in the HAPLESS volume, but ETGs tend to reside preferentially in over-dense regions (most HRS ETGs are in the Virgo cluster) and the H-ATLAS equatorial fields contain no large over-dense regions out to $z = 0.1$.

[4]For HRS, only the brightest ETGs have been included in the sample (brighter selection limit), yet at the same time HRS resides in a cluster environment, where ETGs are more common. Because of this, HRS has a broadly similar fraction of ETGs (23%) than purely stellar mass selected samples in the field (e.g. for GAMA 22.4% of galaxies are spheroid dominated; Moffett et al., 2016).

When we study the correlation between HI and stellar mass (top-right panel of Figure 4.3), we find the strongest correlation for HIGH ($r = 0.77$), a weaker one for HAPLESS ($r = 0.67$) and the weakest for the HRS LTGs ($r = 0.63$). When the ETGs are included, there is no significant correlation for HRS. The HRS and the HIGH sample segregate in this plot because they intrinsically consist of galaxies in different stages of evolution (stellar mass selection favours lower gas fractions and vice versa).

In the bottom panel of Figure 4.3 we find a strong correlation between the HI and dust mass for HAPLESS, the HRS and the HIGH-high sample (Spearman rank coefficient of $r = 0.74$ for the combined samples). However HIGH-low lies significantly below this relation and we will investigate the reasons for this in the following sections. The HRS ETGs now follow the same trend as the LTGs. For a given HI mass, HAPLESS (and HIGH) sources have lower dust masses on average than HRS, contrary to what might be naively expected when comparing a dust and a stellar mass selected sample. This is again because they consist of galaxies in different stages of evolution; the more evolved HRS sources have a more enriched ISM (see also Section 4.3.4).

4.3.2 Gas richness and specific star formation rate

In this section we assess the basic scaling relations between gas, stars and SFR and put our samples into context with other work. Figure 4.4 shows how gas richness ($M_{\rm HI}/M_*$) scales with stellar mass and NUV-r, which is known to be a good proxy for SSFR (e.g. Figure 4.5; Schiminovich et al., 2007). These relations have been extensively studied for HRS (Cortese et al., 2011), ALFALFA (Huang et al., 2012), Hα3 (Gavazzi et al., 2013), GASS (Catinella et al., 2013) and in earlier work (Gavazzi & Scodeggio, 1996; Boselli et al., 2001). As can be seen in Figure 4.4, the HIGH sample follows the same relations as determined for other HI selected samples, such as ALFALFA.

The anti-correlation with stellar mass can be understood in terms of different time-scales on which galaxies of different masses evolve. Massive galaxies go through their evolution faster (so-called downsizing; Cowie et al., 1996 ; Gavazzi & Scodeggio, 1996) and so will have converted more of their HI into stars by the present day. This could explain why the sources in the $M_* < 10^9 M_\odot$ sub-sample tend to have such high gas fractions.

Some of the selection effects for the different samples are evident in the left panel. The HI selection of HIGH (and ALFALFA) selects higher $M_{\rm HI}/M_*$ at fixed M_* compared to the stellar mass selection of HRS. This is due both to the HI selection favouring gas-rich galaxies (and vice versa for stellar mass selection), and also in part to a fraction ($\sim 25\%$) of the HRS sources being in the Virgo cluster. Cortese et al. (2011) found that the scaling relations for cluster galaxies in HRS are shifted towards lower $M_{\rm HI}/M_*$ due to stripping of gas directly from the

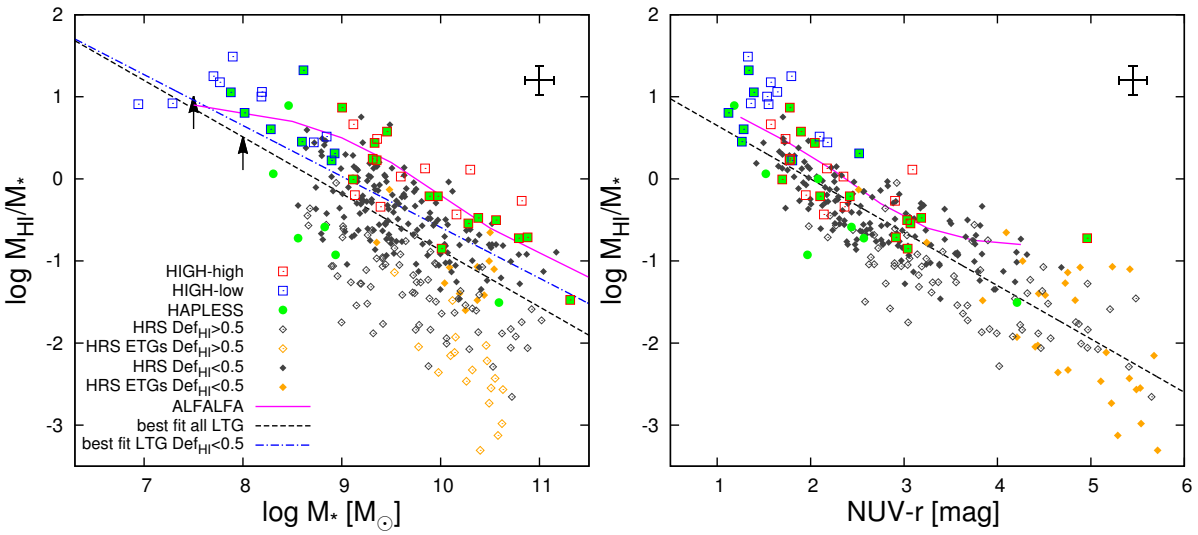

Figure 4.4: Trends with $M_{\rm HI}/M_*$ and SSFR. Symbols are as in Figure 4.3, with open symbols for HI deficient ($\rm Def_{HI} \geq 0.5$) LTGs in HRS and filled symbols for HI normal HRS LTGs. The best fit power law relationship for the combined samples (excluding ETGs) is shown as a black dashed line, and the best relation also excluding HI deficient HRS galaxies as a blue dash-dot line. *Left:* $M_{\rm HI}/M_*$ against stellar mass: A range of HI-to-stellar mass ratio at fixed stellar mass can be noticed. The ALFALFA relation (Huang et al., 2012) is shown in magenta. The HIPASS detection limits at $M_* = 10^{7.5}\,M_\odot$ and $M_* = 10^{8}\,M_\odot$ are shown as black arrows. *Right:* $M_{\rm HI}/M_*$ against NUV-r colour (proxy for SSFR). This strong correlation is applicable to all samples and thus is a very useful scaling relation.

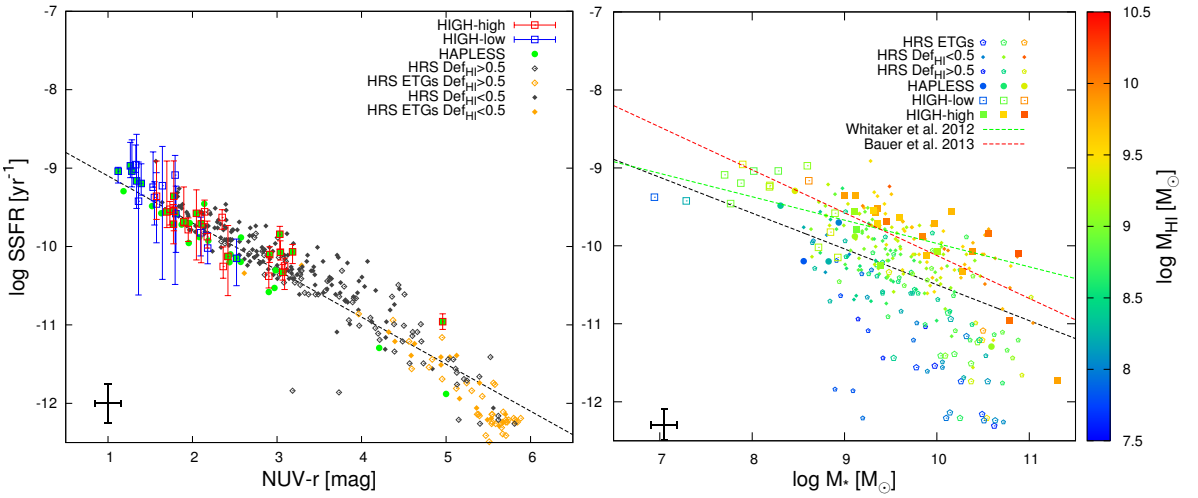

Figure 4.5: Scaling relations with SSFR for HRS, HAPLESS, and our two HI-selected sub-samples. Symbols are as in Figure 4.3. The best fitting trend line for these 4 samples combined is shown as a black dashed line. *Left:* SSFR against NUV-r colour; The strong correlation shows that NUV-r colour is a good proxy for SSFR. *Right:* SSFR against stellar mass, colour-coded by their HI mass; At least part of the scatter arises from differences in gas content.

star-forming disc (i.e. ram pressure). Since HRS contains both cluster and field galaxies, this leads to an increased scatter and an offset towards lower $M_{\rm HI}/M_*$ compared to field galaxies alone. The HI deficiency gives a measure for how much lower the HI content is compared to an isolated galaxy of similar optical diameter and morphological type. In Figure 4.4 we have used open symbols for HI deficient ($\rm Def_{HI} \geq 0.5$) LTGs in HRS. Next to our best fit relation for all samples combined (excluding ETGs), we have also plotted the best fit line excluding HI deficient galaxies to illustrate the effect of including HI deficient galaxies in our scaling relations.

We have also determined the HIPASS detection limit to be $\log M_{\rm HI}/M_\odot > 8.51$, assuming a distance equal to the average distance for HIGH-low (29.2 Mpc). We have added this detection limit as black arrows to Figure 4.4 (left) at $M_* = 10^{7.5}\,M_\odot$ and $M_* = 10^8\,M_\odot$. The lack of sources below the dashed line at low M_* is due to this limit. However, the upper bound of the trend in Figure 4.4 does not suffer these selection effects. The large range of HI-to-stellar mass ratios found at a given stellar mass indicates that, although the star formation history has a well known dependence on halo mass (more massive galaxies are more evolved; e.g. Cowie et al., 1996), local factors such as environment and gas supply play an important role (e.g. De Lucia et al., 2006) and thus cause the scatter in the left panel of Figure 4.4. Note that the fit to the $M_{\rm HI}/M_*$ vs M_* scaling relation depends on the sample used. The relation for HRS (or any stellar mass selected sample) is offset to that derived for an HI-selected sample. It is also sensitive to the environment, with samples from high density regions lying below the scaling relations.

The NUV-r colour is generally accepted to be a good tracer of the specific star formation rate (e.g. Schiminovich et al., 2007), confirmed in the left panel of Figure 4.5 by the strong correlation ($r = -0.92$ for all samples combined) between the NUV-r colour and the SSFR from MAGPHYS, which includes both the obscured and unobscured star formation. Figure 4.4 (right) shows a stronger correlation of HI-to-stellar mass ratio with NUV-r colour than with M_* ($r = -0.84$ and $r = -0.59$ respectively for all samples combined [5]). The different samples collated here (including the HI deficient sources) now lie on the same best fit relation (contrary to the left panel). The range in HI-to-stellar mass ratio at fixed NUV-r is thus significantly smaller than at fixed M_*. This can be understood by realising that the parameters on both axes scale with the cold gas content, and shows that $M_{\rm HI}/M_*$ is a strong driver of the specific star formation rate (either directly, or indirectly through scaling relations with the molecular gas, which is directly involved in star formation; e.g. Bigiel et al., 2011; Schruba et al., 2011; Saintonge et al., 2011; Bothwell et al., 2014). The relation between HI-to-stellar mass ratio and SSFR is thus the more fundamental one and is more useful as it holds for all samples. The

[5] See Table 4.1 for the Pearson correlation coefficients and the best fitting relations in this work.

Table 4.1: The Spearman rank correlation coefficients (r) and lines of best fit ($y = ax + b$, where a is the slope and b is the intercept) for the significant correlations in the form of a powerlaw. The best fitting relations were determined using a BCES linear regression method (Akritas & Bershady, 1996) using the HIGH, HAPLESS and HRS samples combined. For HRS, only late type galaxies are included (both HI deficient and HI normal). The first two columns specify the x and y parameters, the last columns specify whether HIGH-low is offset and whether the derived relation is dependent on the selection used. We caution the use of relations that are strongly dependent on the selection criterea. HIGH-low is not included in the combined sample if it is offset (lower dust mass) compared to the other samples.

y	x	r	Slope	Intercept	HIGH-low offset	strong selection dependence
log $M_{\rm HI}/M_*$	log M_*	-0.59	-0.69 ± 0.05	6.02 ± 0.47		✓
log $M_{\rm HI}/M_*$	NUV-r	-0.84	-0.65 ± 0.03	1.30 ± 0.09		
log SSFR	log M_*	-0.48	-0.46 ± 0.04	-5.90 ± 0.42		✓
log M_d/M_*	log M_*	-0.44	-0.26 ± 0.03	-0.44 ± 0.34	✓	✓
log M_d/M_*	NUV-r	-0.77	-0.33 ± 0.02	-1.92 ± 0.06	✓	
log M_d/M_*	log $M_{\rm HI}/M_*$	0.87	0.47 ± 0.02	-2.59 ± 0.02	✓	
log M_d/M_*	log SSFR	0.72	0.51 ± 0.03	2.30 ± 0.30	✓	
log $M_d/M_{\rm HI}$	log M_*	0.47	0.32 ± 0.04	-5.33 ± 0.37	✓	✓
log $M_d/M_{\rm HI}$	NUV-r	0.66	0.28 ± 0.02	-3.06 ± 0.07	✓	
log $M_d/M_{\rm HI}$	log $M_{\rm HI}/M_*$	-0.86	-0.52 ± 0.02	-2.57 ± 0.02	✓	
log SFR/M_d	log $M_{\rm HI}/M_*$	0.37	0.25 ± 0.03	-7.19 ± 0.03	✓	
log $SFR/M_{\rm HI}$	log $M_{\rm HI}/M_*$	-0.53	-0.29 ± 0.03	-9.80 ± 0.02		
log $SFR/M_{\rm HI}$	log Σ_*	0.58	0.50 ± 0.06	-10.28 ± 0.07		

variation in HI-to-stellar mass ratio at fixed M_* will correspond to a range of SSFR at any given M_*.

We see an equivalent result in the right panel of Figure 4.5, the relation between SSFR and stellar mass or 'main sequence of star forming galaxies' (Noeske et al., 2007). The star forming galaxies in our samples follow a similar trend to previous work (e.g. Whitaker et al., 2012; Bauer et al., 2013), with a scatter of more passive sources at lower SSFR for a given stellar mass. By colour-coding the data points in this plot by their HI mass, it becomes apparent that much of the scatter in this relation comes from the difference in gas richness at fixed stellar mass, with more gas-rich sources having higher SSFR at the same stellar mass. This supports our interpretation of the $M_{\rm HI}/M_*$ scaling relations. The large scatter in gas richness at given M_* (Figure 4.4; left) produces the scatter seen in the right panel of Figure 4.4. *Thus the driver of the scatter in the main sequence of star forming galaxies is the gas supply.* This agrees with the findings by Huang et al. (2012), who showed that the color, SFR, and gas evolution of galaxies are closely related to one another and that the regulation of SFR by $M_{\rm HI}$ is stronger in less massive galaxies ($M_* < 10^{9.5}\,M_\odot$). Similar conclusions are reached through the determination of an HI gas fraction plane (Catinella et al., 2010; Cortese et al., 2011) and also from performing a stacking analysis in *Herschel* data on a large sample of galaxies out to

$z = 2.5$ extracted from the GOODS-S, GOODS-N and COSMOS fields, and inferring the gas content from dust mass measurements (Santini et al., 2014).

4.3.3 Specific dust scaling relations

Cortese et al. (2012b) and Bourne et al. (2012) have studied specific dust (M_d/M_*) scaling relations for HRS and for H-ATLAS stacks on optically selected sources, respectively. They found a strong anti-correlation between M_d/M_* with NUV-r colour and a weaker anti-correlation with stellar mass, similar to the scaling relations for $M_{\rm HI}/M_*$ in the previous section (see also: da Cunha et al., 2010; Smith et al., 2012; Rowlands et al., 2014a). Viaene et al. (2014) also note a similar trend for regions inside M31, indicating that the driving processes for these scaling relations (most likely star formation) are local processes. Cortese et al. (2012b) also found a strong correlation of M_d/M_* with gas fraction. Figure 4.6 shows the specific dust scaling relations for the different samples. We find the scaling relations for HRS, HAPLESS and HIGH-high are consistent with those determined by Cortese et al. (2012b) and Bourne et al. (2012).

For HIGH-low however, we find that the sources lie significantly below the trends for the other samples in each of the scaling relations in Figure 4.6. *The benchmark dust scaling relations identified by Cortese et al. (2012b) and Bourne et al. (2012)*[6] *based on optically selected samples, do not hold for gas-rich, low M_* (unevolved) sources.* A larger sample is necessary to determine the appropriate trend line for these low M_* sources. We find no evidence that group environment[7] affects the dust scaling relations, or contributes to the offset for the HIGH-low sources.

As mentioned in the previous section, the HRS displays an enhanced scatter in the HI-to-stellar mass ratio at fixed stellar mass due to the large fraction of Virgo cluster sources that have suffered gas stripping. Environment seemingly has no effect on the relations in the top-right and bottom panels. As shown by Cortese et al. (2012b), HI deficient galaxies are also dust deficient. This results in the large range in M_d/M_* at fixed stellar mass that can be seen for HRS in Figure 4.6 (top-left). Note that if we exclude the HI deficient sources from our best fit relation, the relation would become steeper and more similar to the Bourne et al. (2012) trend. This would further increase the disparity between HIGH-low and the trend from the higher mass samples.

[6]Note that the H-ATLAS stacks only extend down to $M_* = 10^{8.5} M_\odot$ so the drop in M_d/M_* for our low stellar mass sources does not contradict the statistically significant trend for the stacks.

[7]The large HIPASS beam often includes multiple confused objects, which can easily be part of the same galaxy group.

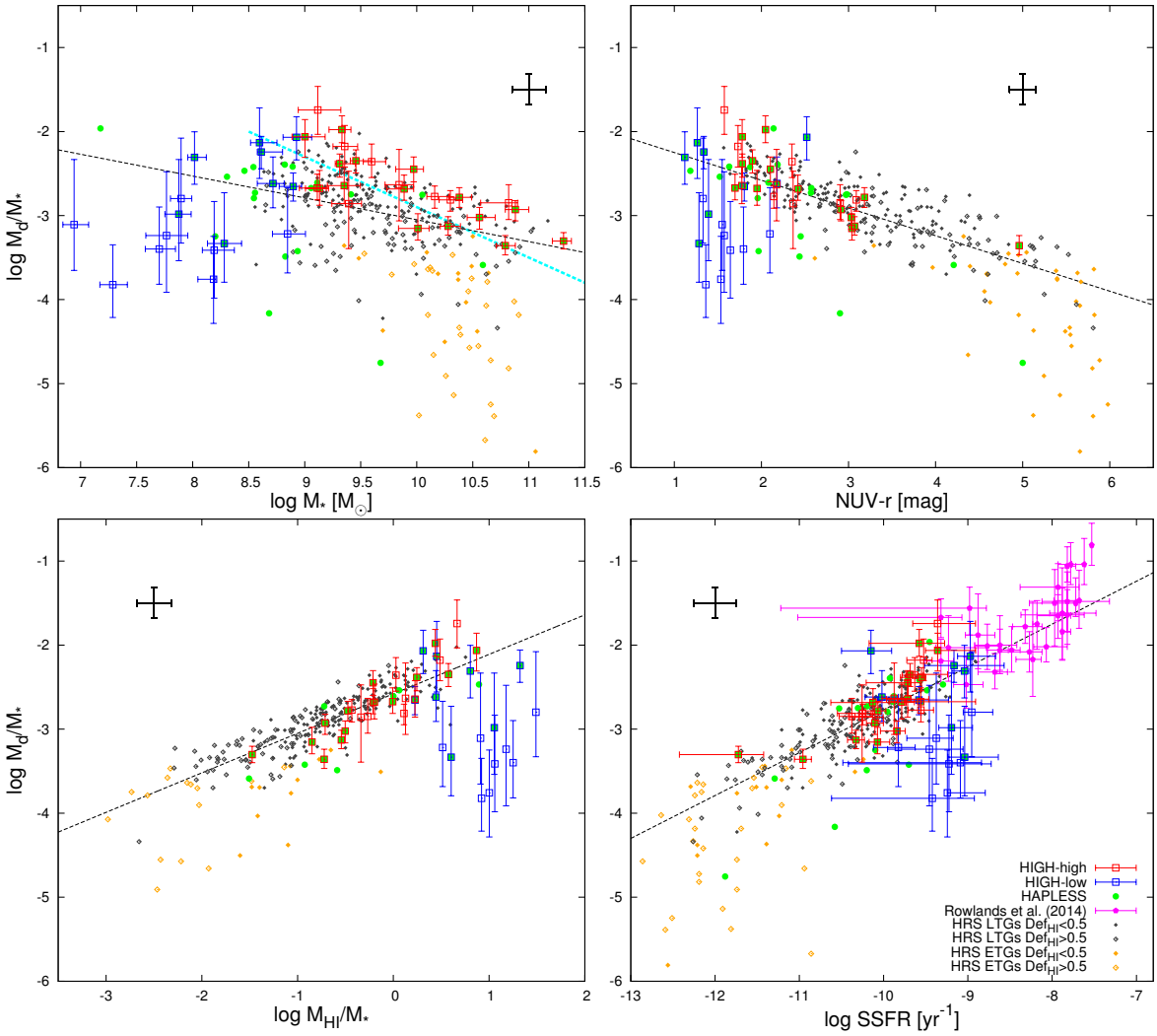

Figure 4.6: M_d/M_* scaling relations for the two HI-selected sub-samples, HRS and HAPLESS. Scaling relations with stellar mass (*top-left*), NUV-*r* colour (*top-right*), $M_{\rm HI}/M_*$ (*bottom-left*) and specific star formation rate (*bottom-right*). Correlations are found for each of the scaling relations for the high stellar mass HI-selected sample, HAPLESS and the HRS and the trend line for these 'evolved' samples combined is shown as a black dashed line. The ETGs are not included in our best fit relations. The low stellar mass HI-selected sample lies significantly below the trend for the other samples. The symbols are as in Figure 4.4; high-redshift SMGs from Rowlands et al. (2014a) have been added as magenta pentagons to the bottom-left panel.

For the HRS, HAPLESS and HIGH-high samples, we find that M_d/M_* correlates most strongly with $M_{\rm HI}/M_*$ ($r = 0.87$ for the three samples combined), followed by NUV-r colour ($r = -0.77$), SSFR ($r = 0.72$) and then stellar mass ($r = -0.44$). For the scaling relations with stellar mass in Figure 4.6 (top-left), we find an offset towards higher M_d/M_* for the HIGH-high and HAPLESS samples compared to HRS, yet this offset is absent for the scaling relations with NUV-r colour and $M_{\rm HI}/M_*$. This behaviour is similar to that in Figure 4.4 and is again due to the various ways the samples are selected, combined with the fact that a large range of HI-to-stellar mass ratio is possible at a given stellar mass. Once again the more fundamental parameter driving the specific dust mass appears to be the SSFR or the HI-to-stellar mass ratio, both of which are intimately linked.

Since $M_{\rm HI}/M_*$ is a proxy for how far a galaxy is through its evolution, the correlation seen in the bottom-left panel of Figure 4.6 implies that M_d/M_* depends on the evolutionary state. As galaxies evolve, they move from high to low $M_{\rm HI}/M_*$ and (for HIGH-high, the HRS and HAPLESS) M_d/M_* decreases. For these more evolved galaxies, the dust mass traces the HI mass:

$$\log M_d/M_* = (0.47 \pm 0.02)\ \log M_{\rm HI}/M_* - (2.59 \pm 0.02) \tag{4.1}$$

for sources with $\log M_{\rm HI}/M_* < 0.5$. This relation can be used to estimate the HI masses for high-redshift sources for which the HI cannot be measured directly (but dust can). However in order to do this reliably, one has to be sure (from other observations) the galaxy is evolved and is not still building up its dust mass (since there is a degeneracy between high and low HI-to-stellar mass ratio sources with the same M_d/M_*).

The unevolved sources in HIGH-low clearly lie below the relation for the other samples and imply a rising M_d/M_* at the earliest stages of evolution ($M_{\rm HI}/M_* > 10^{0.5}$). *At high gas fractions, dust is not a good tracer of the the HI content.* These galaxies are increasing their dust content at a faster fractional rate than their stellar content. The combined samples have allowed us to find a peak[8] in the specific dust mass (M_d/M_*) in the local Universe occurring at a gas fraction of $\sim 75\%$ and a stellar mass of $M_* \simeq 10^{8.5}$. HIGH-low is the first sample of galaxies to be identified as preceding this peak M_d/M_* in an evolutionary sequence. We will return to this in Chapter 6.

We have also plotted M_d/M_* against SSFR in the bottom-right panel of Figure 4.6. This plot is equivalent to the top-right panel of Figure 4.6, but we have added the sample of high-redshift SubMillimetre Galaxies (SMGs) from Rowlands et al. (2014a), which were also fitted with MAGPHYS. These galaxies are forming stars at a remarkably high rate and lie on a relation that extends the trend for HIGH-high, HAPLESS and the HRS (the best fit relation was not fitted to the SMGs). The correlation of M_d/M_* with SSFR holds over 5 orders of magnitude.

[8] These sources at the peak of their specific dust mass (M_d/M_*) are the BADGRS that were identified by C15.

This is consistent with the general idea that dust traces the molecular ISM where star-formation occurs (Dunne et al., 2000; Cortese et al., 2012b; Smith et al., 2012; Rowlands et al., 2014a). Despite the large differences in galaxy properties among the HIGH-high, HAPLESS and HRS samples, there is no evidence that they are forming stars in a fundamentally different way[9], they just have more or less star formation occurring as a result of their varying gas fractions. Figure 4.6 (bottom-right) also shows that dust mass is a reasonable indicator of SFR across a very wide range of M_* and galaxy type. The HIGH-low sample tends towards lower M_d/M_* for a given SSFR. Since dust is not a good tracer of gas content in HIGH-low, there consequently is a poorer correlation with the SSFR.

4.3.4 Dust enrichment relations

We next look at the dust content of the ISM as a function of stellar mass, NUV-r colour and $M_{\rm HI}/M_*$ (Figure 4.7). Once again we find different scaling relations for HIGH-low. For HIGH-high, HAPLESS and the HRS there is a weak but significant correlation between $M_d/M_{\rm HI}$ and M_* ($r = 0.47$). For HIGH-low, however, we find a steeper slope (Table 4.1) and a significantly smaller $M_d/M_{\rm HI}$ than expected from extrapolating the relation for the other samples. We find tighter scaling relations with NUV-r colour ($r = 0.66$) and $M_{\rm HI}/M_*$ ($r = -0.86$) for HIGH-high, HAPLESS and the HRS and again an offset towards lower dust enrichment for HIGH-low. The BADGRS, which were the most dust-rich sources in respect to their stellar mass, now have lower $M_d/M_{\rm HI}$ than the rest of HAPLESS and HRS, but not as low as our HIGH-low sample.

Note again the offset between the HIGH-high/HAPLESS samples and the HRS for the stellar mass scaling relations (cf. Figures 4.4 & 4.6). HI deficient galaxies are offset when $M_d/M_{\rm HI}$ is plotted against M_* (Cortese et al., 2016), yet this offset disappears for the more fundamental relations of $M_d/M_{\rm HI}$ with NUV-r colour and $M_{\rm HI}/M_*$. The offset between the samples is once again caused by differences in HI-to-stellar mass ratios at fixed stellar mass. Our interpretation of these dust enrichment relations is as follows:

Gas is continuously converted into stars and dust is produced at the endpoints of stellar evolution (supernovae and AGB stars). Yet at the same time dust is destroyed by shocks and also via astration as the next generation of stars is formed from gas at the ambient dust-to-gas ratio, and thus dust is also consumed (Tinsley, 1980). For HIGH-high, HAPLESS and the HRS we have found positive correlations of the dust-to-HI ratio with stellar mass and NUV-r colour, together with a negative correlation with the HI richness, showing that $M_d/M_{\rm HI}$ increases monotonically as galaxies move through their evolution. This implies that the dust budget is

[9]Not all galaxies will follow this normal star formation mode. Galaxies can also be in 'starburst' mode, with much higher SFR given their gas fractions, which will consume their gas reservoir on much shorter timescales than the age of the galaxy (e.g. Moorwood, 1996).

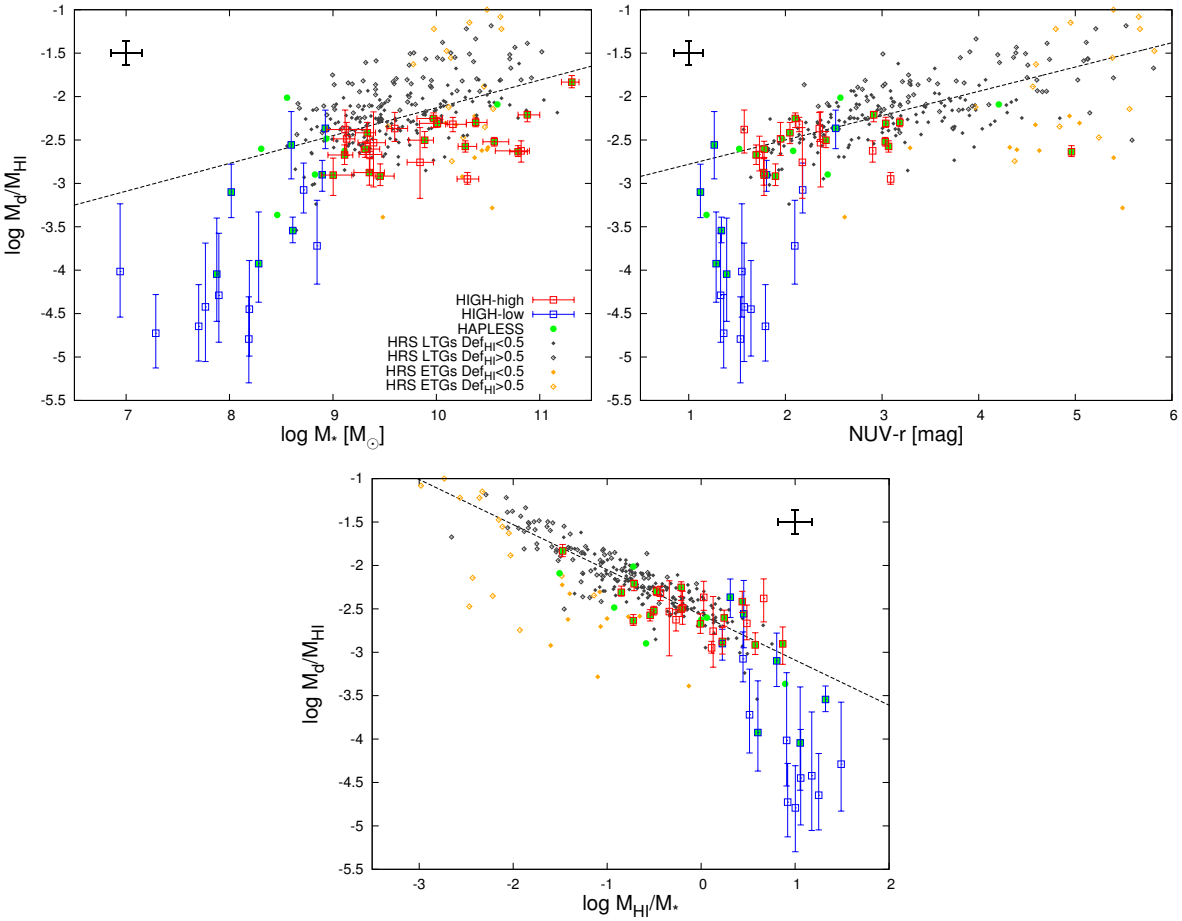

Figure 4.7: Dust enrichment relations for HRS, HAPLESS and HIGH. Scaling relations with stellar mass (*left*), NUV-*r* colour (proxy for SSFR; *right*) and $M_{\rm HI}/M_*$ (*bottom*). The best fitting trend line for the combined 'evolved' samples (HIGH-high, HAPLESS and HRS) is shown as a black dashed line. The HIGH-low sample lies significantly below the trend for the other samples and has a steeper slope. The symbols are as in Figure 4.4.

not dominated by dust destruction through shocks or sputtering. If it was, we would observe a decrease in the dust-to-HI ratio as galaxies evolve. Some of the ETGs in HRS may be an exception to this. These ETGs are bright X-ray sources and some have AGN in their centres. The hot gas in these sources erodes and breaks up the dust grains (sputtering), significantly reducing the dust mass and resulting in the outliers towards low $M_d/M_{\rm HI}$ for HRS in Figure 4.7.

In the previous section, we used scaling relations to suggest that as galaxies evolve (i.e. their gas is consumed in forming stars), the dust-to-stellar mass first increases (at the high gas fraction end), then reaches a peak for a gas fraction of ~ 0.75, plateauing until ~ 0.5. Beyond this 'half way stage', the M_d/M_* decreases and we have now found $M_d/M_{\rm HI}$ increases. This can be explained as the stellar mass in a galaxy builds monotonically with time as stars are

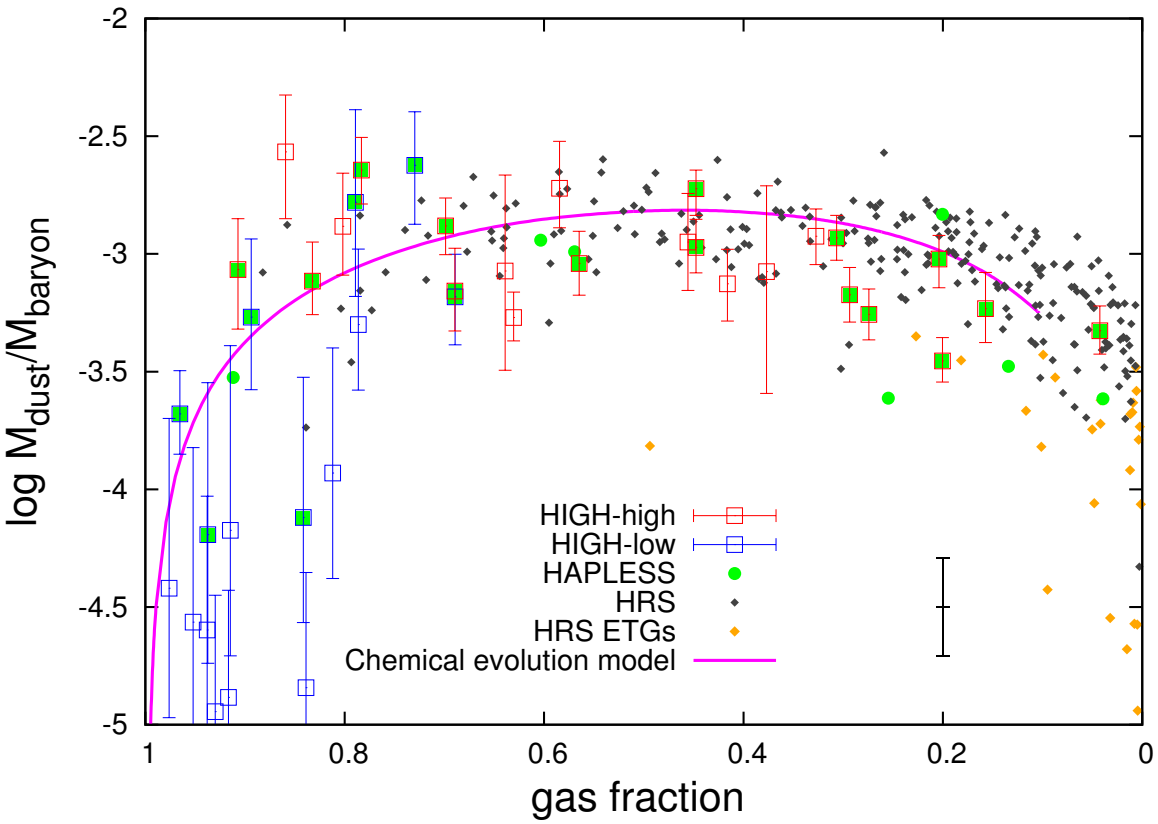

Figure 4.8: $M_d/M_{\rm bary}$ against gas fraction (without molecular hydrogen) reveals the evolution of dust. As galaxies evolve, the dust content first increases (high gas fraction end), then reaches its peak for a gas fraction of ~ 0.5 and afterwards decreases as dust is consumed together with the gas (low gas fraction tail). A chemical evolution model (C15) has been overplotted.

created. On the other hand, dust has a life cycle, being created, mixed in the ISM and then destroyed via astration and destruction. In the later evolutionary stages, this causes the dust mass doubling time to be longer than the stellar mass doubling time and consequently there is a decrease in M_d/M_*. Yet, at the same time, astration always removes gas at the current $M_d/M_{\rm HI}$, and there will be some dust production associated with the stars formed from the consumed ISM. $M_d/M_{\rm HI}$ will thus increase with time as a result of astration. Even when the rate of dust consumption (astration) is greater than the rate of production, there will still be a larger rate of gas consumption and thus an increase in $M_d/M_{\rm g}$.

In Figure 4.8, we follow C15 in plotting $M_d/M_{\rm bary}$ mass ratio vs gas fraction f_g (their Figure 21) where we define the baryon mass as $M_{\rm bary} = 1.32\,M_{\rm HI} + M_*$ and $f_g = 1.32\,M_{\rm HI}/(1.32\,M_{\rm HI} + M_*)$, where the factor 1.32 is to account for helium. We will come back to this plot in detail in Chapter 6, yet we introduce it here given its importance in the interpretation of the scaling relations in this chapter. We also follow C15 in comparing the observations with a simple,

closed box chemical evolution track[10] showing the expected change in $M_d/M_{\rm bary}$ with gas fraction for a Milky Way type star formation history (Yin et al., 2009). The track (solid line; same as C15) shows the evolution of a galaxy as it evolves from gas-rich to gas-poor, with gas consumed by star formation.

Due to its dust selection, the HAPLESS sample consists of galaxies with high $M_d/M_{\rm bary}$ at both the start and end of the evolutionary path (C15). The stellar selection of the HRS means that it is representative of the low gas fraction portion of this plot, where most of the gas has already been converted into stars. Combining the high gas fraction sources in HIGH with HAPLESS and HRS allows us to sample a wider range of f_g. As in C15, $M_d/M_{\rm bary}$ first rises steeply, then levels off and then drops again as galaxies evolve from high to low gas fractions. This supports the idea of the dust content being built up as galaxies move through the early stages of their evolution (gas fraction > 0.8). The dust content then plateaus as dust destruction through astration balances the dust production. Galaxies reach their peak dust content about half way through their evolution (gas fraction $\simeq 0.5$) as predicted by Eales & Edmunds (1996). Note that, while the position of a galaxy in Figure 4.8 does not depend on its total mass, since both axes are ratios, when sampling at the current epoch we find that the highest M_* galaxies are at the right of the plot and the lowest M_* are at the left, because massive galaxies go through their evolution faster. Including the HIGH sample provides crucial information at the highest gas fractions compared to the initial study in C15.

Of course, galaxies are far more complex than our simple closed box model, with inflows and outflows and dust destruction expected to be important factors. A more detailed study of the build-up of dust at high gas fractions will be presented in Chapter 6, and trends with metallicity will also be studied (high gas fraction sources have significantly lower metallicities than low gas fraction sources). However, even with the simplistic approach in C15, *the model is still able to match the observed overall shape of the build-up and destruction of dust as a galaxy evolves.*

4.4 The evolution of star formation efficiency

In Figure 4.9, we look at different measures of the Star Formation Efficiency (SFE) of the galaxies as a function of their HI-to-stellar mass ratio (or evolutionary status). In the top two panels we consider the molecular gas SFE ($SFR/M_{\rm H_2}$), while in the bottom panel we show the atomic gas SFE ($SFR/M_{\rm HI}$). Unfortunately we do not have CO data for the HIGH and HAPLESS sample so we cannot measure the molecular gas mass present in these galaxies. Instead we consider two approaches. Dust is believed to be a good tracer of the molecular

[10]Further details on the model are presented in Rowlands et al. (2014b; see also Morgan & Edmunds, 2003).

gas in galaxies (Dunne et al., 2000; Planck Collaboration et al., 2011b; Corbelli et al., 2012; Rowlands et al., 2014a; Scoville et al., 2014; Santini et al., 2014), and SFR/M_d can be used as a proxy for the molecular SFE. The second approach is to use scaling relations with the atomic gas and stellar mass present in these galaxies to obtain M_{H_2} estimates for HIGH and HAPLESS, and use CO derived H_2 masses from Boselli et al. (2014a) for HRS. The scaling relations to obtain H_2 estimates are presented in Appendix A and are based on the ALLSMOG (Bothwell et al., 2014) and COLDGASS (Saintonge et al., 2011) samples[11]. As molecular gas is directly involved in star formation (e.g. Bigiel et al., 2008; Schruba et al., 2011), SFR/M_{H_2} (i.e. SFR/M_d or $SFR/M_{H_2\,\mathrm{scaling}}$) is an indicator of the efficiency with which gas is converted to stars inside the radius at which molecular clouds are present in the galaxy[12].

On the other hand, atomic hydrogen does typically not form stars directly[13], it first makes a transition to molecular form. SFR/M_{HI} is therefore not a true star formation efficiency but rather an indication how effectively the HI is able to turn into molecular form and subsequently form stars. With this distinction in mind, we now turn to the trends shown in Figure 4.9. Taken at face value, and assuming a canonical value for M_d/M_{H_2} of 0.007 (Draine et al., 2007; see also Corbelli et al., 2012), the top panel of Figure 4.9 shows that the star formation efficiency in galaxies declines slightly as they move from high to low HI-to-stellar mass ratios, with the relationship in Table 4.1 indicating a rise in the molecular gas depletion timescale (τ_{H_2}) from 1.7 Gyr to 4 Gyr over a range in gas fraction from 80-10%. The HIGH-low sample lies well above this relationship indicating either a much shorter molecular gas depletion time (average of 140 Myr), or a much lower M_d/M_{H_2} ratio (by a factor ~ 10). If the former is correct, the molecular gas is depleted very rapidly in high gas fraction galaxies, possibly because the conditions for H_2 formation are not met across much of the disk, resulting in intense pockets of star formation which quickly consume the small molecular gas reservoir in a burst. Note that removing the HI-deficient galaxies would result in a more constant molecular SFE.

If we exclude HIGH-low in the centre panel of Figure 4.9, we again find a weak decline of SFR/M_{H_2} as galaxies evolve, with lower τ_{H_2} than from SFR/M_d. However, now HIGH-low is not offset towards high SFR/M_{H_2}, but instead has slightly lower SFR/M_{H_2} than expected. This makes the overall SFE evolution look more constant. This points towards the HIGH-low offset for SFR/M_d being due to a lower M_d/M_{H_2} ratio. However, we cannot be sure of the reliability of either proxy (dust, or HI and stars) for the H_2 content of HIGH and HAPLESS. Resolving

[11] These samples are the most similar samples available in terms of parameter space, yet only include sources with $M_* > 10^9\ M_\odot$ and $\log M_{HI}/M_* < 0.5$.

[12] For a true measure of the efficiency of converting dense gas into stars within star forming regions, it is necessary to choose a high density molecular tracer (e.g. HCN) Gao & Solomon, 2004; Papadopoulos et al., 2012.

[13] However, there is some debate whether star formation can also be directly fuelled by atomic gas for stars formed out of (newly accreted) metal-poor gas (Michałowski et al., 2015). The very first stars in the Universe (in the absence of dust and molecular gas) have formed directly from HI.

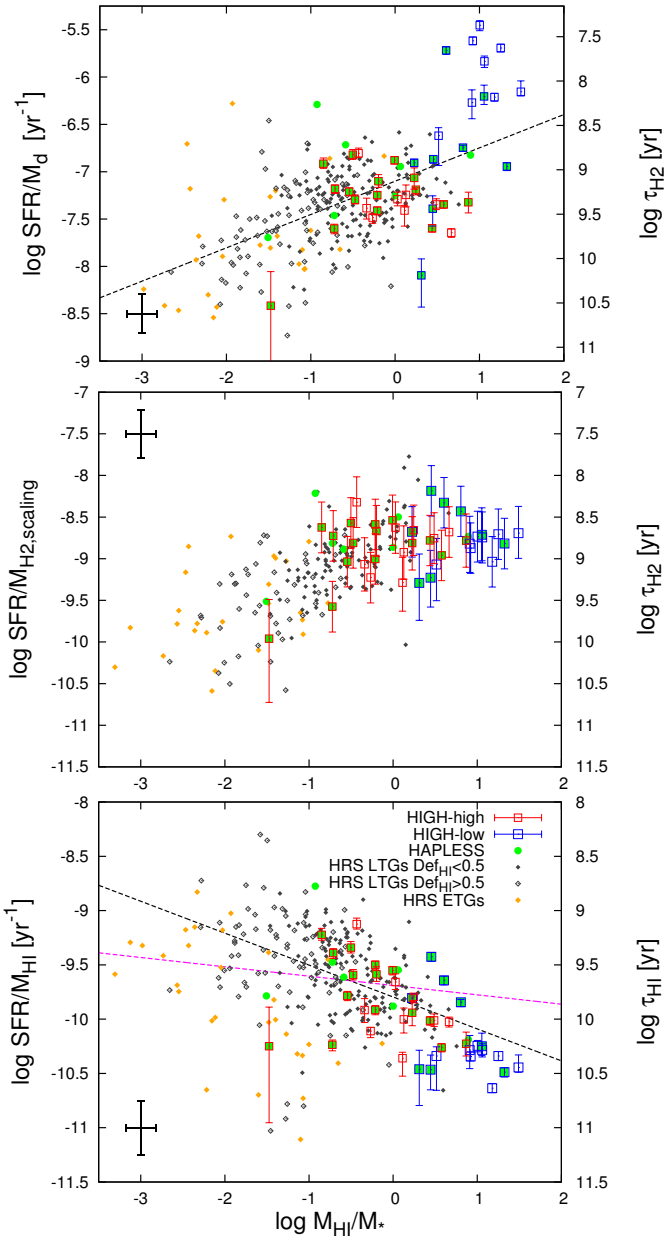

Figure 4.9: *Top:* SFR/M_d against $M_{\rm HI}/M_*$ showing a slow decline of SFR/M_d as galaxies evolve. HIGH-low is significantly offset towards higher SFR/M_d. The right axis shows the molecular gas depletion timescale using M_d as a proxy. *Centre:* $SFR/M_{\rm H_2,scaling}$ against $M_{\rm HI}/M_*$ shows a more constant molecular gas star formation efficiency. The molecular gasses for HIGH and HAPLESS were estimated using scaling relations based on the ALLSMOG (Bothwell et al., 2014) and COLDGASS (Saintonge et al., 2011) samples. *Bottom:* $SFR/M_{\rm HI}$ against $M_{\rm HI}/M_*$. There is a clear evolution towards higher $SFR/M_{\rm HI}$ for more evolved sources (best-fit line shown in dashed black). The correlation resulting from a typical HI error of 0.1 dex has been determined using MC simulations (dashed magenta).

this issue would require resolved CO + HI maps for these sources. However, both estimations agree there is only little evolution in the molecular SFE and the molecular depletion timescale is roughly $\tau_{H_2} \sim 1-4$ Gyr.

Studies of the main molecular gas tracer (CO) in local galaxies, selected over a range of stellar mass from $8.5 < \log M_*/M_\odot < 11.5$, find a similar result. The star formation efficiency increases weakly (or the gas depletion time decreases slightly) as the stellar mass decreases and as SSFR increases (Saintonge et al., 2011; Bothwell et al., 2014; Boselli et al., 2014a)[14]. These studies find a range of τ_{H_2} from 100 Myr – 5 Gyr over the same range of stellar mass as sampled here although our study contains three samples selected in very different ways (dust, gas and stellar content)[15].

In the bottom panel of Figure 4.9 we find that there is considerable evolution in SFR/M_{HI} ($r = -0.53$), such that more evolved galaxies have higher star formation per HI mass (shorter HI depletion times, τ_{HI}, assuming constant star formation rate and no re-supply of gas). We must be cautious in interpreting Figure 4.9 (bottom) as the quantity M_{HI} is present in both the x and y axes. Monte Carlo simulations were used to confirm that this relation cannot be due to biases introduced by the errors in M_{HI}. For each source in the sample, we generated an artificial HI mass so that its SFR/M_{HI} is equal to the average SFR/M_{HI} in the whole sample (the null hypothesis is that there is no evolution in SFR/M_{HI}) and then added Gaussian scatter with a standard deviation of 0.1 dex (typical M_{HI} error). This process was repeated 100 times and the resulting average trend is shown by the magenta line in Figure 4.9 (bottom). The error on M_{HI} does introduce an artificial correlation. However, the observed slope in Figure 4.9 (bottom) is significantly steeper and we believe this is a real effect.

The galaxies with the highest HI-to-stellar mass ratios, which were previously found to be the most actively star forming galaxies in terms of their stellar mass (SSFR) and their dust mass (SFR/M_d), are now least active with respect to their HI mass (they have the lowest SFR/M_{HI}). The HI depletion timescales range from 0.2 – 63 Gyr, with the most gas-rich ($M_{HI} > M_*$) sources capable of sustaining their current star formation rates for longer than the Hubble time. Previous studies find a comparable range in the value of τ_{HI} but no trend with any of the parameters that correlate with τ_{H_2}, such as stellar mass and SSFR (Saintonge et al., 2011; Bothwell et al., 2014; Boselli et al., 2014a). Similarly, we do not find a significant correlation of τ_{HI} with either stellar mass or SSFR.

There is, however, a known relationship between τ_{HI} and stellar mass surface density (Σ_*) *within* galaxies. The THINGS survey (Walter et al., 2008; Leroy et al., 2008) found SFR/M_{HI}

[14] Earlier studies of the molecular gas depletion times in local spiral galaxies found a constant τ_{H_2} of ~ 2 Gyr (e.g. Bigiel et al., 2008; Leroy et al., 2008), however these studies probed a much smaller range of intrinsic stellar mass or HI-to-stellar mass ratio and so are not thought to contradict the later findings of these larger studies.

[15] One of the samples (HRS) is the same as that used by Boselli et al. (2014a).

to be a strong and almost linear function of stellar mass surface density in the outer regions of spirals and in dwarfs, where the ISM is dominated by HI. Within the inner regions of spiral galaxies, the higher stellar mass surface density produces a higher hydrostatic pressure in the ISM (Elmegreen, 1989; Wong & Blitz, 2002) favouring the conversion of HI to H_2 and results in a molecular dominated region where the star formation efficiency (τ_{H_2}) is constant. We find a correlation ($r = 0.58$) between the global τ_{HI} and stellar mass surface density in Figure 4.10.

We can use Figure 4.10 to interpret the different panels in Figure 4.9 as being the result of an increasing efficiency of conversion of HI to H_2 as galaxies become more dominated by their stellar mass. As galaxies build up their stellar mass and increase in Σ_* they create the conditions for H_2 formation across a wider area; and their HI reservoirs are depleted due to conversion to H_2 and thence to stars. As galaxies become very dominated by stars and have large bulges, they can be H_2 dominated over large areas and their HI reservoirs will be relegated to the outskirts of the galaxy. In very evolved galaxies (e.g. ETGs) the presence of gas and star formation will be more strongly correlated with recent interactions or environmental effects (Davis et al., 2011; Kaviraj et al., 2012; 2013; Davies et al., 2015). This may explain the very large scatter in τ_{HI} for the lowest gas fraction galaxies. We also note that dust catalyses the formation of molecular hydrogen, and could thus also play an important role in the conversion from HI to H_2. The small H_2/HI ratios[16] for high gas fraction sources could be partly due to the low dust content of these galaxies ($M_d/M_{\rm HI} < 10^{-3}$).

This general picture is not strongly dependent on an assumption of a constant dust/H_2 ratio, that ratio would need to vary by several orders of magnitude to invalidate this interpretation. And indeed we reach similar conclusions when using scaling relations with $M_{\rm HI}$ and M_* to estimate M_{H_2}. Detailed observations of resolved CO, HI and dust would be required to further elaborate on this.

4.5 Dust heating in the diffuse ISM

Dust in the diffuse ISM is heated by the interstellar radiation field (ISRF), which has contributions from both old and young stellar populations. Dust in birth clouds experiences more intense and harsh radiation fields in the photo-dissociation regions (PDRs). To account for this MAGPHYS has a parameter, f_μ, that represents the fraction of the total dust luminosity arising in the diffuse ISM. The majority of the dust mass resides in a cold ($10 < T < 30$ K) diffuse dust component, whereas in most actively star forming galaxies a large fraction of the dust

[16]Here it only makes sense to consider the H_2 estimates from the scaling relations relations with $M_{\rm HI}$ and M_*, since using M_d as a proxy obviously leads to a correlation with dust.

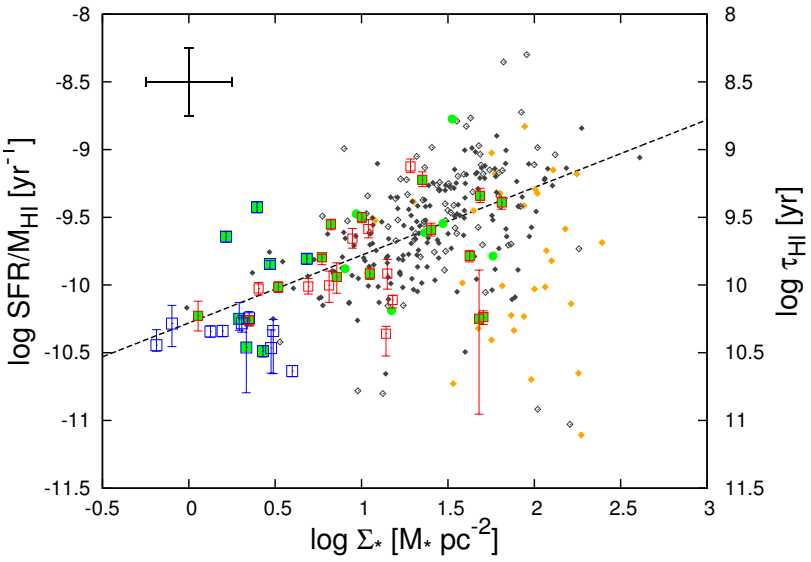

Figure 4.10: Star formation rate per HI mass ($SFR/M_{\rm HI}$) against stellar mass surface density Σ_*. As galaxies build up their stellar mass and increase in Σ_* they create the conditions for H_2 formation, which subsequently leads to increased SFR.

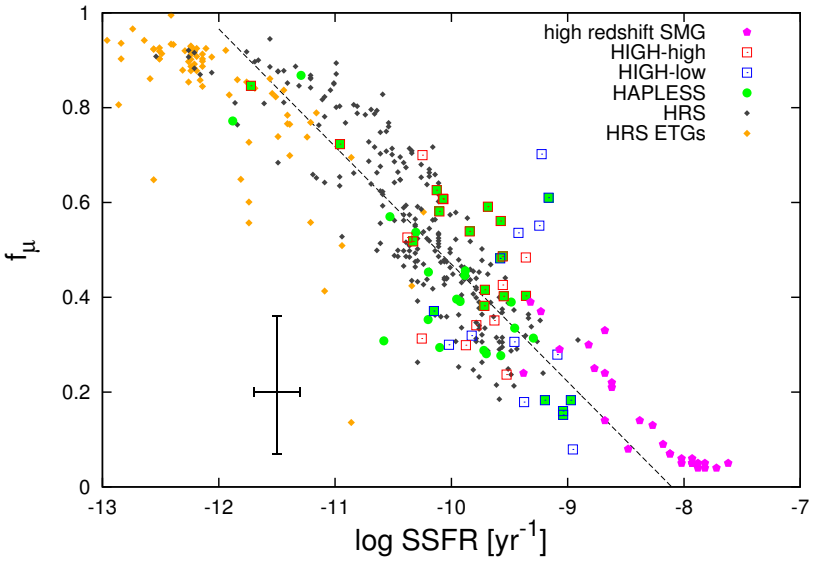

Figure 4.11: Influence of SSFR on the fraction of the total luminosity that originates in the diffuse ISM (f_μ). Less actively star forming galaxies have a larger fraction of their dust luminosity originating in the diffuse ISM. The line of best fit for combined HAPLESS, HIGH and SMG (Rowlands et al., 2014a) samples is shown as a dashed black line.

luminosity is due to a warm ($30 < T < 60$ K) dust component arising in birth clouds (futher details of the MAGPHYS components are found in Section 3.4).

In a typical galaxy in the Local Universe much of the stellar mass is in low mass stars, yet the small fraction of massive, short-lived stars radiate much more strongly at UV wavelengths. This UV radiation is highly susceptible to absorption by dust and the high energy UV photons can cause much of the dust heating (e.g. Draine et al., 2007) even though they only make up a very small fraction of the photons in the ISRF. In birth clouds the UV photons from young stars dominate the dust heating, but even in the diffuse ISM the PAHs, small grains (stochastically heated and emitting at MIR) and warm dust components are still mostly heated by UV photons that leak from the birth clouds and form part of the diffuse ISRF (Devereux & Young, 1990; Kennicutt, 1998; Calzetti et al., 2005; 2007; Boquien et al., 2010; Bendo et al., 2012a; Kirkpatrick et al., 2014). Many literature works have studied the sources of dust heating for the bulk of the dust mass in the diffuse ISM, and found that both the young stars in star forming regions and the diffuse evolved populations heat the diffuse dust (Bendo et al., 2010; Boselli et al., 2010a; 2012; Foyle et al., 2013; Ciesla et al., 2014; Cortese et al., 2014; Kirkpatrick et al., 2014; Draine et al., 2014; Bendo et al., 2015; Viaene et al., 2016, C15). In this section we will study which parameters drive change in f_μ and cold dust temperature and investigate which source of dust heating dominates in a particular galaxy for a wide range of HI-to-stellar mass ratio.

Figure 4.11 shows an anti-correlation of f_μ with SSFR for all the samples[17]. In order to probe to the highest SSFR, we have included the high redshift SMGs from Rowlands et al. (2014a). As expected, for most galaxies the fraction of the total dust luminosity originating in the birth-clouds ($1 - f_\mu$) is proportional to the star forming activity of the galaxy. This would be the case if a reasonable fraction of the energy in the birth clouds was being absorbed locally and re-radiated by dust (i.e. at least moderate A_{FUV}). Outliers can occur if the UV attenuation in the birth clouds is very low, allowing most of the UV energy to escape and heat the dust in the diffuse dust component. We indeed find that the outliers towards high f_μ in Figure 4.11 are all amongst the least attenuated sources in the sample ($A_{FUV} < 0.35$; see next section). On the other hand, outliers can also occur if a considerable fraction of the dust is heated by AGN activity or the hot X-ray halo that is often present in ETGs, as these sources of heating are not included in the MAGPHYS prescription. All the outliers towards low f_μ are ETGs and the strongest outliers are known bright X-ray sources.

C15 has studied the dust heating for HAPLESS and HRS. They found a strong correlation between the cold dust temperature (T_c) and both SFR/M_d ($r = 0.74$) and L_K/M_d ($r = 0.69$). Both the young (traced by SFR) and old stellar populations (traced by L_K, as in C15; or M_*[18])

[17] We note we find a similar but weaker correlation when plotting Ξ_c against SSFR. Ξ_c is a MAGPHYS parameter that gives the fraction of the total dust luminosity contributed by the cold dust component. There is a natural overlap between Ξ_c and f_μ since the cold dust component in MAGPHYS is only present in the diffuse ISM.

[18] Since the vast majority of the stellar mass consists of old stars, M_* also traces the old stellar population.

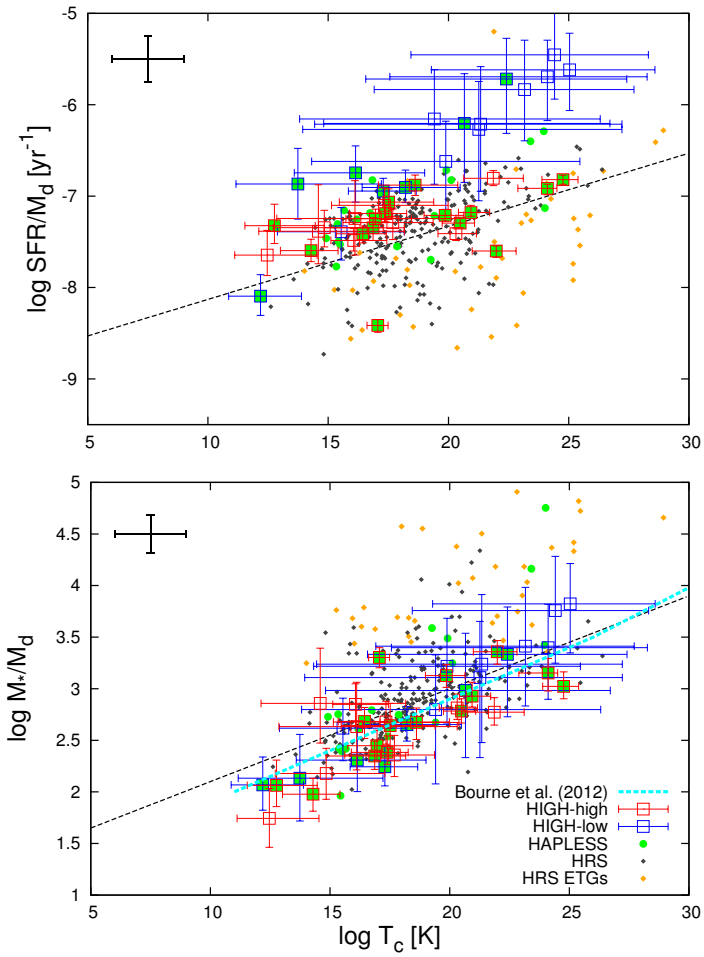

Figure 4.12: Strong correlations of both SFR/M_d (*top*) and M_*/M_d (*bottom*) with cold dust temperature T_c indicate that both the young and old stellar populations are important contributors to the heating of the diffuse cold dust component (C15). The best fitting trend line is shown in dashed black.

are important contributors to the heating of the diffuse cold dust component. Since stellar mass (or L_K) and SFR are correlated themselves for star forming galaxies, it is possible that one of these relations is an indirect result of the other. In Figure 4.12, we find our HIGH-high sample lies on the same relation as C15 found for HAPLESS and HRS. For HIGH-low, we find cold dust temperatures that are consistent with the relation with M_*/M_d, yet colder than expected from their SFR/M_d. The latter offset is not surprising as we will see in the next section that the FUV obscuration for HIGH-low is very small.

Figure 4.13 provides us with a graphical way to better understand the contributions from the old and young stellar populations to the total and cold dust heating. We have plotted M_*/M_d against SFR/M_d and colour-coded the data by cold dust temperature and f_μ respectively (again

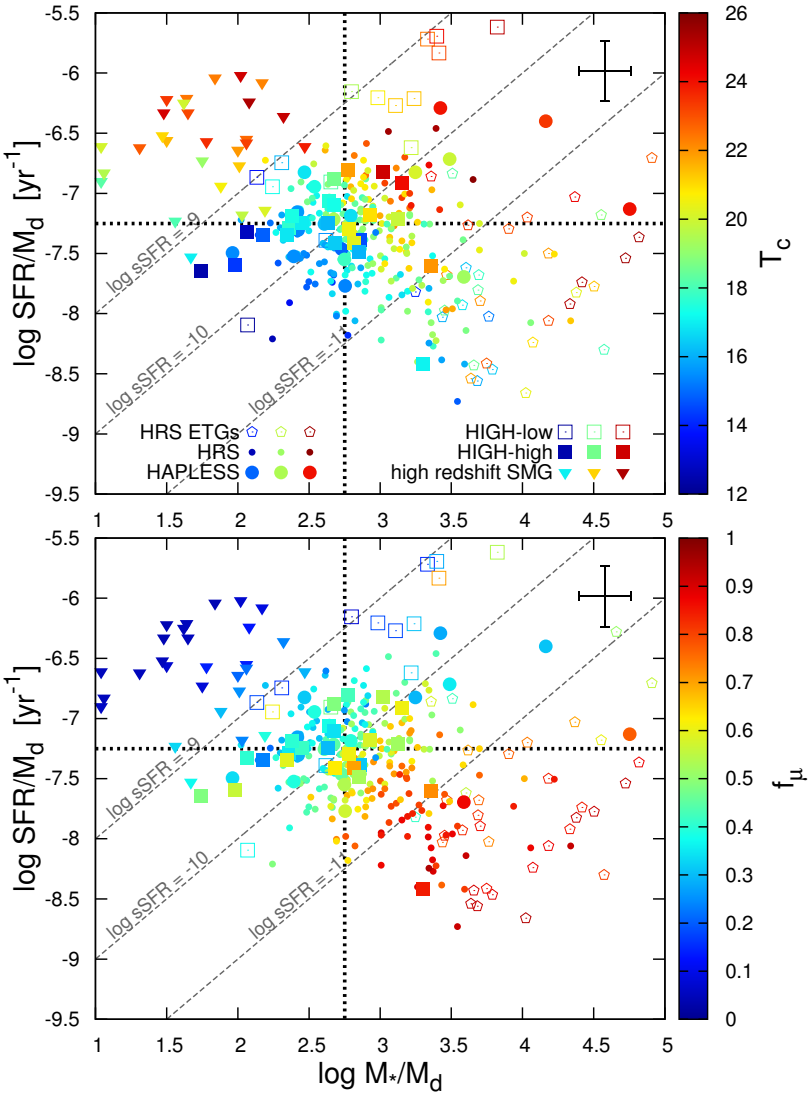

Figure 4.13: SFR/M_d against M_*/M_d, colour-coded by cold dust temperature T_c (*top*) and the fractional contribution of diffuse dust to the total dust luminosity, f_μ (*bottom*) in order to study the sources of dust heating. These plots have been divided in 4 'heating' quadrants to highlight the differences. Lines of constant SSFR are shown in dashed gray.

including the SMGs from Rowlands et al., 2014a). Even discounting the SMGs[19], which generally lie off the main sequence of star formation, we find only a very weak correlation between SFR and M$_*$ *after normalising by dust mass*. There is a clear trend towards higher temperatures as one goes to higher M_*/M_d or SFR/M_d. For a fixed M_*/M_d, we find the spread in temperatures largely follows the differences in SFR/M_d and the same when fixing SFR/M_d and varying M_*/M_d. This explains why ETGs have warm T_c, as despite having low SFR their

[19]Including the SMGs leads to an even weaker correlation.

M_*/M_d are the highest, and so their old stellar radiation fields are intense enough to heat the diffuse dust to warmer temperatures. At $SFR/M_d > 10^{-6.5}\mathrm{yr}^{-1}$, there no longer seems to be any dependence of T_c on M_*/M_d, probably because the dust heating is completely dominated by the young stellar population for these galaxies and the old stellar population has little effect. For galaxies with $SFR/M_d < 10^{-6.5}\mathrm{yr}^{-1}$, both the young and old stellar populations heat the cold dust component, with some dominated by one and some by the other.

Figure 4.13 (bottom) shows that the direction of increasing f_μ (also direction of increasing SSFR) is nearly orthogonal to the direction of increasing T_c. This means that the cold dust temperature is more or less independent of the fraction of the total dust luminosity originating in the diffuse ISM (i.e. T_c is not affected by the SSFR). However the fraction of the dust luminosity originating from heating by old stars is inversely proportional to SSFR (Boquien et al., 2016). We can compare the dust heating in the 4 quadrants of Figure 4.13 to illustrate the differences in dust heating:

I The top-left quadrant is populated mainly by SMG from (Rowlands et al., 2014b). These galaxies are extremely actively forming stars. This causes f_μ to be very small and most of the dust luminosity originates in the birth clouds where the dust has been heated by young stars. On top of that the cold dust temperature is high in spite of the low M_*/M_d, because the cold dust is also heated by the young stellar population. The young stellar population dominates the dust heating completely for these sources.

II Galaxies in the top-right quadrant are dust-poor and moderately actively forming stars (HIGH-low sample), which results in intermediate f_μ (i.e. dust luminosity from both birth clouds and diffuse ISM). Due to both high M_*/M_d and SFR/M_d the cold dust is heated by both young and old stars and reaches high temperatures. Here, the young stellar population significantly heats all components and there likely is a considerable contribution from the old stars to the heating of the cold dust.

III Galaxies in the bottom-left quadrant have similar SSFR and f_μ compared to the top-right quadrant. In contrast, the cold dust temperatures are much smaller due to small M_*/M_d and SFR/M_d. These galaxies are typically blue dust-rich sources with very cold dust temperatures (BADGRS). Again both the young and old stellar contributions play a role in the cold dust heating.

IV The galaxies in the bottom-right quadrant are more quiescently forming stars and have high f_μ. The majority of the dust luminosity will originate in the diffuse dust and the cold dust component. This quadrant includes the ETGs in the HRS. We find moderately high cold dust temperatures due to high M_*/M_d and in spite of low SFR/M_d, thus the

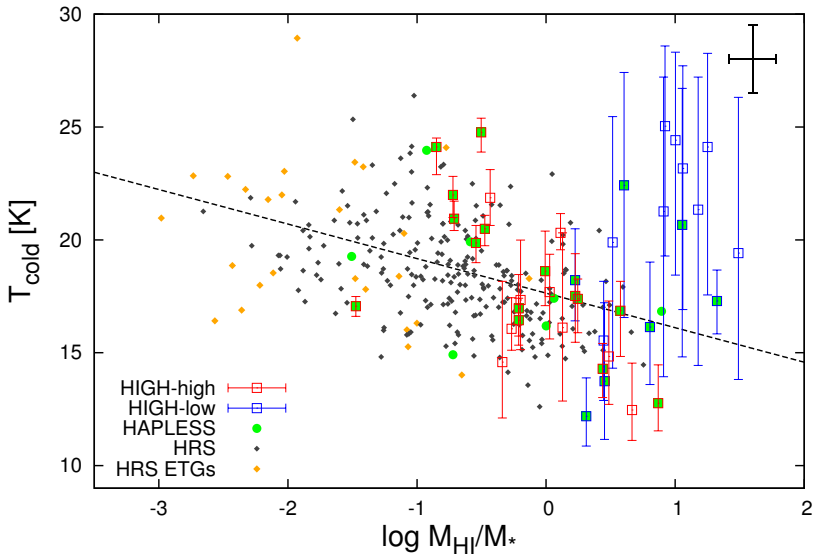

Figure 4.14: $T_{\rm cold}$ against $M_{\rm HI}/M_*$; anti-correlation for HIGH-high, HRS and HAPLESS (trend line shown in dashed black). HIGH-low sources have significantly higher temperatures than predicted from other samples.

cold dust is mainly heated by the old stellar populations. These galaxies have the highest contribution from the old stellar population as they both have a high fraction of the dust luminosity originating from cold dust and a large fraction of that cold dust being heated by the old stellar population.

To study how the cold dust temperatures of galaxies depend on their evolutionary stage, we have also plotted T_c against $M_{\rm HI}/M_*$ in Figure 4.14. We can try to predict how T_c will change based on the evolution of M_*/M_d and SFR/M_d. We have previously found that SFR/M_d remains relatively constant and M_d/M_* first increases for the very immature gas-rich sources and then decreases as galaxies go through the later stages of their evolution. Combining this trend of M_d/M_* with the correlation between T_c and M_*/M_d, we would expect to find galaxies starting out with high temperatures, which would then drop in the early stages of the evolution and then start rising again as M_d/M_* drops. The correlation of T_c with SFR/M_d will introduce extra scatter without adding any trends to the correlation. This is consistent with Figure 4.14. For HIGH-high, HAPLESS and the HRS (i.e. the more evolved sources), we find a weak, yet significant, anti-correlation ($r = -0.42$) for the diffuse cold dust temperature with $M_{\rm HI}/M_*$. Compared to the best fitting trend to these samples, our HIGH-low sample is clearly offset to higher temperatures. C15 and Bourne et al. (2012) also found a positive correlation of T_c with M_*. For this relation our HIGH-high sample is again consistent with HAPLESS and HRS trend from C15 and HIGH-low has significantly higher temperatures.

4.6 Obscuration

4.6.1 IRX as a measure for the UV attenuation by dust

To study and quantify the UV obscuration of galaxies, common approaches are to use the total infrared-to-FUV luminosity ratio ($IRX \equiv L_{\rm dust}/L_{FUV}$) and the UV slope β. Here, it is assumed that the UV regime of the SED can be described by a power law, $F_\lambda \propto \lambda^\beta$. Both quantities have been shown to be correlated in star forming galaxies (e.g. Meurer et al., 1999; Mao et al., 2012; Boquien et al., 2012; Casey et al., 2014), because part of the UV luminosity emitted by galaxies is absorbed and re-radiated by the dust in the far-IR. Figure 4.15 shows our IRX-β relation where β is estimated here in the standard way (Kong et al., 2004) from the *GALEX* UV fluxes as:

$$\beta = \frac{\log(F_{NUV}/F_{FUV})}{\log(\lambda_{NUV}/\lambda_{FUV})} - 2 \tag{4.2}$$

The outliers towards high β are all relatively quiescent galaxies (SSFR $< 10^{-10.5}\,{\rm yr}^{-1}$). The ageing of stellar populations is a primary cause of the variation in intrinsic UV colors of galaxies and therefore dominates the scatter in the IRX-β plane (Mao et al., 2012; Boquien et al., 2012) and causes quiescent sources to move off the main relation towards high β. The IRX-β relation of Casey et al. (2014) for local ($z < 0.085$) star-forming galaxies spans the characteristic range of galaxy environments in the local volume, with $L_{\rm bol} \sim 10^{(8-12.5)}\,L_\odot$ and $SFR \simeq 0.01 - 100\,M_\odot\,{\rm yr}^{-1}$, and matches the combined trend for the HAPLESS, HRS and HIGH starforming galaxies. The relation for Boquien et al. (2012) is based on sub-kpc regions within HRS galaxies and includes quiescent regions. It thus has a strong component from stellar ageing as well as obscuration.

For IRX to be a direct measure of the UV attenuation, it is assumed that all the dust luminosity is due to dust heating by the high energy radiation (UV) originating from short lived stars. In Section 4.5 however, we found that the old stellar population also plays an important role in heating the diffuse dust (also found by Bendo et al., 2010; Bendo et al., 2012a; Groves et al., 2012; C15; Boquien et al., 2016). As galaxies move through their evolution, they will have an increasing ratio of old stars to young stars, and consequently an increasing fraction of their dust luminosity will be powered by photons originating from the old stars. Changes in IRX are thus driven by both changes in the UV attenuation and the fraction of the dust luminosity heated by photons originating from the young and old stars respectively. The MAGPHYS SED-fitting code can be used to estimate the dust attenuation in the FUV (A_{FUV}) by comparing the attenuated and unattenuated model FUV fluxes as each template is fitted to the galaxy. Earlier studies have determined an empirical relation between IRX and the dust attenuation in the FUV, which was found to be dependent on SSFR (Kong et al., 2004; Burgarella et al., 2005; Cortese

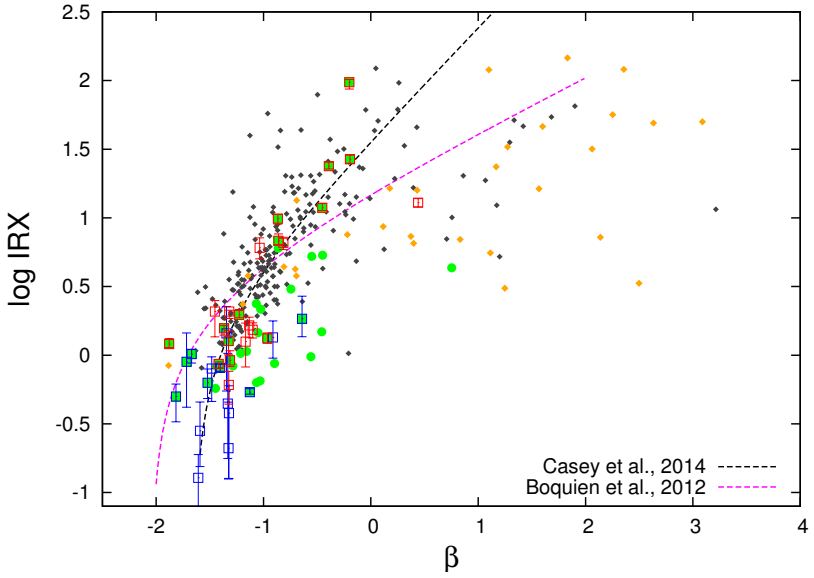

Figure 4.15: $IRX = L_d/L_{FUV}$ versus the UV slope β. The trend for the combined samples is best matched by the relation of Casey et al. (2014). There are outliers toward high β due to ageing effects (Mao et al., 2012). In quiescent sources, IRX is also affected by the contribution of the old stars to the dust luminosity.

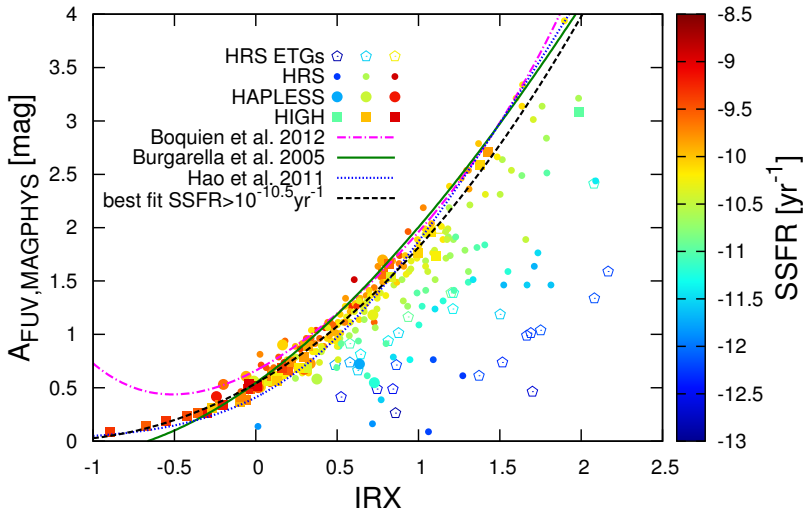

Figure 4.16: Relation between the extinction in the FUV band as determined by MAGPHYS ($A_{FUV,MAGPHYS}$) and $IRX = L_d/L_{FUV}$ for HIGH and HRS. There is decent agreement between the literature relations and our observations for sources with SSFR$> 10^{-10.5}\,\mathrm{yr}^{-1}$. The more quiescent sources are outliers since IRX is biased due to old stellar heating (see text).

et al., 2008; Hao et al., 2011; Boquien et al., 2012; 2013; Viaene et al., 2016). In Figure 4.16, we compare some of the most popular of these relations to the MAGPHYS-produced A_{FUV} and IRX for the sources in our sample. For sources with SSFR $> 10^{-10.5}\,\mathrm{yr}^{-1}$, there is good agreement between MAGPHYS derived and literature relations. We have derived the best fit third-order polynomial to our actively starforming galaxies (SSFR $> 10^{-10.5}\mathrm{yr}^{-1}$):

$$A_{FUV} = -0.022\,IRX^3 + 0.379\,IRX^2 + 0.871\,IRX + 0.542 \tag{4.3}$$

The more quiescent sources are outliers as their dust luminosity is dominated by dust heated by old stars or other dust heating agent (bottom-right quadrant in Figure 4.13). The dependence of the A_{FUV} vs IRX relation on SSFR thus stems from an increasing contribution of dust heated by old stars to the total dust luminosity as we move to more quiescent sources. If we were to use IRX to estimate the UV extinction in quiescent sources using one of the benchmark relations, we would overestimate $\mathrm{A_{FUV}}$ by 1-2 magnitudes. This can in part be mediated by calibrating an A_{FUV} vs IRX relation for different ranges of the SSFR or its observational proxy NUV-r, as done by Viaene et al. (2016) for HRS late type galaxies. However the contribution of the heating by old stars will be different on a source by source basis, which is why Viaene et al. (2016) have large scatter in their A_{FUV} vs IRX at low SSFR. IRX can only reliably be used to estimate the UV attenuation by dust for sources with SSFR $> 10^{-10.5}\,\mathrm{yr}^{-1}$.

4.6.2 Obscuration as a function of galaxy properties

To study how the UV obscuration depends on other galaxy properties we have plotted the MAGPHYS A_{FUV} parameter against M_{HI}/M_*, Σ_* and dust mass in Figure 4.17. In the left panel we find an anti-correlation ($r = -0.54$) for A_{FUV} with M_{HI}/M_*. As galaxies move through their evolution, from gas-rich to gas-poor (right to left on this plot) the obscuration initially increases. This makes sense as dust is continuously produced and mixed with the ISM. Note that all galaxies with $\log M_{\mathrm{HI}}/M_* > 0.5$ approach $A_{FUV} = 0$, which corresponds to the limit of no obscuration[20]. From Figure 4.7 this corresponds to $\log M_d/M_{\mathrm{HI}} < -3$. The sources with the highest obscuration have the highest cold dust temperatures and are on average slightly more inclined than the less obscured galaxies at the same M_{HI}/M_*. In the latest stages of evolution, the obscuration decreases again as most of the dust mass is consumed due to astration (Figure 4.8) or removed.

The large scatter in A_{FUV} at lower HI-to-stellar mass ratios is at least partly due to differences in the intrinsic stellar and dust geometries and inclinations of these galaxies. Attenuation

[20]This is not a selection effect as these sources are HI-selected and have dust measurements from a blank field submm survey.

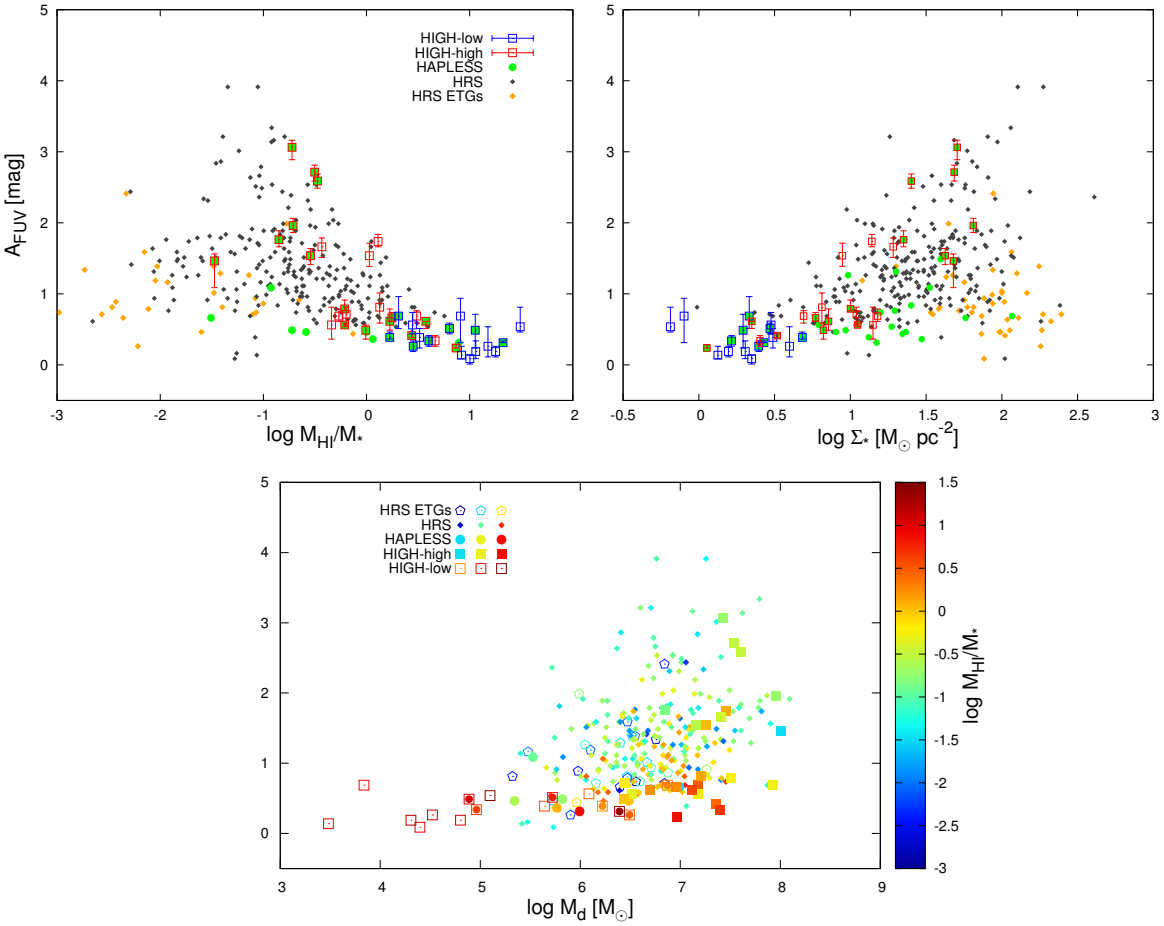

Figure 4.17: The variation of FUV attenuation A_{FUV} with galaxy parameters. *Top-left:* The obscuration increases as one moves from high to low HI-to-stellar mass ratio (i.e. from less to more evolved sources). *Top-right:* Relationship between A_{FUV} and stellar mass surface density Σ_*. *Bottom:* For low dust masses ($M_d < 10^5 M_\odot$) there is little to no obscuration. We find a positive correlation between the obscuration and the dust mass above this value for the HAPLESS and HIGH samples. The outliers towards high obscuration at moderate dust masses are evolved sources in HRS ($\log M_{\rm HI}/M_* < -0.6$). For all three plots there is a large amount of scatter that correspond to a wide range of obscuration for a given M_d (likely due to different dust and stellar geometries).

strongly depends on how much of the dust is mixed into the diffuse ISM as opposed to being distributed in a more clumpy geometry, and on other geometric differences like scale heights and scale lengths of the stellar and dust disks (Baes & Dejonghe, 2001; Bianchi, 2008; Popescu et al., 2011; Holwerda et al., 2012). Investigating whether or not the star-dust geometry is the main factor that drives this scatter is a difficult task. One potential way to do that is by including realistic recipes for dust attenuation in hydrodynamical models of galaxy evolution, and comparing the attenuation properties of simulated mock galaxies to observed data. As both cosmological hydrodynamical simulations (e.g. Vogelsberger et al., 2014; Schaye et al.,

2015) and 3D dust radiative transfer techniques (Steinacker et al., 2013) have reached a level of maturity, this combination has recently become possible (e.g. Camps et al., 2016; Trayford et al., *in prep.*). Such an investigation is beyond the scope of this thesis, but is an interesting subject for future work.

Grootes et al. (2013) found a relationship between the optical depth and stellar mass surface density Σ_* of nearby spiral galaxies. We find a similar relationship ($r = 0.53$) when we plot A_{FUV} against Σ_* in Figure 4.17 (top-right). The increased stellar mass potential associated with higher Σ_* creates instabilities in the cold ISM, which lead to the formation of a thin dust disk (Dalcanton et al., 2004). This changes the relative geometries of dust and stars which provides a possible explanation for the changes in obscuration.

The attenuation by dust is expected to depend on the total column of dust along a photon's trajectory. We show how A_{FUV} varies with the total dust mass[21], colour-coded by HI-to-stellar mass ratio, in the right panel of Figure 4.17. We find a positive correlation ($r = 0.38$) but the relationship is not a simple power law and there is a lot of scatter. At $M_d < 10^{5.5}\,M_\odot$ the obscuration tends to zero, while at higher dust masses, there is a large range in obscuration and again this is likely due to different stellar and dust geometries or different extinction laws. In summary, we find no clear and simple link between UV obscuration and global galaxy properties.

4.7 Conclusions

We have studied the interplay of dust, gas and star formation for combined samples made up of local HI-, dust- and stellar mass selected galaxies. The combined samples cover a wide range of gas fractions (proxy for the evolutionary state of a galaxy; here we define gas fraction as $f_g = 1.32\,M_{\rm HI}/(1.32\,M_{\rm HI} + M_*)$). Our main results are:

- We have identified a sub-sample of HI-selected sources (HIGH-low) with very high gas fractions ($f_g > 80\%$) and low stellar masses ($M_* < 10^9 M_\odot$). These probe the earliest stages of evolution, and have a much smaller dust content than expected from extrapolating published scaling relations for more evolved sources.

- For galaxies in the earliest stages of evolution ($f_g > 80\%$), dust is not a good tracer of the HI content. The dust content relative to stellar mass first rises steeply with decreasing gas fraction, reaches a peak at a gas fraction of $\sim 75\%$ (which for local galaxies is equivalent to a stellar mass of $\sim 10^{8.5}\,{\rm M}_\odot$), and then decreases together with gas fraction.

[21] Plotting A_{FUV} against the dust surface density (which could be argued to be a better tracer of the dust mass along a photon's path), does not change the results in any way.

- The galaxies with the highest gas fractions are the most actively star forming galaxies relative to their stellar masses (SSFR) and relative to their H_2 content (using dust as a proxy for H_2).
- We find a trend of decreasing HI depletion time with decreasing gas fraction, such that the most gas-rich galaxies have the longest τ_{H1}, opposite to the trend found for molecular gas depletion timescale. We interpret this as being due to the increasing efficiency with which HI can be converted to H_2 as galaxies increase in stellar mass surface density with decreasing gas fraction.
- Our data support other observations in the literature that the key driver of the scatter in the 'main sequence of star forming galaxies' is the gas content, such that more gas-rich galaxies have higher SFR at the same stellar mass.
- We confirm literature results that both old and young stellar populations play an important role in heating the diffuse dust component, and either can be the dominant contributor in individual systems. The SSFR determines which one dominates.
- The FUV obscuration of galaxies shows no clear and simple link with global galaxy properties. Galaxies start out barely obscured and increase in obscuration as they evolve until the dust mass decreases significantly in the latest stages of evolution.

The derived scaling relations for the combined samples in this chapter span a wider range in gas fraction than previous relations in the literature, yet admittedly have somewhat complex selection biases. Since the sample size of the stellar mass selected sample (HRS) is 8 times larger than the HI- and dust-selected samples, the scaling relations are therefore heavily weighted towards this sample. This especially affects the scaling relations with stellar mass, which show significant offsets between the differently selected samples. However using the combined sample including the high gas fraction sources, we show that the most robust scaling relations for gas and dust are those linked to NUV-r (SSFR) and gas fraction. These are tight relations which do not depend on sample selection or environment and are thus not affected by the complex selection criteria of the combined sample.

Part II

Chemical Evolution

Chapter 5

Metallicities

5.1 Introduction

There is a wealth of information contained within the optical spectrum emitted by a galaxy. Next to the stellar continuum, there are emission and absorption lines in the spectra, originating from various elements. The absorption lines are mainly caused by atoms or molecules in a star's atmosphere that absorb photons at specific wavelengths. The emission lines are due to various elements in gaseous nebulae (HII regions being ionised or excited to a higher energy level and then re-radiating as they return to the ground state. Young massive stars are often still embedded in the gas they formed from and are thus an important source of the high energy/ionising radiation in the HII regions. By studying the emission lines originating from these HII regions, one can obtain information on the conditions of the gas, such as the temperature, density and the abundances of the heavier elements or 'metals'. This chemical composition of the ISM changes as galaxies evolve as a result of the ongoing star formation. As galaxies evolve, they convert gas into stars, which in turn produce heavy elements in their cores via nucleosynthesis. When these stars end their lives, they enrich the ISM with metals. Massive stars lose metals initially through stellar winds, then explode as supernovae, while low-intermediate mass stars expel metals in their stellar winds and in planetary nebula after the Asymptotic Giant Branch (AGB) stage. This causes a continuous build-up of metals as galaxies evolve, though metals can be lost in outflows of material. Metallicity also affects other processes like dust grain growth, star formation, stellar evolution, etc. Tracking the chemical composition of galaxies thus provides crucial insights into the processes governing galaxy evolution. Accurate metallicity measurements are necessary to reliably constrain the current models of chemical evolution.

One of the first spectroscopic surveys of galaxies (Kennicutt, 1992), focussed on the characterisation of the spectroscopic properties of 90 nearby galaxies along the Hubble sequence.

Since then, many much larger surveys have studied how metallicity scales with galaxy properties. York et al. (2000) provided optical spectroscopy for a large number of SDSS galaxies. This dataset has been instrumental in determining metallicity scaling relations (e.g. the stellar mass - metallicity relation from Tremonti et al., 2004). GAMA also has extensive optical spectroscopy for the many sources in its footprint. Next to providing redshifts, this spectroscopy is used to determine metallicities (e.g. Lara-López et al., 2013), which are in turn combined with the large amount of ancillary information available for each GAMA object. We will use the SDSS and GAMA spectroscopy to determine metallicities for the HIGH and HAPLESS sample. For the HRS sample, integrated spectroscopy is presented in Boselli et al. (2013) and can be readily used to determine the metallicities of the HRS sources (Hughes et al., 2013). Here our aim is not to provide metallicity scaling relations, as these have been determined in the literature using much larger samples. Instead we will use metallicities as a tool to constrain chemical evolution models in Chapter 6, in order to better understand the enigmatic population of galaxies within our sample.

In this chapter we derive metallicities for the sources in the HIGH sample. Metallicities for HAPLESS are determined in exactly the same way and are given at the end of the chapter without further details. The chapter is structured as follows. In the next section, the method for measuring the emission line fluxes is detailed. In Section 5.3, these fluxes are then used to determine the metallicity for several strong line calibrations and the results are compared. Next, Section 5.4 shows how the metallicity scales with other galaxy properties. Finally, Section 5.5 presents the conclusions of this work. Throughout this work, the oxygen abundance is adopted as a tracer of the overall gas phase metallicity and the two terms are used interchangeably. Instead of writing $12+\log(O/H)$ in full, we use the symbol $(O/H)^* \equiv 12+\log(O/H)$ for brevity throughout this chapter.

5.2 Optical spectroscopy

5.2.1 Observed spectra

There is no uniform distribution of metals throughout a galaxy. In order to determine a galaxy's average metallicity, one thus needs to measure the emission lines over the whole galaxy. This can either be done with a spectrometer with a field of view large enough to encompass the whole galaxy (integrated spectroscopy), or with integral field units, which provide spatially resolved spectroscopy. For the HRS sample, integrated spectroscopy is presented in Boselli

et al. (2013). Unfortunately we do not have integrated spectroscopy available for the HIGH sample[1].

The best alternative is to use SDSS (York et al., 2000; Thomas et al., 2013) and GAMA (Hopkins et al., 2013) fibre spectroscopy. These fibres have an aperture of $3''$ and $2''$ for SDSS and GAMA respectively, and thus do not cover the whole galaxy. They do, however, provide us with information that can be used to determine the metallicity at a given (or several) locations in the galaxy, which can then be used to get a first-order approximation of the average metallicity of the galaxy. As discussed in Chapter 2, more than half of our HIGH sources have multiple shredded matches within the same galaxy. The associated spectra (v17 GAMA spectra) have been used to determine the redshift, and can now be used to gain metallicity information. We identify a total of 115 spectra associated with our 40 HIGH galaxies, which can be combined to give the average metallicities for our sources.

The emission lines that are necessary for the analysis in the rest of this chapter, by order of wavelength, are [OII] $\lambda\lambda 3727, 3729$, H$\beta$ $\lambda 4861$, [OIII] $\lambda 4958$, [OIII] $\lambda 5007$, [NII] $\lambda 6584$, $H\alpha$ $\lambda 6563$, [SII] $\lambda 6717$ and [SII] $\lambda 6731$. Note that [OII] $\lambda 3727$ and [OII] $\lambda 3729$ are blended because of the spectral resolution.

5.2.2 Determination of the emission line fluxes

The observed spectra include multiple components such as the stellar continuum, emission lines and absorption lines. In order to get reliable emission line fluxes, these components need to be disentangled. To obtain emission line fluxes for HIGH, we therefore use catalogues with emission lines fluxes extracted using specialised algorithms. The Gas AND Absorption Line Fitting algorithm (GANDALF; Sarzi et al., 2006) is a simultaneous emission and absorption line fitting algorithm designed to separate the relative contribution of the stellar continuum and of nebular emission lines in the spectra of galaxies. Stellar absorption corrected fluxes from GANDALF are available for 101 out of the 115 spectra in our sample (Lara-López, *priv comm.*).

We have three other methods available, which we can use to test and supplement the GANDALF results. The first is the GAMA GaussFitComplexv05 catalogue (hereafter GFC; Gordon et al., 2016), complemented by the GaussFitSimple catalogue (for lines not included in GFC). Although GAMA is an extragalactic survey of thousands of galaxies, we have used GAMA fibre spectra that, for our nearby galaxies, correspond to HII regions within the galaxies. The resulting lines have been corrected for stellar absorption. Second we use the Fit3D tool (Sánchez et al., 2006) to obtain stellar absorption corrected fluxes (Lara-López, *priv comm.*).

[1]Though 18 of the HIGH sources are part of the SAMI Galaxy Survey (Bryant et al., 2015) which will provide spatially resolved spectroscopy based on integral field units in the near future.

Our final method uses the GAMA SpecLinesv4 catalogue and is much less complex as it does not simultaniously fit absorption and emmision lines to the observed spectra (it does remove the stellar continuum). Therefor we account for the absorption lines by applying a constant stellar absorption correction:

$$f(H\alpha)_{\rm corr} = f(H\alpha)_{\rm obs} \times (1 + \frac{2.8}{EW({\rm H}\alpha)_{\rm obs}}) \tag{5.1}$$

$$f({\rm H}\beta)_{\rm corr} = f({\rm H}\beta)_{\rm obs} \times (1 + \frac{4.4}{{\rm EW}({\rm H}\beta)_{\rm obs}}) \tag{5.2}$$

Where the correction to the equivalent width of the Hα and Hβ lines are given by 2.8 ± 0.4 and 4.4 ± 0.6 respectively (Moustakas & Kennicutt, 2006). This simple method is unsurprisingly less accurate than the other 3 methods.

When available, we compare the GANDALF and GFC results, as we have found these two catalogues to be the most reliable. For most of the 115 spectra, there is good agreement (when comparing line ratios), and we use the GANDALF results throughout this work. There are however also 20 spectra for which the two methods lead to different results. In these cases, we inspect the spectra manually and compare to the Fit3D and SpecLinesv4 results. We find that GFC usually gives the better results in the discrepant cases, yet both GANDALF and GFC seem to fail in some cases. There are also 14 spectra for which GANDALF crashed (likely due to a too low SNR in some parts of the spectra). For these we cannot compare to GANDALF and GFC is used instead. We compare these GFC results to Fit3D and SpecLinesv4 results in order to reject poorly fitted spectra, but identify no deviant results above the scatter (which is larger than the scatter between GANDALF and GFC).

5.2.3 Dust attenuation correction

The emission lines of galaxies are attenuated both by internal and external dust. To account for this, the emission line intensities are corrected using the Balmer decrement given by:

$$C({\rm H}\beta) = \frac{1}{{\rm f}(\lambda)} \left[\log\left(\frac{{\rm H}\alpha}{{\rm H}\beta}\right)_{\rm theor} - \log\left(\frac{{\rm H}\alpha}{{\rm H}\beta}\right)_{\rm obs} \right] \tag{5.3}$$

where $f(\lambda)$ is the reddening curve normalized to Hβ using the Cardelli et al. (1989) law with

$$R_v = A_v / E(B-V) = 3.1 \tag{5.4}$$

, $f(\lambda) = -0.297$ for Hα; $\log\left(\frac{\mathrm{H}\alpha}{\mathrm{H}\beta}\right)_{\mathrm{obs}}$ is the observed ratio between Hα and Hβ, and $\log\left(\frac{\mathrm{H}\alpha}{\mathrm{H}\beta}\right)_{\mathrm{theor}}$ the theoretically expected ratio which depends on the electron density and the gas temperature. We assume case B recombination with a density of 100 cm^{-3} and a temperature of 10^4 K, which gives the predicted ratio (unaffected by reddening or absorption) of $\frac{\mathrm{H}\alpha}{\mathrm{H}\beta} = 2.86$ (Osterbrock, 1989). The $C(\mathrm{H}\beta)$ and corrected emission line fluxes for the available HIGH and HAPLESS sources are listed in Table 5.2 and 5.3.

The corrected emission line fluxes are then given by:

$$F_{\mathrm{corr}}(\lambda) = F_{\mathrm{obs}}(\lambda)\ 10^{0.4\ A_\lambda} \tag{5.5}$$

with

$$\begin{aligned} A_{[OII]\ \lambda\lambda 3727,3729} &= 3.303\ C(\mathrm{H}\beta) \\ A_{\mathrm{H}\beta} &= 2.500\ C(\mathrm{H}\beta) \\ A_{[OIII]\ \lambda 5007} &= 2.403\ C(\mathrm{H}\beta) \\ A_{[OIII]\ \lambda 4959} &= 2.433\ C(\mathrm{H}\beta) \\ A_{\mathrm{H}\alpha} &= 1.758\ C(\mathrm{H}\beta) \\ A_{[NII]\ \lambda 6584} &= 1.747\ C(\mathrm{H}\beta) \\ A_{[SII]\ \lambda 6717} &= 1.703\ C(\mathrm{H}\beta) \\ A_{[SII]\ \lambda 6731} &= 1.698\ C(\mathrm{H}\beta) \end{aligned} \tag{5.6}$$

as calculated from the prescription given by Cardelli et al. (1989).

For consistency with the HIGH and HAPLESS samples, we correct the HRS spectroscopy results presented in Boselli et al. (2013) for dust attenuation using the reddening function $f(\lambda)$ of Cardelli et al. (1989). This is not the same reddening correction as the Fitzpatrick & Massa (2007) obscuration curve that is suggested in Boselli et al. (2013) and used in Hughes et al. (2013). However, this does not cause significant changes to the HRS metallicities used throughout the rest of this work.

5.2.4 BPT diagram

In order to have a reliable metallicity estimation, the brightness ratios of certain emission lines should only depend on the abundances of the heavy elements (see next section). However, AGNs also affect the emission line ratios of galaxies and can thus offset our metallicity determination. In order to make our metallicity study more reliable, we aim to discard sources that are affected

by AGN. Fortunately the optical spectroscopy of galaxies can also be used to classify their nuclear activity. AGN have a very energetic radiation field, which causes high intensities of collisionally excited lines (e.g. [OIII] λ5007, [NII] λ6584) relative to recombination lines (such as Hα and Hβ). In normal star forming galaxies, the emission lines are powered by massive stars, and there is an upper limit on the intensity ratios of collisionally excited lines relative to recombination lines. If the ratio between these emission lines exceeds a certain ratio, we know that the emission lines are not powered by massive stars and that an AGN must be present. Since contributions to the emission lines by AGN will bias our metallicity estimates, we discard all spectra classified as AGN.

The diagnostic we use to classify our spectra is the BPT diagram (Baldwin et al., 1981). The diagram we use is consistent with Lara-López et al. (2013). By comparing the ratios of [OIII] λ5007 / Hβ and [NII] λ6584 / Hα, we are able to derive the relative contributions from recombination and collisional excitation emission sources and use predetermined limits to classify the spectra. We show our classification diagram in Figure 5.1. Object that falls below the empirical star forming - AGN line from Kauffmann et al. (2003) and the theoretical starburst line from Kewley et al. (2001) are classified as star forming galaxies (AGNs lie above the line from Kewley et al. (2001) and composite regions between both lines). The equations used are:

- $y = (0.61/(x-0.05)) + 1.3$ for Kauffmann et al. (2003) (5.7)
- $y = (0.61/(x-0.47)) + 1.19$ for Kewley et al. (2001) (5.8)

where $y = \log$ ([OIII] λ5007 / Hβ) and $x = \log$ ([NII] λ6584 / Hα).

Throughout the rest of this work we will only use spectra that can reliably be identified as star forming. For low SNR spectra, we cannot be sure that they are contaminated by AGN. Therefore we also discard sources for which the 1 sigma errors cross the line from Kauffmann et al. (2003). 20 out of 115 spectra are discarded since they cannot be confidently identified as star forming.

5.3 Measuring metallicity

In this section we derive metallicities for the sources in our sample. We compare different metallicity calibrations and discuss which ones are useful to analyse the chemical evolution of our samples. We consider three classes of calibrations: (1) direct, (2) empirical strong-line and (3) theoretical strong-line calibrations. Numerous studies have pointed out (Kewley & Ellison, 2008, hereafter 'KE08', and references therein) that large (0.1-0.7 dex) systematic discrepancies exist among the different empirical and theoretical calibrations. We refer to KE08

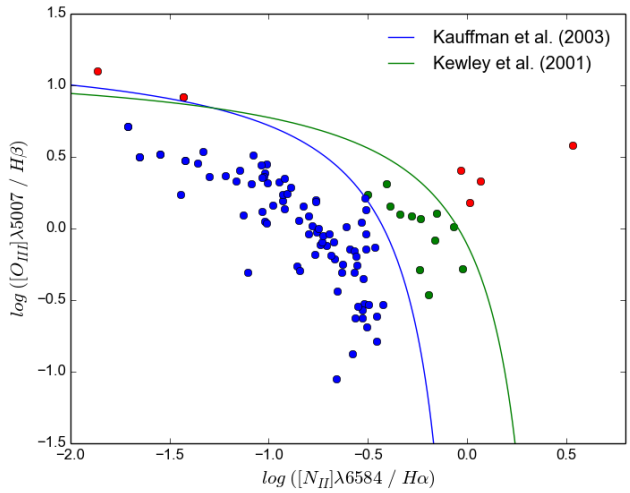

Figure 5.1: BPT (Baldwin et al., 1981) diagram used to classify our spectra of HIGH galaxies based on classification curves (Kewley et al., 2001; Kauffmann et al., 2003). Starforming HII regions are shown in blue, composite regions in green and HII regions containing an AGN in red. We only compute metallicities using star forming HII regions.

for an extensive comparison between 10 calibrations and relations to transform the results of one calibration as well as possible into another calibration. We apply some of these calibrations to our samples and add some other calibrations that have since become available.

The direct method for determining metallicity uses the ratio of the [OIII] λ4363 line to a lower excitation line such as [OIII] λ5007 to provide an estimate of the electron temperature of the gas, assuming a classical HII region model. This electron temperature can then be used to convert line ratios of oxygen and hydrogen lines into a metallicity, after correcting for the emissivity of those lines at that electron temperature. Unfortunately the [OIII] λ4363 line is very weak, especially in metal-rich environments (e.g. Pettini & Pagel, 2004). Even for the metal-poor sources in our sample, the SNR of the [OIII] λ4363 line is too low to reliably estimate the metallicity. Therefore we cannot create a set of direct metallicities for the sources in our sample, and thus we do not use this calibration. It is worth noting temperature fluctuations or gradients within high-metallicity HII regions may cause electron temperature metallicities to be underestimated by as much as 0.4 dex (Stasińska, 2005; Bresolin et al., 2006). This can potentially bias empirical calibrations that use direct metallicities to calibrate their relation.

5.3.1 Empirical calibrations

By using stronger lines than the weak [OIII] λ4363 line, one does not need as high SNR spectra to still obtain reliable metallicities. Many ratios of strong lines have been found to correlate with metallicity. The most commonly used calibrations are based on optical line ratios like N2, O3N2, or R_{23}. We provide details on different strong line calibrations in the following sections. The relations between these ratios and metallicities have been empirically calibrated by obtaining very high SNR spectra for which direct metallicities can be measured, and determining how these scale with the observed line ratios.

5.3.1.1 PP04 - N2 and O3N2

Pettini & Pagel (2004, hereafter PP04) derived two empirical calibrations based on strong line ratios. By using lines that are very close in wavelength, they derived calibrations that do not require a very accurate reddening correction. This is very useful when obtaining a reddening estimate is difficult or impossible, as is often the case for high-redshift galaxies. Even for low-redshift galaxies, the reddening estimates are not always very accurate, yet the PP04 calibrations are robust against reddening uncertainties.

The N2 $\equiv \log([\mathrm{N_{II}}]\ \lambda6584/\mathrm{H}\alpha)$ line ratio was first proposed as a calibrator by Storchi-Bergmann et al. (1994) and uses two lines that are very close in wavelength. PP04 determined their first calibration by fitting a third order polynomial to the relationship between N2 and the direct metallicities for a sample of 137 HII regions. Six high-metallicity HII regions did not have observed direct metallicities and had their metallicity determined using detailed photoionization models. Since only 6 out of the 137 HII regions were computed using theoretical models, we refer to the PP04 method as an empirical calibration. The derived relation is given by:

$$(O/H)^* = 9.37 + 2.03\,\mathrm{N2} + 1.26\,\mathrm{N2}^2 + 0.32\,\mathrm{N2}^3 \tag{5.9}$$

where $(O/H)^* = 12 + \log(O/H)$, this relation is only valid for $-2.5 < \mathrm{N2} < -0.3$ ($7.1 < (O/H)^* < 8.7$). We refer to this calibration as 'N2'.

PP04 also derived a second relation between metallicity and the O3N2 line ratio. Here O3N2 is defined as:

$$\mathrm{O3N2} \equiv \log\left[([\mathrm{O_{III}}]\ \lambda5007/\mathrm{H}\beta)/([\mathrm{N_{II}}]\ \lambda6584/\mathrm{H}\alpha)\right] \tag{5.10}$$

The O3N2 ratio was first investigated by Alloin et al. (1979), yet only more recently has it been used as a calibrator. Comparing the N2 calibrator with the [OIII]/Hβ ratio can improve

the accuracy of the metallicity estimation. The derived relation from PP04 is:

$$(O/H)^* = 8.73 - 0.32\,\mathrm{O3N2} \tag{5.11}$$

and is only valid for O3N2 < 2. O3N2 metallicities are thus only valid for $(O/H)^* > 8.09$ and therefore limited for describing some of the low-metallicity sources in our sample. We will refer to this calibration as 'O3N2'.

5.3.1.2 PT05

The calibration by Pilyugin & Thuan (2005, hereafter PT05) uses the R_{23} line ratio. The relation between R_{23} and direct metallicities was first calibrated by Pagel et al. (1979), and has since been used and recalibrated by many authors to determine metallicities using strong lines. The R_{23} line ratio is given by:

$$R_{23} \equiv \frac{[O_{II}]\ \lambda\lambda 3727,3729\ +\ [O_{III}]\ \lambda 5007\ +\ [O_{III}]\ \lambda 4959}{\mathrm{H}\beta} \tag{5.12}$$

PT05 include an additional parameter P that corrects for the effect of ionisation and is defined as:

$$P \equiv \frac{([O_{III}]\ \lambda 5007\ +\ [O_{III}]\ \lambda 4959)/\mathrm{H}\beta}{R_{23}} \tag{5.13}$$

$$\equiv \frac{[O_{III}]\ \lambda 5007\ +\ [O_{III}]\ \lambda 4959}{[O_{II}]\ \lambda\lambda 3727,3729\ +\ [O_{III}]\ \lambda 5007\ +\ [O_{III}]\ \lambda 4959} \tag{5.14}$$

They perform fits to the relationship between R_{23} and direct metallicities based on these parameters using spectra of more than 700 HII regions. The resulting relationship has two branches. The upper branch is valid for $(O/H)^* > 8.25$:

$$(O/H)^*_{\mathrm{upper}} = \frac{R_{23} + 726.1 + 842.2P + 337.5P^2}{85.96 + 82.76P + 43.98P^2 + 1.793R_{23}} \tag{5.15}$$

The lower branch is valid for $(O/H)^* < 8.0$:

$$(O/H)^*_{\mathrm{lower}} = \frac{R_{23} + 106.4 + 106.8P - 3.4P^2}{17.72 + 6.6P + 6.95P^2 - 0.302R_{23}} \tag{5.16}$$

We use the $[N_{II}]\ \lambda 6548$ / $[O_{II}]\ \lambda\lambda 3727,3729$ ratio to discriminate between the upper (log([NII]/[OII]) > -1.2) and lower (log([NII]/[OII]) < -1.2) branches. PT05 estimate that the uncertainty on their calibration is 0.1 dex.

5.3.1.3 P10

Pilyugin et al. (2010, hereafter P10) suggest improved empirical calibrations for the determination of electron temperatures and oxygen and nitrogen abundances in HII regions from the strong emission lines of oxygen, nitrogen, and sulfur. Their relations are calibrated using spectra of 118 HII regions with measured direct metallicities. P10 give calibration relations for three classes of HII regions: cool, warm, and hot ones. The following line ratios are used:

$$R_2 \equiv ([O_{II}]\ \lambda\lambda 3727,3729)\ /\ \mathrm{H}\beta \tag{5.17}$$

$$N_2 \equiv ([N_{II}]\ \lambda 6548 + [N_{II}]\ \lambda 6584)\ /\ \mathrm{H}\beta \tag{5.18}$$

$$S_2 \equiv ([S_{II}]\ \lambda 6717 + [S_{II}]\ \lambda 6731)\ /\ \mathrm{H}\beta \tag{5.19}$$

$$R_3 \equiv ([O_{III}]\ \lambda 4959\ +\ [O_{III}]\ \lambda 5007)\ /\ \mathrm{H}\beta \tag{5.20}$$

and the ionisation parameter P, defined as for PT05.

The HII regions are divided into the three classes based on the N_2 and S_2 ratios. HII regions with $\log N_2 > -0.1$ are labelled cool and we use following relation:

$$(O/H)^*_{\mathrm{cool}} = 8.28 + 0.657P - 0.399 \log\ R_3 - 0.061\ \log(N_2/R_2) + 0.005\ \log(S_2/R_2) \tag{5.21}$$

Warm HII regions have $\log N_2 < -0.1$ and $\log(N_2/S_2) > -0.25$ and are calibrated as:

$$(O/H)^*_{\mathrm{warm}} = 8.82 - 0.733P + 0.454 \log\ R_3 + 0.710\ \log(N_2/R_2) - 0.337\ \log(S_2/R_2) \tag{5.22}$$

Finally the relation for the hot HII regions ($\log N_2 < -0.1$ and $\log(N_2/S_2) < -0.25$) is given by:

$$(O/H)^*_{\mathrm{hot}} = 8.77 - 1.855P + 1.517 \log\ R_3 + 0.304\ \log(N_2/R_2) + 0.328\ \log(S_2/R_2) \tag{5.23}$$

The given relations are the ONS oxygen abundance calibrations from PG16. ON calibrations (i.e. without sulfur emission lines) and relations for nitrogen abundances and electron temperatures are available as well.

5.3.1.4 PG16 - R and S

One of the most recent empirical calibrations are the two relations of Pilyugin & Grebel (2016, hereafter PG16). They use a sample of 313 HII regions to calibrate relationships using two sets of line ratios. The R_2, R_3 and N_2 ratios are used for the 'R calibration', and the S_2, R_3 and N_2

ratios for the 'S calibration'. Here the line ratios are defined as for P10. For both calibrations, the HII regions are divided into 2 classes. The upper branch consists of high-metallicity objects, identified using $\log\ N_2 > -0.6$. The low-metallicity sources on the lower branch have $\log\ N_2 < -0.6$. The ranges of the applicability of the calibration relations for the upper and lower branches overlap in the boundary region within a range of $-0.7 < \log\ N_2 < -0.45$, which is an important improvement on previous work.

The derived relations for the R and S calibrations are:

$$(O/H)^*_{\rm R,upper} = 8.589 + 0.022\ \log(R_3/R_2) + 0.399\ \log\ N_2 + (-0.137 + 0.164\ \log(R_3/R_2) + 0.589\ \log\ N_2) \times \log\ R_2 \quad (5.24)$$

$$(O/H)^*_{\rm R,lower} = 7.932 + 0.944\ \log(R_3/R_2) + 0.695\ \log\ N_2 + (0.970 - 0.291\ \log(R_3/R_2) - 0.019\ \log\ N_2) \times \log\ R_2 \quad (5.25)$$

$$(O/H)^*_{\rm S,upper} = 8.424 + 0.030\ \log(R_3/S_2) + 0.751\ \log\ N_2 + (-0.349 + 0.182\ \log(R_3/S_2) + 0.508\ \log\ N_2) \times \log\ S_2 \quad (5.26)$$

$$(O/H)^*_{\rm S,lower} = 8.072 + 0.789\ \log(R_3/S_2) + 0.726\ \log\ N_2 + (1.069 - 0.170\ \log(R_3/S_2) + 0.022\ \log\ N_2) \times \log\ S_2 \quad (5.27)$$

PG16 also provide calibration relations for nitrogen abundances and the N/O ratio.

5.3.2 Theoretical calibrations

We also include two theoretical calibrations. These provide calibrations between emission lines and metallicity based on a combination of detailed stellar population synthesis and photoionization models. Theoretical calibrations are typically higher than empirical calibrations using the same emission lines. This discrepancy is unsolved and remains an active area of research.

5.3.2.1 KD02

Kewley & Dopita (2002, hereafter KD02) derived a theoretical calibration between metallicity and the $[N_{II}]\ \lambda 6548\ /\ [O_{II}]\ \lambda\lambda 3727,3729$ ratio. Since these lines are far apart in wavelength, a correct dust correction is particularly important. The derived relation from KD02:

$$(O/H)^* = \log(a + bR + cR^2) + 8.93 \quad (5.28)$$

where a=1.54020, b=1.26602, c=0.167977, and R=log($[N_{II}]\ \lambda 6548\ /\ [O_{II}]\ \lambda\lambda 3727,3729$)

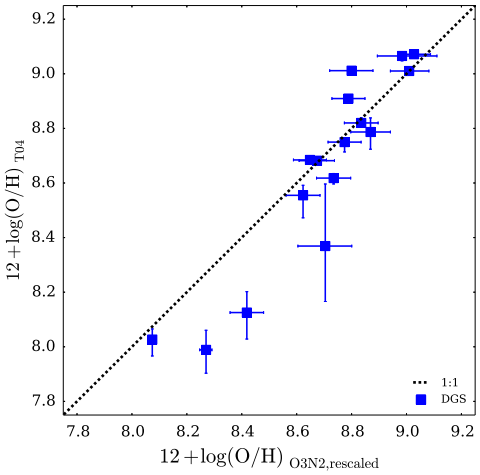

Figure 5.2: Measured T04 metallicities for SF SDSS HII regions compared to KE08/T04 metallicities as estimated from rescaling from the O3N2 (using KE08 relation). The dashed line gives the 1:1 relation.

5.3.2.2 T04

Another important theoretical calibration is the one by Tremonti et al. (2004, hereafter T04). T04 estimated the metallicity for each galaxy based on bayesian methods using theoretical model fits to the strong emission lines [OII], Hβ, [OIII], [NII], Hα, and [SII]. They computed metallicities for all star forming galaxies in SDSS. By fitting to all the lines at once, they are able to better constrain the metallicity. Unfortunately we do not have access to the T04 method to apply to our own sample. However, KE08 derived relations between different calibrations including T04 using 27,730 star-forming galaxies from the SDSS Data Release 4. They find a strong correlation between the T04, and O3N2 and N2 calibrations. Their derived relations for O3N2 and N2 are:

$$(O/H)^*_{\rm T04} = -738.1 + 259.0\,(O/H)^*_{\rm O3N2} - 30.06\,(O/H)^{*\,2}_{\rm O3N2} + 1.168\,(O/H)^{*\,3}_{\rm O3N2} \quad (5.29)$$

$$(O/H)^*_{\rm T04} = -1661.9 + 585.2\,(O/H)^*_{\rm N2} - 68.47\,(O/H)^{*\,2}_{\rm N2} + 2.677\,(O/H)^{*\,3}_{\rm N2} \quad (5.30)$$

These relations are only valid in the range $8.05 < (O/H)^* < 8.9$ for both O3N2 and N2.

Throughout the rest of this work, we include T04 metallicity estimates based on O3N2 metallicities in the allowed range using the relation from KE08, and refer to this calibration as KE08/T04. This is done to illustrate where the metallicity scaling relations for theoretical calibrations lie compared to empirical calibrations. We do not aim to derive exact scaling relations for the KE08/T04 calibration, yet it is important to show this part of the calibration discrepancy when studying metallicity.

Since we have some HII regions available that have spectra from SDSS, we can compare the rescaled O3N2 metallicities to measured T04 metallicities provided by the MPA–JHU group database[2] for all SDSS SF galaxies. We show this comparison in Figure 5.2 for the 17 SDSS HII regions in our sample. Overall, there is decent agreement between the two estimations, albeit with some outliers. We have checked that the extracted fluxes for the outlying sources were robust using GANDALF and GFC. Potential inconsistencies exist as the provided measured T04 metallicities have used different reddening and stellar absorption corrections.

Instead of the K08 O3N2 recalibration, we have also estimated T04 metallicities using a linear relation with O3N2, which was derived for all SDSS-SF galaxies with $z < 0.1$ (Lara-López, *priv comm.*). This resulted in only very minor changes.

5.3.3 Bootstrap uncertainties

To determine the uncertainties on the metallicity for each HII region for which we have a spectrum, we perform a bootstrapping analysis. For each used line, we generate 1000 new emission line fluxes assuming a normal distribution with the the measured flux as mean and the measured error as the standard deviation of the distribution. For each source we thus get 1000 sets of emission lines. For each calibration we then calculate metallicities using these new emission lines and appropriately discard the invalid ones (not possible to take the log of a negative flux). We then determine the bootstrap uncertainties for each source and each calibration as half the difference between the 16^{th} and 84^{th} percentiles of the distribution of the 1000 metallicities from randomly generated fluxes. For the highest SNR spectra, this results in an error as small as 0.0025 dex. For the lowest SNR spectra that could still reliably be identified as starforming, the resulting uncertainty is 0.66 dex.

5.3.4 Comparing calibrations

There exist systematic discrepancies between the different theoretical and empirical metallicity calibrations in the literature (KE08, Liang et al., 2006; Yin et al., 2007; Moustakas et al., 2010; Hughes et al., 2013). To derive metallicities from the emission line spectra we compared the results from different empirical and theoretical methods in order to understand any systematic differences that may result from our methods. Empirical calibrations are only valid for the same range of excitation and metallicity as the HII regions that were used to build the calibration. Since they are determined assuming an electron temperature, these methods may systematically underestimate the true metallicity if there are temperature inhomogeneities in a galaxy. This is thought to be more severe in metal-rich HII regions because the higher efficiency of metal-line

[2] http://www.mpa-garching.mpg.de/SDSS/

cooling leads to stronger temperature gradients (Garnett, 1992; Stasińska, 2005; Moustakas et al., 2010). On the other hand, theoretical calibrations require inputs including stellar population synthesis and photoionization models, which include some simplifying assumptions; often the theoretical metallicities are higher than those found with the empirical calibrations.

Therefore it is not a priori clear what is the most reliable method for measuring the metallicity. Here we compare some of the most used calibrations, listed in Table 5.1, and determine which calibrations we will use for studying the chemical evolution of our galaxies. KE08 has performed an extensive comparison between 10 calibrations, and we refer to this work for a detailed analysis. To compare the calibrations, we follow KE08 in plotting the stellar mass - metallicity, hereafter *M-Z*, relation and fitting a third order polynomial to each calibration. The *M-Z* relation provides important constraints on galaxy evolution models as it is possible to predict the *M-Z* relation using semianalytical models of galaxy formation and hydrodynamical simulations (De Lucia et al., 2004; de Rossi et al., 2007; Schaye et al., 2015). However, this is not an easy task and the current generation of simulations only achieve a moderately good match with observations.

Figure 5.3 shows the best fits for each calibration to the *M-Z* relations for the star forming HII regions in HIGH sources. For the stellar mass we here use the total stellar mass of the galaxy, as derived in Chapter 3. Since we are only interested in the variation due to different calibrations, we have excluded all HII regions that have a bootstrap uncertainty larger than 0.1 dex in any calibration. This way we include as many of the HII regions as possible, yet still discard sources that are too offset due to low SNR. We see similar discrepancies between the different calibrations as in KE08 and other work. In Table 5.1, we find some relatively strong correlations (Spearman correlation coefficient $r > 0.8$) as well as weaker calibrations (as low as $r = 0.39$ for P05). The same conclusion is reached when we look at the rms deviation from the best fit polynomial. Some calibrations clearly have a stronger *M-Z* relation than others. Since we do expect a correlation between stellar mass and metallicity from theoretical work (e.g Schaye et al., 2015), the calibrations that show less scatter in the *M-Z* relation are preferential over the weaker relations like P05 and KD02.

Even if we ignore the relations that show a lot of scatter, there is still large deviation between the different calibrations. There is thus an inherent uncertainty in the metallicity of galaxies. As a result of this discussion, for the remainder of this work, we will compare results and differences in the galaxy samples using three different metallicity techniques: N2, KE08/T04 and PG16S. This allows us to consider the robustness of any results with chosen metallicity calibration. These three calibrations all have high Pearson coefficient, and together sample most of the discrepancy between the calibrations. The O3N2 and N2 methods are robust against reddening uncertainties due to their close wavelength range, though the former is only

Table 5.1: The calibrations that were compared in this work. The *M-Z* relation for these have been fitted by a third order polynomial (see Figure 5.3), the rms deviation from the best fitting trend is given in the third column. The fourth column gives the Spearman rank coefficient of the *M-Z* relation.

calibration	class	rms	r
N2	Empirical	0.10	0.80
O3N2	Empirical	0.11	0.84
P05	Empirical	0.31	0.39
P10	Empirical	0.19	0.76
PG16R	Empirical	0.18	0.70
PG16S	Empirical	0.13	0.86
KD02	Theoretical	0.30	0.56
KE08/T04	Theoretical	0.15	0.82

calibrated for metallicities $(O/H)^* > 8$ (Pettini & Pagel, 2004; Marino et al., 2013). Both the N2 and PG16S methods are valid at lower metallicities ($(O/H)^* = 7.1$) but the N2 method does run into difficulties at the lowest metallicities due to the large scatter observed in N/O ratios (Morales-Luis et al., 2014). Comparison with photoionisation models however show that the N2 method is useful for providing an upper limit to the true metallicity for galaxies when $(O/H)^*_{N2} < 8$. We note again that the KE08/T04 method was rescaled from the O3N2 method using the relation from KE08. However, it is necessary to include this calibration separately in the scaling relations as it is representative for the theoretical scaling relations which result in higher metallicities than empirical calibrations (which might be underestimated due to temperature inhomogeneities, especially in metal-rich sources).

5.3.5 Fibre vs integrated metallicities

Unfortunately there is no integrated spectroscopy available for the HIGH and HAPLESS samples. Instead we derive metallicities for each of the available SDSS and GAMA fibres (using the different calibrations). These give us information on individual HII regions and we only include the ones classified as star forming on the BPT diagram (Section 5.2.4). This results in 95 HII regions between 33 sources. 22 out of the 95 HII regions have emission line fluxes measured with GFC method, and the other 73 using GANDALF. Not all HIGH sources have reliable star forming spectra available, yet many have multiple spectra. In order to get a global estimate of the metallicity for each galaxy, and in order to compare to integrated HRS metallicities, we need to combine the different HII regions for the same source into a single

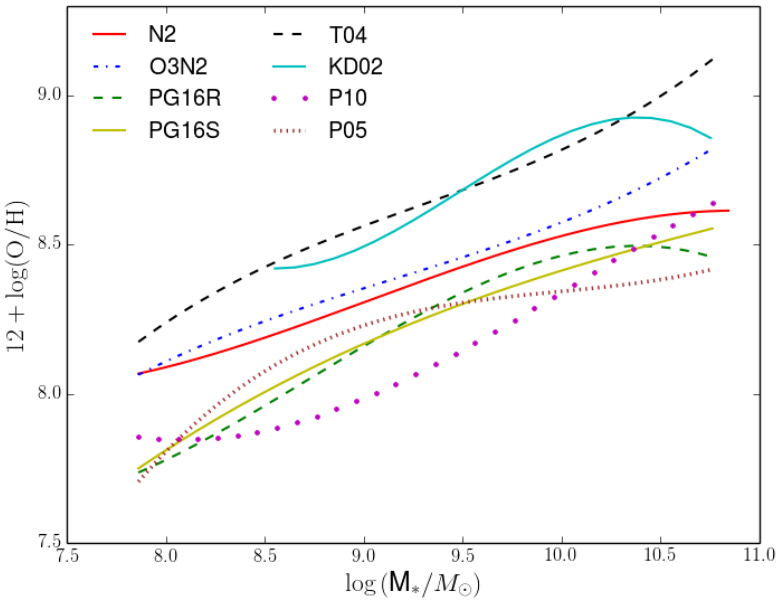

Figure 5.3: Best fit *M-Z* relations to the calibrations in Table 5.1. There are large discrepancies between the different calibrations.

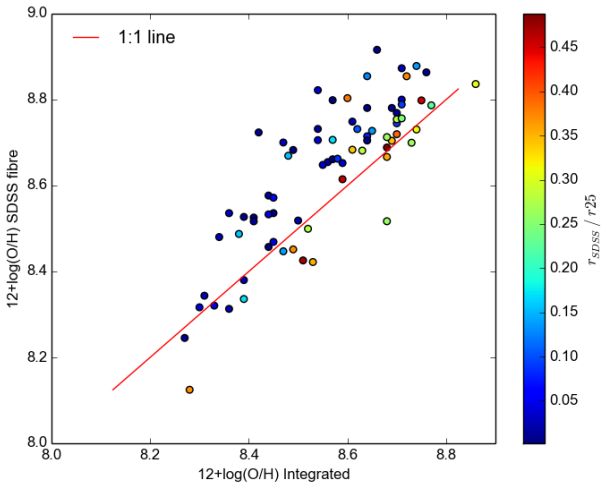

Figure 5.4: N2 metallicities from SDSS fibres compared to integrated metallicities from (Hughes et al., 2013), colour-coded by the distance of each SDSS fibre to the centre, relative to the r_{25} isophotal radius. The red line gives the 1:1 relation, SDSS fibre metallicities are on average 0.07 dex higher than the integrated metallicities.

metallicity estimate. This is done by taking a weighted[3] average of the metallicities in the available fibres for each source. The weight for each is given by the squared inverse of the uncertainty on the metallicity. This uncertainty does not include uncertainties in the calibration and we will address these uncertainties by comparing the different calibrations in the next section. Instead it is a measure for the variation between the measured metallicity and true global metallicity (using the same calibration).

The bootstrap error and the intrinsic variation between individual HII regions are added in quadrature to provide the total uncertainty. Here the intrinsic variation between different HII regions is taken to be 0.06 dex for all fibres. This value for the intrinsic scatter was based on results from Bresolin & Kennicutt (2015). This work looked at metallicities from spectra of 141 HII regions in ten late-type low surface brightness galaxies. The results from this work are expected to be more appropriate for the HIGH and HAPLESS sample than other work (e.g. Sánchez et al., 2014) looking at individual HII regions in higher metallicity sources. The authors find a mean gradient of -0.133 dex r_{25}^{-1} and a mean scatter from the best fit of 0.044 dex for the individual HII regions. To obtain the total intrinsic variation we take the scatter from the best fit and add to this in quadrature the expected variation from uniformly sampling metallicities for different radii between $r = 0$ and $r = r_{25}$ (assuming the mean gradient), which is $0.133/\sqrt{12}$ dex. The total intrinsic variation between individual HII regions will then be given by:

$$\Delta(O/H)^*_{\rm intrinsic} = \left[(0.044 \text{ dex})^2 + (0.133/\sqrt{12} \text{ dex})^2\right]^{0.5} = 0.06 \text{ dex} \tag{5.31}$$

The total uncertainty is then:

$$\Delta(O/H)^*_{\rm tot,i} = \sqrt{(\Delta(O/H)^*_{\rm bootstrap,i})^2 + (\Delta(O/H)^*_{\rm intrinsic})^2} \tag{5.32}$$

$$= \sqrt{(\Delta(O/H)^*_{\rm bootstrap,i})^2 + (0.06)^2} \tag{5.33}$$

The metallicity for each source will then be given by:

$$(O/H)^* = \frac{\sum w_i \times (O/H)^*_i}{\sum w_i} \tag{5.34}$$

[3]By using a weighted average we make sure that the average is not dominated by the most noisy sources, yet at the same time we need to add intrinsic scatter in order to not weight the highest SNR sources too heavily (as these could still be offset from the average due to their position within the galaxy).

where

$$w_i = \frac{1}{(\Delta(O/H)^*_{\mathrm{tot,i}})^2} = \frac{1}{(\Delta(O/H)^*_{\mathrm{bootstrap,i}})^2 + (0.06)^2} \tag{5.35}$$

and the uncertainty for each source as:

$$\Delta(O/H)^* = \frac{\sqrt{\sum w_i \times (\Delta(O/H)^*_{\mathrm{tot,i}})^2}}{\sum w_i} \tag{5.36}$$

We then compare the metallicities for each of the HII regions to the mean for this source. The standard deviation from the mean is 0.077 dex. This includes both the intrinsic scatter and the bootstrap error for all the 95 star forming HII regions. The final metallicity error on the combination of multiple HII regions for the same source will be smaller, depending on the number of combined regions. We have inspected the sources with the largest deviation from the mean manually. The three HII regions that are deviant outside $2\sigma = 0.154$ dex have emission lines consistent between the different methods and are within 3σ. We therefore do not discard them. By comparing the results for the different emission line flux measurement methods, we have effectively removed erroneous line measurements which result in strongly outlying metallicities[4].

As a test of our method, we can apply the same process using SDSS fibre spectroscopy for HRS (instead of HIGH and HAPLESS) and compare to the integrated HRS metallicities from Hughes et al. (2013). There are fewer spectra available per source for HRS than for HIGH and HAPLESS, which overlap with GAMA. Figure 5.4 shows how the (averaged) N2 metallicities using SDSS fibres compare to the integrated N2 metallicity. We find the SDSS fibres have on average slightly higher (by 0.07 dex) metallicities than the integrated values. This is likely due to most of the SDSS fibres being rather central. For most sources, central HII regions have higher metallicities than HII regions at larger radii (Moustakas et al., 2010; Sánchez et al., 2014; Bresolin & Kennicutt, 2015). The colour scale in Figure 5.4 shows the distance of each SDSS fibre to the centre, relative to the r_{25} isophotal radius. Central fibres are indeed found to be more offset than fibres at larger radii. Unfortunately we cannot correct for this in a rigorous way as we do not have enough HII regions to determine the radial profile for each source and use this to correct the integrated metallicity. On average, the HIGH SDSS fibres are slightly less central ($\langle r_{SDSS}/r_{25}\rangle = 0.22$ instead of $\langle r_{SDSS}/r_{25}\rangle = 0.16$ for HRS). HIGH will thus be slightly less affected by this issue, yet there will likely also be an offset for HIGH and the used metallicities throughout the rest of this work should be taken with the caveat that they could be

[4]When the GANDALF results are used without comparison to other methods, there are a few sources that result in strongly deviant metallicities at this stage.

overestimated by about 0.07 dex on average. This offset is much smaller than the uncertainty between the different calibrations and will not affect the conclusions of our work.

5.4 Metallicity scaling relations

In the previous sections we have shown our method of obtaining emission lines and using these to determine the metallicity. For HRS LTGs[5], we have used integrated spectroscopy, whereas for HIGH and HAPLESS[6], fibre spectroscopy is used and combined into one listing per source. In the next chapter we use these metallicities to put constraints on chemical evolution models. In this section we will first briefly show two of the strongest relations between metallicity and galaxy properties for samples selected on their stellar, dust and gas content.

Stellar mass and metallicity are among the most fundamental physical properties of galaxies, and increase monotonically as galaxies evolve (as gas is converted into stars). Understanding the build-up of stellar mass and metallicity with time and in respect to each other is key to understanding the processes that drive chemical evolution. The mass-metallicity (M - Z) relation has been studied by many authors with larger samples of galaxies (e.g. Garnett, 1992; T04; KE08; and references therein) and in hydrodynamical models of galaxy formation (De Lucia et al., 2004; de Rossi et al., 2007; Schaye et al., 2015).

In Figure 5.5, we show the *M-Z* relation for HRS, HAPLESS and HIGH for the N2, KE08/T04 and PG16S calibrations. As expected, there is a positive correlation between M_* and metallicity for each of the samples and each of the calibrations. As we already knew from Figure 5.3, the KE08/T04 calibration results in the highest metallicities for the total sample (with average $\langle(O/H)^*\rangle = 8.73$[7]), followed by N2 ($\langle(O/H)^*\rangle = 8.54$) and then PG16S ($\langle(O/H)^*\rangle = 8.42$). For N2 and KE08/T04, we have also shown the best fit relation to the 27,730 SDSS star-forming galaxies in KE08. We find our results are consistent with this larger sample. For the more recent PG16S calibration, no *M-Z* relations from the literature are available.

Compared to the scaling relations with stellar mass in Chapter 4, we find the offset between samples in metallicity at fixed M_* is smaller relative to the scatter. Here it has to be noted that there could be an offset between integrated and fibre metallicities. It is possible that this difference between HIGH/HAPLESS and HRS has reduced the selection offset between the samples (at fixed M_*, HIGH galaxies have higher gas content and thus potentially lower metallicity than HRS, however HIGH uses fibre rather than integrated spectroscopy which

[5]There is no integrated spectroscopy available for ETGs in HRS.

[6]We use exactly the same method for HAPLESS as the one described for HIGH throughout this chapter.

[7]Note that for the KE08/T04 *M-Z* relation the lowest metallicity sources are not included as they fall outside the allowed range for the conversion from O3N2 and N2.

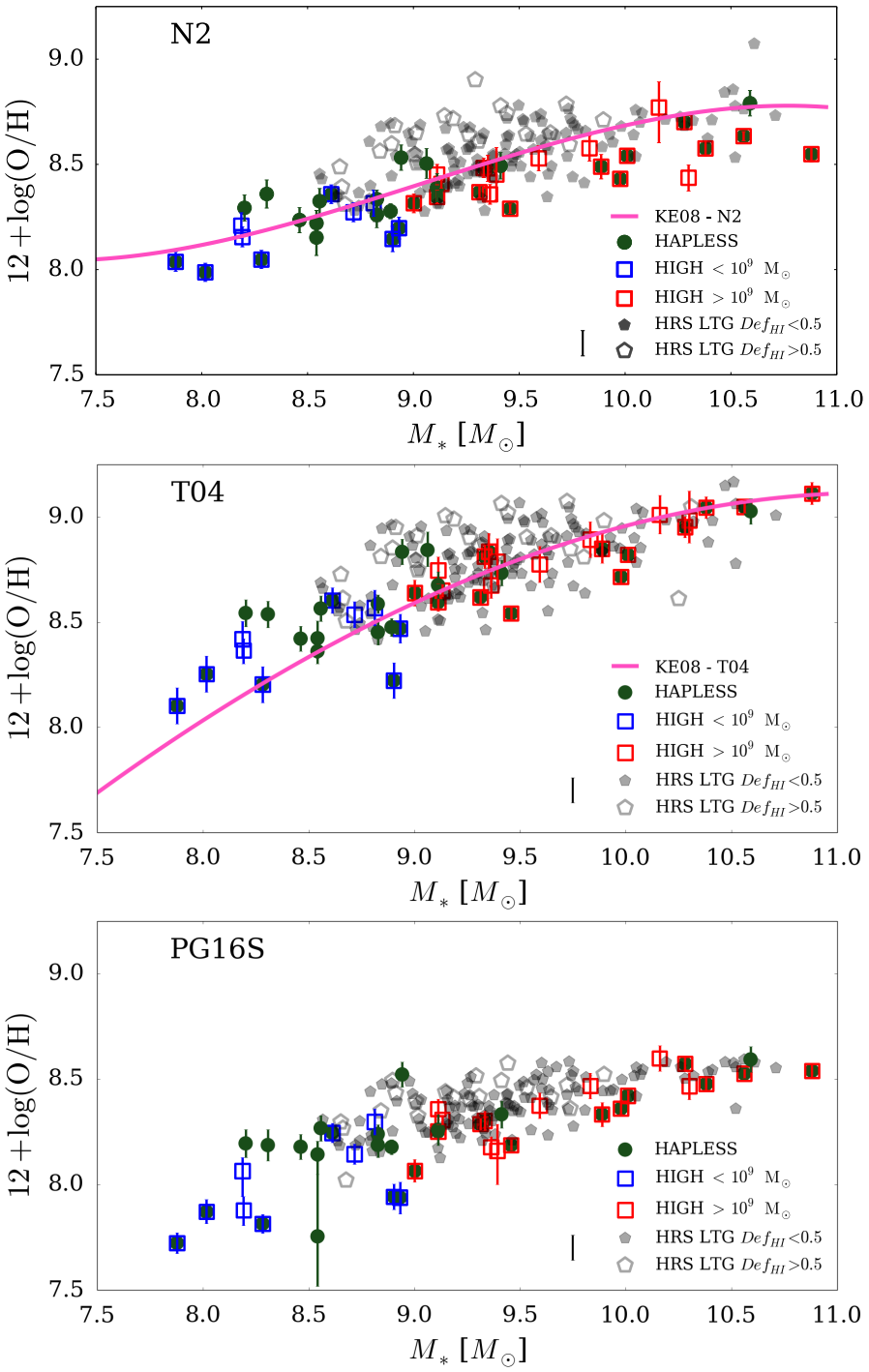

Figure 5.5: *M-Z* relations for the HIGH-low (blue squares), HIGH-high (red squares), HAPLESS (green circles), and HRS (gray pentagons) samples for the three metallicity calibrations used throughout this work. HI deficient sources (open symbols) have slightly higher metallicities at fixed M_*. Relations from KE08 have been shown in magenta for the available calibrations. The typical uncertainty for HRS metallicities is shown in black next to the legend.

could lead to higher metallicities). The SAMI IFU data that will become available in the near future for a sub-sample of our sources will allow us to resolve this issue.

We find that HI deficient ($\mathrm{Def_{H\,I}} > 0.5$, as in Chapter 4 and Cortese et al., 2011) sources have on average slightly higher metallicities than HI normal galaxies at the same M_*. Hughes et al. (2013) have studied the effects of environment on the *M-Z* relation for HRS. They find no offset between cluster and field environments, though they find a similar offset to ours when comparing HI deficient and HI normal galaxies. Ram pressure gas stripping provides a possible interpretation of this as metal-poor gas from the outer regions is stripped and thus the inflow to the central regions is cut off. If a galaxy's metallicity is the result of an equilibrium between the metal-poor inflow and SFR (Finlator & Davé, 2008), then cutting gas inflow would cause an increase in metallicity as the galaxy continues to form stars (Hughes et al., 2013).

To study how the metallicity of galaxies changes as they go through their evolution, we use the same approach as in Chapter 4 and use M_{HI}/M_* as a proxy for how far a galaxy is through its evolution. The correlation between the gas content and metallicity of galaxies is well known from both observations (e.g. Hughes et al., 2013; Ascasibar et al., 2015) and chemical evolution models (Edmunds, 1990; and references therein). Figure 5.6 shows the relation between oxygen abundances and M_{HI}/M_*. Galaxies are found to monotonically increase their metallicity as they evolve. The relation between metallicity and gas fraction will be studied in depth in the next chapter, using chemical evolution models to interpret the build-up of metals as galaxies evolve.

We find no offsets between the differently selected samples. However now the HI deficient galaxies have slightly lower metallicities than other galaxies at the same gas fraction (opposite than for *M-Z* relation). Even though HI deficient galaxies have higher metallicities at a given stellar mass, so much of their gas has been removed/consumed that they end up with much lower M_{HI}/M_* and thus fall below the relation between metallicity and gas fraction for HI normal sources (see also the much lower HI content of HI deficient galaxies in the M_{HI}/M_* vs M_* relation in Chapter 4).

There is an intimate link between metallicity, stellar mass, gas fraction and SFR in galaxies. Lara-López et al. (2013) (see also Lara-López et al., 2010; Mannucci et al., 2010) show that it is possible to form a fundamental plane between stellar mass, metallicity and SFR, that shows a smaller scatter than the *M-Z* relation. Hughes et al. (2013) show that for HRS, there is an even stronger fundamental plane when stellar mass and metallicty are combined with gas fraction. Overall we find that the higher the stellar mass and the lower the gas content (or SFR), the higher the metallicity will be. Higher mass galaxies convert their gas into stars more efficiently, and in this process produce more metals and end up with lower gas content.

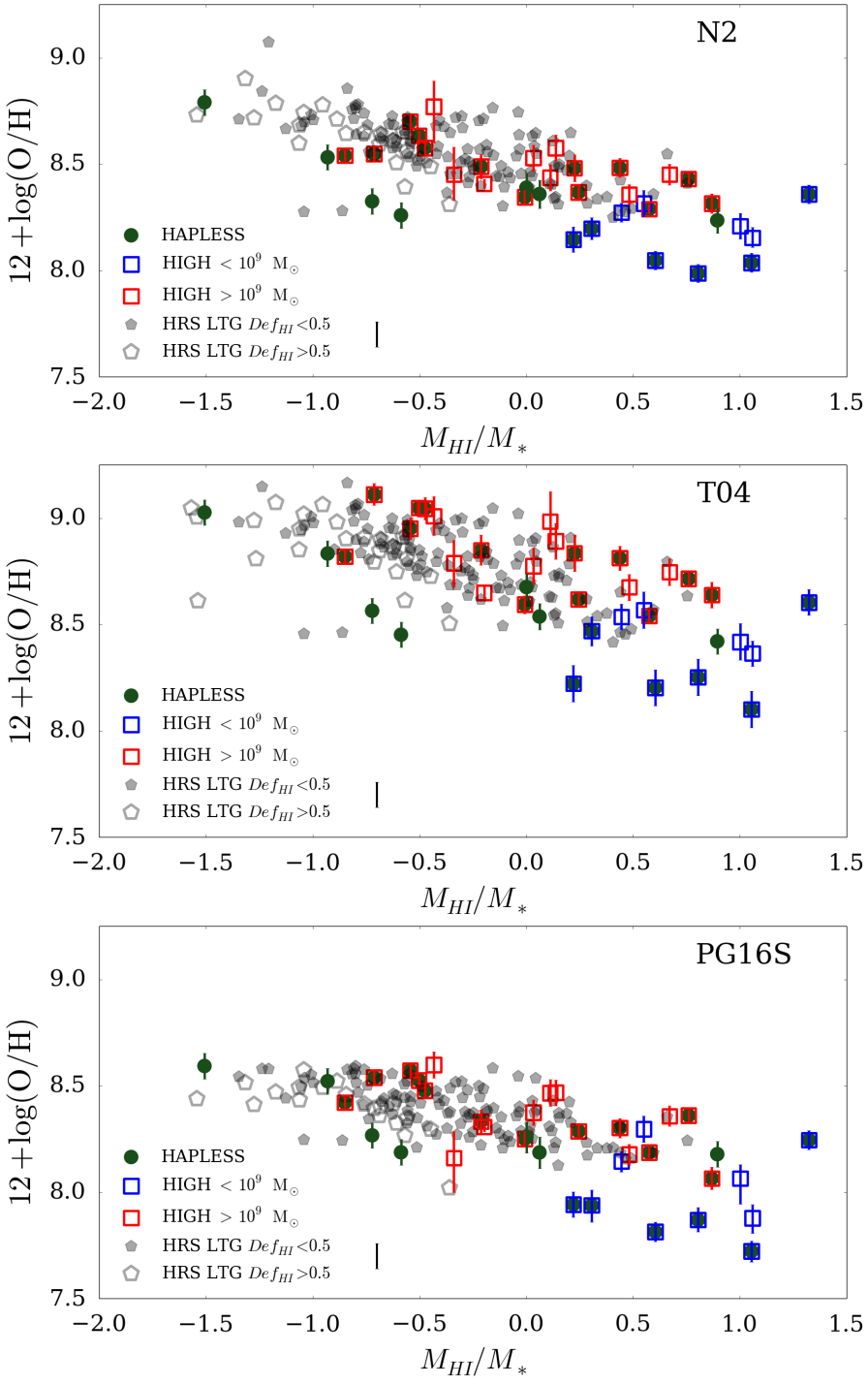

Figure 5.6: Scaling relations between metallicity and $M_{\rm HI}/M_*$ for the HIGH, HAPLESS, and HRS samples for the three metallicity calibrations used throughout this work. Symbols are as in Figure 5.5.

5.5 Conclusions

In this chapter we have derived metallicities for the HIGH sample based on fibre optical spectroscopy. All star forming HII regions associated with HIGH sources are identified and metallicities determined for each of them. These metallicities are combined into a single listing per galaxy. By combining and comparing different flux extraction methods (in particular GANDALF and GFC), we have ensured our extraction method is robust. The stellar absorption corrected flux measurements are corrected for dust attenuation using the Balmer decrement and the Cardelli et al. (1989) dust obscuration curve. Metallicity uncertainties for each individual HII region are determined using a bootstrap method. These are then combined with an intrinsic scatter of 0.06 dex to provide the total uncertainty. Multiple HII regions within the same galaxy are combined using a weighted average.

Eight different calibrations were studied: PP04 N2 and O3N2, PT05, P10, PG16 R and S, KD02, and KE08/T04. There are large discrepancies and systematic offsets between the different calibrations, as also observed by previous studies (e.g. KE08). Theoretical calibrations (KD02, and KE08/T04) result in significantly higher metallicities than empirical calibrations. In order to sample the uncertainty from using different calibrators, we have chosen three calibrations with a strong *M*-*Z* correlation as representative calibrations: N2, KE08/T04, and PG16 S.

We briefly discuss the *M*-*Z* relation and the relation between metallicity and gas richness. We find our *M*-*Z* results are consistent with other work in the literature, which is a good validation of our method.

Table 5.2: HIGH emission lines. The first three columns give the common name, the ID from DV16 (and Chapter 4) and the GAMA cataID respectively. All emission lines have been corrected for reddening using the Balmer decrement $C(\mathrm{H}\beta)$ and the Cardelli et al. (1989) dust obscuration curve. The Origin column specifies whether the stellar absorption corrected fluxes were extracted using GANDALF or the GaussFitComplexv05 (GFC) catalogue.

galaxy	DV16-ID	cataID	$C(\mathrm{H}\beta)$	$I_\lambda/I_{\mathrm{H}\beta}$								Origin
				[OII]	Hβ	[OIII,4959]	[OIII,5007]	Hα	[NII]	[SII,6713]	[SII,6731]	
2MASXJ142...	24	106616	0.53	2.36 ± 0.10	1.00 ± 0.02	0.37 ± 0.01	1.04 ± 0.02	2.86 ± 0.03	0.703 ± 0.010	0.674 ± 0.013	0.539 ± 0.011	GANDALF
FGC1412	16	611445	0.24		1.00 ± 1.27	0.17 ± 2.52	0.49 ± 7.17	2.86 ± 0.40	0.224 ± 1.491	0.154 ± 0.794		GANDALF
FGC1412	16	611446	0.18	2.61 ± 20.76	1.00 ± 1.32	0.37 ± 0.63	1.05 ± 1.80	2.86 ± 0.91	0.476 ± 0.676	0.927 ± 0.587	0.620 ± 0.757	GANDALF
IC1011	25	106717	0.92		1.00 ± 0.05	0.14 ± 0.02	0.41 ± 0.03	2.87 ± 0.68	1.211 ± 0.028	0.458 ± 0.019	0.359 ± 0.017	GFC
NGC4030	12	31521	0.0	0.35 ± 0.15	1.00 ± 0.03	0.05 ± 0.01	0.13 ± 0.03	2.09 ± 0.02	0.554 ± 0.020	0.149 ± 0.017	0.108 ± 0.016	GANDALF
NGC4030	12	31523	0.55	2.55 ± 0.22	1.00 ± 0.03	0.03 ± 0.01	0.09 ± 0.02	2.86 ± 0.05	0.630 ± 0.015	0.281 ± 0.012	0.240 ± 0.009	GANDALF
NGC4030	12	690077	0.0	14.76 ± 2.09	1.00 ± 0.05	0.08 ± 0.02	0.24 ± 0.04	2.31 ± 0.04	0.689 ± 0.031	0.230 ± 0.036	0.159 ± 0.036	GANDALF
NGC4030b	11	584731	0.0	3.94 ± 0.37	1.00 ± 0.04	0.60 ± 0.01	1.73 ± 0.04	2.53 ± 0.03	0.298 ± 0.017	0.265 ± 0.015	0.168 ± 0.015	GANDALF
NGC4202	15	32362	2.57	4.25 ± 25.06	1.00 ± 0.18	0.44 ± 0.16	0.21 ± 0.12	2.88 ± 0.08	0.538 ± 0.027	0.256 ± 0.019	0.164 ± 0.015	GFC
NGC5496	21	496980	0.0	2.20 ± 5.24	1.00 ± 0.42	0.33 ± 0.03	0.89 ± 0.05	1.65 ± 0.05	0.170 ± 0.031	0.378 ± 0.028	0.262 ± 0.022	GFC
NGC5496	21	463393	0.25	2.35 ± 0.30	1.00 ± 0.03	0.48 ± 0.01	1.36 ± 0.03	2.86 ± 0.02	0.342 ± 0.015	0.513 ± 0.016	0.367 ± 0.015	GANDALF
NGC5496	21	463394	1.25	2.46 ± 0.25	1.00 ± 0.04	0.83 ± 0.03	2.30 ± 0.08	2.86 ± 0.07	0.272 ± 0.009	0.265 ± 0.009	0.185 ± 0.007	GANDALF
NGC5496	21	496979	0.91	5.29 ± 0.86	1.00 ± 0.13	0.74 ± 0.08	2.05 ± 0.23	2.86 ± 0.24	0.234 ± 0.022	0.289 ± 0.024	0.209 ± 0.018	GANDALF
NGC5496	21	496981	1.21	10.32 ± 0.71	1.00 ± 0.03	0.81 ± 0.01	2.24 ± 0.02	2.86 ± 0.02	0.344 ± 0.008	0.423 ± 0.008	0.295 ± 0.008	GANDALF
NGC5496	21	496982	0.0	6.06 ± 0.59	1.00 ± 0.04	0.89 ± 0.01	2.54 ± 0.04	2.05 ± 0.02	0.147 ± 0.013	0.273 ± 0.012	0.199 ± 0.013	GANDALF
NGC5496	21	496985	0.35	4.85 ± 0.72	1.00 ± 0.06	0.43 ± 0.02	1.22 ± 0.05	2.86 ± 0.06	0.454 ± 0.032	0.664 ± 0.031	0.462 ± 0.034	GANDALF
NGC5496	21	496986	0.0	11.33 ± 1.72	1.00 ± 0.08	0.46 ± 0.02	1.32 ± 0.06	2.57 ± 0.06	0.238 ± 0.044	0.436 ± 0.041	0.299 ± 0.045	GANDALF
NGC5584	22	693091	0.29	1.38 ± 7.39	1.00 ± 0.05	0.43 ± 0.02	1.26 ± 0.04	2.86 ± 0.04	0.448 ± 0.018	0.532 ± 0.031	0.383 ± 0.023	GFC
NGC5584	22	63349	0.0	187.48 ± 0.84	1.00 ± 0.12	0.18 ± 0.04	0.51 ± 0.12	2.56 ± 0.10	0.365 ± 0.089	0.149 ± 0.124	0.179 ± 0.116	GANDALF
NGC5584	22	63351	0.0	1.91 ± 0.27	1.00 ± 0.09	0.35 ± 0.02	1.00 ± 0.07	2.86 ± 0.17	0.509 ± 0.028	0.448 ± 0.030	0.320 ± 0.022	GANDALF
NGC5584	22	63353	0.86	2.54 ± 0.32	1.00 ± 0.04	0.33 ± 0.01	0.92 ± 0.04	2.86 ± 0.05	0.577 ± 0.014	0.428 ± 0.012	0.300 ± 0.013	GANDALF
NGC5584	22	63354	0.66	2.84 ± 0.70	1.00 ± 0.14	0.31 ± 0.04	0.89 ± 0.12	2.86 ± 0.23	0.535 ± 0.054	0.569 ± 0.059	0.397 ± 0.042	GANDALF
NGC5584	22	693086	0.01	3.23 ± 0.77	1.00 ± 0.18	1.14 ± 0.20	3.25 ± 0.56	2.86 ± 0.43	0.239 ± 0.032	0.173 ± 0.023	0.138 ± 0.018	GANDALF
NGC5584	22	693088	0.27	2.16 ± 0.22	1.00 ± 0.02	0.25 ± 0.01	0.72 ± 0.02	2.86 ± 0.02	0.882 ± 0.013	0.555 ± 0.011	0.445 ± 0.010	GANDALF
NGC5690	29	262444	1.63	4.54 ± 25.79	1.00 ± 0.07	0.08 ± 0.03	0.22 ± 0.05	2.87 ± 0.05	0.984 ± 0.029	0.499 ± 0.037	0.352 ± 0.031	GFC
NGC5690	29	262445	2.13	11.63 ± 25.93	1.00 ± 0.05	0.05 ± 0.02	0.16 ± 0.04	2.87 ± 0.03	0.625 ± 0.010	0.356 ± 0.008	0.251 ± 0.007	GFC
NGC5690	29	716324	0.73	2.00 ± 0.88	1.00 ± 0.07	0.10 ± 0.02	0.28 ± 0.04	2.86 ± 0.07	0.805 ± 0.032	0.542 ± 0.027	0.340 ± 0.023	GANDALF
NGC5691	30	64554	0.4	3.71 ± 0.34	1.00 ± 0.03	0.25 ± 0.01	0.70 ± 0.03	2.86 ± 0.02	0.773 ± 0.015	0.698 ± 0.015	0.488 ± 0.015	GANDALF
NGC5691	30	693423	0.0	6.78 ± 0.25	1.00 ± 0.01	0.39 ± 0.00	1.11 ± 0.01	2.75 ± 0.01	0.804 ± 0.005	0.529 ± 0.005	0.442 ± 0.006	GANDALF
NGC5691	30	693424	0.0	1.67 ± 0.10	1.00 ± 0.02	0.23 ± 0.01	0.64 ± 0.01	2.50 ± 0.02	0.688 ± 0.011	0.510 ± 0.011	0.365 ± 0.010	GANDALF
NGC5691	30	693425	0.75	1.90 ± 0.12	1.00 ± 0.01	0.33 ± 0.00	0.92 ± 0.01	2.86 ± 0.01	0.888 ± 0.006	0.669 ± 0.008	0.527 ± 0.007	GANDALF
NGC5691	30	693426	0.62	3.13 ± 0.16	1.00 ± 0.02	0.29 ± 0.00	0.81 ± 0.01	2.86 ± 0.01	0.611 ± 0.007	0.397 ± 0.007	0.283 ± 0.007	GANDALF
NGC5691	30	756783	0.58		1.00 ± 0.02	0.24 ± 0.00	0.66 ± 0.01	2.86 ± 0.03	0.491 ± 0.008	0.370 ± 0.008	0.248 ± 0.007	GANDALF
NGC5705	32	49167	0.0	2.18 ± 0.46	1.00 ± 0.07	0.25 ± 0.02	0.71 ± 0.07	2.29 ± 0.09	0.590 ± 0.054	0.772 ± 0.059	0.532 ± 0.050	GANDALF
NGC5705	32	49169	0.21	4.11 ± 0.19	1.00 ± 0.03	0.28 ± 0.01	0.81 ± 0.02	2.86 ± 0.07	0.530 ± 0.018	0.567 ± 0.018	0.431 ± 0.015	GANDALF
NGC5705	32	49171	0.0	4.53 ± 1.82	1.00 ± 0.33	0.20 ± 0.05	0.57 ± 0.15	0.98 ± 0.14	0.233 ± 0.134	0.336 ± 0.103	0.211 ± 0.148	GANDALF

Table 5.2: *Continued*

galaxy	DV16-ID	cataID	$C(H\beta)$	$I_\lambda/I_{H\beta}$								Origin
				[OII]	Hβ	[OIII,4959]	[OIII,5007]	Hα	[NII]	[SII,6713]	[SII,6731]	
NGC5713	34	693034	1.38	1.11 ± 9.33	1.00 ± 0.02	0.06 ± 0.01	0.19 ± 0.01	2.87 ± 0.01	1.001 ± 0.007	0.443 ± 0.005	0.328 ± 0.004	GFC
NGC5713	34	64772	1.52	7.49 ± 0.43	1.00 ± 0.02	0.16 ± 0.00	0.45 ± 0.01	2.86 ± 0.04	0.855 ± 0.012	0.386 ± 0.006	0.279 ± 0.006	GANDALF
NGC5713	34	64773	0.53	1.18 ± 0.06	1.00 ± 0.01	0.10 ± 0.00	0.29 ± 0.01	2.86 ± 0.01	0.912 ± 0.005	0.454 ± 0.005	0.334 ± 0.004	GANDALF
NGC5713	34	693033	0.51	2.10 ± 0.11	1.00 ± 0.01	0.11 ± 0.00	0.30 ± 0.01	2.86 ± 0.01	0.871 ± 0.005	0.387 ± 0.004	0.285 ± 0.004	GANDALF
NGC5713	34	693035	0.94		1.00 ± 0.01	0.09 ± 0.00	0.24 ± 0.00	2.86 ± 0.02	0.779 ± 0.006	0.326 ± 0.004	0.227 ± 0.004	GANDALF
NGC5713	34	693036	0.19	1.24 ± 0.07	1.00 ± 0.01	0.06 ± 0.00	0.16 ± 0.01	2.86 ± 0.01	1.001 ± 0.008	0.483 ± 0.007	0.348 ± 0.006	GANDALF
NGC5713	34	693037	0.62	1.29 ± 0.16	1.00 ± 0.02	0.07 ± 0.01	0.21 ± 0.02	2.86 ± 0.02	0.895 ± 0.013	0.452 ± 0.011	0.330 ± 0.010	GANDALF
NGC5713	34	693038	0.63	0.76 ± 0.29	1.00 ± 0.04	0.09 ± 0.01	0.24 ± 0.03	2.86 ± 0.02	1.005 ± 0.017	0.501 ± 0.016	0.359 ± 0.015	GANDALF
NGC5725	33	343415	0.24	5.46 ± 25.00	1.00 ± 0.28	0.31 ± 0.13	0.92 ± 0.21	2.86 ± 0.33	0.550 ± 0.151	0.942 ± 0.161	0.622 ± 0.123	GFC
NGC5725	33	343407	1.02	9.35 ± 69.01	1.00 ± 0.04	0.57 ± 0.02	1.75 ± 0.04	2.87 ± 0.02	0.435 ± 0.012	0.482 ± 0.011	0.339 ± 0.009	GFC
NGC5725	33	343410	0.34	3.74 ± 15.39	1.00 ± 0.14	0.34 ± 0.02	0.96 ± 0.04	2.86 ± 0.05	0.461 ± 0.023	0.539 ± 0.021	0.354 ± 0.016	GFC
NGC5725	33	343414	0.69	3.97 ± 11.92	1.00 ± 0.10	0.44 ± 0.05	1.32 ± 0.09	2.86 ± 0.06	0.491 ± 0.037	0.766 ± 0.070	0.481 ± 0.065	GFC
NGC5725	33	343405	0.0		1.00 ± 0.01	0.55 ± 0.01	1.59 ± 0.02	2.72 ± 0.04	0.471 ± 0.008	0.443 ± 0.009	0.333 ± 0.006	GANDALF
NGC5725	33	343409	0.31	1.34 ± 0.29	1.00 ± 0.05	0.68 ± 0.02	1.94 ± 0.06	2.86 ± 0.04	0.369 ± 0.022	0.418 ± 0.023	0.306 ± 0.022	GANDALF
NGC5725	33	343411	0.0	2.80 ± 0.27	1.00 ± 0.03	0.54 ± 0.01	1.53 ± 0.03	2.63 ± 0.02	0.453 ± 0.016	0.419 ± 0.018	0.306 ± 0.017	GANDALF
NGC5725	33	343413	0.15	1.22 ± 0.50	1.00 ± 0.14	0.80 ± 0.10	2.27 ± 0.28	2.86 ± 0.28	0.265 ± 0.038	0.232 ± 0.036	0.139 ± 0.028	GANDALF
NGC5725	33	722438	0.0	5.81 ± 0.42	1.00 ± 0.04	0.47 ± 0.02	1.35 ± 0.05	2.66 ± 0.05	0.824 ± 0.033	0.721 ± 0.032	0.635 ± 0.039	GANDALF
NGC5740	38	321075	1.87		1.00 ± 0.04	0.20 ± 0.01	0.58 ± 0.03	2.87 ± 0.04	1.116 ± 0.019	0.324 ± 0.013	0.268 ± 0.013	GFC
NGC5740	38	321076	0.11	2.46 ± 0.57	1.00 ± 0.06	0.10 ± 0.02	0.30 ± 0.05	2.86 ± 0.08	1.078 ± 0.039	0.452 ± 0.028	0.318 ± 0.027	GANDALF
NGC5740	38	321077	0.0	2.64 ± 0.29	1.00 ± 0.03	0.26 ± 0.01	0.74 ± 0.02	2.72 ± 0.02	0.930 ± 0.015	0.415 ± 0.013	0.296 ± 0.015	GANDALF
SDSSJ08...	1	622084	0.19	1.75 ± 0.09	1.00 ± 0.02	0.20 ± 0.01	0.56 ± 0.02	2.86 ± 0.02	0.796 ± 0.011	0.480 ± 0.013	0.356 ± 0.011	GANDALF
UGC04673	2	517868	0.65		1.00 ± 0.17	0.21 ± 0.07	0.63 ± 0.12	2.86 ± 0.24	0.776 ± 0.060	0.672 ± 0.071	0.568 ± 0.056	GFC
UGC04673	2	517869	0.53	2.89 ± 0.33	1.00 ± 0.07	0.51 ± 0.03	1.42 ± 0.09	2.86 ± 0.12	0.426 ± 0.025	0.372 ± 0.021	0.257 ± 0.017	GANDALF
UGC04684	3	600168	0.31		1.00 ± 0.05	0.22 ± 0.01	0.62 ± 0.04	2.86 ± 0.05	0.615 ± 0.027	0.629 ± 0.025		GANDALF
UGC04996	4	198771	0.0	1.66 ± 0.20	1.00 ± 0.07	0.27 ± 0.02	0.78 ± 0.06	1.91 ± 0.05	0.346 ± 0.033	0.531 ± 0.040	0.396 ± 0.036	GANDALF
UGC04996	4	198772	0.22	6.01 ± 0.89	1.00 ± 0.07	0.51 ± 0.02	1.44 ± 0.06	2.86 ± 0.05	0.301 ± 0.037	0.466 ± 0.035	0.405 ± 0.032	GANDALF
UGC06578	5	6821	0.0	0.62 ± 14.85	1.00 ± 0.21	1.39 ± 0.00	4.13 ± 0.01	1.19 ± 0.00	0.013 ± 0.000	0.031 ± 0.000	0.023 ± 0.000	GFC
UGC06578	5	6822	0.25		1.00 ± 0.02	1.01 ± 0.01	2.88 ± 0.03	2.86 ± 0.03	0.126 ± 0.005	0.292 ± 0.005	0.200 ± 0.007	GANDALF
UGC06780	6	177588	0.13	1.76 ± 0.39	1.00 ± 0.05	0.33 ± 0.02	0.95 ± 0.05	2.86 ± 0.06	0.500 ± 0.043	0.640 ± 0.044	0.459 ± 0.045	GANDALF
UGC06780	6	177591	0.0	3.09 ± 0.28	1.00 ± 0.05	0.43 ± 0.01	1.24 ± 0.04	2.28 ± 0.03	0.169 ± 0.016	0.317 ± 0.021	0.207 ± 0.018	GANDALF
UGC06903	9	22742	0.0	4.11 ± 3.47	1.00 ± 0.25	0.17 ± 0.08	0.49 ± 0.24	1.93 ± 0.29	0.524 ± 0.126	0.445 ± 0.091	0.323 ± 0.134	GANDALF
UGC06903	9	272331	0.33	2.04 ± 0.44	1.00 ± 0.06	0.23 ± 0.02	0.65 ± 0.07	2.86 ± 0.07	0.592 ± 0.043	0.678 ± 0.050	0.429 ± 0.043	GANDALF
UGC06970	10	185266	0.0	1.42 ± 0.90	1.00 ± 0.19	0.27 ± 0.07	0.76 ± 0.21	1.88 ± 0.12	0.370 ± 0.125	0.687 ± 0.121	0.463 ± 0.127	GANDALF
UGC07000	39	144491	0.56	3.52 ± 13.57	1.00 ± 0.15	0.44 ± 0.06	1.64 ± 0.15	2.86 ± 0.08	0.450 ± 0.051	0.442 ± 0.041	0.362 ± 0.036	GFC
UGC07000	39	144493	0.0	2.97 ± 0.14	1.00 ± 0.02	0.74 ± 0.01	2.11 ± 0.02	2.11 ± 0.02	0.238 ± 0.010	0.301 ± 0.011	0.206 ± 0.010	GANDALF
UGC07000	39	144494	0.23	3.24 ± 0.37	1.00 ± 0.04	0.32 ± 0.01	0.91 ± 0.03	2.86 ± 0.04	0.453 ± 0.023	0.544 ± 0.023	0.395 ± 0.025	GANDALF
UGC07000	39	144495	0.0	5.38 ± 1.69	1.00 ± 0.20	0.62 ± 0.12	1.77 ± 0.34	2.69 ± 0.34	0.332 ± 0.057	0.430 ± 0.062	0.286 ± 0.054	GANDALF
UGC07000	39	700775	0.27	1.02 ± 0.50	1.00 ± 0.36	1.00 ± 0.34	2.83 ± 0.97	2.86 ± 0.71	0.279 ± 0.085	0.395 ± 0.097	0.328 ± 0.075	GANDALF
UGC07053	13	185622	0.21		1.00 ± 0.05	1.04 ± 0.03	3.09 ± 0.08	2.86 ± 0.06	0.145 ± 0.021	0.233 ± 0.037	0.178 ± 0.027	GFC
UGC07053	13	185623	0.64	0.74 ± 0.53	1.00 ± 0.20	0.15 ± 0.15	0.67 ± 0.17	2.86 ± 0.27	0.328 ± 0.213	0.614 ± 0.142	0.561 ± 0.134	GFC
UGC07053	13	791635	0.0	4.10 ± 0.89	1.00 ± 0.05	0.60 ± 0.02	1.72 ± 0.06	2.35 ± 0.05	0.085 ± 0.025	0.258 ± 0.028	0.185 ± 0.027	GANDALF

Table 5.2: *Continued*

galaxy	DV16-ID	cataID	$C(\mathrm{H}\beta)$	$I_\lambda / I_{\mathrm{H}\beta}$								Origin
				[OII]	Hβ	[OIII,4959]	[OIII,5007]	Hα	[NII]	[SII,6713]	[SII,6731]	
UGC07332	14	85881	0.0	86.23 ± 52.80	1.00 ± 1.30	0.39 ± 0.48	1.12 ± 1.37	1.62 ± 0.57	0.155 ± 1.762	1.524 ± 0.572	1.116 ± 0.439	GANDALF
UGC07394	18	221194	0.52	2.97 ± 6.90	1.00 ± 0.19	0.37 ± 0.18	0.69 ± 0.24	2.86 ± 0.24	0.302 ± 0.101	0.563 ± 0.133	0.555 ± 0.134	GFC
UGC07394	18	221195	0.5	0.72 ± 0.12	1.00 ± 0.07	0.82 ± 0.05	2.31 ± 0.14	2.86 ± 0.11	0.143 ± 0.012	0.272 ± 0.015	0.177 ± 0.013	GANDALF
UGC09215	23	238952	0.7	2.50 ± 56.85	1.00 ± 0.16	0.52 ± 0.02	1.38 ± 0.03	2.86 ± 0.03	0.503 ± 0.018	0.461 ± 0.014	0.318 ± 0.011	GFC
UGC09215	23	714924	0.0	43.90 ± 191.72	1.00 ± 0.04	0.41 ± 0.01	1.09 ± 0.03	1.97 ± 0.02	0.321 ± 0.007	0.326 ± 0.006	0.234 ± 0.005	GFC
UGC09215	23	714923	0.43	2.82 ± 39.15	1.00 ± 0.02	0.60 ± 0.01	1.82 ± 0.02	2.86 ± 0.01	0.478 ± 0.006	0.365 ± 0.008	0.267 ± 0.004	GFC
UGC09215	23	319800	0.13	1.91 ± 0.07	1.00 ± 0.01	0.97 ± 0.00	2.76 ± 0.01	2.86 ± 0.01	0.263 ± 0.005	0.309 ± 0.005	0.223 ± 0.005	GANDALF
UGC09215	23	319801	0.0	1.95 ± 0.09	1.00 ± 0.02	0.40 ± 0.01	1.13 ± 0.02	1.91 ± 0.01	0.272 ± 0.010	0.329 ± 0.012	0.214 ± 0.010	GANDALF
UGC09299	27	593645	0.29		1.00 ± 0.07	0.60 ± 0.04	1.80 ± 0.07	2.86 ± 0.06	0.483 ± 0.035	0.684 ± 0.033	0.474 ± 0.026	GFC
UGC09299	27	593646	0.0	2.95 ± 0.24	1.00 ± 0.03	0.55 ± 0.01	1.56 ± 0.03	2.82 ± 0.03	0.330 ± 0.017	0.430 ± 0.018	0.308 ± 0.016	GANDALF
UGC09432	31	367146	0.1		1.00 ± 0.03	0.74 ± 0.01	2.15 ± 0.03	2.86 ± 0.05	0.195 ± 0.014	0.450 ± 0.018	0.313 ± 0.014	GANDALF
UGC09470	37	16827	0.0	5.06 ± 0.13	1.00 ± 0.01	1.21 ± 0.00	3.44 ± 0.01	2.22 ± 0.01	0.103 ± 0.001	0.173 ± 0.002	0.121 ± 0.002	GANDALF
UGC09482	36	16863	0.0	5.18 ± 0.38	1.00 ± 0.02	0.86 ± 0.01	2.45 ± 0.03	2.65 ± 0.02	0.252 ± 0.011	0.404 ± 0.013	0.265 ± 0.011	GANDALF
UGC09482	36	16899	0.0	6.51 ± 0.69	1.00 ± 0.05	0.38 ± 0.02	1.08 ± 0.05	2.49 ± 0.05	0.243 ± 0.034	0.492 ± 0.039	0.342 ± 0.038	GANDALF
UM456	7	559583	0.0	1.61 ± 0.12	1.00 ± 0.01	1.80 ± 0.01	5.15 ± 0.02	1.93 ± 0.01	0.037 ± 0.003	0.078 ± 0.003	0.053 ± 0.003	GANDALF
UM456	7	559584	0.0	4.76 ± 0.16	1.00 ± 0.02	1.05 ± 0.01	3.00 ± 0.02	2.06 ± 0.01	0.078 ± 0.005	0.197 ± 0.006	0.138 ± 0.006	GANDALF
UM456A	8	559608	0.0	3.65 ± 0.13	1.00 ± 0.02	1.15 ± 0.01	3.30 ± 0.02	1.73 ± 0.01	0.049 ± 0.006	0.125 ± 0.006	0.083 ± 0.006	GANDALF
UM456A	8	559610	0.0	2.27 ± 0.13	1.00 ± 0.02	1.10 ± 0.01	3.15 ± 0.02	2.67 ± 0.02	0.060 ± 0.006	0.166 ± 0.006	0.110 ± 0.006	GANDALF

Table 5.3: Emission lines for HAPLESS galaxies that are not in HIGH. The first three columns give the common name, the ID from C15 and the GAMA cataID respectively. All emission lines have been corrected for reddening using the Balmer decrement $C(\mathrm{H}\beta)$ and the Cardelli et al. (1989) dust obscuration curve. The Origin column specifies whether the stellar absorption corrected fluxes were extracted using GANDALF or the GaussFitComplexv05 (GFC) catalogue.

galaxy	C15-ID	cataID	$C(\mathrm{H}\beta)$	$I_\lambda/I_{\mathrm{H}\beta}$								Origin
				[OII]	Hβ	[OIII,4959]	[OIII,5007]	Hα	[NII]	[SII,6713]	[SII,6731]	
CGCG014-014	36.0	86115	0.69	5.78 ± 0.53	1.00 ± 0.31	0.59 ± 0.05	1.50 ± 0.09	2.86 ± 0.09	0.139 ± 0.043	0.357 ± 0.035	0.237 ± 0.029	GFC
CGCG019-003	38.0	227753	0.0	3.32 ± 0.11	1.00 ± 0.01	1.05 ± 0.01	3.00 ± 0.02	2.60 ± 0.02	0.190 ± 0.008	0.309 ± 0.009	0.206 ± 0.008	GANDALF
CGCG019-084	32.0	240108	1.2		1.00 ± 0.22	0.23 ± 0.07	0.63 ± 0.19	2.86 ± 0.10	0.658 ± 0.066	0.884 ± 0.066		GANDALF
LEDA1241857	13.0	367540	0.1		1.00 ± 0.14	0.63 ± 0.03	1.78 ± 0.05	2.86 ± 0.06	0.305 ± 0.022	0.452 ± 0.025	0.325 ± 0.016	GFC
MGC0066574	42.0	594420	0.0	3.79 ± 4.23	1.00 ± 0.55	0.20 ± 0.65	0.58 ± 1.87	0.77 ± 0.28	0.226 ± 0.382	0.257 ± 0.296	0.399 ± 0.331	GANDALF
NGC5733	18.0	64893	0.43		1.00 ± 0.04	0.84 ± 0.02	2.60 ± 0.05	2.86 ± 0.05	0.361 ± 0.020	0.542 ± 0.019	0.378 ± 0.015	GFC
NGC5733	18.0	64894	0.0	2.85 ± 0.12	1.00 ± 0.02	0.81 ± 0.01	2.30 ± 0.02	2.69 ± 0.02	0.237 ± 0.007	0.329 ± 0.007	0.232 ± 0.007	GANDALF
NGC5733	18.0	64895	0.0	0.98 ± 0.11	1.00 ± 0.03	0.85 ± 0.01	2.42 ± 0.04	2.66 ± 0.02	0.225 ± 0.014	0.412 ± 0.015	0.278 ± 0.012	GANDALF
NGC5750	25.0	65076	0.0	2.42 ± 0.20	1.00 ± 0.02	0.13 ± 0.01	0.38 ± 0.02	2.68 ± 0.02	1.177 ± 0.012	0.456 ± 0.012	0.336 ± 0.011	GANDALF
PGC037392	2.0	288461	0.06		1.00 ± 0.05	0.85 ± 0.02	2.44 ± 0.06	2.86 ± 0.06	0.406 ± 0.046	0.815 ± 0.046	0.492 ± 0.046	GANDALF
PGC051719	12.0	92677	0.32	2.66 ± 0.20	1.00 ± 0.05	0.85 ± 0.04	2.41 ± 0.13	2.86 ± 0.11	0.244 ± 0.011	0.331 ± 0.014	0.236 ± 0.011	GANDALF
PGC051719	12.0	92676	0.22	4.08 ± 0.32	1.00 ± 0.04	0.35 ± 0.02	1.00 ± 0.04	2.86 ± 0.06	0.511 ± 0.022	0.656 ± 0.025	0.427 ± 0.024	GANDALF
PGC052652	5.0	240202	0.46	3.20 ± 0.25	1.00 ± 0.02	0.65 ± 0.01	1.83 ± 0.02	2.86 ± 0.01	0.352 ± 0.006	0.389 ± 0.007	0.274 ± 0.006	GANDALF
UGC06877	1.0	70114	1.02	2.48 ± 0.06	1.00 ± 0.02	0.24 ± 0.01	0.72 ± 0.01	2.87 ± 0.02	0.712 ± 0.005	0.251 ± 0.007	0.193 ± 0.003	GFC
UGC07396	35.0	9163	0.02	5.82 ± 1.15	1.00 ± 0.10	0.43 ± 0.02	1.24 ± 0.07	2.86 ± 0.06	0.455 ± 0.050	0.590 ± 0.059	0.447 ± 0.064	GANDALF
UGC09348	16.0	619104	0.39	5.13 ± 0.62	1.00 ± 0.07	0.43 ± 0.02	1.22 ± 0.06	2.86 ± 0.04	0.637 ± 0.032	0.734 ± 0.028	0.554 ± 0.030	GANDALF
UM452	4.0	54103	0.21	2.46 ± 0.07	1.00 ± 0.01	0.85 ± 0.00	2.42 ± 0.01	2.86 ± 0.01	0.258 ± 0.004	0.366 ± 0.005	0.266 ± 0.004	GANDALF
UM491	33.0	290172	0.0	4.52 ± 0.10	1.00 ± 0.01	0.87 ± 0.00	2.47 ± 0.01	2.53 ± 0.01	0.201 ± 0.005	0.277 ± 0.005	0.191 ± 0.004	GANDALF

Chapter 6

Chemical evolution

6.1 Introduction

One can learn about dust sources and sinks by comparing models that predict the build-up of dust, gas and metals with the observed properties of galaxies. Throughout Chapter 4 we have build a consistent picture of how the dust and gas content changes as galaxies evolve. Here we will study what drives this evolution and attempt to explain the distribution in galaxy properties of the different samples. C15 attempted to model the HRS and HAPLESS galaxies using a simple closed box chemical evolution model and found that, as galaxies evolve, the dust-to-baryon ratio first increases steeply, then levels off and reaches its peak about half way through its evolution, and finally declines towards lower gas fractions (see also Figure 4.8). In Chapter 4 we show HIGH recovered similar dust- and gas- rich galaxies as was seen in HAPLESS, but also revealed gas-rich sources *with much lower dust content*. The dust-poor galaxies in HIGH are not consistent with the closed box model in C15 (Figure 4.8). As previously discussed, they have some of the highest gas fractions ($f_g > 0.8$) seen in local galaxies and offer a unique probe into the dust properties of these sources. In this chapter, we add the Dwarf Galaxy Survey (DGS; Madden et al., 2013; Rémy-Ruyer et al., 2013), the largest sample (48 sources) of low metallicity sources surveyed with *Herschel* to our nearby galaxy samples.

Following Zhukovska (2014) and Feldmann (2015), we apply an updated chemical evolution model to interpret the data by relaxing the closed box model assumption from C15 and adding inflows and outflows, using different SFHs, allowing for dust grain growth in the ISM and dust destruction. Combining the HIGH, HAPLESS and HRS sources with the DGS, increases the sample size by 377 sources (compared to 126 sources in Rémy-Ruyer et al. (2014), including DGS). Zhukovska (2014) compared the sample from Rémy-Ruyer et al. (2014) with a chemical evolution model to show that the observed variation in dust-to-gas ratio and metallicity in local star-forming dwarfs can be explained using models with bursty star formation histories,

Table 6.1: The average properties for the samples used in this work quoted as the mean ± standard deviation. Where data is not available for all the sample we quote the number of sources in the brackets. We only show the late type galaxies in the HRS (LTGs).

Galaxy Sample	SFR ($M_\odot\,yr^{-1}$)	log M_{HI} ($M_\odot$)	log M_* ($M_\odot$)	log M_d ($M_\odot$)	f_g
DGS	1.4 ± 2.0 (45)	8.57 ± 0.78 (35)	8.10 ± 0.99	5.12 ± 1.77	0.74 ± 0.23 (35)
HIGH-low	0.11 ± 0.10	9.02 ± 0.46	8.17 ± 0.56	5.21 ± 0.97	0.87 ± 0.09
HIGH-high	1.4 ± 1.5	9.76 ± 0.39	9.89 ± 0.65	7.12 ± 0.43	0.50 ± 0.24
HRS (LTGs)	0.50 ± 0.79	8.94 ± 0.56 (231)	9.64 ± 0.57	6.70 ± 0.54 (239)	0.28 ± 0.22 (231)

low dust yields from core-collapse SNe and additional grain growth in the ISM. Feldmann (2015) took the same sample of 126 local galaxies and used both an analytic approximation and dynamic one-zone chemical evolution models to fit the observed relationships. These models require very rapid grain growth, which activates at a critical metallicity, to match the observed dust-to-metal ratio in the galaxies. Feldmann (2015) also argues that there is a balance between metal-poor inflows and enriched outflows which regulates the dust-to-metal ratio. While outflows remove dust and metals from the galaxy, it is thought to be inflows which dilute the metal content of the ISM and keep the galaxy from reaching the critical metallicity (and thus maintain a low dust-to-metal ratio for longer).

A detailed description of the HRS, HAPLESS and HIGH samples is provided in detail in previous chapters. We use metallicity information from Chapter 5 in order to investigate the dust-to-gas and dust-to-metal properties and to discriminate between different chemical evolution models and dust sources. We derive consistent galaxy properties and metallicities for DGS in Section 6.2. The average properties for all the galaxy samples are listed in Table 6.1. The combined sample here allows one to sample a wider range of gas fractions than possible before (from $0.05 < f_g < 0.97$). This provides an opportunity to model the evolution of dust, metals, stars and gas content as galaxies consume their gas into stars and evolve from gas-rich to gas-poor. Importantly, we also increase the number of low metallicity sources (additional 67 sources with $Z < 1/3 Z_\odot$), which lie of the scaling relations for more evolved sources. This is particularly important given the relevance of immature, unevolved sources as analogues for the first galaxies. Section 6.3 briefly describes the chemical model and the combination of parameters modelled in this work. The results are discussed in Section 6.4. Our conclusions are listed in Section 6.6. This investigation was performed in collaboration with Simon Schoffield, who ran all the chemical evolution models used in this chapter. The work presented here has been submitted for publication in MNRAS (De Vis et al., *submitted*).

6.2 Dwarf Galaxy Survey

In this work, we also include results from the Dwarf Galaxy Survey (DGS; Madden et al., 2013) to improve our sampling of galaxies at the high gas fraction and low stellar mass regime. The DGS sources were selected from several other surveys in order to make a broad sample of 50 galaxies ranging from very low ($\sim 1/50 Z_{\odot}$) to moderate metallicity ($\sim 1/3 Z_{\odot}$). In order to compare the samples, we need consistent methods to calculate the different galaxy properties.

6.2.1 Dust and HI masses

Unfortunately we do not have the same complete UV-submm coverage for DGS sources as we have available for the H-ATLAS and HRS. Consequently, we redetermined the dust properties (following C15) using a modified blackbody (MBB) fit to the 70-500 μm photometry from Rémy-Ruyer et al. (2013; 2015). This method produces consistent results with the dust masses output by MAGPHYS for all but the coldest sources (as shown in Section 3.4.6.1) and both methods assume the same dust absorption coefficient of $\kappa_{850} = 0.07\,\mathrm{m^2\,kg^{-1}}$ (James et al., 2002). The re-evaluated dust masses for the DGS sources in this work are higher than those presented in Rémy-Ruyer et al. (2013) (estimated using one-temperature MBB fitting, which is known to produce lower dust masses - Bendo et al. 2015, C15) and Rémy-Ruyer et al. (2015, hereafter 'RR2015') (based on amorphous carbon/graphite dust grains consistent with Draine et al. 2007 models). On close inspection, the higher dust mass estimates for the warmer DGS sources in this work are entirely consistent with scaling the Rémy-Ruyer et al. (2015) masses for graphite grains by the difference in κ used in their work and MAGPHYS, and the remaining offset for some of the cold sources is of the same magnitude as the offset between MAGPHYS and the MBB method. Therefore in what follows, we simply *scale the RR2015 dust masses for the difference in κ to be consistent across samples.* HI masses are available for 35 DGS sources from Madden et al. (2013), and were compiled from the literature.

6.2.2 Stellar mass and SFR

We have also compared the DGS stellar mass estimation method (Eskew et al., 2012) to the MAGPHYS stellar masses for all the sources in HIGH in Figure 6.1 and found the DGS stellar masses needed to be scaled down by a factor of ~ 3.2 to be consistent[1]. Here we have used HIGH since, compared to DGS, it is the most similar sample for which we have MAGPHYS results available. The re-evaluated stellar masses for the DGS are compared to the HIGH

[1] We note that using a linear rescaling between both methods instead of a constant offset would slightly reduce the offset between both methods. However, this would not significantly affect our results and we stick to a constant offset for simplicity.

properties in Fig. 6.2. The stellar masses of the HIGH-low and DGS samples extend from $10^7 - 10^9\,M_\odot$ with the latter also extending down to $10^5\,M_\odot$. The DGS sample also includes large stellar mass galaxies $> 10^9\,M_\odot$, these overlap with the HIGH-high sample and the HRS.

SFRs are taken from RR2015 and for 90% of the DGS sources[2] the SFR were estimated using a combination of $L_{\rm TIR}$ and the observed Hα luminosity (Kennicutt et al., 2009). We have compared this SFR method with MAGPHYS SFRs for HRS[3] in Figure 6.3 and found excellent agreement between the methods for all but the most quiescent (SSFR $< 10^{-11}\ M_\odot\ {\rm yr}^{-1}$) galaxies and no rescaling is necessary. The offset for the quiescent galaxies is because the $L_{\rm TIR}$ in the Kennicutt et al. (2009) SFR calibration is affected by sources of heating other than the SFR (Boquien et al., 2016; Section 3.4.6.2). None of the DGS sources are quiescent and thus none are affected by this issue and we can safely use the SFR from RR2015.

6.2.3 Metallicities

We have also included metallicities for the DGS sources (Rémy-Ruyer et al., 2013). These were originally estimated using the Pilyugin & Thuan (2005, hereafter PT05) calibration (Madden et al., 2013). PT05 is calibrated over a similar range of metallicity to N2 and PG16S, but there are a number of reasons we did not choose this as a method to determine metallicities in this study. First, PT05 is not a good estimator for metal-rich galaxies that have low excitation parameters P and high values of R_{23} (such as the HRS and HIGH-high galaxies). PT05 is therefore more suited for the DGS and HIGH-low sources that have appropriate P and R_{23} values but this means we cannot apply a consistent method to derive metallicities across the different samples of nearby galaxies. Second, PT05 metallicities have been shown to have a lot of scatter with stellar mass compared to other calibrators (Kewley & Ellison, 2008), suggesting it is not a good tracer of metallicity across a wide range of galaxy properties. Third, the PT05 method requires has two 'branches' of metallicity values versus the R_{23} emission line ratio with a transition region between the two branches. Because of this, a large difference in Z can be derived for galaxies with very small changes in emission line ratio. The PG16S calibration also uses different relations for high and low metallicities. However the appropriate ranges where the high- and low-metallicity relations can be used, overlap for adjacent metallicities, and the transition zone thus disappears.

[2]For galaxies with small Hα luminosities ($L_{\rm H\alpha} < 2.5\ 10^{39}\ {\rm erg\,s^{-1}}$), Lee et al. (2009) cautioned the use of Hα to derive the SFR. For the 10 DGS sources for which this is the case, RR2015 instead use the calibration provided by Lee et al. (2009), which results in SFRs that are a factor of 2 larger than the previously estimated SFRs from Hα and $L_{\rm TIR}$.

[3]Hα luminosities from Boselli et al. (2015) are used. We do not have integrated Hα luminosities available for HIGH and HAPLESS.

Therefore, we rederive the metallicities for the DGS sources using the line measurements from the literature (Table 6.2; S. Madden, *priv. comm.*[4].) in the same way as for the HRS, HAPLESS and HiGH samples (Chapter 5). Fig. 6.4 compares the DGS metallicities derived here with the published PT05 values from Madden et al. (2013). On average, the O3N2, N2, PG16S and KE08/T04 metallicities are higher than PT05 by 0.17, 0.14, 0.09 and 0.30 dex respectively. In the low metallicity regime ($12+\log(\mathrm{O/H})_{\mathrm{PT05}} < 8.0$), the PT05 values for some sources are significantly lower than those derived using the PG16S method, suggesting that the PT05 method underestimated the metallicities for some galaxies by up to 0.3-0.5 dex. At the higher metallicity end, the O3N2, N2 and PG16S calibrations tend to produce lower metallicities than PT05, though only for a few sources. The significant offset at the lowest metallicities seen with O3N2 in particular may be the result of this calibration no longer being valid in this range (Pettini & Pagel, 2004), therefore from now on we restrict our comparison to the N2, PG16S and KE08/T04 methods.

At a given stellar mass or gas fraction, there are some DGS sources with significantly lower N2, PG16S and KE08/T04 metallicities when compared to the other samples. These offset sources are also the most actively star forming galaxies. DGS was selected to have a broad sample of ~ 50 galaxies ranging from very low to moderate (1/3 $Z_{\odot}$; 12+log(O/H)=8.43) metallicity using the PT05 calibration (Madden et al., 2013). This effectively selects the interesting low metallicity sources that DGS was aimed at, though result in a selection offset towards low metallicities at given gas fraction that can be seen in Figure 6.8. At fixed stellar mass, galaxies with lower metallicities are known to have higher SFR (Mannucci et al., 2010; Lara-López et al., 2013). Selecting low metallicities (at a given gas fraction) also selects galaxies that are more actively forming stars. This explain why the DGS sources are much more actively star forming than the other samples in this work. Additionally, higher SFR (and thus brighter) sources are easier to observe with Herschel, and it is easier to obtain high signal-to-noise spectra (in order to determine metallicities). This is another reason DGS consists mainly of high SFR sources.

6.3 The chemical evolution model

A chemical and dust evolution model can be used to build a consistent picture of how the metals, dust and gas content changes as galaxies evolve (Tinsley, 1980). The simple chemical evolution model used in C15 to understand the different scaling relations for dust, gas and stellar mass selected samples neglected dust destruction and grain growth, and assumed that the system was

[4]We include the DGS metallicities in Table 6.2, and in some cases use updated references in order to include all necessary lines.

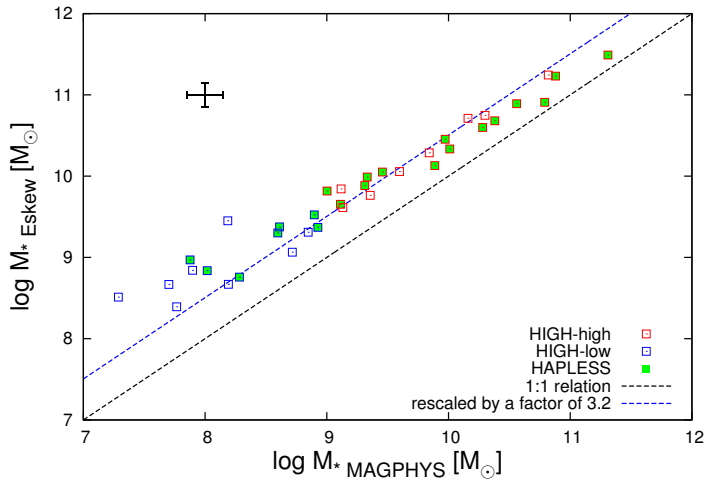

Figure 6.1: MAGPHYS stellar masses for HIGH against the stellar masses from the method in RR2015 (based on Eskew et al. (2012) using 3.6 μm and 4.5 μm fluxes). The stellar masses are offset and need to be rescaled by a factor of 3.2 to be consistent.

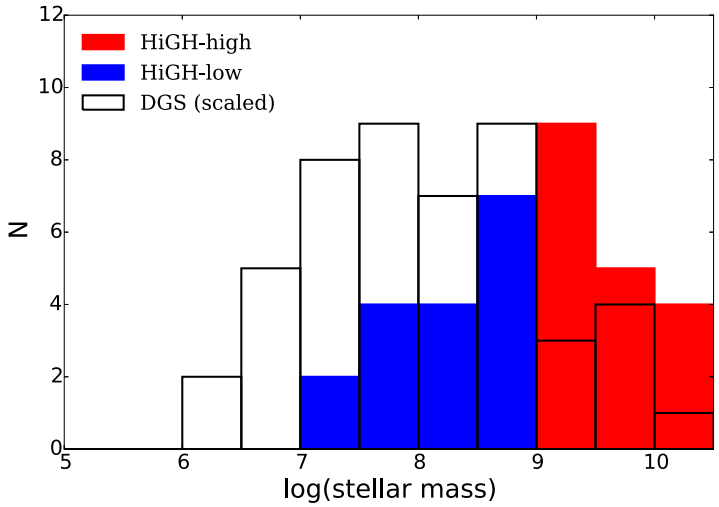

Figure 6.2: The stellar masses of galaxies in the HIGH-high (red) and HIGH-low (blue) samples in comparison with the Dwarf Galaxy Survey sources (black unfilled). Stellar masses for HIGH are obtained from the MAGPHYS UV-submm SED-fitting routine. The DGS stellar masses from Rémy-Ruyer et al. (2015) have been scaled by a factor of 3.2 to be consistent with the MAGPHYS estimates.

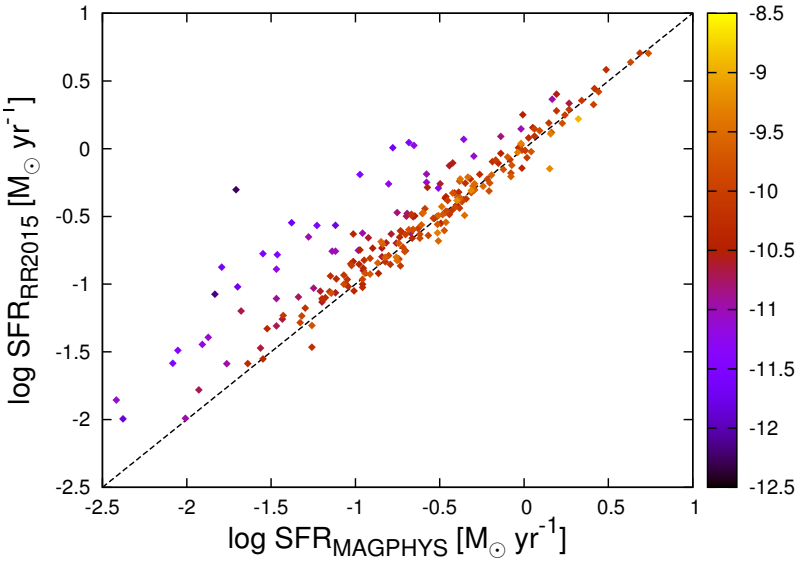

Figure 6.3: MAGPHYS SFR against the SFR from the method in RR2015 (based on Hα and $L_{\rm TIR}$) for the HRS sample. There is excellent agreement for all but the most quiescent galaxies and we can thus consistently use the RR2015 SFR for DGS.

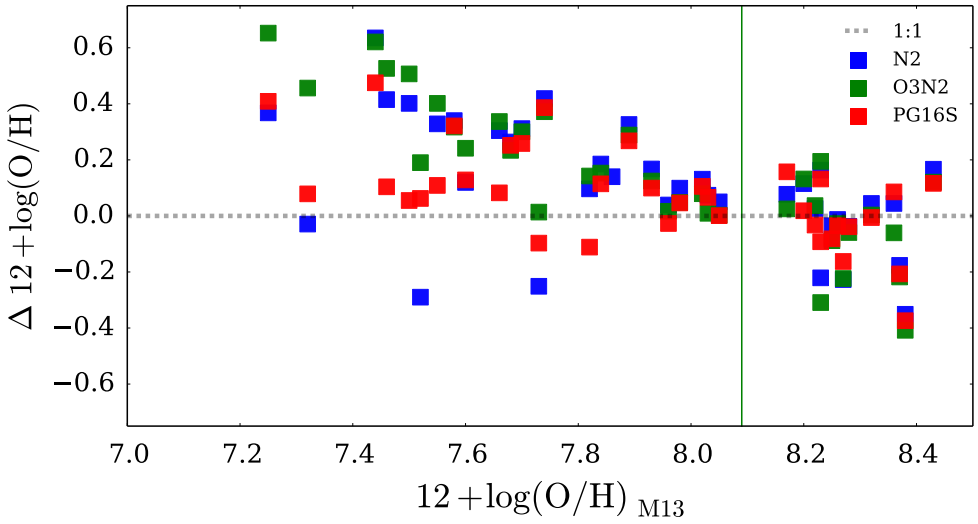

Figure 6.4: A comparison of the differences in metallicity calibrations $\Delta 12 + \log(\mathrm{O/H})$ using the N2 (blue), O3N2 (green) and PG16S (red) methods with the published DGS metallicities derived using PT05 (M13, Madden et al., 2013). The significant offset between the O3N2 and PT05 at the lowest metallicities may be because this calibration is known to break down here (indicated by the vertical line Pettini & Pagel, 2004), though the N2 and PG16S results also suggest PT05 tends to underestimate metallicities in this regime.

Table 6.2: Emission line measurements and derived metallicities for the Dwarf Galaxy Survey using the O3N2, N2, PG16S and KE08/T04 methods. The literature emission lines have been corrected for stellar absorption and reddening using methods in the listed references.

name	$I_\lambda/I_{H\beta}$							12+log(O/H)				Ref
	Hα	[OII]	[OIII,4959]	[OIII,5007]	[NII]	[SII,6713]	[SII,6731]	N2	O3N2	PG16S	KE08/T04	
Haro II	2.91	1.08	1.19	3.72	0.488	0.156	0.102	8.40	8.30	8.45	8.49	1
Haro 2	2.86	3.41	0.55	1.45	0.461	0.297	0.298	8.39	8.42	8.36	8.65	2
Haro 3	2.86	2.71	1.08	3.22	0.236	0.223	0.180	8.24	8.22	8.24	8.37	1
He 2-10	3.00	2.29	0.36	1.06	0.878	0.301	0.266	8.60	8.55	8.55	8.8	3
HS0822+3542	2.75	0.31	1.19	3.58	0.010	0.026	0.018	7.29	7.78	7.40		4
HS1304+3259	2.86	1.85	1.52	4.51	0.100	0.330[a]		8.10	8.05	8.03	8.07	5
HS1319+3224	2.86	1.24	1.63	5.03		0.140[a]						4
HS1330+3651	2.86	0.48	1.64	4.9	0.090	0.350[a]		8.08	8.03	8.03		4
HS1442+4250	2.76	0.54	1.75	4.98	0.023	0.042	0.029	7.72	7.84	7.73		6
I Zw 18	2.74	0.408	0.636	1.906	0.012	0.029	0.022	7.39	7.88	7.15		7,13
II Zw 40	2.87	0.84	2.46	7.41	0.063	0.067	0.054	8.09	7.92	8.14		8
IC10	2.85	1.01	1.35	3.97	0.241	0.118	0.094	8.25	8.20	8.33	8.33	9
Mrk 1089	2.86	1.50	0.74	2.24	0.315	0.141	0.101	8.30	8.31	8.38	8.51	10
Mrk 1450	2.83	1.35	1.79	4.76	0.067	0.117	0.083	8.02	7.99	7.95		11
Mrk 153	2.81	0.00	1.51		0.059	0.247[a]		7.99				12
Mrk 209	2.78	0.72	1.96	5.54	0.029	0.061	0.045	7.80	7.86	7.80		13
Mrk 930	2.85	2.37	1.39	4.17	0.143	0.269	0.198	8.15	8.12	8.11	8.19	14
NGC 1140	2.88	2.32	0.97	0.29	0.256	0.231	0.175	8.25	8.57	8.28	8.81	15
NGC 1569	2.84	0.99	1.50	4.51	0.137	0.205	0.147	8.15	8.10	8.13	8.16	16
NGC 1705	2.86	3.74	1.05	3.00	0.105	0.060[a]		8.10	8.12	7.99	8.2	17
NGC 1705	2.86	3.37	1.66	4.87		0.026[a]						16
NGC 1705	2.91	2.54	1.47	4.25	0.111	0.034[a]		8.11	8.07	8.24	8.11	16
NGC 1705	2.76	2.43	1.52	3.83								16
NGC 1705	2.85	4.00	1.03	3.15	0.039	0.049[a]		7.89	7.97	7.73		16
NGC 1705	2.86	4.75	1.32	3.67	0.122	0.016[a]		8.13	8.07	8.33	8.18	16
NGC 1705	2.81	2.74	1.67	4.86	0.098	0.037[a]		8.09	8.04	8.25		16
NGC 1705	2.86	3.12	1.71	4.94	0.069	0.036[a]		8.03	7.99	8.15		16
NGC 1705	2.84	3.49	1.69	4.87	0.095	0.038[a]		8.09	8.04	8.24		16
NGC 1705	2.84	4.36	1.45	4.27	0.148	0.047[a]		8.16	8.12	8.28	8.2	16
NGC 1705	2.83	2.64	1.13	3.40		0.033[a]						16
NGC 1705	2.86	5.13	0.59	2.04								16
NGC 1705	2.86	4.01	1.09	3.19	0.097	0.043[a]		8.09	8.10	8.03	8.16	16
NGC 1705	2.86	4.02	1.26	3.59	0.154	0.043[a]		8.17	8.15	8.23	8.25	16
NGC 1705	2.86	4.08	1.57	4.39	0.122	0.046[a]		8.13	8.09	8.24	8.14	16
NGC 1705	2.86	3.52	1.63	4.64	0.016	0.038[a]		7.42	7.80	7.67		16
NGC 1705	2.79	3.02	1.37	3.93	0.062	0.036[a]		8.01	8.01	8.02		16
NGC 2366	2.86	0.84	1.34	3.93	0.139	0.234	0.167	8.15	8.12	8.08	8.2	18
NGC 2366	2.86	1.75	1.93	5.73	0.037	0.099	0.074	7.87	7.88	7.84		17
NGC 4214	2.85	3.04	1.00	3.03	0.241	0.267	0.194	8.24	8.23	8.23	8.39	15
NGC 4214	2.80	3.08	2.47	7.52	0.041	0.035	0.033	7.91	7.86	8.08		17
NGC 4449	2.87	3.89	0.69	2.07	0.338	0.476	0.334	8.32	8.33	8.22	8.53	15
NGC 4861	2.86	1.41	1.26	3.76	0.204	0.346	0.173	8.22	8.18	8.16	8.3	17

[a] The [SII] λ6717 and [SII] λ6731 lines are blended.

Table 6.2: Continued

name	$I_\lambda/I_{H\beta}$							12+log(O/H)				Ref
	Hα	[OII]	[OIII, 4959]	[OIII, 5007]	[NII]	[SII, 6713]	[SII, 6731]	N2	O3N2	PG16S	KE08/T04	
NGC 5253	2.83	2.60	1.42	4.22	0.200	0.270	0.205	8.21	8.16	8.17	8.28	15
NGC 625	2.86	1.76	1.52	4.53	0.123	0.136	0.101	8.13	8.08	8.10	8.13	19
NGC 625	2.84	2.31	0.99	2.95	0.204	0.197	0.146	8.21	8.21	8.24	8.36	18
NGC 625	2.82	3.38	0.87	2.55	0.262	0.341	0.240	8.27	8.27	8.21	8.45	18
NGC 625	2.86	4.86	0.33	1.03	0.422	0.676	0.520	8.37	8.46	8.2	8.69	18
NGC 6822	2.85	0.94	1.77	5.35	0.051	0.067	0.050	7.96	7.94	7.94		20
NGC 6822	2.85	1.47	1.44	4.26	0.071	0.103	0.072	8.03	8.02	7.92		19
Pox 186	2.86	0.35	2.09	6.22								21
SBS 0335-052	2.86	0.30	1.09	3.24	0.009	0.021	0.020	7.17	7.77	7.33		17
SBS 0335-052	2.86	0.25	1.1	3.29	0.009	0.020	0.017	7.17	7.76	7.35		17
SBS 0335-052	2.86	0.26	1.42	4.27	0.061	0.124	0.084	8.00	7.99	7.87		17
SBS 0335-052	2.86	0.23	1.50	4.49	0.124	0.221	0.215	8.13	8.09	8.09	8.13	17
SBS 1159+545	2.76	0.65	1.29	3.80	0.085	0.187	0.133	8.07	8.06	7.92	8.08	17
SBS 1211+540	2.71	0.80	2.04	6.07	0.041	0.093	0.069	7.92	7.90	7.90		17
SBS 1249+493	2.86	1.24	2.01	5.88	0.047	0.097	0.072	7.94	7.91	7.93		17
SBS 1415+437	2.86	1.18	1.19	3.54	0.037	0.090	0.067	7.87	7.95	7.66		12
SBS 1533+574	2.81	2.46	1.30	3.80	0.122	0.234	0.170	8.13	8.11	8.03	8.18	12
SBS 1533+574	2.85	2.04	1.79	5.33	0.087	0.167	0.117	8.07	8.01	8.05		12
Tol 0618-402	2.86	2.11	1.62	4.95								22
Tol 0618-402	2.86	2.35	1.60	4.92								21
Tol 1214-277	2.74	0.36	1.76	5.28	0.009	0.019	0.016	7.23	7.71	7.58		14
UGC 4483	2.86	1.32	0.90	2.73	0.037	0.070	0.052	7.88	7.99	7.56		17
UGCA 20	2.76	0.92	0.89	2.60	0.035	0.073	0.050	7.87	7.99	7.53		23
UGCA 20	2.76	1.35	0.85	2.58	0.044	0.088	0.064	7.93	8.02	7.58		22
UM 133	2.86	1.81	1.25	3.74	0.043	0.118	0.083	7.91	7.96	7.71		17
UM 311	2.89	1.80	1.32	3.98	0.180	0.167	0.124	8.19	8.15	8.16	8.26	17
UM 448	2.85	2.78	0.87	2.60	0.409	0.366	0.285	8.36	8.33	8.31	8.53	13
UM 461	2.78	0.53	2.04	6.02	0.021	0.052	0.042	7.68	7.80	7.74		13
VII Zw 403	2.83	1.36	1.17	3.52	0.051	0.105	0.077	7.96	8.00	7.74		17

References: (1) Guseva et al. (2012), (2) Kong & Cheng (2002), (3) Kobulnicky et al. (1999), (4) Pustilnik et al. (2003), (5) Popescu & Hopp (2000), (6) Guseva et al. (2003), (7) Skillman & Kennicutt (1993), (8) Guseva et al. (2000), (9) Magrini & Gonçalves (2009), (10) López-Sánchez et al. (2004), (11) Izotov et al. (1994), (12) Izotov et al. (2006), (13) Izotov et al. (1997), (14) Izotov & Thuan (1998), (15) Izotov & Thuan (2004), (16) Kobulnicky & Skillman (1997), (17) Lee & Skillman (2004), (18) Izotov et al. (2007), (19) Skillman et al. (2003), (20) Peimbert et al. (2005), (21) Guseva et al. (2007), (22) Masegosa et al. (1994), (23) van Zee et al. (1996).

a closed box (no inflows or outflows). Here we relax all of these assumptions. The chemical model is presented in full in Rowlands et al. (2014b; see also Morgan & Edmunds, 2003). In short, the model uses a prescription for the Star Formation History (SFH) and a Chabrier (2003) initial mass function[5] (IMF) to calculate how much of the initial gas is converted into stars at any given time. The model also tracks the continuous build-up of metals as stars end their lives, though metals can be removed in outflows of material.

For dust, the picture is more complex. Dust is produced by both supernovae and evolved low-intermediate mass stars, and destroyed by SN shocks and astration (the removal of gas and dust due to star formation). Many studies (e.g. Draine & Salpeter, 1979; Dwek & Scalo, 1980; Draine, 2009; Dunne et al., 2011; Mattsson et al., 2012; Asano et al., 2013a; Zhukovska, 2014; Mattsson et al., 2014; Rowlands et al., 2014b; Mancini et al., 2015) have found that significant dust grain growth in the interstellar medium is needed to explain observed dust masses at low- and high-redshifts. Adding in grain growth also helps balance the dust decline due to destruction (Asano et al., 2013a; Zhukovska, 2014).

In this model we include simple analytical prescriptions for grain growth and dust destruction via shocks as described in Rowlands et al. (2014b). The timescale for dust destruction ($\tau_{\rm dest}$, following Dwek et al. 2007) is described as a function of the rate of SN ($R_{\rm SN}$):

$$\tau_{\rm dest} = \frac{M_g}{m_{\rm ISM} R_{\rm SN}(t)} \tag{6.1}$$

where M_g is the gas mass and $m_{\rm ISM}$ is the mass of ISM that is swept up by each individual SN event. In some models we set this to $m_{\rm ISM} = 100\,{\rm M}_\odot$, indicative of SN shocks ploughing into typical interstellar densities of $10^3\,{\rm cm}^{-3}$ (Gall et al. 2011a; Dwek & Cherchneff 2011), although we also explore models with $1000\,{\rm M}_\odot$ (Dwek et al., 2007), consistent with dust destruction in the diffuse ISM.

The grain growth prescription is taken from Mattsson et al. (2012) where the timescale for dust growth is given by:

$$\tau_{\rm grow} = \tau_0 \left(1 - \frac{\eta_d}{Z}\right)^{-1} \tag{6.2}$$

and η_d is the dust-to-gas ratio, Z is the metallicity and τ_0 is given by:

$$\tau_0 = \frac{M_g}{\varepsilon Z \psi(t)} \tag{6.3}$$

ε is a free parameter, which is set to $\varepsilon = 500$ in Mattsson et al. (2012), appropriate for timescales of 10^7 yr for a galaxy similar to the Milky Way.

[5] We have also experimented with other IMFs, such as Kroupa (2001) and Salpeter (1955).

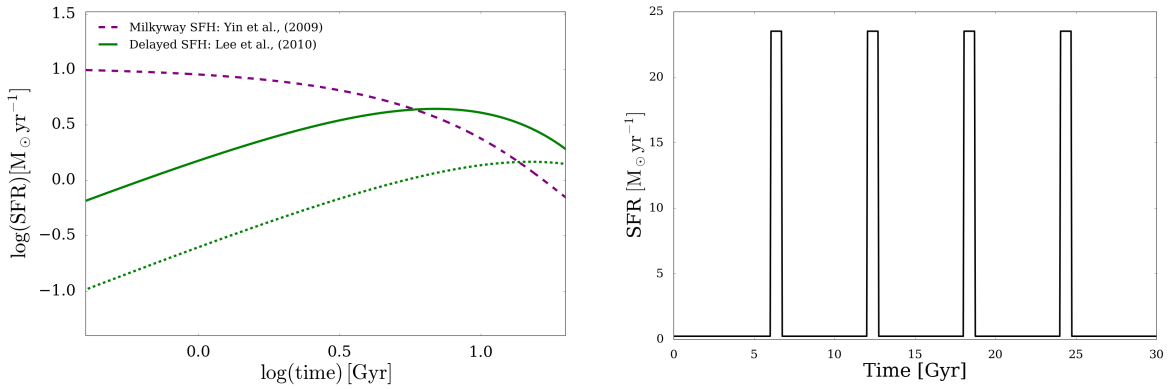

Figure 6.5: Star formation histories used in this work. *Left:* Model I has a SFH consistent with the Milky Way (Yin et al., 2009). Other models in this work assume a delayed SFH (Equation 6.5) one that produces roughly the same stellar mass as Model I, and one 3 times lower, with an extended delay. *Right:* We also test a bursty SFH similar to that used to model the Dwarf Galaxy Survey sources in Zhukovska (2014).

Full details of the model are given in Rowlands et al. (2014b) and the python code used is freely available on GITHUB[6]. Here we reproduce the equation for the dust mass evolution, M_d, and highlight some minor changes in this work:

$$\begin{aligned}\frac{d(M_d)}{dt} = \int_{m_{\tau_m}}^{m_U} \left([m - m_R(m)]\, Z(t-\tau_m)\delta_{\rm lims} + m p_z \delta_{\rm dust}\right) \\ \times \psi(t-\tau_m)\phi(m)dm - (M_d/M_g)\psi(t) \\ - (1-f_c)\frac{M_d}{\tau_{\rm dest}} + f_c\left(1-\frac{M_d}{M_g}\right)\frac{M_d}{\tau_{\rm grow}} \\ + M_{d,i} + \left(\frac{M_d}{M_g}\right)_I I(t) - \left(\frac{M_d}{M_g}\right)_O O(t). \end{aligned} \tag{6.4}$$

M_g is the gas mass, $\psi(t)$ is the star formation rate, $\phi(m)$ is the stellar IMF, Z is the metal mass fraction defined as M_Z/M_g and m_R is the remnant mass of a star of mass m (Ferreras & Silk, 2000). The first term accounts for dust formed in stars and supernovae. This includes metals re-released by stars after they die, and newly synthesised metals ejected in winds and supernovae. The second term describes the removal of dust due to astration and the grain destruction and growth timescales are given in terms three and four. The fifth term allows us to include primordial dust in the galaxy for example associated with Pop III stars, we set this to zero (Rowlands et al., 2014b). Finally, $I(t)$ and $O(t)$ are simple parameterisations of dust removed or contributed via inflows and outflows. The lifetime τ_m of stars with initial

[6]https://github.com/zemogle/chemevol

Table 6.3: Parameters for the different chemical evolution models used.

Name	SFH	Reduced SN dust	Destruction	Grain Growth	Inflow	Outflow
Model I	Milky Way	N	N	N	N	N
Model II	Delayed	N	N	N	N	N
Model III	Delayed	N	N	N	N	1.5× SFR
Model IV	Delayed	x6	$m_{\rm ISM} = 100$	$\varepsilon = 800$	1.5× SFR	1.5× SFR
Model V	Delayed	x12	$m_{\rm ISM} = 1000$	$\varepsilon = 6000$	2.0× SFR	2.0× SFR
Model VI	Delayed/3	x25	$m_{\rm ISM} = 100$	$\varepsilon = 10000$	2.0× SFR	2.0× SFR
Model VII	Bursty	x12	$m_{\rm ISM} = 100$	$\varepsilon = 10000$	6.0× SFR	6.0× SFR

mass m is derived using the model in Schaller et al. (1992) and yields for LIMS and massive stars are taken from van den Hoek & Groenewegen (1997) and Maeder (1992) respectively. A full discussion on the effect of using different yields can be seen in Rowlands et al. (2014b), and Romano et al. (2010). We note that this work differs from Rowlands et al. (2014b) in the following ways: (i) The initial remnant mass function is updated. (ii) We now take into account the formation of a black hole for stars with initial mass $m_i > 40\,{\rm M}_{\odot}$ when accounting for gas and metals released into the ISM. Stars with progenitor mass above this cut-off mass only contribute gas and metals lost via stellar winds before the collapse. (iii) We add an additional term f_c to account for the fraction of gas that is cold enough for grain growth in the ISM. We follow Mancini et al. (2015) and Inoue (2003) by setting this equal to 0.5. This parameter is likely to be higher at earlier times (e.g. Popping et al. 2014; Nozawa et al. 2015) though we choose to keep it constant here. (iv) We no longer interpolate the yields from stars of a given mass but just choose the nearest neighbour value, this has a small effect on the resulting stellar yields. (v) We directly input the dust masses for core collapse SN for stars with initial mass $8.5 < M_i \leq 40$ from Todini & Ferrara (2001). Rowlands et al. (2014b) used the Todini & Ferrara (2001) dust masses to estimate a condensation efficiency for SN dust ($\delta_{\rm SN}$) and applied that to the metal yields from Maeder (1992). Using the former technique reduces the dust mass by a factor of $\sim$1.8 for a MW-like galaxy at early times ($< 0.8\,$Gyr) compared to the latter.

In the remainder of this section, we test various parameter combinations in order to interpret the observed dust, metal, gas and star formation rates of the samples from DV16. First we repeat the simple model used in C15 (Section 6.4.1). The parameters for this model (Model I) are listed in Table 6.3. Next, in Sections 6.4.2-6.4.6, we use different model combinations and relax the closed box assumption, including changing SFHs, IMFs, inflows, outflows and including different dust sources (Table 6.3). We have varied inflows and outflows using simple parameterisations where the rate is proportional to $N \times$ SFR and $0 < N < 6.5$ and different initial gas masses. We also test four 'representative' star formation histories (Figure 6.5)

including a Milky Way-type exponentially declining SFR (Yin et al., 2009), and two versions of a delayed SFH as parameterised by Lee et al. (2010):

$$\mathrm{SFR}(t) \propto \frac{t}{\tau^2} e^{-t/\tau} \tag{6.5}$$

where t is the age of the galaxy and τ is the star formation timescale. First, we assume a SFH with $\tau = 6.9\,\mathrm{Gyr}$ with peak SFR $4.4\,\mathrm{M}_\odot\,\mathrm{yr}^{-1}$ in order to produce the same stellar mass as the Milky Way-type SFH. The second delayed SFH is reduced by a factor of 3, and has $\tau = 15\,\mathrm{Gyr}$ (see Section 6.4.3). Finally, a model including a bursty SFH (Figure 6.5) similar to that used in Zhukovska (2014) to explain the SFR properties of the DGS sources is also included. The results are discussed throughout the rest of this section.

6.4 Results

6.4.1 A simple model fit to dust in nearby galaxies

In Figure 6.6, we repeat Figure 4.8 (see also C15) and compare the evolution of the dust-to-baryonic mass ratio (M_d/M_{bary}) with gas fraction for the different nearby galaxy samples, including the DGS sample (highlighted with triangles). We here define the baryon mass and gas fraction as $M_{\mathrm{bary}} = M_g + M_*$ and $f_g = \frac{M_g}{M_* + M_g}$ respectively, where $M_g = 1.32\,M_{\mathrm{HI}}$ to take into account the mass of neutral helium. Due to the difficulty in obtaining homogeneous sample of CO maps for all the different samples considered here, particularly for low stellar mass sources, we do not take into account any molecular component. This assumption is sensible if the HI mass dominates the total gas mass. Indeed, to affect the subsequent discussions in this chapter, the molecular mass would have to be larger than the HI mass, which does not agree with the observed $M_{\mathrm{HI}}/M_{\mathrm{H_2}}$ ratios for our sources (Appendix A). In Figure A.2 we illustrate the expected difference from including molecular gas masses to the relation of dust-to-baryonic mass ratio (M_d/M_{bary}) with gas fraction. Our conclusions are unaffected.

Figure 6.6 is an excellent starting point as it tracks the relative changes in dust mass in terms of the evolutionary state. As previously discussed, the total dust content of a galaxy changes as it evolves and the dust-selected and stellar mass selected galaxies are well fit by a simple model of a galaxy with stardust and no inflows or outflows. M_d/M_{bary} follows a tight relation at low gas fractions. However at high gas fraction there is more scatter, at least in part due to differences in the contributions from the different dust sources. In Figure 6.6, we again show how the observations from the different samples compare with a chemical evolution track with a SFH consistent with the Milky Way (Yin et al., 2009). In Figure 4.8 we used the same track as in C15, though here we use our updated code (Model I, Table 6.3).

We see that the observed increase and decrease in $M_d/M_{\rm bary}$ with gas fraction for the HRS, HIGH-high and HAPLESS samples is well-matched within the scatter of the data, albeit with a small offset in the maximum $M_d/M_{\rm bary}$. We note that our model peaks at a lower gas fraction (~ 0.3) than in C15 and Figure 4.8 due to the changes made to the assumptions and dust inputs described in Section 6.3. Indeed, as our model has less dust injection from supernovae but the same dust injection from low-intermediate stars compared to Rowlands et al. (2014b), this shifts the peak $M_d/M_{\rm bary}$ towards lower gas fractions. In this work we assume a dust condensation efficiency for LIMS of 0.45. Morgan & Edmunds (2003) show that the dust condensation efficiency of LIMS can range between 0.16-0.45, though the latter value is closer to the high condensation efficiencies from theoretical models of dust formation in stellar winds (Zhukovska et al., 2008; Ventura et al., 2012). By choosing a lower value for the dust condensation efficiency we can obtain a better fit to $M_d/M_{\rm bary}$ at low gas fractions for the closed box model of C15.

Although galaxies are more complex than this simple model, Model I does explain the overall trend in these samples at gas fractions $> 50\%$. However, it does not fit the data well for all sources at gas fractions below this. Model I also shows a steep rise in $M_d/M_{\rm bary}$ at the highest gas fractions ($f_g > 90\%$). In Figure 6.6, we see that the highest gas fraction galaxies ($f_g > 85\%$, HIGH-low) have significantly lower $M_d/M_{\rm bary}$ than expected from Model I. We note, however, that these galaxies have large error bars due to unconstrained dust temperatures from the MAGPHYS fitting. In order to ensure the offset in $M_d/M_{\rm bary}$ for these sources is not due to this, we stacked the MIR-submm fluxes for the 8 HIGH-low sources with poorly constrained temperatures. The resulting stacked SED is well fitted by a single modified blackbody curve with dust temperature $T \sim 35$ K. The lower dust masses for these sources are therefore consistent with them having warmer dust temperatures than the HAPLESS and HRS sources (on average). However, it is possible that a different set of chemical model properties are necessary to explain this slower build-up of dust for these high gas fraction sources, we will test this in Sections 6.4.2-6.4.4.

6.4.2 Relaxing the closed box assumption

Figure 6.6 now compares the $M_d/M_{\rm bary}$ of these samples with different chemical evolution tracks including different SFHs and/or relaxing the closed box assumption from Model I (Models II-VI, Table 6.3). We also add the DGS sample (highlighted with triangles). There are significant differences between some of the models and the data, especially at $f_g \sim 80\%$. Here we clearly see that even for the same gas fraction, in this regime, nearby low M_* galaxies split into two categories: dust-rich and dust-poor and require *different chemical evolution models* to explain their dust-to-baryonic mass properties. Models I-III show a steep rise in

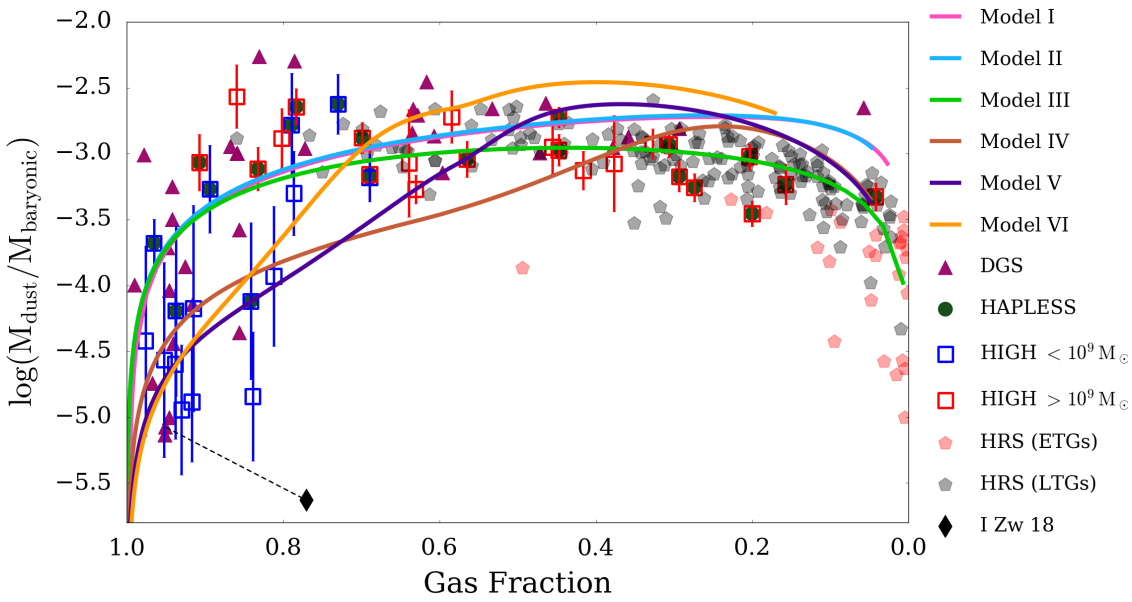

Figure 6.6: Variation of $M_d/M_{\rm bary}$ with gas fraction for the nearby galaxy samples in this work. The solid lines show how galaxies with the same initial gas mass but different combinations of SFHs, inflows, outflows and dust sources evolve as the gas is consumed into stars (Models I-VI defined in Table 6.3). Models I and II overlap on this plot. The observed properties of dust-poor local galaxy I Zw 18 (black diamond) are also added for comparison (Fisher et al., 2014), with dashed line indicating where this source 'moves' using the methods and calibrations in this work.

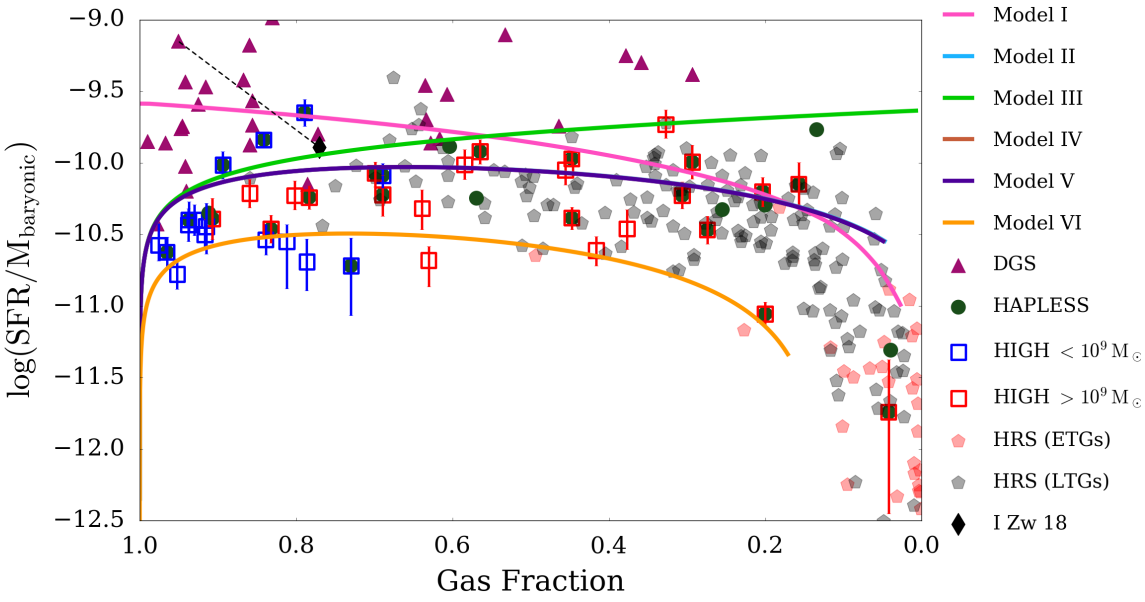

Figure 6.7: SFR$/M_{\rm bary}$ against the gas fraction reveals the need for delayed SFH (Models II-VI) at high gas fractions. In this parameter space, Model II overlaps with Model IV and partly with Model V as they have the same SFH and their inflows and outflows are balanced. At low gas fractions, a model with only outflows of gas (Model III) has a continuous rise in SFR$/M_{\rm bary}$ due to the ejection of gas from the system, this model does not match the data.

$M_d/M_{\rm bary}$ at the highest gas fractions ($f_g > 95\%$). Given the scatter in the observations, we cannot distinguish between Models I-III at the high gas fraction regime when trying to interpret the HAPLESS, HIGH-high, HRS or some of the DGS sources. Even though the SFH for models I and II are very different (Figure 6.5), their chemical evolution tracks in Figure 6.6 nearly overlap. Independent of the shape of the SFH, the chemical evolution model results predict similar changes in the dust content of galaxies as they evolve from gas-rich to gas-poor when normalised by baryonic mass.

To reach the regime where the dust-poor HIGH-low and DGS sources are (and to explain their flatter increase in $M_d/M_{\rm bary}$ with f_g), we have to signficantly reduce the amount of dust from stars (e.g. Models IV - VI)[7]. Models IV-VI therefore require a reduction in the dust production in SNe by a factor of 6-25 compared to the models required to fit the HRS, HIGH-high and HAPLESS. At late times (low gas fractions), Models I and II overestimate the amount of $M_d/M_{\rm bary}$ and require inflows and dust-rich outflows of gas (Models III-VI) or a reduced dust contribution from LIMS (e.g. a condensation efficiency of 0.15 instead of 0.45) to explain the observed properties.

Note that in Figure 6.6 we also highlight the well-studied galaxy I Zw 18 (part of the DGS sample) thought to be a local analogue of low-metallicity, high-redshift systems (e.g. Herrera-Camus et al. 2012; Fisher et al. 2014). The location of this source on this $M_d/M_{\rm bary}$ 'scaling relation' (and in later sections) is indicated by the black diamond using the measured properties from Fisher et al. (2014). As we have re-evaluated the DGS measurements to be consistent across all samples (Section 6.4.6), we have indicated where this galaxy moves with our revised measurements (dashed line). We will see in later sections that the dust properties of I Zw 18 are entirely consistent with its gas fraction and metallicity.

6.4.3 Star formation rates and gas mass

Next we briefly attempt to explain the observed SFR properties with these models by comparing the change in SFR$/M_{\rm bary}$ with gas fraction. Figure 6.7 compares the HAPLESS, HRS, HIGH, and DGS samples. In the high gas fraction regime ($f_g > 80\%$), we see that Model I overpredicts the SFR$/M_{\rm bary}$, particularly in comparison to the HIGH-low sources. Delayed SFH models provide a closer match to this sample (as used in Models II-VI) by reducing the SFR per unit baryonic mass at early evolutionary stages. The values of the delayed SFHs in Figure 6.5 and Eq. 6.5 were chosen to match the data in Figure 6.7, with Model VI reaching the HIGH-low

[7]Note that changing the IMF to a more bottom heavy form, e.g. Salpeter, would reduce the dust and metals produced in the first generation of stars. However as the observations are determined using a Chabrier IMF, we would also have to scale these by the appropriate factor between Chabrier-Salpeter. A more bottom heavy IMF therefore does not explain the dust-poor sources.

regime. In models with strong outflows but no inflows (Model III), the baryonic mass is significantly reduced at low gas fractions, and therefore SFR/$M_{\rm bary}$ increases as the gas fraction decreases. Model III thus poorly matches the observed SFR/$M_{\rm bary}$ at low gas fractions and can be discarded as an unrealistic model. However, when the outflow is matched by an equal inflow as in Model V, $M_{\rm bary}$ stays constant and we find the same SFR/$M_{\rm bary}$ track as for the same model without inflows and outflows (ie Models II, IV and V overlap in Figure 6.7).

The DGS sources lie significantly above the HRS, HIGH and HAPLESS samples, with higher SFR/$M_{\rm bary}$ for the same gas fraction. This can be explained given the different SFRs and gas fractions of the DGS with respect to HIGH-low and HAPLESS sources with similar stellar masses. The DGS has a lower average gas fraction of 0.74 than HIGH-low (0.87, Table 6.1) due to the latter having more atomic gas on average (as expected given this sample is HI-selected). At the highest gas fractions, the HIGH-low and DGS offset is explained by their SFRs: while the SFR in the DGS sample spans four orders of magnitude and includes many quiescent objects, it tends to contain more actively star-forming galaxies (average SFR $1.39\,{\rm M}_{\odot}\,{\rm yr}^{-1}$, Table 6.1) than is typical of nearby dwarfs (e.g. Hunter et al. 2012). Their selection towards more star-forming, low-stellar mass systems could be a consequence of their original selection of galaxies with moderate to very low PT05 metallicities. We return to this in the next section. The intensely SF nature of the DGS was highlighted in Zhukovska (2014) where they found they required bursty SFRs similar to the one in Figure 6.5 to fit the gas and dust properties of these dwarf galaxies. Even with the revised dust masses and metallicities and the different model assumptions in this work, we also find a bursty SFH is required to fit the DGS properties (Section 6.4.6). This demonstrates that despite having similar stellar masses, dust temperatures and gas fractions as the HIGH-low sources, the DGS are more actively star forming than the HIGH galaxies and *do not appear to be the same sources at a different evolutionary stage*. However, we cannot rule out that DGS and HIGH-low are both part of the same evolutionary sequence, with DGS sources undergoing a burst and HIGH-low sources in a quiescent period between bursts. The HIGH-low and HAPLESS samples therefore complement the DGS and provide additional, new, information of more normal star-forming systems with low Z, high f_g, and potentially different dust properties.

6.4.4 The dust-to-gas ratio with metallicity

We next wish to compare how the metallicity of galaxies changes as they evolve from high to low gas fractions. The chemical evolution code traces both the total metal mass fraction Z and the oxygen mass, we can directly convert the models to oxygen abundance using:

$$12 + \log\left(\frac{\mathrm{O}}{\mathrm{H}}\right) = 12 + \log\left(\frac{\mathrm{oxygen\,mass}/16}{\mathrm{gas\,mass}/1.32}\right) \tag{6.6}$$

In Figure 6.8 we see in both the model behaviour and the observations that, in general, the metallicity increases monotonically as galaxies evolve from high to low gas fractions, consistent with an increasing dust-to-gas ratio with increasing Z as gas is consumed into stars. The models are almost indistinguishable at gas fractions $> 80\%$ in this parameter space, even when changing the SFH (Models I, II, VI and VII, Figure 6.5). When comparing with the chemical evolution tracks at low gas fractions, Models I and II clearly overestimates the amount of metals. As with the observed $\mathrm{SFR}/M_{\mathrm{bary}}$ trend, this suggests models with moderate outflows of enriched gas and metal-poor inflows are necessary (Models V-VI).

In the high gas fraction regime, Models I-VI have difficulty reproducing the high metallicities derived using the N2 and KE08/TO4 calibrators. As Morales-Luis et al. (2014) showed that the N2 calibrator overestimates the oxygen abundance for the most metal-poor galaxies, we note for the rest of this work, that N2 and KE08/T04 methods should be thought of as upper limits for the lowest metallicity galaxies in HIGH-low and DGS. The PG16S calibrator is well-matched by the models at all gas fractions when both inflows and outflows are included.

Figure 6.8 also shows that the HRS galaxies are more metal-rich at a given gas fraction than the DGS, HIGH-low and HAPLESS sources, regardless of whether using the N2, KE08/T04 or PG16S calibrators. The high gas fraction DGS sources and HIGH-low lie approximately on the same general trend with increasing metallicity with f_g as the HRS and Models I-VI, consistent with their high gas fraction (early stage). However, the DGS appears to have lower metallicities than the HRS at low gas fractions and, to a lesser extent[8], the HIGH-low sources at high gas fractions, i.e. *the DGS are, on average, more metal-poor given their evolutionary state*. From Table 6.1, the average $\mathrm{SFR}/M_{\mathrm{HI}}$ for the DGS is ~ 20 times larger than both the HRS and HIGH-low samples, with SFR/M_d higher by ~ 300 compared to the HRS. If M_d is used as a proxy for the molecular gas, this suggests DGS sources have a higher star formation efficiency than the HRS, HAPLESS and HIGH sources. The DGS galaxies are thus, on average, more actively forming stars. The offset in the DGS towards low Z could be a consequence of their selection method. Selecting galaxies ranging from low to moderate metallicity at a given gas fraction could result in a sample selection biased towards galaxies with very high

[8]This offset is only seen in the N2 calibrator.

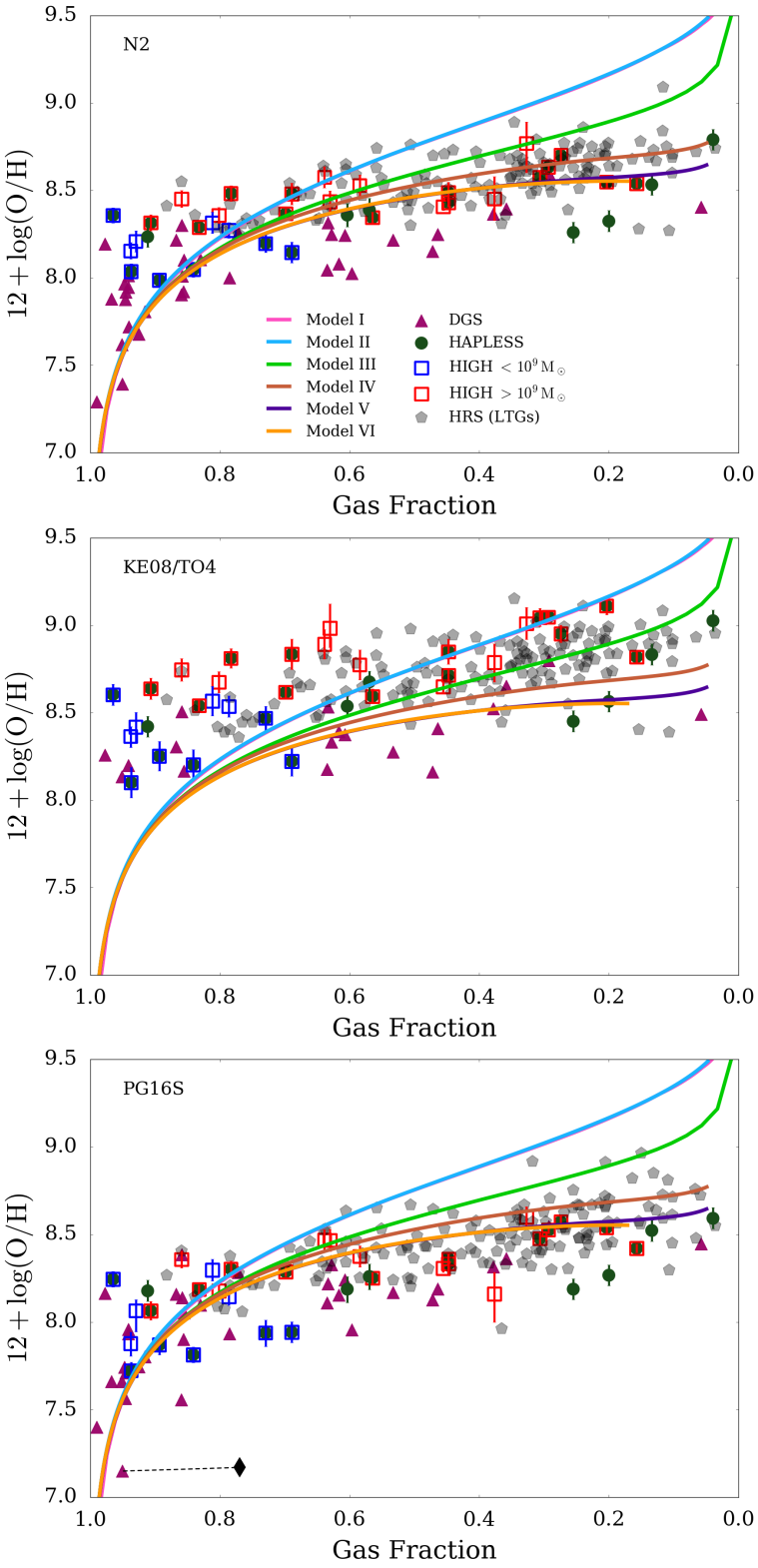

Figure 6.8: Metallicity variation with gas fraction for the different samples using the three different metallicity calibrations (from top to bottom: N2, KE08/T04 and PG16S). The error bars are derived by combining bootstrap uncertainties and an intrinsic scatter of 0.06 dex between fibres. The different chemical evolution models (see text and Table 6.3) are also included.

SFRs due to the mass-metallicity-SFR relation (Mannucci et al., 2010; Lara-López et al., 2013). Additionally higher SFR galaxies are brighter and thus easier to detect. This also explains why a bursty SFH (Zhukovska, 2014) is needed. Although this SFH may match the $M_d/M_{\rm bary}-f_g$ and SFR$/M_{\rm bary}-f_g$ properties, it does not explain their $Z-f_g$ properties. Indeed we find it very difficult to reach such low metallicites for a given gas fraction with any of our standard models (I-VI). As suggested in Feldmann (2015), this requires the addition of very strong inflows and outflows to regulate the build-up of metals in the DGS galaxies as they evolve towards lower gas fractions. The only model that explains the $Z-fg$ properties of the DGS sample is Model VII (Figure 6.11), with inflows and outflows a factor of 3 higher than the models (V and VI) used to match the other nearby galaxy samples in this work.

To increase or decrease the metallicity reached in these models, one can also vary the IMF. For example the offset between models and the HRS at low gas fractions in Figure 6.8 could potentially be explained by changing the model IMF to a Salpeter or bottom-heavy function (e.g. Cappellari et al. 2012). Similarly at high gas fractions, a top-heavy IMF in the model could increase Z. But to change the model IMF we must also scale the observational parameters which have been determined using the Chabrier function. For example, using a top-heavy IMF with slope $\alpha=-1.5$ (Cappellari et al., 2012; Madau & Dickinson, 2014b) we would have to scale the dust mass by a factor of 3, and the stellar mass and SFRs by a factor of 0.32 (Michałowski, 2015). When we do this, we find a slight improvement in comparing the models and data at high f_g for the N2 and KE08/T04 metallicities but this is well within the scatter, indeed this model is indistinguishable (in terms of a 'good-fit') from Models IV-VI. Similarly there is no strong evidence for a Salpeter IMF to explain the metallicities of the low gas fraction sources.

Next we compare metallicity with the dust-to-gas ratio (Figure 6.9). For the DGS, HRS and HAPLESS we see that, in general, galaxies with high dust-to-gas ratios are also sources with high metallicity (as expected if dust traces the metals or a constant fraction of metals remain in dust grains). Some of the galaxies follow a linear trend in increasing dust-to-gas ratio as the metallicity increases, which is well-matched by Models I-III (models with different SFHs are indistinguishable in this parameter space if there is no dust grain growth).

Some of the HIGH-low and DGS sources are consistent with the linear M_d/M_g-Z relationship, though others are offset from these linear trends. For low stellar mass sources, we observe galaxies that are dust-poor given their metallicity regardless of which metallicity calibrator is used (though the N2-derived values are likely upper limits). Thus we caution the use of dust masses as a method to derive gas masses, since in these galaxies, the available atomic (or total) gas mass is not a good tracer of the dust. We also caution against statements made in the

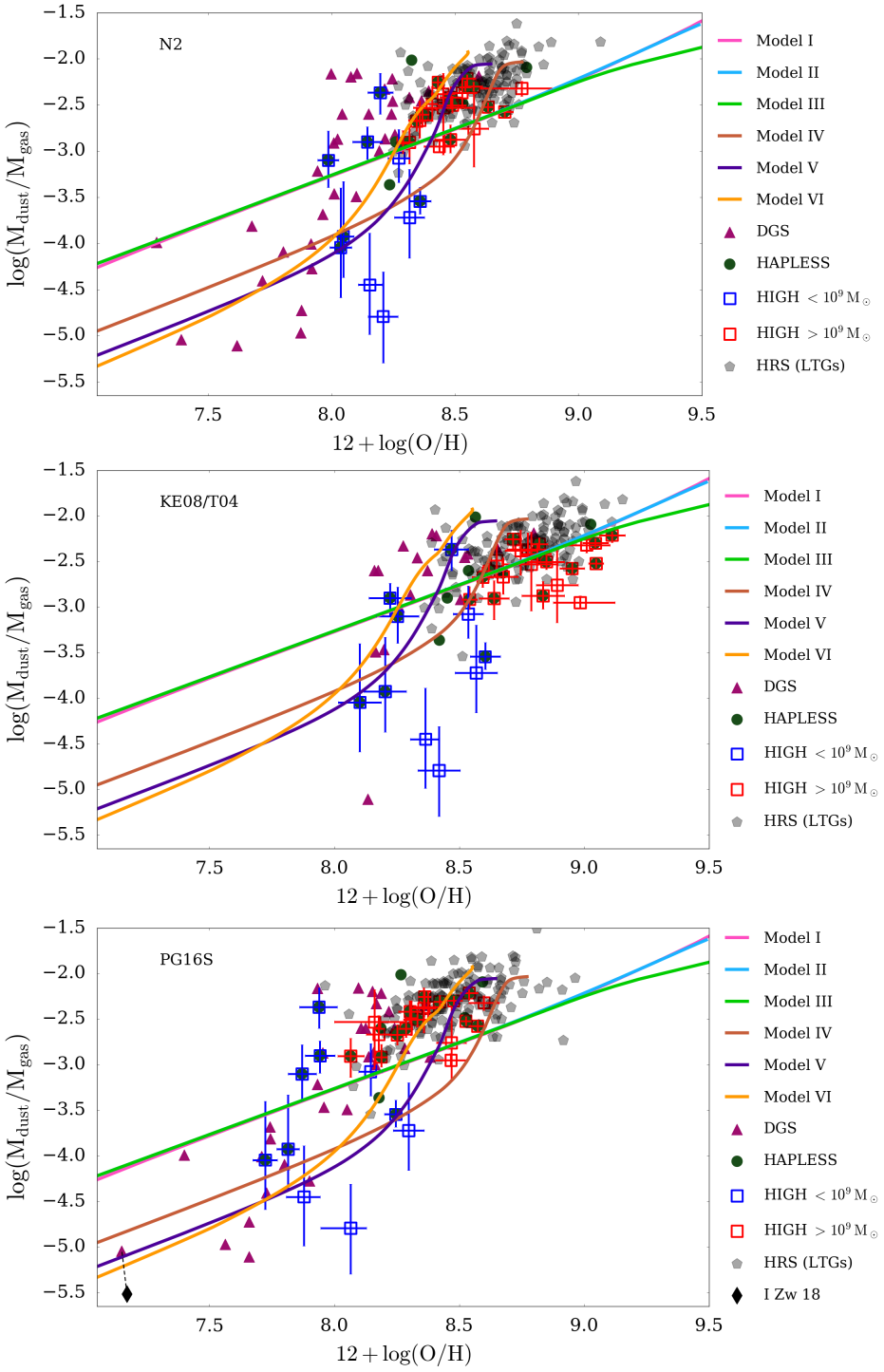

Figure 6.9: Metallicity variation with gas-to-dust ratio M_d/M_g with the three different metallicity calibrations shown in Figure 6.8. Models IV, V and VI provide a better match between metallicity and M_d/M_g for the HIGH-low and many DGS sources than Models I-III. Note that metallicities derived using N2 (and therefore KE08/T04) for the most metal-poor systems are likely to be upper limits.

literature regarding that low metallicity galaxies are always dust-poor (particularly when using local systems such as I Zw 18 as analogues for high-redshift galaxies).

This offset from the linear trends was already discussed in Rémy-Ruyer et al. (2013; 2014; 2015); Zhukovska (2014), who explained this by suggesting the supernova contribution to the dust budget needs to be reduced and a dust grain growth term added. Feldmann (2015) also used reduced supernova dust yields and added dust grain growth to reach the higher dust content at later evolutionary stages. In contrast to Zhukovska (2014), Feldmann (2015) even uses reduced supernova dust yields for sources that are not dust-poor given their metallicity. Instead they use extremely fast dust grain growth to obtain the steep rise in dust content at the earliest stages of galaxy evolution. There is thus a degeneracy between using a significant contribution from supernova dust, and using very fast dust grain growth. Their gain growth timescales of ~ 5 Myr are much faster than typically found in nearby galaxies (Mattsson et al., 2012; 2014) or from basic theoretical calculations of the underlying growth rate (Draine, 2009). Here we will show that our HIGH-low sample also requires a reduced supernova dust production compared to MW-like models (required to fit the HRS) despite having star formation properties that are an order of magnitude lower than the DGS sources. The argument is such: for the highest gas fraction galaxies in Figure 6.9 the dust mass needs to be significantly suppressed without reducing the metals. The only way to do this is to reduce the amount of dust formed by stars in each stellar population. As the dust-to-gas ratio is already lower than expected from a linear trend at high gas fractions, this suggests the SN dust production must be suppressed.

Therefore Models IV, V and VI include a reduced SN dust component (by a factor of 6-25 in mass, Table 6.3) compared to the MW model. Since there is less stardust in these models, if we require galaxies to ultimately evolve to the typical dust-to-gas ratios observed at low f_g (Figure 6.9), we need to also include interstellar grain growth. This dust source is strongly metal-dependent and only becomes important once the galaxy reaches a critical metallicity (Asano et al., 2013a), this means that different values of the grain growth parameters ε, and consequently $\tau_{\rm grow}$, would move the model tracks. An increase of ε will steepen the slope of M_d/M_g (shown by Models IV-VI as they reach the end of their tracks); any offset from the linear trend in Figure 6.9 can therefore be mitigated by changing ε such that grain growth starts at a lower metallicity (thereby increasing the dust-to-gas ratio). Alternatively, offsets in Figure 6.9 can also be explained through the use of different bursty SFHs, because long quiescent phases allow accretion of existing metals after short active enrichment episodes (Zhukovska, 2014).

To summarize this section, the best matches for explaining the observed evolution in $M_d/M_{\rm bary}$, SFR$/M_{\rm bary}$, and now metallicity with gas fraction for most of the galaxies in our

sample are Models IV-V, while a better fit for HIGH-low can be obtained with Model VI. The DGS sources require more extreme SFH and outflows (Section 6.4.6, Model VII).

6.4.5 Dust-to-metal ratio

We use our larger sample at low Z to further support the Feldmann (2015) result that the dust-to-metal ratio varies as a function of metallicity. For HRS, the average $M_d/M_Z = 0.32, 0.46, 0.51$ for the N2, KE08/T04, PG16S calibrators respectively and for HIGH-low we find a much lower dust-to-metal ratio for each calibration ($M_d/M_Z = 0.07, 0.09, 0.10$ respectively). The location of the low stellar mass samples (HIGH-low and DGS galaxies) is contrary to what we would expect if stellar sources were the dominant source of dust in the galaxies, which again shows we cannot model these sources without grain growth. We note that the Milky Way and other low gas fraction sources are also poorly matched by Model I. Feldmann (2015) attributes the rising dust-to-metal ratio to requiring a balance between strong enriched inflows and unenriched outflows, and extremely efficient interstellar grain growth (timescale of ~ 4 Myr). Instead we also acquire a decent match using the less extreme Models IV, V and VI, which have reduced stellar dust production (by a factor of $6-25$) and moderate inflows, outflows and dust grain growth. Our models are more similar to those proposed in Zhukovska (2014), yet for normal star forming galaxies.

6.4.6 Model for the Dwarf Galaxy Survey

We can model the properties of the DGS sources by including strong inflows and outflows (Feldmann, 2015) and a bursty SFH (Figure 6.5, Zhukovska, 2014) in the chemical evolution (Model VII). The results are shown in Figure 6.11 using the original DGS metallicities (transparent triangles), and the revised PG16S metallicities derived in this work. In the top-left panel, we compare the $M_d/M_{\rm bary}$ of the DGS with Model VII (as we did with the HRS, HIGH and HAPLESS in Figs 4.8 & 6.6). Model VII matches the observed trend well. In the top-right panel of Figure 6.11, we compare the predicted SFR$/M_{\rm bary}$ with gas fraction for Model VII. Here we see that the bursty model is required to explain the elevated SFR$/M_{\rm bary}$ of the DGS galaxies compared to the HAPLESS, HRS and HIGH samples. In the bottom-left panel, we find the observed metallicities for DGS tend to be lower than for the other samples and are well-matched by Model VII, due to including strong inflows and outflows at a rate of 6 times the SFR. The observed steep rise in $M_d/M_{\rm HI}$ with gas fraction is similar to the trend for Model VII in Figure 6.11 (bottom-right). Note the steep rise in the model $M_d/M_{\rm HI}$ at a $12+\log({\rm O/H}) \sim 7.6$, due to an inactive period during which dust grain growth produced dust,

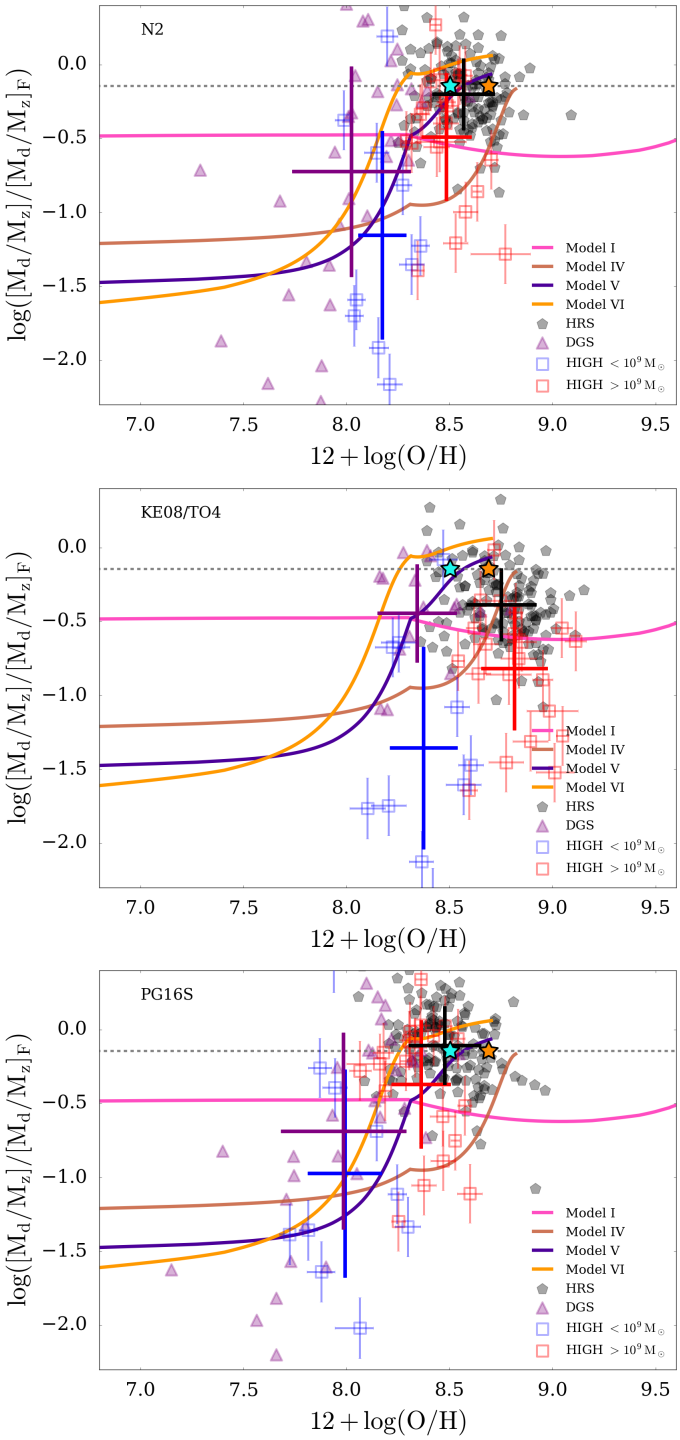

Figure 6.10: Dust-to-metal ratio versus metallicity (to allow comparison with Feldmann (2015), we use a normalisation of $[M_d/M_Z]_F = 0.7$) for HiGH, HRS, HAPLESS and DGS. The normalisation in Feldmann (2015) is given by their model M_d/M_Z at solar metallicity. Models with stardust only (Model I) predict an almost constant dust-metals ratio and do not match the low M_d/M_z at low metallicities. However, Models with grain growth and reduced supernova dust (Models IV-VI) show the observed increase in M_d/M_z with metallicity. The large crosses show the mean $\pm$ standard deviation of dust-to-gas within the samples. We also highlight the MW ($M_d/M_Z = 0.5$, orange star) and recent estimates for galaxies in the Virgo Cluster (Davies et al., 2014, cyan star).

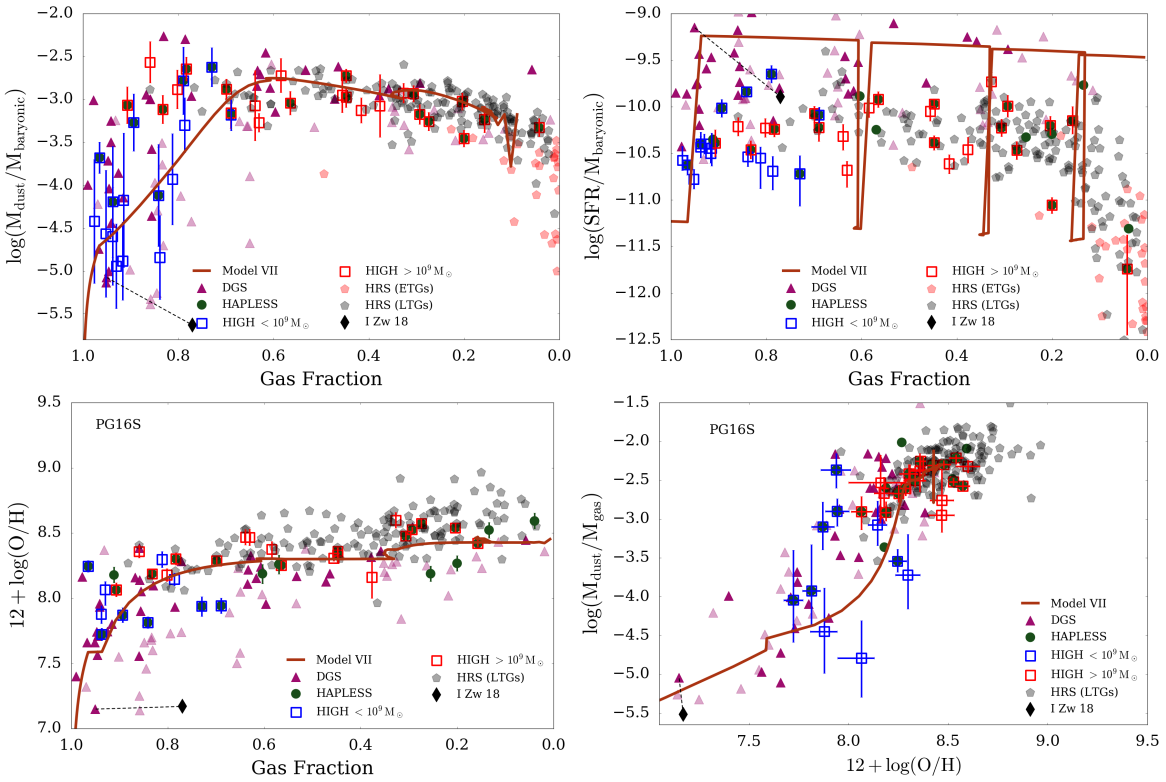

Figure 6.11: *Top:* $M_d/M_{\rm bary}$ and SFR$/M_{\rm bary}$ evolution with gas fraction using the bursty SFH in Figure 6.5. *Bottom:* the metallicity variation is compared with gas fraction (*left*) and $M_d/M_{\rm HI}$ (*right*). The chemical evolution model shown is Model VII which requires a bursty SFH to provide a good fit to the DGS galaxies (see also Zhukovska 2014 and Rémy-Ruyer et al. 2015). As shown in Feldmann (2015), the observed metallicity of the DGS galaxies can be explained by a chemical model that incorporates strong inflows and outflows of gas.

but there is little star formation. It is possible to use different SFH that lead to an increases in $M_d/M_{\rm HI}$ that is enough to reach the high $M_d/M_{\rm HI}$ DGS sources (Zhukovska, 2014).

6.5 Discussion

In order to get satisfactory fits to the observed $M_d/M_{\rm bary}$, SFR$/M_{\rm bary}$, $12+\log({\rm O/H})$, M_d/M_g and M_d/M_Z for the different nearby galaxy samples in this work, it is necessary to reduce the SNe dust contribution (by a factor of ~ 25) and including moderate inflows and outflows, dust destruction and moderate grain growth. For each of the parameters in Table 6.3, we have tried a range of different values. The combinations of the various parameters leads to a large number of models. For brevity, we have chosen Models I-VII as good representations for the sampled parameter-space. The chosen models provide satisfying fits to the observed data, though our aim is not to find the best possible fit, but rather to study the global effects of varying the used

parameters, especially in terms of determining the contributions from the different sources of dust. We have focussed on modelling the dust sources for low metallicity sources, both for normal star forming galaxies (HIGH-low) and very actively star forming galaxies (DGS). Model VI provides the best fit to the HIGH-low sources and Model VII best matches the DGS sources. In this section, we discuss how the parameter values for our models compare to observations and theoretical predictions.

In the absence of dust grain growth in the ISM, the average dust yield per SN required to explain dusty galaxies at high redshifts is of order $0.5-1\,M_{\odot}$ (Morgan & Edmunds, 2003; Abazajian et al., 2009). Initial measurements of the dust mass in SN remnants based on MIR wavelengths yielded small dust masses $M_d < 10^{-3}\,M_{\odot}$ (Sugerman et al., 2006; Kotak et al., 2009; Fabbri et al., 2011). However with the advent of *Herschel* and ALMA, it has become possible to detect the cold dust present in core-collapse supernovae (CCSN). This has increased the observed dust masses to $0.1-1.0\,M_{\odot}$ (Barlow et al., 2010; Gomez et al., 2012a; Matsuura et al., 2015; De Looze et al., 2016). These observations are in line with our models without grain growth for nearby galaxies: Models I-III correspond to core-collapse SNe producing $0.17-1.0\,M_{\odot}$ of dust per explosion. The theoretical model of nucleation of dust grains in supernova gas from Todini & Ferrara (2001) predicts condensation efficiencies of 0.2 - 0.8 for Type II CCSM, and can thus explain the dust content in many of the observed galaxies both at high and low redshift.

However, in order to model the dust-poor HIGH-low galaxies (Model VI), we have reduced the SN dust content by a factor of 25 and thus core-collapse SN produce $0.007-0.04\,M_{\odot}$ of dust per explosion. The observations of CCSN remnants seem to be in contradiction to the reduced SN contribution in Model VI. However, the reverse shock in the remnants of CCSN likely reduces the produced dust (Bianchi & Schneider, 2007; Gall et al., 2011a). Since most of the dust in observations of CCSN remnants has not gone through this shock yet, we expect the effective SN dust yields to be smaller. Bianchi & Schneider (2007) have revisited the model of Todini & Ferrara (2001) and used a semi-analytical model to describe the dynamics of the reverse shock and found a dust mass reduction that depends on the density of the surrounding ISM: for $\rho_{ISM} = 10^{-25}, 10^{-24}$ and 10^{-23} g cm^{-3} about 20, 7 and 2 %, respectively, of the initial dust mass survives. De Looze et al. (2016) have observed the dust in Cassiopeia A is mainly distributed interior to the reverse shock. They find the drop in dust mass implies 30% of the dust survives the reverse shock. In our models we are interested in how much of the dust survives into the ISM and thus need to account for destruction by the reverse shock. The Todini & Ferrara (2001) SN dust prescription used in our models does not include a correction for dust destruction by reverse shocks. The need to reduce the SN dust contribution in Models IV-VI could thus, at least in part, be due to dust destruction by the reverse shock. Another

potential explanation for the reduced SN yields are differences in the condensation efficiencies. Progenitor stars of different masses (and to a lesser extend different metallicities) have different condensation efficiencies (Todini & Ferrara, 2001). Differences in the IMF can thus carry through to differences in the average dust yields per SN. If the dust-poor HIGH-low galaxies have a different IMF than more evolved galaxies, this could help to explain the reduced SN dust contribution.

There is a growing number of studies that suggest significant amounts of dust grain growth are required to model observations in both high and low redshift studies (Dwek et al., 2007; Matsuura et al., 2009; Michałowski et al., 2010; Mattsson et al., 2012; Asano et al., 2013a; Grootes et al., 2013; Calura et al., 2014; Rowlands et al., 2014a; Zhukovska, 2014; Nozawa et al., 2015; De Cia et al., 2016). Additionally, if there is rapid dust destruction (timescale of the order of $\sim 100-500$ Myr have been predicted), then the majority of the dust grains must be (re-)formed there (Jones & Nuth, 2011), and dust grain growth in the ISM is necessary. On the other hand, Ferrara et al. (2016) point out the difficulties in obtaining high enough grain growth efficiencies to explain the observations. The subject of dust grain growth thus remains a debated subject. For Model VI, we find grain growth timescales ranging from 1 Gyr - 200 Myrs, similar to those quoted for the Milky Way and local galaxies(e.g. Asano et al., 2013a; Mattsson et al., 2012)). There is also evidence for shorter timescales (Draine, 2009; Zhukovska et al., 2008; Feldmann, 2015), which might be more appropriate for the more dust-rich sources at low-metallicity or higher metallicity sources. Variations in the dust growth timescales might also help to explain the differences between dust-rich and dust-poor sources at the same (high) gas fraction. If the reverse shock destroys the majority of the dust grains in CCSN for all galaxies (and not only the ones modelled well by Model IV-VI), then the higher dust mass sources (which are now fitted by Models I-III) could be explained by shorter dust grain growth timescales, and high dust mass can be reached in spite of a reduced SN contribution. In this scenario, all galaxies have a strongly reduced SN dust contribution compared to Todini & Ferrara (2001), and galaxies with short dust grain growth timescales result in a higher dust content (on the level of Model I), and galaxies with long dust grain growth timescales (such as in Model VI) will have a lower dust content at high gas fractions.

6.5.1 Caveats

In the previous sections we have build models to explain the dust properties in dust-poor low-Z sources, as well as dust-rich lower gas fraction sources. We acquire a good fit to the observations by reducing the stardust contribution by a factor of ~ 25 (particularly from core-collapse SNe) and including moderate inflows and outflows, dust destruction and moderate grain growth

(timescales ranging from 1 Gyr - 200 Myrs). In this section we discuss potential caveats of our approach.

- **Dust Emissivity** - If the dust emissivity is different across the samples, this could explain the reduced $M_d/M_{\rm HI}$ (Figure 6.9) and in M_d/M_Z (Figure 6.10). For the dust-poor HIGH-low sample to have a dust/metals ratio similar to the DGS, HRS and HIGH-high samples (i.e. $\sim 0.4-0.5$), κ would have to be $\sim$4 times lower (i.e. the dust in the HIGH-low and DGS galaxies would have to be less emissive than evolved spirals such as the MW). This is beyond the scope of this work.

- **Missing molecular gas** - We lack sufficient molecular gas information for the HAPLESS and HIGH samples. Though to remove the offset in dust-to-gas ratios observed in the HIGH-low sample, the molecular gas would need to dominate the total gas mass for all the other samples. This does not agree with observed molecular gas masses for the HRS and DGS (see also scaling relations from Saintonge et al. 2011 and Bothwell et al. 2014). In Appendix A, we estimate the H_2 content of HIGH and HAPLESS and illustrate the differences to the $M_d/M_{\rm bary}$ with gas fraction relation for the different samples. Using CO derived H_2 masses for HRS from Boselli et al. (2014a), we find that including the molecular gas component does not change the conclusions of our work, as $M_{\rm H_2}/M_{\rm bary}$ is small at all evolutionary phases. At low gas fractions, $M_{\rm H_2}/M_{\rm HI}$ is large for some sources, and subsequently these will shift to higher gas fractions and higher total gas masses when molecular gas is included. This shift results in a better fit to the Models at low f_g (e.g. Figure 6.9).

  To study the effects of molecular gas at high gas fraction, we took $M_{\rm H_2}$ for DGS from Rémy-Ruyer et al. (2014). These were derived by converting CO fluxes using a constant conversion factor $X_{\rm CO,MW}$ (Ackermann et al., 2011) or a metallicity-dependent conversion from CO $X_{\rm CO,Z}$ (Schruba et al., 2012). Using $X_{\rm CO,MW}$, we again find $M_{\rm H_2}/M_{\rm HI}$ is small for all but the lowest gas fractions. The small shift at low gas fractions again results in a better fit with the Models. However, if we use $M_{\rm H_2}$ derived using $X_{\rm CO,Z}$, we find significantly higher $M_{\rm H_2}/M_{\rm HI}$ at high gas fractions and thus again a shift towards higher gas masses and gas fractions compared to not including molecular gas masses. For the high gas fraction sources this results in a poorer fit to the models assumed here, though the offset does not change the conclusions of this work. However, we do not believe the metallicity-dependent conversion from CO used in Rémy-Ruyer et al. (2014) is realistic for the following reasons: I) The $X_{\rm CO,Z}$ values were determined using the PT05

metallicities, which we have found to be smaller than other metallicity calibrations[9]. II) Other $X_{\rm CO,Z}$ factors (see Bolatto et al. 2013 for a review) are also typically smaller than the used $X_{\rm CO,Z}$ from Schruba et al. (2012), and would thus result in smaller molecular gas contributions. III) Additionally Bothwell et al. (2014) found that low stellar mass sources have small $M_{\rm H_2}/M_{\rm HI}$, which is inconsistent with the metallicity dependent DGS results. If we therefore do not use the metallicity dependent $M_{\rm H_2}$, we find that molecular gas does not dominate the total gas and thus does not affect the conclusions of this work. Though even for the metallicity dependent $M_{\rm H_2}$, the $M_d/M_{\rm bary}$ relation with gas fraction is only weakly affected (Figure A.2).

6.6 Conclusions

In this chapter, we have brought together the HI-selected HIGH, dust-selected HAPLESS, stellar mass selected HRS and the metallicity selected DGS sources to provide the largest sample of nearby galaxies covering a wide range of gas fraction ($0.05 < f_g < 0.97$) and metallicity (over 2 dex). We derived their dust, stars, gas and metallicity properties in a consistent way. The low stellar mass HIGH-low galaxies share similar properties to many sources in the well-studied DGS sample (stellar mass, sub-Solar metallicities, high gas fractions), including being dust-poor relative to a linear M_d/M_g-metallicity relationship and having different dust-to-metal ratio compared to larger more evolved galaxies. In this work, we have introduced 377 sources from HIGH, HAPLESS and the HRS. We have increased the number of sources with less than $1/5\,Z_\odot$ by 15 galaxies, and we have an additional 67 sources less than $1/3\,Z_\odot$ compared to the 126 sources (including 37 DGS sources with $Z < 1/5\,Z_\odot$) from Rémy-Ruyer et al. (2014). We have therefore increased the sample size in the critical range where sources lie off the typical published scaling relations, derived from benchmark studies of local galaxies with *Herschel* (e.g. the HRS), in terms of their dust-to-gas and dust-to-metal trends with metallicity.

Following Zhukovska (2014) and Feldmann (2015), we have investigated the dust trends of these samples using an updated version of the chemical evolution model of Rowlands et al. (2014b) and Morgan & Edmunds (2003). We have taken extra care in deriving appropriate metallicities, which is key given the importance of metallicity to discriminate between different chemical evolution models and dust sources. Additionally, we use gas fraction as a proxy for the evolutionary state. This allows us to track and constrain the build-up of dust and metals as

[9]The $X_{\rm CO,Z}$ description from Schruba et al. (2012) was calibrated with metallicities using the average of two calibrations: PT05, and a theoretical calibration (Kobulnicky & Kewley, 2004) which produces higher metallicities than PT05. The average metallicity used in Schruba et al. (2012) will thus be larger than the PT05 metallicities used to determine $X_{\rm CO,Z}$.

gas is converted into stars, from very high ($f_g = 0.97$) to very low ($f_g = 0.05$) gas fractions. We find that:

- There are significant differences between different metallicity calibrations in the literature. By comparing the N2, PG16S and KE08/T04 calibrations, we are able to judge the uncertainty in the metallicity relations in this work. We find PG16S is the most reliable calibration for the low metallicity sources, and shows less scatter with other calibrations and stellar mass than the PT05 calibration often used in literature (and indeed for Zhukovska 2014 and Feldmann 2015) for low metallicity sources.

- DGS sources are selected to have low metallicities, which consequently leads to a selection of very actively star forming galaxies. These sources require a bursty SFH as originally shown in Zhukovska (2014). For a given gas fraction or stellar mass, we have found our low M_* HIGH and HAPLESS samples to be more normal in terms of star formation properties and metallicity. Our samples thus complement the DGS, and provide additional, new information on more normal star-forming galaxies in the nearby Universe. Delayed star formation history models are necessary to match the evolution of $\mathrm{SFR}/M_{\mathrm{bary}}$ for our normal star-forming galaxies.

- To model the dust-poor HIGH-low sources, we follow Zhukovska (2014) and Feldmann (2015) and relax the closed box assumption, reduce the contribution from supernova dust, and include dust grain growth in our model. We can model the dust-poor HIGH-low sources using either moderately reduced (factor of 6) supernova dust and moderate (timescale of ~ 750 Myr) dust grain growth, or strongly reduced (factor of 25) supernova dust and fast (timescale of ~ 200 Myr) dust grain growth. There are also relatively dust-rich high gas fraction sources, that either have a non-reduced supernova dust contribution, or reduced supernova dust and extremely fast (timescale of ~ 5 Myr) grain growth (as in Feldmann 2015).

- In order to reproduce the observed metallicity, particularly at low gas fractions (late evolutionary stages e.g. the HRS sources), metal-poor inflows and metal-rich outflows of gas at a rate of twice the SFR are required to keep the metallicity from rising to higher than observed metallicities. The DGS requires inflows and outflows at a rate of 6 times the SFR (Model VII).

- The M_d/M_g ratio correlates with the gas-phase metallicity over a wide range $7.5 < 12 + \log(\mathrm{O/H})_{\mathrm{PG16S}} < 9.0$. However we find that low metallicity galaxies can have dust properties that (a) are consistent with a linear $Md/Mg - Z$ relationship or (b) dust masses well below this trend. Zhukovska (2014) showed the scatter in this relation can be

produced by using different bursty SFHs. Instead, we show differences in the strength of the contribution of supernova dust, as well as differences in the dust growth time-scales and galactic winds (and thus critical metallicity) also produce the observed scatter.

In summary, we have found a very small dust content for some of the high gas fraction, low metallicity sources in our sample. Instead of attributing this result to requiring a balance between metal-poor inflows and enriched outflows with extremely efficient interstellar grain growth (timescales of Myrs needed), as in Feldmann (2015), we suggest a simpler solution following Zhukovska (2014). The small dust content of low-Z sources is driven by reducing the stardust contribution by ~ 25 (particularly from core-collapse SNe as the reduced dust component has to act at very high gas fractions) with moderate outflow, dust destruction and less extreme grain growth (timescales ranging from 1 Gyr - 200 Myrs similar to those quoted for the MW and local galaxies; Draine 2009; Asano et al. 2013a; Mattsson et al. 2012; 2014). We show this model (Model VI) is consistent with all of the observed properties of the HIGH-low sources, the first normal star forming population of low stellar mass galaxies studied in this way. Combined with a bursty SFH (as shown originally in Zhukovska 2014) and three times stronger outflows (Feldmann, 2015, Model VII), this scenario is also consistent with the DGS galaxies at similar f_g, M_* and Z (Figure 6.11).

Part III

HI-stacking

Chapter 7

Studying HI properties of galaxies out to z = 0.1 with HI-stacking

7.1 Introduction

It has been shown (Fabello et al., 2012; Delhaize et al., 2013) that it is possible to get meaningful statistical results by using average ('stacked') HI profiles of large samples of individually undetected galaxies out to $z \simeq 0.13$. In Part I of this thesis, we studied the dust and HI content for local galaxies out to $z \simeq 0.04$ for HI-detected galaxies in the equatorial H-ATLAS fields. Here we will extend the redshift-range over which the HI content can be studied in the same fields by using spectral stacking of sources with $0.04 \leq z \leq 0.11$. Our methods are in line with Delhaize et al. (2013, hereafter D13) and we use an adapted pipeline based on their work for the stacking and extraction of spectra (Delhaize, *priv. comm*). We use the same observations as presented in Delhaize (2014, hereafter D14), yet here we focus on stacking dust-selected sources. There is significant RFI contamination in the observations, which requires additional care to remove.

Due to the large Parkes beam, multiple galaxies often lie within the same beam and redshift range, and their HI profiles cannot be distinguished. These galaxies are 'confused', and we need to correct the HI signal of each source to account for this. We also encountered this issue at low redshifts (Section 2.3.2), though at higher redshift this issue is much more severe. An average of five galaxies are confused for each Parkes pointing, and consequently we have determined deconfusion factors to correct each signal. There are a number of uncertainties in our method (especially for the RFI subtaction, baseline subtraction and deconfusion method) that require further thought. This investigation is thus currently still in progress.

Section 7.2 overviews the observations and methods for stacking 21 cm spectra, which will be used throughout the following sections to obtain significant HI detections for individually undetected sources. Section 7.3 discusses how we deconfuse the HI signals in order to get meaningful results for individual sources. In Section 7.4 we present our preliminary results and compare stacks for 1325 dust-selected and 4118 stellar mass selected sources. Finally, in Section 7.5 we discuss some caveats to our method and Section 7.6 lists our conclusions.

7.2 HI-stacking methods

7.2.1 21 cm observations and extracted spectra

The 21 cm observations used in this work were conducted with the Parkes telescope and are presented in D14. In this section we briefly summarise the observations and data reduction. We use observations for the GAMA-I (Baldry et al., 2010) G09 and G15 fields. G12 is not suitable for stacking as it is close to the bright radio continuum source 3C 273 which would strongly contaminate the HI observations. The GAMA-I G09 and G15 each cover $12 \times 4\,\mathrm{deg}^2$, but not the additional $12 \times 1\,\mathrm{deg}^2$ provided by GAMA-II (see also Figure 2.1). There is considerable overlap with the G09 and G15 H-ATLAS fields, yet currently the additional GAMA-II strip is lacking.

The observations were obtained over a total of 175 and 78 hours for G09 and G15 respectively, with an estimated 104 and 61 hours on-source integration. An identical observing strategy to that of D13 was used. Two 64 MHz bands were centred on 1285 MHz and 1335 MHz, providing a 14 MHz band overlap to reduce the impact of the bandpass subtraction. This resulted in a bandwidth coverage of 1253-1367 MHz and a 62.5 kHz frequency channel spacing (125 kHz after Hanning smoothing). Radio Frequency Interference (RFI) in the data was identified and flagged using the default strategy of the RFI-removal software AOFLAGGER (Offringa, 2010; Offringa et al., 2012). The fraction of RFI occupancy in the data per spectral channel is shown in Figure 7.1. There are multiple narrow-band RFI signals present (e.g. 1312 MHz and 1316 MHz). Additionally there is a wide band of severe RFI centred on 1275 MHz, which is caused by a navigation satellite and worsened over time as the satellite system advanced. We therefore do not use any G09 data at frequencies below 1280 MHz, nor any G15 data at frequencies below 1290 MHz. This limits the usable data for this work to $z < 0.109$ for G09 and $z < 0.101$ for G15. Even below this redshift, AOFLAGGER does not get rid of all RFI and additional channels need to be flagged manually to remove the residual RFI. The reduced data are gridded to a pixel size of $4' \times 4'$. The resolution of the gridded Parkes data is $15.5'$ ($14.4'$ before gridding).

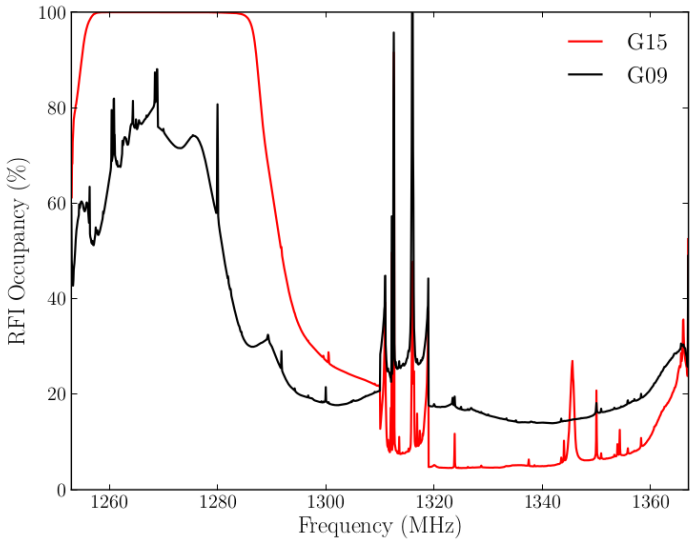

Figure 7.1: The percentage of data flagged by AOFLAGGER due to RFI presence per spectral channel in the G09 (black) and G15 (red) Parkes data. This image was taken from Delhaize (2014).

For each source in our sample, we extract the full 1250 – 1365 MHz spectrum from the data cubes using weighting according to the beam shape. Following D13, this weighting is done in such a way the SNR of the spectrum is optimised, yet this results in an expanded effective beam width of $21.2'$. The observed fluxed in each channel can be converted to $M_{\rm HI}$ per unit of frequency ($M_{\rm HI}$ spectrum) in the observed frame:

$$M_{{\rm HI},\nu_{\rm obs}} = 4.98 \times 10^7 \; D_L^2 \; S_{\nu_{\rm obs}} \tag{7.1}$$

where $M_{{\rm HI},\nu_{\rm obs}}$ is in units of $M_\odot\,{\rm MHz}^{-1}$, D_L is the luminosity distance in Mpc (based on Hubble flow corrected redshifts; Tonry et al., 2000), and $S_{\nu_{\rm obs}}$ is the observed-frame HI flux density in Jy. This equation is equivalent to Equation 1.8, though here we need to integrate over frequency ν (in MHz) instead of radial velocity (in $\rm km\,s^{-1}$) to determine the integrated $M_{\rm HI}$.

7.2.2 Baseline subtraction and RFI mitigation

Even though the observations were made using a 14 MHz overlap between the two observed bands, the low frequency band has a much higher baseline level, and there thus is a discontinuity between the bands. Therefore, as a first step we subtract the average of each band from the spectrum of each source. In Figure 7.2 we show the average $M_{\rm HI}$ spectra for our dust-selected sources and the standard deviation between the observed $M_{\rm HI}$ spectra for the different sources for G09 and G15. The HI signals are not aligned and thus not visible in this plot. There are multiple narrow regions of the spectrum where RFI significantly affects the measured

Table 7.1: Frequency ranges affected by RFI. These frequencies are masked throughout the rest of this work.

masked frequencies ν (MHz)			
low frequency band		high frequency band	
G09	G15	G09	G15
$\nu < 1280$	$\nu < 1290$	$1312.3 < \nu < 1313.0$	$1312.3 < \nu < 1313.0$
$1299.7 < \nu < 1300.2$		$1315.5 < \nu < 1316.5$	
$1309.5 < \nu < 1311.0$	$1309.5 < \nu < 1310.1$		$1345.2 < \nu < 1346.0$
			$1349.8 < \nu < 1350.1$

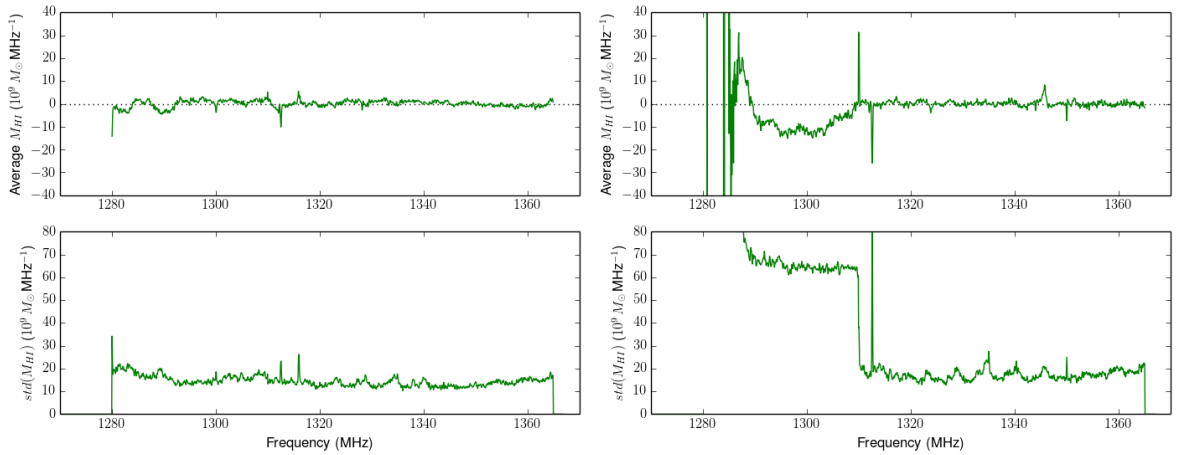

Figure 7.2: Average $M_{\rm HI}$ spectra (*top*) for 1493 dust-selected sources and the standard deviation (*bottom*) between observed fluxes $M_{\rm HI}$ spectra for G09 (*left*) and G15 (*right*). There are significant offsets from zero in the average $M_{\rm HI}$ spectra, and we need to mask certain frequency ranges and subtract a baseline from the spectra.

fluxes, causing offsets in the average fluxes. These regions are listed in Table 7.1 and are masked so they do not contaminate our measurements. There are also additional continuous offsets from zero. Therefore we subtract the best fitting fourth order polynomial from the spectra of both bands. We exclude the masked regions, as well as frequencies we expect to be affected by the target flux, from the fitting process. The resulting average fluxes and standard deviations are shown in Figure 7.3. There are no strong remaining offsets in the average $M_{\rm HI}$ spectra, nor strong peaks in the standard deviation. The standard deviation is higher for G15 for all frequencies due to the smaller integration time. The low frequency band has even higher standard deviation because a significant fraction of sources in G15 has been flagged for each channel. Potentially there is also a contribution from residual RFI in the low frequency observations.

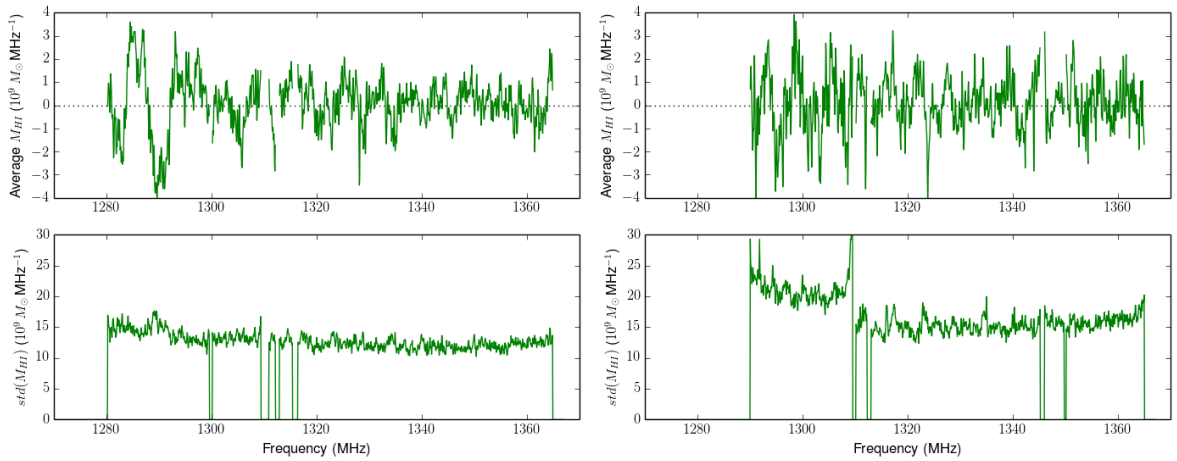

Figure 7.3: Average $M_{\rm HI}$ spectra (*top*) for the dust-selected sources and the standard deviation (*bottom*) between observed $M_{\rm HI}$ spectra for G09 (*left*) and G15 (*right*). Note the y-axis is zoomed in significantly compared to Figure 7.2.

For the G09 spectrum, there is some deviation from zero at the low frequency end. Therefore we have tried a second method for baseline removal. Instead of subtracting a fourth order polynomial from each band, we remove all large scale variation from the spectra by filtering the spectra with a high-pass filter. This is done by first applying a fast Fourier transform to each of the spectra, and then removing all large-scale components in the resulting power spectrum (values lower than a given cut-off value). We set this cut-off value so that all variation on scales lager than 5.7 MHz is removed (for comparison the width of the typical HI signal will be about 1.4 MHz). This scale was chosen since it is the largest scale that effectively removes the variation at the low frequency end of the G09 spectrum in Figure 7.3. We have again masked frequencies affected by RFI or the target HI signal. The resulting average spectra and standard deviations are shown in Figure 7.4. At the high frequency end, there is little difference between both methods. However at the low frequency end, the average spectra show less variation than the spectra with fourth order baselines removed, especially for G09.

As a sanity check we have compared our stacking results from Section 7.4 for both baseline subtraction methods. We find they are not completely consistent. When using fourth order polynomials, we find that the HI masses at the highest redshifts (i.e. low frequency band) are severely underestimated. The large scale variation has thus not been properly subtracted (which also leads to the offsets in Figure 7.3). Throughout the rest of this work we will use high-pass filtering to remove the large scale variation in the lower frequency band. When comparing the stacked results for both methods in the high frequency bands, we also find some inconsistencies. Here we have divided our dust-selected sample in bins of redshift and look at the confused HI masses in the bins, which we expect to increase monotonically with redshift (D13). For the

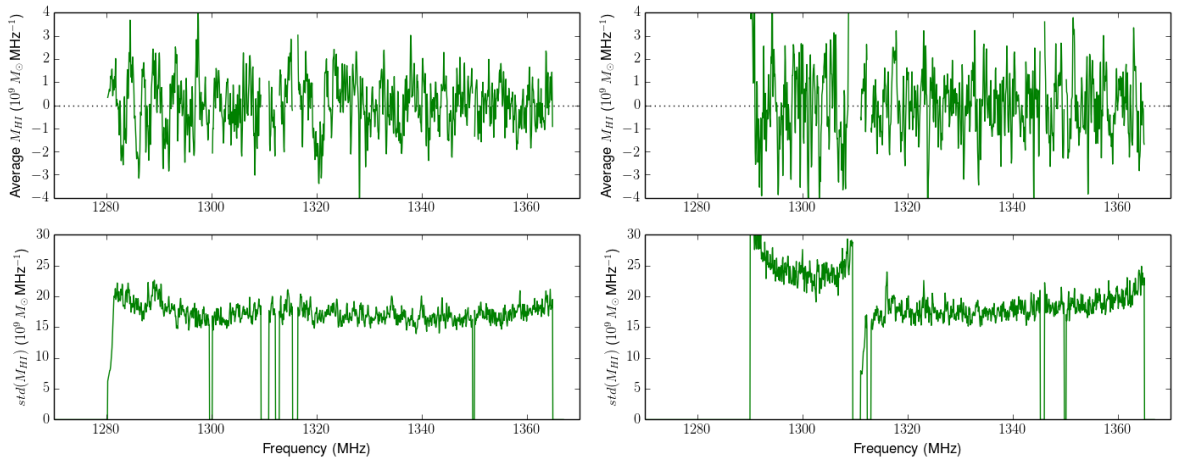

Figure 7.4: Average $M_{\rm HI}$ spectra (*top*) for the dust-selected sources and the standard deviation (*bottom*) between observed $M_{\rm HI}$ spectra for G09 (*left*) and G15 (*right*). Note the y-axis is zoomed in significantly compared to Figure 7.2.

fourth order polynomials we find this is indeed the case, yet for the high-pass filtering we find more noisy results. Therefore in what follows we remove large scale variation from the high frequency band by subtracting a fourth order polynomial.

This strategy for subtracting the baseline using the combination of the two methods is not entirely consistent. However, each method fails in part of the spectrum, and there is no good alternative for subtracting the baseline consistently over the entire spectrum. Our combination of different subtraction methods in the low and high frequency bands gives results in Section 7.4 that are closest to expectations from the literature (Fabello et al., 2011a; Brown et al., 2015).

Another reason we tested two subtraction methods is that both of these are inconsistent with the method from D14, who produced stacked spectra using the same observations. D14 stacked unsubtracted spectra, and removed a fourth order polynomial from the stacked spectrum around the HI signal. When this method is used, we find our results are significantly different, and the shape of the stacked signal is not what we would expect (Figure 7.5). Furthermore, D14 show the results for their high-redshift ($0.04 \leq z \leq 0.1$) sample, which uses the same observations as in this work, are underestimated compared to expectations from other work (Freudling et al., 2011; Rhee et al., 2013, D13). This is at least in part due to the large discontinuity between the two frequency bands. By removing the baselines early on, we obtain more reliable results.

7.2.3 Source selection

We have constructed our dust-selected sample by taking all H-ATLAS DR1 v1.2 catalogue sources (detected at 4σ in any of the SPIRE bands) in the GAMA I G09 and G15 fields (see

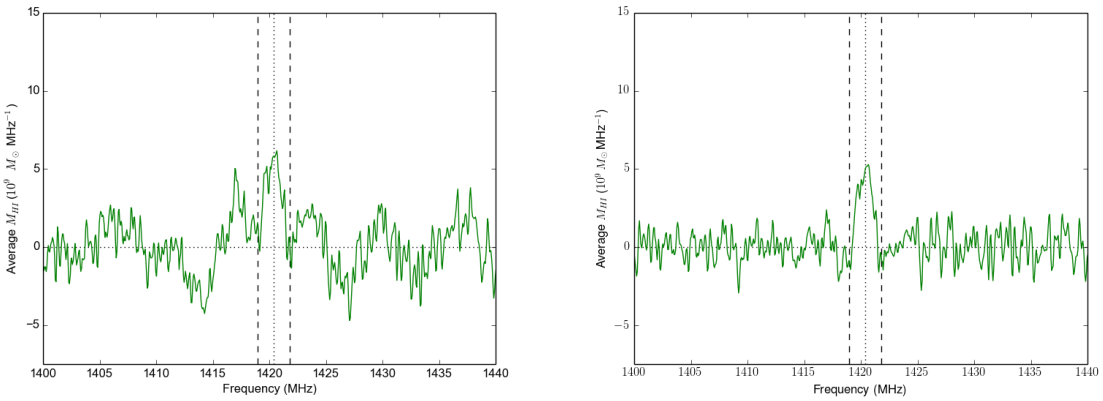

Figure 7.5: *Left:* Stacked HI signal with baseline subtraction from the stacked spectrum (after spectra have been stacked), as in D13 and D14. *Right:* Stacked HI signal with baseline subtraction from the spectrum of each source before stacking the spectra. Removing a baseline from each individual spectrum leads to a more reliable signal.

Figure 2.1 for the locations of the GAMA I fields compared to GAMA II and H-ATLAS fields). We selected sources with reliable spectroscopic redshifts (catalogue $z_{\rm qual} > 2$) in the redshift range of the HI observations ($0.040 < z < 0.109$ for G09 and $0.040 < z < 0.101$ for G15). Residual continuum emission in our data could contaminate our spectra. Therefore, we exclude all sources within a beam width of strong ($S_{1.4\rm GHz} > 200$ mJy) continuum sources ($\sim 15\%$ of the sample). There are 25 strong continuum sources in the G09 field and 33 in G15, as identified in the NRAO VLA Sky Survey (NVSS; Condon et al., 1998). We also remove sources within half a beam width of the edge of the GAMA II maps, as we will not be able to properly deconfuse these sources (Section 7.3). We arrive at a final sample of 1493 dust-selected sources.

In Section 7.4, we compare results for our dust-selected sample to those for a stellar mass selected sample. We select this sample by selecting all GAMA II sources within the Parkes observations (over the GAMA I fields) with stellar masses available from GAMA (Taylor et al., 2011). We use the same redshift range as for our dust-selected sources and again exclude sources within a beam width of a strong continuum source, as well as sources within half a beam width of the edge of the maps. This leads to a sample of 7307 optically selected sources. We then select our stellar mass selected sample by only including sources with stellar masses above $M_* > 10^9\,M_\odot$ (5114 sources).

7.2.4 HI-stacking process

The stacking process outlined in this section can be used to obtain average fluxes as well as average HI masses for a given sample of galaxies. In this work we focus on HI masses and we thus present our method based on stacking the HI mass spectra obtained from Equation 7.1. The first step in the stacking process is shifting the extracted spectra to their rest frame in order to align the HI emission at 1420.4 MHz. In order to conserve the total mass when shifting the spectra, we need to keep:

$$\int M_{\mathrm{HI},\nu_{\mathrm{obs}}}\, d\nu_{\mathrm{obs}} = \int M_{\mathrm{HI},\nu_{\mathrm{rest}}}\, d\nu_{\mathrm{rest}} \tag{7.2}$$

or:

$$M_{\mathrm{HI},\nu_{\mathrm{rest}}} = M_{\mathrm{HI},\nu_{\mathrm{obs}}}\,(1+z) \tag{7.3}$$

In order to determine the stacked spectrum, we determine the average M_{HI} in each channel as:

$$\langle M_{\mathrm{HI}} \rangle_{\nu_{\mathrm{rest}}} = \frac{\sum_{i=1}^{n} w_i\, M_{\mathrm{HI},\nu_{\mathrm{rest}},i}}{\sum_{i=1}^{n} w_i} \tag{7.4}$$

where $M_{\mathrm{HI},\nu_{\mathrm{rest}},i}$ is the value of the M_{HI} spectrum for source i at rest frequency ν_{rest}. We have experimented with several weighting schemes. For the first, we just set $w_i = 1$, which just gives us the linearly averaged spectrum. Second we set $w_i = \sigma_i^{-2}$, where σ is the rms noise of the observed flux density spectrum. This method improves the SNR of the stacked spectrum, and will be our preferred weighting technique throughout this chapter. We have also tested $w_i = (\sigma_i D^2)^{-2}$, which further increases the SNR of the stacked M_{HI} spectrum ($\sigma_i D^2$ is proportional to the rms noise of the observed M_{HI} spectrum). However, this reduces the effective volume by down-weighting distant galaxies and increases cosmic variance in our results, and will thus not be used further. For each of these weighting schemes, the weights for sources that are masked in that channel due to RFI, are set to $w_i = 0$. To obtain HI masses, we integrate the M_{HI} spectrum. The integration bounds are defined by the target redshift $\pm$ 0.001, or equivalently ± 300 km s^{-1} or ± 1.42 MHz. We obtain uncertainties by determining the standard deviation of the obtained fluxes when integrating the stacked spectra near to (but excluding) the HI signal, over the same width (random redshift $\pm$ 0.001). We have done some preliminary work on uncertainties using a Jackknife method (Kott, 2001), as well as using randomly extracted spectra (as in D13 and D14), though further work is necessary.

7.3 HI-deconfusion method

7.3.1 Deconfusion factor

In order to deconfuse our confused dust-selected sources, we need to estimate what fraction of the total HI signal these sources make up. In other words, we have to multiply the HI signal by a deconfusion factor d where:

$$d = M_{\mathrm{HI,dust}}/M_{\mathrm{HI,tot}} \tag{7.5}$$

where $M_{\mathrm{HI,dust}}$ is the predicted HI mass for the dust-selected source in question and $M_{\mathrm{HI,tot}}$ the sum of predicted HI masses for all matches (corrected for location) that lie within beam of the dust-selected source. We estimate the HI mass of each confused counterpart from scaling relations presented in the next section.

There are on average five galaxies confused within the beam of our dust-selected sources, though not all of these will contribute all of their HI mass to the confused signal. We apply two correction factors to account for the separation of the different confused galaxies to the center of the extracted spectrum. First we correct for separation in redshift by estimating how much of the HI signal of the confused source will lie within the integration bounds we use for determining the total HI mass of the target source (target redshift $\pm$ 0.001). We assume a triangular HI profile and estimate the width of the profile from scaling relations between the HI width at half maximum and stellar mass (equivalent to Tully-Fisher relation) for the HRS galaxies used in the previous chapters. We do not account for the inclination, nor account for the fact that many galaxies will not have a triangular HI profile. However, by using the average over all inclinations and an average HI profile (the stacked HI profile is triangular), we can make an estimation. We limit the sensible HI width to be between 60 and 300 $\mathrm{km\,s^{-1}}$. This method only gives us a first order approximation, yet is still better than simply including or excluding sources in the deconfusion factor calculation based on whether the central redshift lies within the integration bounds or not. We have also tested a box HI profile, and tried different Tully-Fisher relations. Neither of these changes significantly affect our conclusions.

The second correction we apply is a correction for the angular separation. We do this by assuming the sensitivity of the observations declines with angular separation following a Gaussian profile with FHWM $= 21.2'$, the effective beam width of the extracted spectra. This way we account for the appropriate amount of HI within the beam for each confused counterpart. Due to these two correction factors, on average our galaxies are effectively confused with ~ 3 galaxies[1], instead of ~ 5 galaxies when not applying these corrections.

[1] We determine this number by assuming the HI mas of all galaxies is the same and calculating the average deconfusion factors from Equation 7.5.

7.3.2 Best deconfusion relation

Rather than deconfusing the HI signals, D13 artificially confused the stellar mass (and optical emission), and studied ratios of $M_{\rm HI}/M_*$ (and $M_{\rm HI}/L_r$) to account for confusion. This is effectively the same as applying a deconfusion factor d, where the individual contributions from the confused counterparts are proportional to the stellar mass. As a first estimation, we have calculated deconfusion factors d under the (somewhat unrealistic) assumption that $M_{\rm HI}/M_*$ of the individual confused counterparts is the same. This way we can compare consistently to results in D13 and D14.

A better estimation of the $M_{\rm HI}$ of the individual counterparts can be obtained from scaling relations of $M_{\rm HI}/M_*$ with observed galaxy colours. We have tried a number of approaches to determine appropriate scaling relations to estimate the HI content of our galaxies based on their colour. Our first approach is to use literature relations between $M_{\rm HI}/M_*$ and NUV-r colour. There are many surveys available, yet the ones with the highest sensitivity for large samples are those from stacking stellar mass selected sources (Fabello et al., 2011a; Brown et al., 2015). The sample of Brown et al. (2015) probes to lower stellar masses than Fabello et al. (2011a) ($M_* > 10^9\,M_\odot$ rather than $M_* > 10^{10}\,M_\odot$), and is thus more applicable for our sample. Additionally, we determine scaling relations with colour based on our observational data from Part I of this thesis. We have determined colours using every possible combination of two bands (out of the 21 available bands), and found the strongest correlation to be between $M_{\rm HI}/M_*$ and NUV-r. When GALEX colours are not available, the strongest correlation is for g-r. The used deconfusion relations are shown in Figure 7.6.

We use galaxy colours based on GAMA LAMBDAR photometry (LambdarCatv01 catalogue; Wright et al., 2016; see also Section 3.3.6), and stellar masses based on the same photometry (StellarMassesLambdarv19 catalogue) using the method of Taylor et al. (2011), including the recommended aperture correction. The obtained fluxes are Galactic extinction corrected and a k-correction is applied to enable a consistent comparison of galaxies at different redshifts. Because of the difficulty of obtaining HI data of large samples beyond the local Universe, we can only use scaling relations for local galaxies. In Chapter 4 we found a strong correlation of $M_{\rm HI}/M_*$ with NUV-r colour. 8.3% of the sources in our sample do not have NUV photometry available, and a further 33% are outliers when plotting NUV-r against M_* (similar to SSFR against M_*). Some of these outliers clearly have unreliable stellar masses. These are discarded together with other sources with unreliable stellar masses (catalogue PPP = 0). Other outliers have reliable stellar masses but outlying NUV-r colours. For these sources, we inspect if they have more sensible g-r colours. If they do, we instead estimate $M_{\rm HI}/M_*$ from the observed g-r colour. If not, we discard these sources together with the sources with unreliable stellar masses. The excluded sources are typically contaminated by other foreground/background

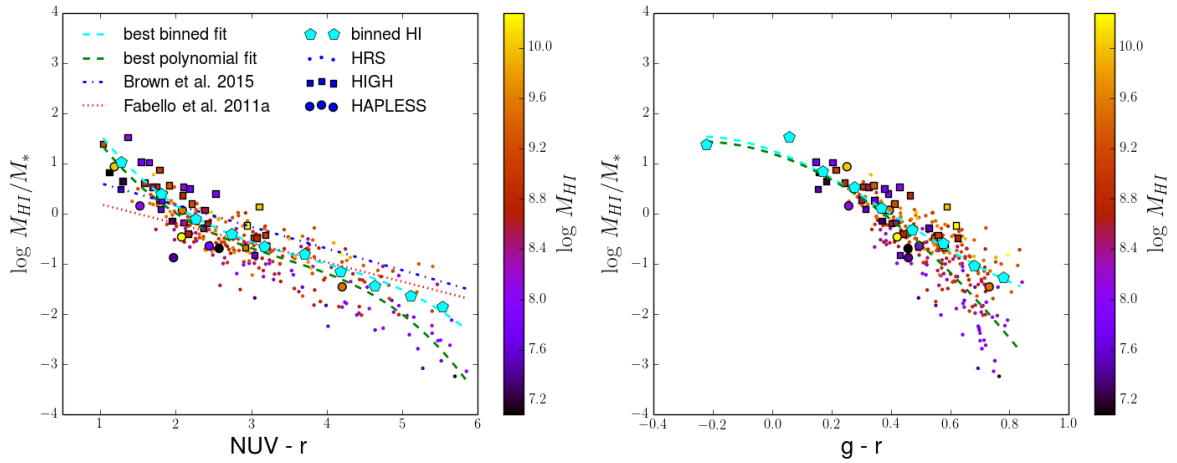

Figure 7.6: $M_{\rm HI}/M_*$ against NUV-r (*left*) and g-r (*right*) colour plot for our nearby galaxy samples from Part I, colour-coded by HI mass. The relations used to deconfuse our sources are shown as dashed lines. We determine the average $M_{\rm HI}/M_*$ in bins of colour (cyan) and fit a third order polynomial to use as the deconfusion relation throughout this work. We have included the best polynomial fit for comparison as a green dashed line. For $M_{\rm HI}/M_*$ against NUV-r, we also include relations from literature that were obtained using stacking.

galaxies or stars. Not including these sources leads to a small underestimation of the total confused HI mass. Instead, we can also estimate the HI content of the discarded sources as the average HI mass of the other confused counterparts within the same beam, without affecting our conclusions.

The scaling relations are typically quasi-linear when using logarithmic values on each axis. However, within the confused beam, we add the HI masses linearly (non-logarithmic), which means we have to be very careful in deriving appropriate deconfusion relations. When determining a best-fit relation, the scatter around the best trend line is symmetric in logarithmic space, yet not in linear space. If a value 0.3 dex above the trend is added to a value 0.3 dex below the trend, their average will be 0.096 dex ($\log((10^{0.3}+10^{-0.3})/2)$) above the trend. Therefore we cannot simply determine best fit relations as in Chapter 4. Instead, we divide the NUV-r and g-r values in bins and determine the average $M_{\rm HI}/M_*$ linearly. We then fit a third order polynomial to the resulting data points and use these relations to estimate the HI mass of each confused counterpart. We have discarded ETGs in HRS from the fitting process as, due to the Virgo cluster environment, there is a unusually large fraction of very gas poor, red galaxies in HRS.

7.3.3 Lognormal and Gaussian distributions

The distribution of $M_{\rm HI}/M_*$ in the local Universe is more likely lognormal than Gaussian (Cortese et al., 2011). Therefore it would be more ideal to determine $\langle \log M_{\rm HI}/M_* \rangle$ instead of $\log\langle M_{\rm HI}/M_* \rangle$ as we do. However stacking only works in linear space and so we cannot compute $\langle \log M_{\rm HI}/M_* \rangle$ directly. This complicates our discussion as linear scaling relations of $\langle \log M_{\rm HI}/M_* \rangle$ will still be linear when computing $\log\langle M_{\rm HI}/M_* \rangle$, yet $\log\langle M_{\rm HI}/M_* \rangle$ will be offset above the trend when averaging $M_{\rm HI}$ over a large range (because $(10^a + 10^b)/2 > 10^{(a+b)/2}$ and the difference increases for an increasing difference between a and b). For quasi-linear scaling relations this means that the offset will increase when dividing the sample in fewer and fewer bins. Additionally, increasing scatter in the underlying relation also leads to an increasing offset above the underlying trend with lognormal distribution. Simulations are necessary to quantify this issue.

The same issue also affects our determination of the deconfusion relation. We need to add the lognormally distributed $M_{\rm HI}$ linearly in the confused signal. As previously mentioned, the confused signal will thus be larger than expected from simply estimating the contribution using a polynomial fit, and we therefore use binned datapoints. Even though the binned data are more appropriate for this situation, they will be biased towards higher $M_{\rm HI}$ when the bin sizes or measurement errors become large. In order to further study this issue and to test how good our deconfusion relations perform, we have produced a database of artificially confused sources. Here, we use only two confused counterparts but we have tested up to 5 counterparts without a change to our discussion. The counterparts are artificially confused by simply adding their HI masses. This is done for every possible combination of the sources in our samples (HIGH, HAPLESS and HRS) for which we have HI masses available. These sources then have a confused HI mass, an observed HI mass and their stellar mass and g-r colour. Using the deconfusion relations, we can then estimate the HI mass for each of the confused counterparts and compare the combined HI mass to the confused HI mass (from adding the observed $M_{\rm HI}$). We find that the binned estimates are indeed offset towards slightly higher (0.1 dex) than expected.

One way we have tried to correct for the offset in the colour bins is by making a recursive routine that generates a new $M_{\rm HI}/M_*$ data point in each colour bin, based on the offset between the average estimated and observed $M_{\rm HI}/M_*$. Here we have combined all sources in the bin linearly. If the estimated $M_{\rm HI}/M_*$ is too high, the new $M_{\rm HI}/M_*$ datapoint will be reduced slightly. This is done in each colour bin, and an additional correction for the overall average is applied. As a result the new $M_{\rm HI}/M_*$ datapoints will force the best fitting trend line to be raised/lowered so the offset between the new estimated and observed $M_{\rm HI}/M_*$ will now be smaller. In each iteration we add some scatter and then repeat the process thousands of times.

We select the trend line with the smallest offset (we minimise both the total average offset and the offsets for the individual colour bins), which closely resembles the stacked trend, yet has slightly lower $M_{\rm HI}/M_*$ (Figure 7.6). From comparing results for both these methods, we find they are nearly indistinguishable (as the same offset will be present in $M_{\rm HI,dust}$ and $M_{\rm HI,tot}$ and the correction factor d is thus not affected.)

7.4 Results

7.4.1 Average HI mass for dust-selected galaxies

In Figure 7.7 we show the confused and deconfused $M_{\rm HI}$ stacks for our dust-selected and stellar mass selected samples. By combining the galaxies in our sample we are able to obtain a 25σ-detection for the average of our dust-selected sources and 21σ for the stellar mass selected sources. Figure 7.7 also shows the number of contributing sources at the different frequencies. This number is variable as we only count unmasked sources at each frequency. Due to the masking, the effective number of sources contributing to the HI signal is 1325 for the dust-selected sources and 4118 for the stellar mass selected sources. In Figure 7.8 we show how the rms noise for our spectra depends on the number of stacked spectra for the low and high frequency bands. The noise scales nearly quadratically with the number of sources, though levels off towards the highest sample sizes, indicative of non-Gaussian noise remaining in the observations. This level-off is more pronounced for the low frequency band, which is indeed known to be more strongly affected by RFI. We note the total stack for stellar mass selected sources does have a smaller uncertainty due to the larger number of sources, though the average HI mass is also smaller, leading to the smaller SNR than for dust-selected sources.

Our results for the total stacks are listed in Table 7.2. The deconfusion factors used are those derived from binned scaling relations to our nearby galaxy samples from Part I of this thesis, and are on average $d = 0.32$ for dust-selected sources and $d = 0.23$ for stellar mass selected sources. We find the dust-selected sources have higher $M_{\rm HI}$ on average than stellar mass selected samples. Surprisingly, when we compare $M_{\rm HI}/M_*$, we find the dust-selected sources are now more gas-poor. This is in contrast to our results in Chapter 4. A probable explanation for this apparent discrepancy is that the dust-selected HAPLESS sample probes down to much lower dust masses than our higher redshift dust-selected sources. At the average redshift of our sample ($z = 0.074$), the faintest observable H-ATLAS sources ($4\sigma \simeq 24\,$mJy) correspond to a dust mass of $M_d \sim 10^7\,M_\odot$. Such high dust masses are only present in massive galaxies with high stellar masses (see also Figure 4.3). Indeed we find the average stellar mass of the dust-selected sample is $M_* = 10^{10.2}\,M_\odot$. In Chapter 4 we found that, as the stellar

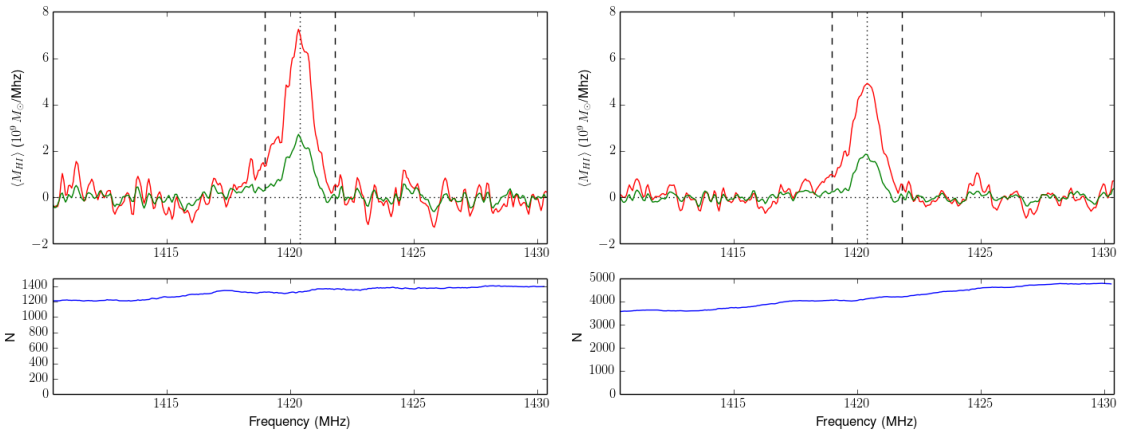

Figure 7.7: Total stacked $M_{\rm HI}$ profile (*top*) and number of contributing sources (*bottom*) for dust-selected (*left*) and stellar mass selected (*right*) sources. The confused profile is shown in red and the deconfused profile in green.

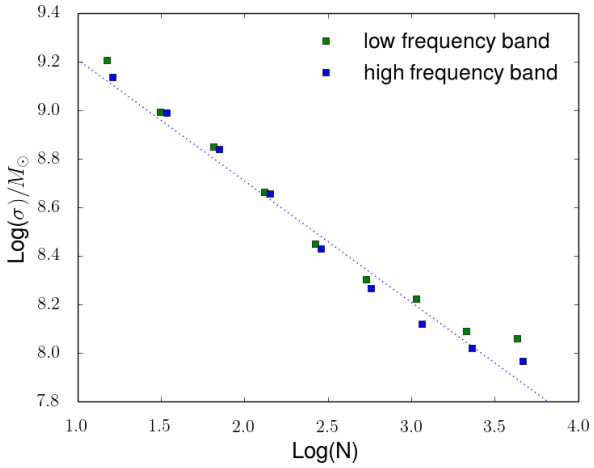

Figure 7.8: The rms noise of the stacked spectrum plotted against the number of sources contributing to the stack. The sample has been divided into sources with central redshift in the low frequency band and in the high frequency band. We have shown a dashed line with the expected gradient of 0.5 for comparison.

mass increases, $M_{\rm HI}$ increases as well and $M_{\rm HI}/M_*$ decreases. The high stellar masses for the dust-selected sources thus explain the observed differences in the stacks of the dust- and stellar mass selected sources. When we select a sample with all high stellar masses ($M_* > 10^{10.5}\,M_\odot$) sources in the G09 and G15 fields, we find an average $M_{\rm HI}$ as high as the dust-selected stack ($M_{\rm HI} = 3.1\,10^9\,M_\odot$). Though for this stack the $M_{\rm HI}/M_*$ is significantly lower ($M_{\rm HI}/M_* = 0.07$). Among the most massive galaxies, dust-selected sources are thus on average more gas-rich than stellar mass selected sources.

Table 7.2: Average stacked HI properties derived for dust-selected and stellar mass selected samples. The number of sources excludes sources that were masked due to RFI over the HI signal.

	dust-selected	stellar mass selected
number of sources	1325	4118
confused $\langle M_{\rm HI}/10^9\,M_\odot\rangle$	9.80 ± 0.33	7.08 ± 0.28
deconfused $\langle M_{\rm HI}/10^9\,M_\odot\rangle$	3.17 ± 0.12	1.69 ± 0.08
confused $\langle M_{\rm HI}/M_*\rangle$	1.09 ± 0.09	2.69 ± 0.06
deconfused $\langle M_{\rm HI}/M_*\rangle$	0.28 ± 0.05	0.55 ± 0.04

We have compared results using different deconfusion relations and found there are only small differences to the resulting stacks. For the total dust-selected stacks, the difference between results for the deconfusion relations from fitting binned scaling relations to nearby galaxies, and for the scaling relations from Brown et al. (2015), vary by only 3% (the differences are negligible even when only selecting the reddest sources, for which the offset between the deconfusion relations is largest). The differences to artificially confusing M_* as in D13 and D14 (equivalent to deconfusing the HI using a constant $M_{\rm HI}/M_*$), only amount to 10% lower fluxes. The different deconfusion methods can thus not account for the offset between our results and D14. D14 found $M_{\rm HI}/M_* = 0.15$ for their deconfused stack, which is a factor of two lower than our results. Their confused HI mass of $M_{\rm HI} = 2.48\times10^9\,M_\odot$ is almost 4 times lower than ours. We attribute these differences to the different sample selection (D14 includes sources below $M_* = 10^9\,M_\odot$), and to different RFI removal and baseline subtraction. The confused HI mass from D13 for the SGP sample (which is similar in redshift) is $M_{\rm HI} = 6.93\pm0.17\times10^9\,M_\odot$, and thus a little smaller than our confused result. We note that in the following section we will see that our HI scaling relations are in fact offset to lower $M_{\rm HI}$ than other literature results at lower redshifts. It is thus unlikely our HI masses are overestimated.

7.4.2 Scaling relations

We now investigate how the HI content of galaxies scales with stellar mass and colour. By splitting our sample into bins of these parameters, we can achieve a statistically significant stack in each bin and study trends in the HI content. Table 7.3 and 7.5 list the used bins for each parameter, the effective parameter values and the results from stacking the HI spectra. We show how $M_{\rm HI}$ and $M_{\rm HI}/M_*$ scale with stellar mass in Figure 7.9. As expected, we find a positive correlation with $M_{\rm HI}$ and an anti-correlation with $M_{\rm HI}/M_*$ for both our samples. At a given stellar mass, dust-selected sources are more gas-rich than stellar mass selected sources. The trend lines have a similar slope to the ones for our nearby galaxy samples. We find the stacked scaling relations have a smaller HI content than HIGH, which is not surprising considering

Table 7.3: Average stacked HI properties in bins of stellar mass ($\log(M_*/M_\odot)$) derived for dust-selected sources. The number of sources excludes sources that were masked due to RFI over the HI signal. The mean stellar mass is the mean value for the unmasked sources in that bin.

sample	range			mean	N	$\langle M_{\rm HI}/10^9 M_\odot \rangle$	$\langle M_{\rm HI}/M_* \rangle$
dust-selected	7.0	-	10.0	9.63	461	1.68 ± 0.26	0.483 ± 0.138
	10.0	-	10.5	10.24	530	4.01 ± 0.21	0.228 ± 0.015
	10.5	-	12.0	10.75	334	4.05 ± 0.24	0.066 ± 0.005
stellar mass selected	9.0	-	9.5	9.12	1816	1.43 ± 0.06	1.246 ± 0.097
	9.5	-	10.0	9.74	1056	1.01 ± 0.17	0.123 ± 0.034
	10.0	-	10.4	10.20	683	2.75 ± 0.23	0.170 ± 0.017
	10.4	-	10.8	10.57	439	1.95 ± 0.08	0.054 ± 0.002
	10.8	-	12.0	10.95	121	3.69 ± 0.21	0.046 ± 0.002

HIGH requires HI detections and thus selects only the most gas-rich sources. At the same time, the stacked HI content is higher than the average for HRS, because of the large fraction of HI-deficient galaxies in HRS. Compared to Brown et al. (2015) and Fabello et al. (2011a), who stacked stellar mass selected sources with $M_* > 10^9 M_\odot$ and $M_* > 10^{10} M_\odot$ respectively, we find our stellar mass selected stacks are offset towards lower $M_{\rm HI}/M_*$. We have also included results for the low-redshift (HIPASS stacking) sample from D14. We find our scaling relations to be more noisy than these literature works, likely due to remaining poor RFI mitigation and baseline subtraction for some sources.

Next, we study the evolution of $M_{\rm HI}/M_*$ with colour in Figure 7.10. We find there is no offset between our differently selected samples, though both samples have lower $M_{\rm HI}/M_*$ compared to Brown et al. (2015) and Fabello et al. (2011a). This offset is surprising since our sample was selected similarly to the sample of Brown et al. (2015). Even in the case of different sample selection, we found in Chapter 4 that there is no offset between samples when plotting $M_{\rm HI}/M_*$ against NUV-r colour. The apparent offset could be due to poor RFI mitigation and baseline removal, or a wrong angular separation correction, as discussed in the following section. However, even with the offset, our stacked results still lie well within the scatter of the nearby galaxy samples from Part I. The absent offset between our dust-selected and stellar selected sources again indicates that the scaling relations of $M_{\rm HI}/M_*$ with NUV-r (proxy for SSFR) and g-r colour are more fundamental than the relations with M_* (consistent with our findings in Section 4.3.2).

Finally we also study the evolution of $M_{\rm HI}/M_d$ with stellar mass and NUV-r colour for the dust-selected sources in Figure 7.11. Here the dust masses have been determined using a modified black body fit consistent with C15. We again find that the stacked signals lie well within the scatter of the local scaling relations, and follow a similar slope. For the plot with stellar mass, there is very little evolution (less then for our nearby galaxies, though not entirely

Table 7.4: Average stacked $\langle M_{\rm HI}/M_* \rangle$ in bins of NUV-r and g-r colour derived for dust-selected and stellar mass selected sources. The number of sources excludes sources that were masked due to RFI over the HI signal. The mean colour is the mean value for the unmasked sources in that bin.

sample	colour	range			mean	N	$\langle M_{\rm HI}/M_* \rangle$
dust-selected	NUV-r	0	-	3.5	2.58	861	0.351 ± 0.058
		3.5	-	4.1	3.76	192	0.073 ± 0.011
		4.1	-	7	4.67	163	0.016 ± 0.011
	g-r	-0.5	-	0.4	0.335	216	0.632 ± 0.249
		0.4	-	0.55	0.480	405	0.397 ± 0.027
		0.55	-	1.5	0.676	698	0.104 ± 0.017
stellar mass selected	NUV-r	0	-	2.5	1.99	1616	1.116 ± 0.069
		2.5	-	3.15	2.80	758	0.609 ± 0.026
		3.15	-	4.1	3.59	671	0.082 ± 0.049
		4.1	-	5.7	4.89	863	0.026 ± 0.010
		5.7	-	7	5.90	78	0.009 ± 0.014
	g-r	-0.5	-	0.3	0.255	237	2.013 ± 0.261
		0.3	-	0.45	0.379	1177	0.770 ± 0.037
		0.45	-	0.6	0.521	1008	0.269 ± 0.029
		0.6	-	0.775	0.678	1128	0.038 ± 0.010
		0.75	-	1.5	0.788	564	0.002 ± 0.006

inconsistent). However, when plotting against NUV-r colour, we find a slope consistent with the scaling relations for nearby galaxies.

7.5 Caveats

Throughout this chapter we have stacked the HI signals of dust-selected and stellar mass selected sources, corrected for deconfusion based on scaling relations for nearby galaxies in the same fields, and obtained average $M_{\rm HI}$ and $M_{\rm HI}/M_*$ estimates in different bins. However,

Table 7.5: Average stacked $\langle M_{\rm HI}/M_d \rangle$ in bins of M_* and NUV-r colour derived for dust-selected sources. The number of sources excludes sources that were masked due to RFI over the HI signal. The mean colour is the mean value for the unmasked sources in that bin.

parameter	range			mean	N	$\langle M_{\rm HI}/M_d \rangle$
M_*	7.0	-	10.0	9.63	461	110 ± 17
	10.0	-	10.5	10.24	530	125 ± 15
	10.5	-	12.0	10.75	334	107 ± 11
NUV-r	0	-	3.5	2.58	861	139 ± 11
	3.5	-	4.1	3.76	192	73 ± 10
	4.1	-	7	4.67	163	30 ± 14

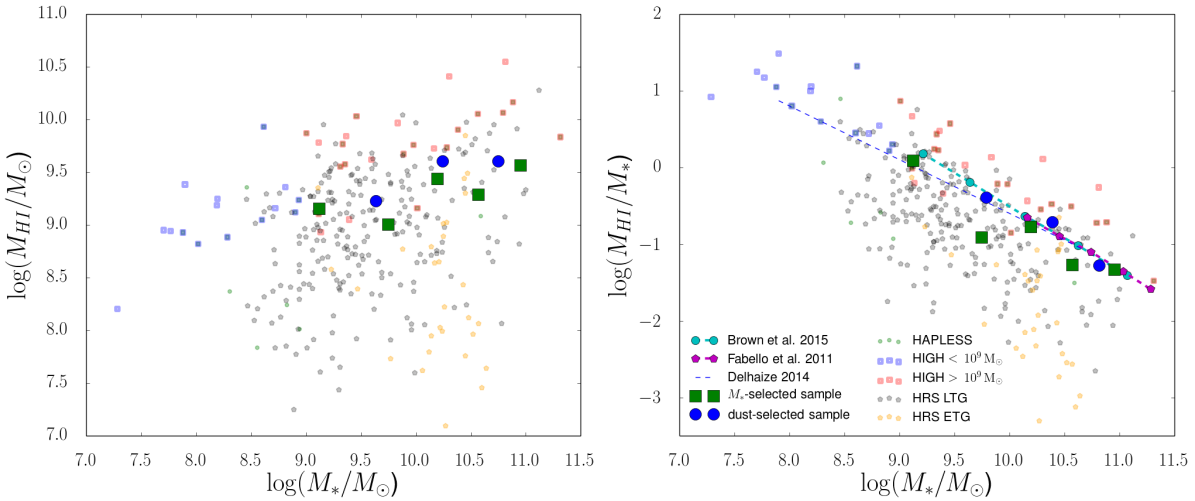

Figure 7.9: Trends of average $M_{\rm HI}$ (*left*) and $M_{\rm HI}/M_*$ (*right)* with stellar mass for our dust-selected and stellar selected sources. For comparison, we have added our nearby galaxy samples and relations from other stacking work in the literature (D13, Fabello et al., 2011a; Brown et al., 2015).

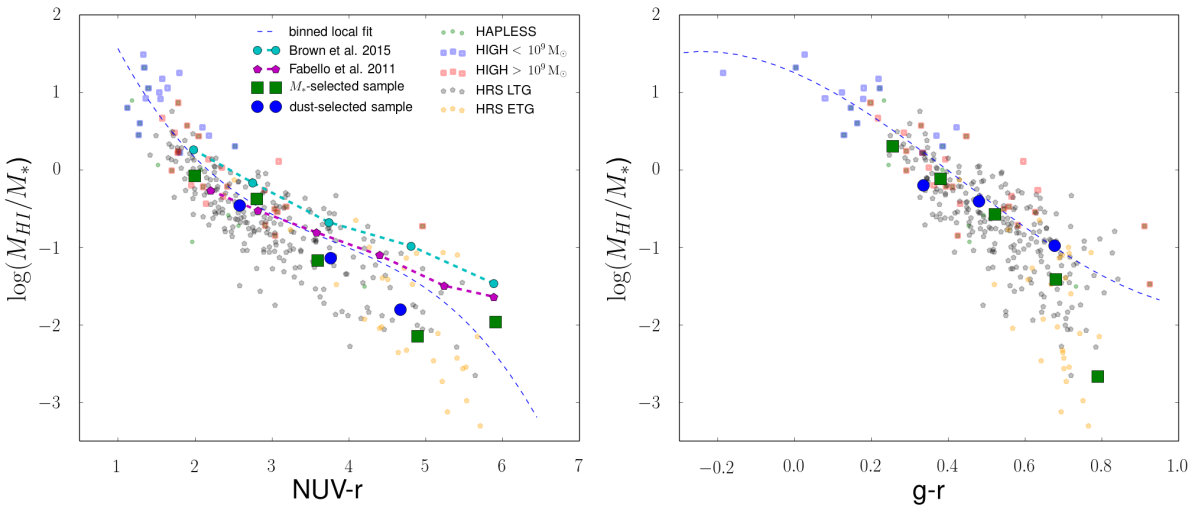

Figure 7.10: Average HI-to-stellar mass ratio in function of NUV-*r* (*left*) and *g*-*r* (*right*) colour. There is no offset between our dust-selected and stellar mass selected sample. Both our samples are offset from literature works.

there are significant uncertainties in our methods that could corrupt our stacking process. Here we list the most important caveats and topics for further investigation:

- Before stacking the spectra, we tried to carefully subtract the baselines and mask RFI. However, the low frequency band was severely affected by RFI and this has forced us to use high-pass filtering. There is a possibility that this method does not reliably estimate

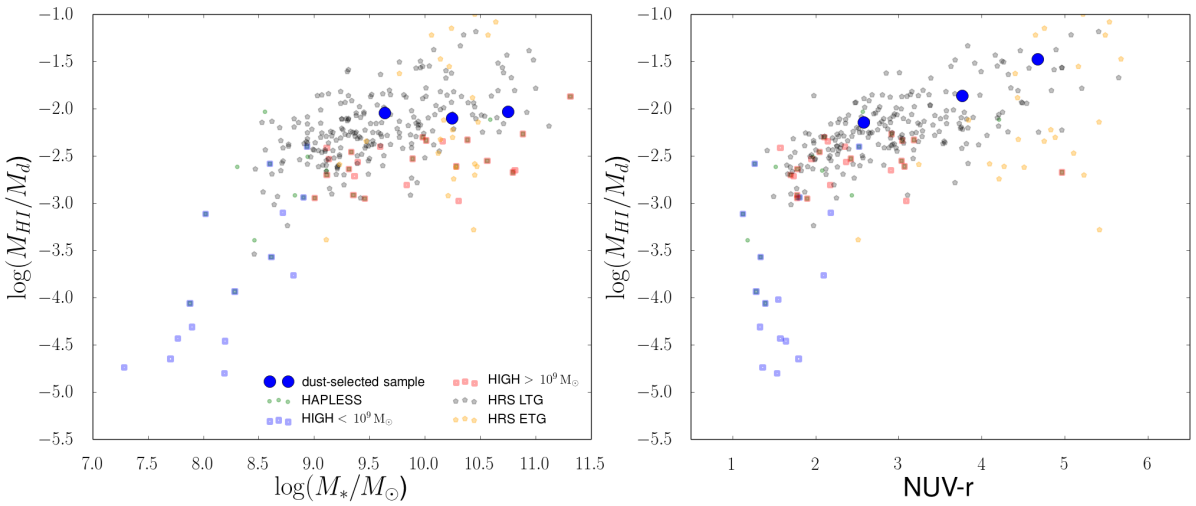

Figure 7.11: Average $M_{\rm HI}/M_d$ in function of M_* (*left*) and NUV-r colour (*right*). Both relations are well within the scatter of nearby galaxies. The found relation with M_* is slightly less steep then expected.

the baseline under the HI signal, since this region was masked and there are many degrees of freedom for the subtracted baseline.

- For some of our binned stacks, there are significant differences above the noise between the results for G09 and G15. These differences could be in part due to cosmic variance between the fields. However, in some cases the difference is suspiciously large and we suspect this is caused by some residual RFI in the observations of either field.

- Our results generally predict a smaller HI content than results in the literature (e.g. Brown et al., 2015). The only way we are able to effectively eliminate this offset is by using a smaller FWHM when determining the angular separation correction. When we use the unweighted Parkes FWHM of $15.5'$ instead of the effective beam after pixel weighting of $21.2'$, we find our results are more consistent with other work. Further study, potentially including simulated mock observations is necessary to determine to appropriate FWHM for deconfusing sources.

- As discussed in Section 7.3.3, the lognormal distribution of HI masses causes an overestimation of the underlying relation when determining the averages from a large range of HI masses, and a corresponding overestimation of the trend line when using wide bins. One approach that could potentially alleviate this issue is the use of median stacking rather than mean stacking, i.e. taking the median of the HI fluxes in each channel when performing the stacks.

Apart from these caveats, there are various uncertainties in our method that are hard to quantify. These include the uncertainties in the aperture corrected stellar masses, the observed colours, the chosen deconfusion relation, and the RFI masking and baseline subtraction process. Therefore the results presented in this chapter should be regarded as preliminary results, and further work to quantify these uncertainties is necessary.

7.6 Conclusions

We present an HI stacking analysis of dust-selected galaxies in the G09 and G15 H-ATLAS fields between $0.04 < z < 0.11$. The observations were obtained with the Parkes telescope in two frequency bands totalling 253 hours of integration time. We subtract a fourth order polynomial baseline from the high frequency band and filter the low frequency band with a high-pass filter. Galaxies in this field are, on average, confused with 5 other galaxies within the same beam. We therefore estimate the contribution of the target source to the confused HI signal based on scaling relations with observed galaxy colours and stellar mass, and positional information for each individual source.

We have selected all H-ATLAS sources within the available observations. When excluding sources that do not contribute to the HI signal due to masking, we obtain a sample of 1325 dust-selected sources. We compare the average HI content for this sample to a sample of 4118 stellar mass selected ($M_* > 10^9\,M_\odot$) sources. We find average HI masses of $(3.17 \pm 0.12) \times 10^9\,M_\odot$ and $(1.69 \pm 0.08) \times 10^9\,M_\odot$ for the dust- and stellar mass selected samples respectively. The average $M_{\rm HI}/M_*$ are found to be 0.28 ± 0.05 and 0.55 ± 0.04 respectively. The low $M_{\rm HI}/M_*$ for the dust-selected sample is consistent with this sample consisting of sources with high stellar masses.

We have studied scaling relations for our stacked samples, and found our results are similar to scaling relations based on HI detections in the nearby Universe, as well as relations from stacking in the literature, though our relations do show more scatter. At fixed stellar mass, we now find the dust-selected sources have higher $M_{\rm HI}/M_*$ than stellar mass selected sources. At a given colour, the $M_{\rm HI}/M_*$ are similar for both samples. There is, however, a small offset between our stacking results and those in Fabello et al. (2011a) and Brown et al. (2015). We attribute this offset to uncertainties in our methods, especially for the baseline removal and deconfusion. Due to these uncertainties, the results in this chapter should be regarded as preliminary results.

Chapter 8

Conclusions

8.1 Summary and conclusions

In this thesis, we have studied the evolution of the dust and gas content for galaxies in the local Universe. We selected galaxies in the equatorial H-ATLAS fields, as these have excellent multiwavelength observations available from FUV to submm. We have performed three investigations in order to study the dust and gas content in these fields. In Part I, a sample of 40 local galaxies was selected on their HI content. We derived galaxy properties using the MAGPHYS code applied on aperture matched photometry in 21 bands. We then studied scaling relations for this sample in comparison to the dust-selected HAPLESS and stellar mass selected HRS. In Part II, we have derived metallicities and added the DGS to our nearby galaxy samples, together covering a wide range of gas fraction ($0.05 < f_g < 0.97$). We compared observations to chemical evolution models in order to study dust sources and sinks. Finally, in Part III, in order to probe the dust and gas content of galaxies out to larger redshifts, we have stacked the HI signal of galaxies between $0.04 < z < 0.1$ and produced a detection for the average dust-selected and stellar mass selected galaxy.

Dust and gas scaling relations. In Chapter 2, we have selected the HI-Selected Galaxies in H-ATLAS (HIGH) sample. We started from the 32 HIPASS sources in the equatorial H-ATLAS footprint. Because some of these are 'confused' (HI signal of multiple sources indistinguishable), we used higher resolution ALFALFA or literature data where available. This allowed to arrive at a sample of 40 unconfused nearby ($z < 0.035$) HI-selected galaxies. This sample was divided into HIGH-high ($M_* > 10^9 M_\odot$) and HIGH-low ($M_* < 10^9 M_\odot$) to highlight the enigmatic dust-poor population of immature galaxies in the latter sample. In Chapter 3, we have presented the aperture photometry process applied to the HIGH sample. Key

features include automated aperture determination, careful contaminant removal, background subtraction and an emphasis on the uncertainty determination. The acquired photometry was compared to results from different methods, including H-ATLAS and LAMBDAR (GAMA) results. Our photometry process was shown to be reliable. MAGPHYS was used to obtain galaxy properties for our sources from their SEDs.

In order to study the interplay of dust, gas and star formation, we have studied scaling relations in Chapter 4. We compared the HIGH sample to the dust-selected HAPLESS and stellar mass selected HRS. The combined samples span a wide range of gas fraction ($f_g = 1.32M_{\rm HI}/(1.32M_{\rm HI}+M_*)$), which is used as a proxy for the evolutionary state of a galaxy. The derived scaling relations for the combined samples in this chapter are affected by selection biases. Scaling relations with stellar mass show significant offsets between the differently selected samples. However, the gas and dust scaling relations linked to NUV-r (SSFR) and gas fraction are robust. These are tight relations which do not depend on sample selection or environment and are thus not affected by the complex selection criteria of the combined sample.

Most of the HIGH-low galaxies have very high gas fractions ($f_g > 80\%$) and a much smaller dust content than expected from extrapolating published scaling relations for more evolved sources. For these galaxies in the earliest stages of evolution, dust is not a good tracer of the HI content. They are also the most actively star forming galaxies relative to their stellar masses (SSFR) and relative to their dust content, yet least active relative to the atomic gas content. Our *Herschel* study of HI-selected sources has opened a window into the interesting properties of these dust-poor immature sources.

For galaxies in later evolutionary stages, M_d/M_* and SSFR decrease and $M_d/M_{\rm HI}$ increases as they move from high to low gas fractions. There is also a trend of decreasing HI depletion time with decreasing gas fraction, opposite to the trend found for molecular gas depletion timescale. We interpreted this as being due to the increasing efficiency with which HI can be converted to H_2 as galaxies increase in stellar mass surface density with decreasing gas fraction.

Our data confirmed literature results that both old and young stellar populations play an important role in heating the diffuse dust component, and either can be the dominant contributor in individual systems, depending on the SSFR. Finally, we have shown that galaxies start out barely obscured and increase in obscuration as they evolve, yet there is no clear and simple link between obscuration and global galaxy properties.

Chemical evolution models. In order to study the build-up and decline of dust, we have compared our observations of the combined nearby galaxy samples, including the DGS, to chemical evolution models in Chapter 6. These models predict the dust, metal, gas and stellar

content of galaxies as they evolve (we again use gas fraction as a proxy for evolutionary stage). We focused on the evolution of $M_d/M_{\rm bary}$, SFR$/M_{\rm bary}$, $12+\log({\rm O/H})$, M_d/M_g and M_d/M_Z. Metallicities (derived in Chapter 5) can be used to discriminate between different chemical evolution models and dust sources. We have compared the N2, PG16S and KE08/T04 calibrations to include the uncertainty in the metallicity calibrations. We found PG16S is most reliable for the low-metallicity sources, and shows less scatter with other calibrations and stellar mass than the popular PT05 calibration. In order to reproduce the observed metallicity, particularly at low gas fractions, inflows and outflows of gas at a rate of twice the SFR are required to keep the metallicity from rising to higher than observed metallicities.

Using a simple closed box chemical evolution model one can explain the $M_d/M_{\rm bary} - f_g$ relations using the following picture: as galaxies evolve, their dust content first rises steeply, then levels off and reaches its peak about half way through its evolution. The dust content starts declining towards lower gas fractions as more dust is destroyed/consumed than produced. However, some of the HIGH-low sources have significantly lower dust content than this model. This hints that a slower build-up of dust is necessary in the most immature galaxies that have yet to convert much of their gas into stars. Following Zhukovska (2014) and Feldmann (2015), we relaxed the closed box assumption, reduced the contribution from supernova dust, and included dust grain growth in our model. We have found that the dust-poor HIGH-low sources can be modelled using either moderately reduced (factor of 6) supernova dust yields and moderate (timescale of $\sim$ 500 Myr) dust grain growth, or strongly reduced (factor of 25) supernova dust yields and fast (timescale of $\sim$ 200 Myr) dust grain growth. For the dust-rich high gas fraction sources, there is either a non-reduced supernova dust contribution, or a reduced supernova dust contribution and extremely fast (timescale of $\sim$ 5 Myr) grain growth.

In order to match the evolution of SFR$/M_{\rm bary}$ for high gas fraction sources, delayed star formation history models are necessary. However, the DGS selection towards low metallicities means that these galaxies tend to be more actively star forming and require a bursty SFH as originally shown in Zhukovska (2014). In contrast, the HIGH-low galaxies have lower star formation rates and lie on a similar $Z - f_g$ relationship to the more evolved, typical spirals in the HRS, and the dust-rich HAPLESS galaxies. This has allowed us to populate the low-metallicity, dust-poor regime previously studied only using the DGS sample with more normal star-forming systems.

The dust-to-gas mass ratio correlates with metallicity over a wide range ($7.5 < 12 + \log({\rm O/H})_{\rm PG16S} < 9.0$). However, we have found that low-metallicity galaxies can have dust properties that (a) are consistent with a linear $M_d/M_g - Z$ relationship or (b) dust masses well below this trend. Zhukovska (2014) showed the scatter in this relation can be produced by using different bursty SFH. We have shown differences in the strength of the contribution of

supernova dust, as well as differences in the dust growth time-scales and galactic winds (and thus critical metallicity) can also produce the observed scatter, without the need for bursty SFH.

In summary, following Zhukovska (2014) and Feldmann (2015) we have produced chemical evolution models to explain the observed galaxy properties, yet using a significantly larger combined sample (425 sources instead of 126) of nearby galaxies. We constructed models with reduced supernova dust yields (factor of 25), moderate outflows (2×SFR), delayed SFH, dust destruction and grain growth (timescales ranging from 1 Gyr - 200 Myr). We have shown this model (Model VI) is consistent with all of the observed properties of the HIGH-low sources, the first normal star forming population of low stellar mass galaxies studied in this way.

HI-stacking. We have performed a spectral stacking analysis on low SNR HI spectra in order to study the average HI content of 1325 dust-selected galaxies and 4118 stellar mass selected galaxies between $0.04 < z < 0.11$. We use available Parkes observations over the G09 and G15 fields, which unfortunately are significantly affected by RFI. We therefore perform additional masking, and extra care has been taken to subtract an accurate baseline. There are, on average, 5 galaxies confused within the Parkes beam, and we estimate the contribution of the target source to the confused HI signal based on scaling relations with observed galaxy colours and stellar mass.

We find an average HI mass of $(3.17 \pm 0.12) \times 10^9 M_\odot$ for the dust-selected sample, and $(1.69 \pm 0.08) \times 10^9 M_\odot$ for the stellar mass selected sample. The average $M_{\rm HI}/M_*$ are found to be 0.28 ± 0.05 and 0.55 ± 0.04 for the dust- and stellar mass selected samples respectively. The low $M_{\rm HI}/M_*$ for the dust-selected sample is consistent with this sample consisting of sources with high stellar masses. We have also studied scaling relations with stellar mass and colour, and found similar relations to those in the nearby Universe. At fixed stellar mass, we find the dust-selected sources have higher $M_{\rm HI}/M_*$ than stellar mass selected sources. At a given colour, the $M_{\rm HI}/M_*$ are similar for both samples. There is, however, a small offset between our stacking results and stacking results in the literature. We attribute this offset to uncertainties in our baseline removal and deconfusion methods. The presented results should thus be regarded as preliminary results.

In conclusion, we have studied the dust and gas content of galaxies in the Local Universe ($z \lesssim 0.1$). We have compared HI-selected, dust-selected and stellar mass selected samples and concluded these consist of galaxies at different evolutionary stages. We have found there is

significant evolution in galaxy properties with gas fraction and NUV-*r* colour, and the trend is not dependent on how the sample was selected (in contrast to scaling relations with e.g. stellar mass). By selecting nearby ($z \lesssim 0.04$) galaxies on their HI-content, we have identified a sub-sample of the highest gas fraction sources that have much lower dust content than expected from extrapolating benchmark scaling relations in the literature (e.g. HRS). We modelled our sources using chemical evolution models and found we need reduced supernova dust yields (factor of 25), moderate inflows and outflows ($2\times$SFR), delayed SFH, dust destruction and grain growth (timescales ranging from 1 Gyr - 200 Myr) in order to model the sources in our sample (including the gas-rich low-metallicity sources with low dust content). We have thus gained deeper understanding of the sources and sinks of dust in galaxies in the Local Universe, especially at high gas fractions. We have significantly increased the sample size of nearby gas-rich, normal star forming galaxies, for which the dust content is studied with *Herschel*.

8.2 Outlook

This thesis has answered a series of questions on the dust and gas properties of galaxies in the local universe. However, as always in science, these answers are not complete and open doors to new questions and other avenues of research. In this section, we discuss some potential follow-up projects that come to mind.

The equatorial H-ATLAS fields are ideal for studying the dust and gas content of galaxies. However, the extracted HI-selected sample is somewhat limited in size. Next to our sample in the H-ATLAS fields, it is also possible to use the *Herschel* maps at the North Galactic Plane (NGP). This NGP field spans 150 deg^2 and has been covered by the ALFALFA survey, which provides HI coverage with higher resolution and sensitivity than HIPASS. Even though the NGP is of similar size as the equatorial fields combined, the higher sensitivity of ALFALFA leads to a sample of 337 unconfused HI-selected NGP sources. Due to the smaller ALFA beam ($3.5'$ instead of $15.5'$) there are fewer (14 confused sources out of 351 ALFALFA sources) confused sources. Although there is good HI-coverage, the NGP has significantly poorer ancillary observations. The SDSS and GALEX coverage of the NGP field is not as deep and there is no VIKING coverage (though there is 2MASS coverage). The large number of sources in this sample outweighs these disadvantages though, especially since the *Herschel* observations, which often have the lowest SNR in HIGH, have the same sensitivity as for the equatorial fields. The photometry pipeline used in this work could easily be adapted for these maps, and the resulting photometry run through MAGPHYS. These HI-selected sources (as well as dust-selected sources in the NGP), could then readily be used to increase statistics for the scaling relations in this work.

The South Galactic Plane (SGP), which measures approximately 290 deg^2, has coverage from the KIDS and VIKING surveys in the optical through to K band. There is only shallow GALEX coverage. Many sources will likely not have strong enough multiwavelength detections to properly constrain MAGPHYS results. However, even in those cases, sufficient photometry is available to obtain reliable stellar masses. These stellar masses could be combined with HIPASS (and literature) unconfused HI masses to determine gas fractions. We could then divide all HI-selected NGP and SGP sources in bins of gas fraction and stack the *Herschel* maps. This would allow us to significantly better constrain the average dust temperature and mass for the highest gas fraction sources, which currently have somewhat large uncertainties.

In this thesis we have identified two populations of enigmatic blue gas-rich sources with small stellar masses, irregular or flocculent morphologies and extended UV disks. The dust-poor HIGH-low sources are enigmatic with respect to their position in the scaling relations and their dust sources. The dust-rich BADGRS sources follow scaling relations for more evolved sources, yet have some surprising characteristics. From their blue colours, extended UV disks and high specific star formation rates, it would be expected to find only a moderate dust mass and relatively warm (~ 25 K) dust, whereas in reality they are cold and dusty. A subset of four BADGRS (NGC5496, NGC5584 ,UGC09215 and UGC09299) has been selected for further study (PI Loretta Dunne). These sources have been observed with SCUBA2 at 850 μm to search for a submm excess, which could indicate different dust composition/size distribution. Additionally, high-resolution ($2''$ beam) HI observations have been carried out with GMRT to reveal the distribution of atomic hydrogen. To study the molecular gas in these sources, observations of the ^{12}CO(2-1) line were made with the EMIR instrument on the IRAM 30m telescope. Preliminary results show the 4 BADGRS are CO faint, in spite of relatively high dust and metal content. Furthermore ALMA time has been awarded in order to observe the low-J transitions of ^{12}CO(J = 3, 2, 1) and 350 GHz dust emission at $0.7''$ resolution. The analysis of these observations will be very interesting and would e.g. allow to study the atomic-to-molecular transition on scales of a few hundred pc.

To fully understand the strange properties of these galaxies though, it is necessary to study how the dust and stars are distributed and how their radiation propagates through the galaxy. The best way to study how a certain distribution affects the observations is by properly solving the continuum radiative transfer equation, taking into account realistic geometries and the physical processes of absorption and multiple anisotropic scattering. For realistic settings, this can only be done computationally in a Monte Carlo radiative transfer code such as SKIRT (Baes et al., 2011). Much can be learned from studying which distribution of dust and stars best matches the observations for our blue sources. This would for example shed light on why the BADGR sources can be both blue and dusty. Another interesting project would be to study the

effect of geometry (in particular clumpiness of the dust distribution) on the FUV obscuration of galaxies, which was found to show large scatter at fixed dust mass or fixed gas fraction.

Throughout this work we have used integrated photometry and models to study the global evolution of the dust and gas in local galaxies. However, if higher resolution HI observations are available, it is possible to study the galaxy properties on a resolved scale. It is possible (e.g. Viaene et al., 2014) to convolve all bands to the same pixel size, and then perform photometry and fit SEDs on a pixel by pixel basis. This would allow us to zoom in on interesting regions and study the variation within a galaxy (e.g. radial profiles). Having resolved distributions of the various galaxy components available would also be a great starting point to model the input distributions going into the SKIRT code for radiative transfer.

Our current chemical evolution models are 'one-zone' models, meaning they study the integrated properties of galaxies without spatial resolution. However it is possible to include spatial resolution and even combine chemical evolution with the evolution of the distributions of the baryonic galaxy components from smoothed-particle hydrodynamical simulations (e.g. Bekki, 2015; Aoyama et al., 2016). The interplay of both these aspect would allow to study variation and make predictions about the distribution of dust within a galaxy. Differences in the local conditions could mean that some areas of the galaxy reach their critical metallicity for grain growth earlier, which could lead to an earlier increase in the dust mass. As the critical metallicity is reached at different times throughout the galaxy, this will lead to a more gradual build-up of the overall dust mass, rather then a rather steep increase at the critical metallicity. For a more realistic comparison of simulations and observations, the output from the chemical evolution + smoothed-particle hydrodynamical simulations could be post-processed using the SKIRT code (e.g. Camps et al., 2016).

Our HI-stacking analysis is limited by the deconfusion issue. A logical next step is to try to determine better deconfusion-factors. One very useful tool would be the combination of low resolution observations Parkes data and higher resolution HI observations over the same part of sky. Overlap between HIPASS and ALFALFA is widely available, however in order to use scaling relations with colour and stellar mass, we need to select a part of the sky with good ancillary observations. Additionally, machine learning could be a good technique to determine the most likely HI contribution based on all the available multiwavelength information. Another obvious way to reduce the confusion issue is to use better resolution observations (e.g. HI-stacking of ALFALFA spectra). We also note that our spectral stacking method can be applied to other spectral lines such as CO, to study the molecular gas for individually undetected galaxies.

Our investigating has been limited to the local Universe due to the limited resolution and sensitivity of the current generation of HI telescopes. The next major leap forward in this

field will be provided by the SKA and the pathfinder radio telescopes including ASKAP and MeerKAT. The planned DINGO survey will provide deep HI data over the equatorial H-ATLAS/GAMA fields out to $z \simeq 0.44$. This will allow a much more detailed study of the dust and gas scaling relations in these fields, and will drastically improve statistics, as well as allow the study of trends with redshift. Stacking of the HI spectra as well as *Herschel* maps will be useful tools in the analysis of these sources.

Chapter 9

Samenvatting

9.1 Inleiding

In dit proefschrift bestuderen we de evolutie van de stof- en gas inhoud van sterrenstelsels in het nabije Universum. We selecteren deze galaxieën in de equatoriale H-ATLAS velden, omdat deze uitstekende multi-golflengte waarnemingen beschikbaar hebben van FUV tot submm golflengtes. We hebben drie onderzoeken uitgevoerd om de stof- en gas inhoud in deze velden te bestuderen. Ten eerste, bestuderen we 40 lokale galaxieën die geselecteerd werden op hun HI (atomisch waterstof gas) inhoud. We bepalen galaxie eigenschappen met behulp van de MAGPHYS code toegepast op fotometrie met dezelfde aperture in 21 banden. Vervolgens hebben we schalingsrelaties voor dit sample onderzocht in vergelijking met een stof-geselecteerd sample en een stermassa geselecteerd sample. In een tweede project, hebben we metalliciteiten afgeleid en het DGS sample aan onze nabijgelegen sterrenstelsel samples toegevoegd. Samen hebben deze sterrenstelsels een grote verscheidenheid in gasfractie ($0.05 < f_g < 0.97$). We vergelijken deze observaties met chemische evolutiemodellen om de bronnen van het aanwezige stof te onderzoeken. Tot slot onderzoeken we de stof- en gas inhoud van sterrenstelsels met grotere roodverschuiving. We doen dit met behulp van een 'HI-Stacking' analyse waarbij de HI signalen van sterrenstelsels tussen roodverschuiving $0.04 < z < 0.1$ gecombineerd worden. Deze produceren samen een detectie voor de gemiddelde stof-geselecteerd en stermassa-geselecteerd sterrenstelsels (die individueel niet gedetecteerd waren).

9.2 Schalingsrelaties voor stof en gas in lokale sterrenstelsels

In hoofdstuk 2, selecteren we de 'HI-Selected Galaxies in H-ATLAS' (HIGH) sample. We vertrekken vanuit de 32 HIPASS objecten in de equatoriale H-ATLAS velden. Omdat sommige van deze objecten 'confused' zijn (het HI signaal van meerdere bronnen valt niet te onderscheiden), maken we gebruik van hogere resolutie ALFALFA of literatuur observaties indien beschikbaar. Op deze manier bekomen we een sample van 40 niet-confused lokale ($z < 0.035$) HI-geselecteerde stelsels. Dit sample werd verdeeld in HIGH-high ($M_* > 10^9\,M_\odot$) en HIGH-low ($M_* < 10^9\,M_\odot$), om de raadselachtige stofarme bevolking van ongeëvolueerde sterrenstelsels in HIGH-low in meer detail te onderzoeken. In hoofdstuk 3 presenteren we het fotometrie proces, toegepast op het HIGH sample. De belangrijkste kenmerken van het fotometrie proces zijn een geautomatiseerde aperture bepaling, het voorzichtig verwijderen van vervuilende sterren en stelsels, een lokale achtergrond aftrekking en een nadruk op het bepalen van de onzekerheid. De resulterende fotometrie werd vergeleken met resultaten van andere methodes, met inbegrip van H-ATLAS en LAMBDAR (GAMA) resultaten. Ons fotometrie proces blijkt betrouwbaar te zijn. Vervolgens gebruiken we MAGPHYS om galaxie eigenschappen te verkrijgen voor onze sterrenstelsels.

Met het oog op de wisselwerking tussen stof, gas en stervorming, bestuderen we schalingsrelaties in hoofdstuk 4. We vergelijken HIGH met het stof-geselecteerde HAPLESS en het stermassa geselecteerde HRS. De gecombineerde samples bestrijken een grote verscheidenheid in gasfractie ($f_g = 1.32\,M_{\rm HI}/(1.32\,M_{\rm HI} + M_*)$), die wordt gebruikt als een proxy voor de evolutionaire toestand van een sterrenstelsel. De afgeleide schalingsrelaties voor de gecombineerde samples in dit hoofdstuk worden beïnvloed door selectie afwijkingen. Schalingsrelaties met stermassa tonen significante gemiddelde afwijkingen tussen de verschillend geselecteerde samples (Figuur 9.1 links). De gas en stof schalingsrelaties gekoppeld aan NUV-r (SSFR) en gasfractie, daarentegen, zijn robuust tegen dit soort afwijkingen (Figuur 9.1 rechts). Dit zijn strakke relaties die niet afhankelijk zijn van selectie methode en omgeving van het stelsel en worden dus niet beïnvloed door de complexe selectiecriteria van ons gecombineerd sample.

Het merendeel van de HIGH-low sterrenstelsels hebben een zeer hoge gasfracties ($f_g >$ 80%) en een veel kleiner stofgehalte dan verwacht uit het extrapoleren van gepubliceerde schalingsrelaties voor verder geëvolueerde stelsels (Figuur 9.1). Voor deze stelsels in de vroegste stadia van ontwikkeling is stof geen goede tracer van de HI inhoud. De HIGH-low sterrenstelsels zijn ook de meest actief stervormende sterrenstelsels in verhouding tot hun stermassa (SSFR) en in verhouding tot hun stofmassa, maar minst actief ten opzichte van HI massa. Onze *Herschel* studie van HI-geselecteerde galaxieën laat ons voor het eerst toe de interessante eigenschappen van deze stofarme onvolwassen sterrenstelsels te bestuderen.

Sterrenstelsels evolueren van hoge naar lage gasfracties. Voor sterrenstelsels in latere evolutionaire stadia nemen, doorheen dit proces, de M_d/M_* en SSFR af en de $M_d/M_{\rm HI}$ neemt toe. Er is ook een trend van afnemende HI depletie tijd ($M_{\rm HI}/SFR$) met afnemende gasfractie, tegenovergesteld van de gevonden trend voor de moleculair gas depletie tijd ($M_{\rm H_2}/SFR$). We interpreteren dit als gevolg van de toenemende efficiëntie waarmee HI kan worden omgezet in H_2 wanneer stelsels toenemen in stellaire oppervlaktedichtheid met afnemende gasfractie. Bovendien, onze gegevens bevestigen resultaten in de literatuur dat zowel oude als jonge sterpopulaties een belangrijke rol spelen bij het verwarmen van de diffuse stof component, en beide kunnen de dominante bijdrage leveren voor individuele systemen. De SSFR bepaald welke domineert. Tot slot tonen we aan dat sterrenstelsels nauwelijks verduisterd aan hun evolutie beginnen en toenemen in verduistering wanneer ze zich verder ontwikkelen. Toch is er geen duidelijke en eenvoudige koppeling tussen verduistering en globale galaxie eigenschappen.

9.3 Chemische evolutie modellen

Om de opbouw en de daling van de stof inhoud van sterrenstelsels te bestuderen, vergelijken we onze observaties van de gecombineerde nabijgelegen sterrenstelsel samples, inclusief de DGS, met chemische evolutie modellen in hoofdstuk 6. Deze modellen voorspellen de stof, metaal, gas en stellaire inhoud van sterrenstelsels doorheen hun evolutie (hier maken we weer gebruik van gasfractie als proxy voor evolutionair stadium). We concentreren ons op de evolutie van $M_d/M_{\rm bary}$, SFR$/M_{\rm bary}$, $12+\log({\rm O/H})$ en M_d/M_g (Figuur 9.2). Metalliciteiten (verkregen in hoofdstuk 5) kunnen worden gebruikt om tussen verschillende chemische evolutiemodellen en stofbronnen te onderscheiden. We vergelijken de N2, PG16S en KE08/T04 kalibraties om de onzekerheid in de metalliciteit kalibraties te schatten. We vinden dat PG16S het meest betrouwbaar is voor de lage metalliciteit stelsels, en minder spreiding geeft met andere kalibraties en stermassa dan de populaire PT05 kalibratie. Om de waargenomen metalliciteiten in Figuur 9.2 (links-onder) te reproduceren, vooral bij lage gasfracties (late evolutionaire stadia; bijvoorbeeld de HRS stelsels), is het nodig om in- en uitstroom van gas toe te voegen (met een tempo van twee keer de SFR) om te vermijden dat de metalliciteit in de modellen hoger stijgt dan de waargenomen metalliciteiten.

Met behulp van een eenvoudig 'gesloten doos' chemische evolutie model (Model I, Figuur 9.2) kan men de $M_d/M_{\rm bary}-f_g$ relaties verklaren met behulp van het volgende beeld: Wanneer sterrenstelsels evolueren, stijgt hun stofgehalte eerst steil, daarna vlakt het af en

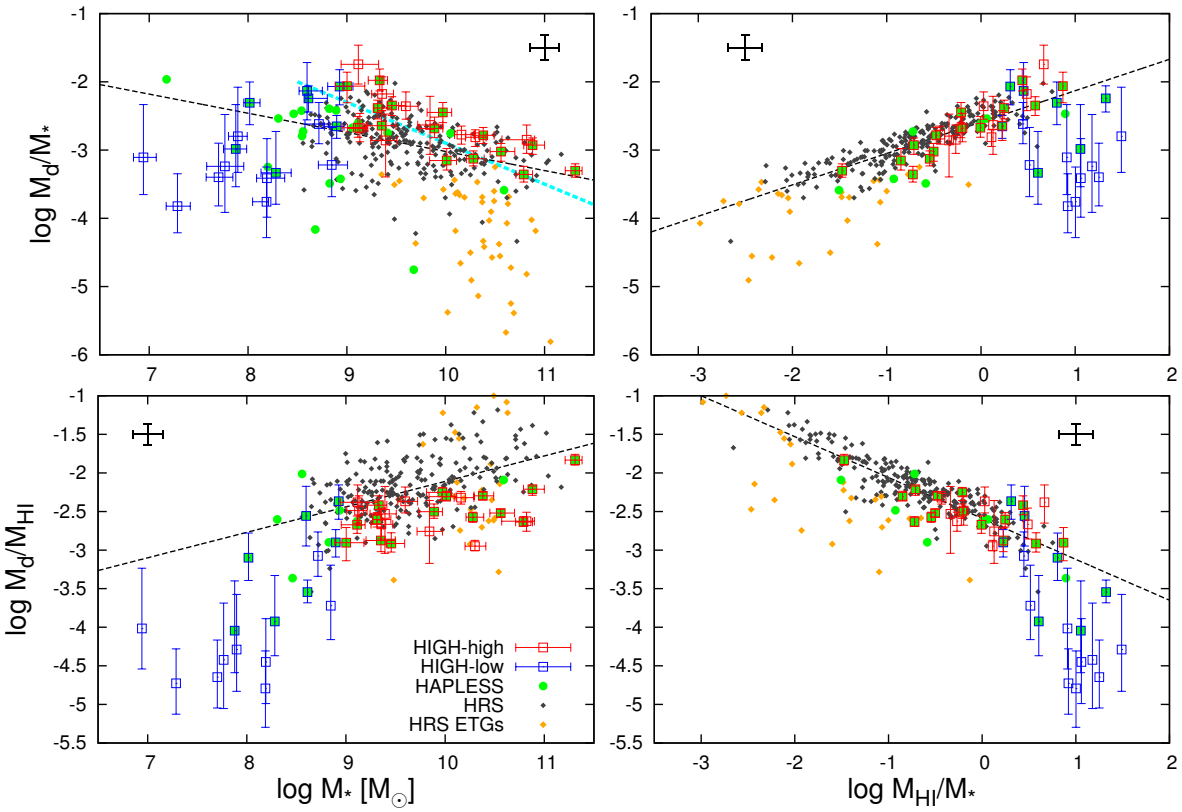

Figure 9.1: Stof schalingsrelaties voor HIGH-high, HIGH-low, HAPLESS en HRS (opgesplitst in laat-type stelsels and vroeg-type of ETG stelsels). De best fittende lineaire relatie voor HIGH-high, HAPLESS en laat-type HRS stelsels is voorgesteld als een gestreepte lijn. De HIGH-low stelsels hebben duidelijk minder stof dan voorspeld door deze relatie voor zowel M_d/M_* (*boven*) als $M_d/M_{\rm HI}$ (*onder*). De relaties met $M_{\rm HI}/M_*$ (*rechts*) zijn strakker dan diegene met stermassa $M*$ (*links*) en tonen ook minder afwijking tussen de verschillende samples.

bereikt een piek ongeveer halverwege doorheen de evolutie. Het stofgehalte begint te dalen voor lagere gasfracties naarmate er meer stof wordt vernietigd/geconsumeerd dan geproduceerd. Sommige van de HIGH-low stelsels hebben een beduidend lager stofgehalte dan dit model (Figuur 9.2; links-boven). Dit wijst dat een langzamer opbouw van stof noodzakelijk is voor deze ongeëvolueerde stelsels die nog niet veel van hun gas hebben omgezet in sterren. Net zoals Zhukovska (2014) en Feldmann (2015), ontspannen we de gesloten doos veronderstelling, verminderen we de bijdrage van supernova stof, en voegen we stof korrelgroei toe aan ons model. We vinden dat we de stofarme HIGH-low stelsels kunnen verklaren met behulp van matig verminderd (factor 6) supernova stof en matige (tijdschaal van $\sim$ 500 Myr) stof korrelgroei, of sterk verminderd supernova stof (factor 25) en snelle (tijdschaal van $\sim$ 200 Myr) stof korrelgroei (Model VI, Figuur 9.2). Voor de stofrijke hoge gasfractie stelsels, is er ofwel een

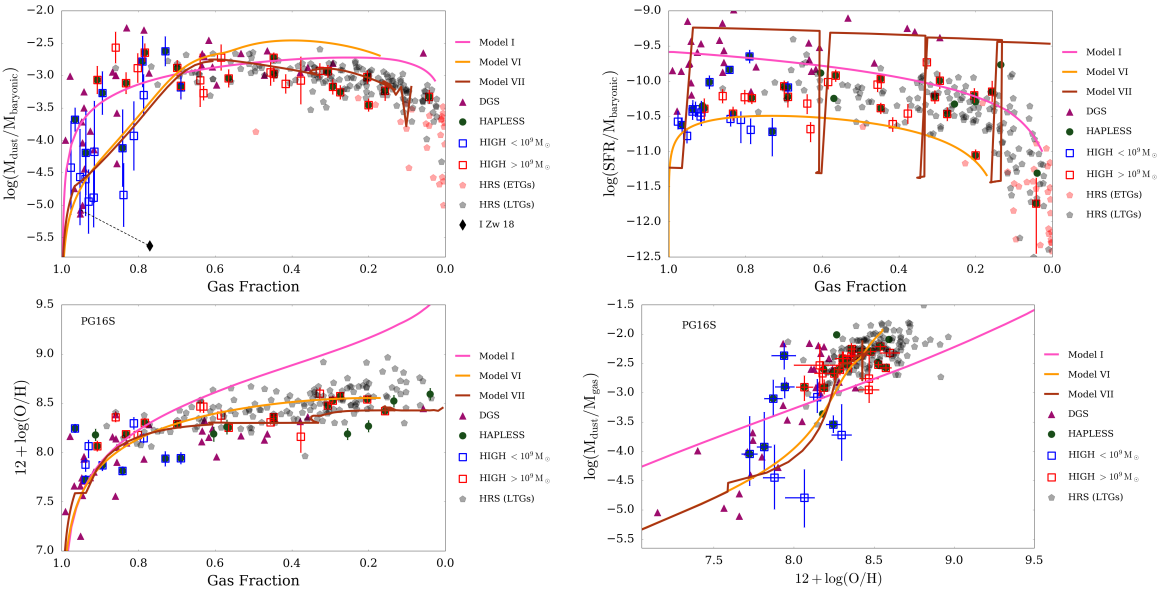

Figure 9.2: *Boven:* $M_d/M_{\rm bary}$ (*links*) en SFR$/M_{\rm bary}$ (*rechts*) evolutie met gasfractie voor de verschillende samples en 3 Modellen uit dit onderzoek. *Onder:* de variatie in metalliciteit wordt vergeleken met gasfractie (*links*) en $M_d/M_{\rm HI}$ (*rechts*). Model I is een eenvoudig model zonder stof korrelgroei of in- en uitstromen, en kan de waargenomen eigenschappen niet verklaren. Model VI heeft een gereduceerde supernova stof bijdrage, matige in- en uitstromen en korrelgroei, en geeft het beste model om onze HIGH-low galaxieën te verklaren. De DGS eigenschappen worden best verklaard door Model VII met een gereduceerde supernova stof bijdrage, sterke in- en uitstromen, matige korrelgroei, en een bursty SFH.

niet-gereduceerde supernova stof bijdrage, of verminderd supernova stof en extreem snelle (tijdschaal van ~ 5 Myr) korrelgroei.

Om de observaties van SFR$/M_{\rm bary}$ voor hoge gasfractie stelsel te laten overeenkomen met de modellen, is het nodig een vertraagde SFH (stervorming geschiedenis) te gebruiken (Model VI, Figuur 9.2 rechts-boven). De DGS selectie naar lage metalliciteiten betekent dat deze sterrenstelsels ook een selectie naar meer actieve stervorming hebben en daarom vereisen deze een bursty SFH, zoals oorspronkelijk aangegeven in Zhukovska (2014) (Model VII, Figuur 9.2). In tegenstelling tot DGS hebben de HIGH-low sterrenstelsels een lagere SFR en liggen op gelijkaardige $Z - f_g$ relaties als de meer ontwikkelde, typisch spiralen in de HRS, en de stofrijke HAPLESS sterrenstelsels. Dit stelt ons in staat om het lage metaalgehalte, stofarme regime dat voorheen alleen onderzocht was met gebruik van DGS, met meer normale-stervorming systemen te bevolken.

Zoals getoond in Figuur 9.2 (rechts-onder) correleert de M_d/M_g met metalliciteit over een breed bereik ($7.5 < 12+\log({\rm O/H})_{\rm PG16S} < 9.0$). We vinden dat lage metalliciteit sterrenstelsels, stof eigenschappen kunnen hebben die (a) in overeenstemming zijn met een lineaire $M_d/M_g - Z$ relatie of (b) stof massa's hebben ver onder deze trend. Zhukovska (2014) toonden aan dat

de spreiding in deze relatie kan worden verklaard door gebruik te maken van verschillende bursty SFH. We tonen aan dat verschillen in de bijdrage van supernova stof, en de verschillen in de stof korrelgroei en de in- en uitstroom van gas (en dus ook in de kritische metalliciteit) eveneens de waargenomen spreiding kunnen verklaren zonder bursty SFH.

Samengevat, zoals in Zhukovska (2014) en Feldmann (2015), hebben we chemische evolutie modellen geproduceerd om de waargenomen galaxie eigenschappen te verklaren, maar hier gebruiken we een aanzienlijk groter gecombineerd sample (425 stelsels in plaats van 126) van nabijgelegen sterrenstelsels. We maken modellen met gereduceerd supernova stof (factor 25), matige uitstroom (2$\times$ SFR), vertraagde SFH, stof vernieling en stof korrelgroei (tijdschalen variërend van 1 Gyr – 200 Myr). We tonen aan dat dit model (Model VI) in overeenstemming is met de waargenomen eigenschappen van de HIGH-low stelsels, de eerste normale-stervorming populatie van lage stermassa stelsels die bestudeerd is op deze manier.

9.4 HI-Stacking

We hebben een 'HI-Stacking' analyse toegepast om de gemiddelde HI inhoud van 1325 stof-geselecteerde sterrenstelsels en 4118 stermassa geselecteerde sterrenstelsels tussen $0.04 < z < 0.11$ te bestuderen. We maken gebruik van beschikbare Parkes observaties over de G09 en G15 velden, die helaas significant beïnvloed zijn door RFI. Daarom hebben we de beïnvloede frequenties niet gebruikt, en extra aandacht geschonken aan het nauwkeurig aftrekken van de baseline. Er zijn gemiddeld 5 sterrenstelsels 'confused' binnen de Parkes beam, en we schatten de bijdrage van ieder sterrenstelsel op basis van schalingsrelaties met de waargenomen kleuren en stermassa's van de sterrenstelsels.

We vinden een gemiddelde HI massa van $(3.17 \pm 0.12) \times 10^9\, M_\odot$ voor de stof-geselecteerde stelsels, en $(1.69 \pm 0.08) \times 10^9\, M_\odot$ voor de stermassa geselecteerde stelsels. De gemiddelde $M_{\rm HI}/M_*$ zijn 0.28 ± 0.05 en 0.55 ± 0.04 voor de stof- en stermassa geselecteerde samples respectievelijk. De lage $M_{\rm HI}/M_*$ voor de stof-geselecteerde stelsels is in overeenstemming met de hoge stermassa's voor deze sterrenstelsels. We hebben ook schalingsrelaties met stermassa en kleur onderzocht, en vonden gelijkaardige relaties met die in het nabije heelal. Bij vaste stermassa, vinden we dat stof-geselecteerde stelsels een hogere $M_{\rm HI}/M_*$ hebben dan stermassa geselecteerde sterrenstelsels. Bij een vaste kleur, zijn de gemiddelde $M_{\rm HI}/M_*$ gelijk voor beide samples. Onze stacking resultaten hebben een iets lagere HI inhoud dan verwacht uit de literatuur. We schrijven dit toe aan onzekerheden in onze werkwijze, vooral in het aftrekken van de baseline en de correctie voor 'confusion'. De gepresenteerde resultaten worden dus best beschouwd als voorlopige resultaten.

9.5 Besluit

In dit werk hebben we de stof- en gas inhoud van sterrenstelsels in het Lokale Universum ($z \lesssim 0.1$) bestudeerd. We vergeleken HI-geselecteerde, stof-geselecteerde en stermassa geselecteerde samples en besluiten dat dit resulteert in samples met sterrenstelsels in verschillende evolutionaire stadia. We vonden dat er aanzienlijke evolutie is in de galaxie eigenschappen met gasfractie en NUV-r kleur en dat deze trends niet afhankelijk zijn van hoe het sample werd geselecteerd (in tegenstelling tot schalingsrelaties met bijvoorbeeld stermassa). Door nabijgelegen ($z \lesssim 0.04$) stelsels te selecteren op hun HI-inhoud, bekomen we een sub-sample van stelsels met de hoogste gasfracties die een veel lager stofgehalte hebben dan verwacht uit extrapolatie van referentie-schalingsrelaties in de literatuur (bv HRS). We modelleren onze galaxieën met behulp van chemische evolutie modellen en vinden dat we een verminderde supernova stof bijdrage (factor 25), matige in- en uitstromen ($2\times$ SFR), vertraagde SFH, stof vernietiging en korrelgroei (tijdschalen variërend van 1 Gyr - 200 Myr) nodig hebben om de bronnen in ons sample te modelleren (inclusief de gasrijke lage metalliciteit stelsels met laag stofgehalte). We komen dus tot een dieper begrip over het evenwicht tussen de productie en destructie van stof in sterrenstelsels in het Plaatselijk Universum, vooral bij hoge gasfracties. We hebben dus een aanzienlijk groter sample van nabijgelegen gasrijke, normale-stervorming sterrenstelsels, waarvoor het stofgehalte bestudeerd is met *Herschel*.

Appendix A

Molecular gas

Unfortunately we do not have CO data for the HIGH and HAPLESS sample so we cannot measure the molecular gas mass present in these galaxies. To determine an appropriate estimation of the H_2 mass, we have compiled published M_{H_2}, M_{HI} and M_* derived for the APEX Low-redshift Legacy Survey for MOlecular Gas (ALLSMOG; Bothwell et al., 2014) and the CO Legacy Database for the GALEX Arecibo SDSS Survey (COLDGASS; Saintonge et al., 2011). These samples were then used to derive scaling relations for M_{H_2}/M_{HI} and M_{H_2}/M_* with stellar mass and M_{HI}/M_*. The strongest correlation was found between M_{H_2}/M_{HI} and M_{HI}/M_* and is shown in Figure A.1. The best fitting trend is given by:

$$log\, M_{H_2}/M_{HI} = -1.02 - 0.49\, log\, M_{HI}/M_* \tag{A.1}$$

We have used this relation to estimate H_2 masses for HIGH and HAPLESS. We find that the estimated molecular gas component is small compared to the HI masses for HI-selected sources. For the HRS, CO derived H_2 masses are presented in Boselli et al. (2014a) and can be large compared to their HI (Figure A.1). However, they are still small compared to the total baryon mass. We have also included M_{H_2} for DGS, which are taken from Rémy-Ruyer et al. (2014). Here we include results for converting CO fluxes using a constant conversion factor $X_{CO,MW}$ (Ackermann et al., 2011), and for a metallicity-dependent conversion from CO $X_{CO,Z}$ (Schruba et al., 2012).

In Figure A.2 we illustrate the difference to the scaling relation when including H_2 in the total (HI+H_2+He[1]) gas masses instead of only HI and He. We repeat Figure 4.8 (see also Figure 6.6), as this plot is important for the interpretation of our results, and the plotted gas fractions and baryon masses are both dependent on the contribution of H_2. We find there are

[1] We assume the helium mass is 32% of the HI mass.

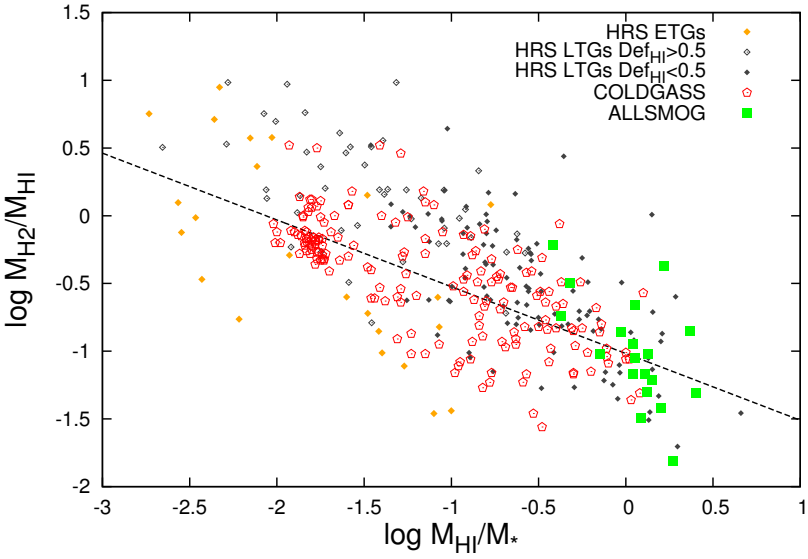

Figure A.1: Relation between the molecular-to-atomic gas mass ratio ($M_{\rm H_2}/M_{\rm HI}$) and $M_{\rm HI}/M_*$ for the ALLSMOG, COLDGASS and HRS samples. The best fitting relation to the combined ALLSMOG and COLDGASS (shown as dashed line) is used to estimate molecular gas masses for HIGH and HAPLESS.

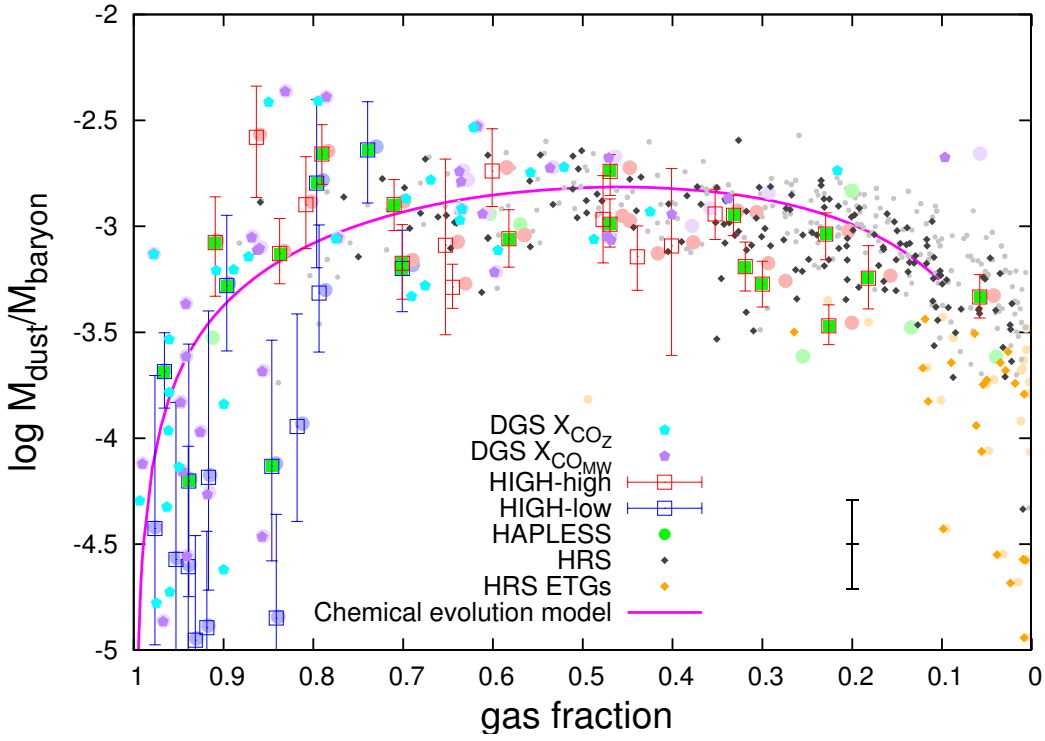

Figure A.2: $M_d/M_{\rm bary}$ against total gas fraction (see also Figure 4.8). The transparent markers use gas fraction and baryon masses excluding H_2 (yet including He). For the solid markers, H_2 has been included (measured for HRS and estimated for HIGH and HAPLESS) in the total gas mass (HI+H_2+He).

only small differences to the results when including H_2. The difference is largest at low gas fractions, yet even there these differences would not affect our conclusions.

There will also only be small differences to the other scaling relations throughout this work[2], and were differences do occur, they will be mostly to the HRS, which is a comparative sample, and not the focus of this work. Considering we only have a quite uncertain estimation of the M_{H_2} for HIGH and HAPLESS, and the H_2 does not affect our conclusions, we opt to not include H_2 masses in the relations throughout this work.

[2]The gas scaling relations in Section 4.3.2 will be affected, and the difference will be proportional to the relation shown in Figure A.1

References

Abazajian, K. N., Adelman-McCarthy, J. K., Agüeros, M. A., et al. 2009, ApJS, 182, 543

Ackermann, M., Ajello, M., Baldini, L., et al. 2011, ApJ, 726, 81

Adelman-McCarthy, J. K., Agüeros, M. A., Allam, S. S., et al. 2008, ApJS, 175, 297

Ahn, C. P., Alexandroff, R., Allende Prieto, C., et al. 2012, ApJS, 203, 21

Akritas, M. G. & Bershady, M. A. 1996, ApJ, 470, 706

Alloin, D., Collin-Souffrin, S., Joly, M., & Vigroux, L. 1979, A&A, 78, 200

Aoyama, S., Hou, K.-C., Shimizu, I., et al. 2016, ArXiv e-prints

Asano, R. S., Takeuchi, T. T., Hirashita, H., & Inoue, A. K. 2013a, Earth, Planets, and Space, 65, 213

Asano, R. S., Takeuchi, T. T., Hirashita, H., & Inoue, A. K. 2013b, Earth, Planets, and Space, 65, 213

Ascasibar, Y., Gavilán, M., Pinto, N., et al. 2015, MNRAS, 448, 2126

Baes, M. & Dejonghe, H. 2001, MNRAS, 326, 733

Baes, M., Verstappen, J., De Looze, I., et al. 2011, ApJS, 196, 22

Baldry, I. K., Driver, S. P., Loveday, J., et al. 2012, MNRAS, 421, 621

Baldry, I. K., Robotham, A. S. G., Hill, D. T., et al. 2010, MNRAS, 404, 86

Baldwin, J. A., Phillips, M. M., & Terlevich, R. 1981, PASP, 93, 5

Barlow, M. J. 1978, MNRAS, 183, 367

Barlow, M. J., Krause, O., Swinyard, B. M., et al. 2010, A&A, 518, L138

Barnes, D. G., Staveley-Smith, L., de Blok, W. J. G., et al. 2001, MNRAS, 322, 486

Barnes, J. E. & Hernquist, L. 1992, ARA&A, 30, 705

Bastian, N., Covey, K. R., & Meyer, M. R. 2010, ARA&A, 48, 339

Bauer, A. E., Hopkins, A. M., Gunawardhana, M., et al. 2013, MNRAS, 434, 209

Bekki, K. 2013, MNRAS, 432, 2298

Bekki, K. 2015, MNRAS, 449, 1625

Bendo, G. J., Baes, M., Bianchi, S., et al. 2015, MNRAS, 448, 135

Bendo, G. J., Boselli, A., Dariush, A., et al. 2012a, MNRAS, 419, 1833

Bendo, G. J., Galliano, F., & Madden, S. C. 2012b, MNRAS, 423, 197

Bendo, G. J., Wilson, C. D., Pohlen, M., et al. 2010, A&A, 518, L65

Bertin, E. & Arnouts, S. 1996, A&AS, 117, 393

Bianchi, S. 2008, A&A, 490, 461

Bianchi, S. & Schneider, R. 2007, MNRAS, 378, 973

Bigiel, F., Leroy, A., Walter, F., et al. 2008, AJ, 136, 2846

Bigiel, F., Leroy, A. K., Walter, F., et al. 2011, ApJ, 730, L13

Blanton, M. R., Dalcanton, J., Eisenstein, D., et al. 2001, AJ, 121, 2358

Bocchio, M., Bianchi, S., & Abergel, A. 2016, A&A, 591, A117

Bolatto, A. D., Wolfire, M., & Leroy, A. K. 2013, ARA&A, 51, 207

Boquien, M., Boselli, A., Buat, V., et al. 2013, A&A, 554, A14

Boquien, M., Buat, V., Boselli, A., et al. 2012, A&A, 539, A145

Boquien, M., Calzetti, D., Kramer, C., et al. 2010, A&A, 518, L70

Boquien, M., Kennicutt, R., Calzetti, D., et al. 2016, A&A, 591, A6

Boselli, A., Ciesla, L., Buat, V., et al. 2010a, A&A, 518, L61

Boselli, A., Ciesla, L., Cortese, L., et al. 2012, A&A, 540, A54

Boselli, A., Cortese, L., & Boquien, M. 2014a, A&A, 564, A65

Boselli, A., Cortese, L., Boquien, M., et al. 2014b, A&A, 564, A66

Boselli, A., Eales, S., Cortese, L., et al. 2010b, PASP, 122, 261

Boselli, A., Fossati, M., Gavazzi, G., et al. 2015, A&A, 579, A102

Boselli, A., Gavazzi, G., Donas, J., & Scodeggio, M. 2001, AJ, 121, 753

Boselli, A., Hughes, T. M., Cortese, L., Gavazzi, G., & Buat, V. 2013, A&A, 550, A114

Bothwell, M. S., Wagg, J., Cicone, C., et al. 2014, MNRAS, 445, 2599

Bourne, N., Dunne, L., Maddox, S. J., et al. 2016, ArXiv e-prints

Bourne, N., Maddox, S. J., Dunne, L., et al. 2012, MNRAS, 421, 3027

Bresolin, F. & Kennicutt, R. C. 2015, MNRAS, 454, 3664

Bresolin, F., Pietrzyński, G., Urbaneja, M. A., et al. 2006, ApJ, 648, 1007

Brown, T., Catinella, B., Cortese, L., et al. 2015, MNRAS, 452, 2479

Bruzual, G. & Charlot, S. 2003, MNRAS, 344, 1000

Bryant, J. J., Owers, M. S., Robotham, A. S. G., et al. 2015, MNRAS, 447, 2857

Buat, V., Giovannoli, E., Takeuchi, T. T., et al. 2011, A&A, 529, A22

Burgarella, D., Buat, V., Gruppioni, C., et al. 2013, A&A, 554, A70

Burgarella, D., Buat, V., & Iglesias-Páramo, J. 2005, MNRAS, 360, 1413

Butcher, H. & Oemler, Jr., A. 1978, ApJ, 219, 18

Calura, F., Gilli, R., Vignali, C., et al. 2014, MNRAS, 438, 2765

Calvi, V., Trenti, M., Stiavelli, M., et al. 2016, ApJ, 817, 120

Calzetti, D. 2001, PASP, 113, 1449

Calzetti, D., Kennicutt, R. C., Engelbracht, C. W., et al. 2007, ApJ, 666, 870

Calzetti, D., Kennicutt, Jr., R. C., Bianchi, L., et al. 2005, ApJ, 633, 871

Camps, P., Misselt, K., Bianchi, S., et al. 2015, A&A, 580, A87

Camps, P., Trayford, J. W., Baes, M., et al. 2016, MNRAS, 462, 1057

Cappellari, M., McDermid, R. M., Alatalo, K., et al. 2012, Nature, 484, 485

Cardelli, J. A., Clayton, G. C., & Mathis, J. S. 1989, ApJ, 345, 245

Casey, C. M., Scoville, N. Z., Sanders, D. B., et al. 2014, ApJ, 796, 95

Catinella, B., Schiminovich, D., Cortese, L., et al. 2013, MNRAS, 436, 34

Catinella, B., Schiminovich, D., Kauffmann, G., et al. 2010, MNRAS, 403, 683

Chabrier, G. 2003, PASP, 115, 763

Charlot, S. & Fall, S. M. 2000, ApJ, 539, 718

Chengalur, J. N., Braun, R., & Wieringa, M. 2001, A&A, 372, 768

Ciesla, L., Boquien, M., Boselli, A., et al. 2014, A&A, 565, A128

Ciesla, L., Boselli, A., Smith, M. W. L., et al. 2012, A&A, 543, A161

Clark, C. J. R., Dunne, L., Gomez, H. L., et al. 2015, MNRAS, 452, 397

Clark, C. J. R., Schofield, S. P., Gomez, H. L., & Davies, J. I. 2016, MNRAS, 459, 1646

Clemens, M. S., Negrello, M., De Zotti, G., et al. 2013, MNRAS, 433, 695

Cluver, M. E., Jarrett, T. H., Hopkins, A. M., et al. 2014, ApJ, 782, 90

Colless, M., Peterson, B. A., Jackson, C., et al. 2003, ArXiv Astrophysics e-prints

Condon, J. J., Cotton, W. D., Greisen, E. W., et al. 1998, AJ, 115, 1693

Corbelli, E., Bianchi, S., Cortese, L., et al. 2012, A&A, 542, A32

Cortese, L., Bekki, K., Boselli, A., et al. 2016, MNRAS, 459, 3574

Cortese, L., Boissier, S., Boselli, A., et al. 2012a, A&A, 544, A101

Cortese, L., Boselli, A., Franzetti, P., et al. 2008, MNRAS, 386, 1157

Cortese, L., Catinella, B., Boissier, S., Boselli, A., & Heinis, S. 2011, MNRAS, 415, 1797

Cortese, L., Ciesla, L., Boselli, A., et al. 2012b, A&A, 540, A52

Cortese, L., Fritz, J., Bianchi, S., et al. 2014, MNRAS, 440, 942

Cowie, L. L., Songaila, A., Hu, E. M., & Cohen, J. G. 1996, AJ, 112, 839

Croton, D. J., Springel, V., White, S. D. M., et al. 2006, MNRAS, 365, 11

da Cunha, E., Charlot, S., & Elbaz, D. 2008, MNRAS, 388, 1595

da Cunha, E., Eminian, C., Charlot, S., & Blaizot, J. 2010, MNRAS, 403, 1894

Dalcanton, J. J., Yoachim, P., & Bernstein, R. A. 2004, ApJ, 608, 189

Dale, D. A., Gil de Paz, A., Gordon, K. D., et al. 2007, ApJ, 655, 863

Davies, J. I., Baes, M., Bendo, G. J., et al. 2010, A&A, 518, L48

Davies, J. I., Bianchi, S., Baes, M., et al. 2014, Monthly Notices of the Royal Astronomical Society, 438, 1922

Davies, L. J. M., Robotham, A. S. G., Driver, S. P., et al. 2015, MNRAS, 452, 616

Davis, T. A., Alatalo, K., Sarzi, M., et al. 2011, MNRAS, 417, 882

Davis, T. A., Rowlands, K., Allison, J. R., et al. 2015, MNRAS, 449, 3503

Davis, T. A., Young, L. M., Crocker, A. F., et al. 2014, MNRAS, 444, 3427

De Cia, A., Ledoux, C., Mattsson, L., et al. 2016, ArXiv e-prints

De Looze, I., Baes, M., Bendo, G. J., et al. 2016, MNRAS, 459, 3900

De Lucia, G., Kauffmann, G., & White, S. D. M. 2004, MNRAS, 349, 1101

De Lucia, G., Springel, V., White, S. D. M., Croton, D., & Kauffmann, G. 2006, MNRAS, 366, 499

de Rossi, M. E., Tissera, P. B., & Scannapieco, C. 2007, MNRAS, 374, 323

Delhaize, J. 2014, PhD thesis

Delhaize, J., Meyer, M. J., Staveley-Smith, L., & Boyle, B. J. 2013, MNRAS, 433, 1398

Demyk, K., Meny, C., Leroux, H., et al. 2013, in Proceedings of The Life Cycle of Dust in the Universe: Observations, Theory, and Laboratory Experiments (LCDU2013). 18-22 November, 2013. Taipei, Taiwan.

Devereux, N. A. & Young, J. S. 1990, ApJ, 350, L25

Dole, H., Lagache, G., Puget, J.-L., et al. 2006, A&A, 451, 417

Draine, B. T. 2003, ARA&A, 41, 241

Draine, B. T. 2009, in Astronomical Society of the Pacific Conference Series, Vol. 414, Cosmic Dust - Near and Far, ed. T. Henning, E. Grün, & J. Steinacker, 453

Draine, B. T., Aniano, G., Krause, O., et al. 2014, ApJ, 780, 172

Draine, B. T., Dale, D. A., Bendo, G., et al. 2007, ApJ, 663, 866

Draine, B. T. & Salpeter, E. E. 1979, ApJ, 231, 438

Driver, S. P., Allen, P. D., Liske, J., & Graham, A. W. 2007, ApJ, 657, L85

Driver, S. P., Hill, D. T., Kelvin, L. S., et al. 2011, MNRAS, 413, 971

Driver, S. P., Liske, J., Cross, N. J. G., De Propris, R., & Allen, P. D. 2005, MNRAS, 360, 81

Driver, S. P., Norberg, P., Baldry, I. K., et al. 2009, Astronomy and Geophysics, 50, 050000

Driver, S. P., Robotham, A. S. G., Bland-Hawthorn, J., et al. 2013, MNRAS, 430, 2622

Driver, S. P., Wright, A. H., Andrews, S. K., et al. 2016, MNRAS, 455, 3911

Dunne, L., Eales, S., Edmunds, M., et al. 2000, MNRAS, 315, 115

Dunne, L., Eales, S., Ivison, R., Morgan, H., & Edmunds, M. 2003, Nature, 424, 285

Dunne, L. & Eales, S. A. 2001, MNRAS, 327, 697

Dunne, L., Gomez, H. L., da Cunha, E., et al. 2011, MNRAS, 417, 1510

Dunne, L., Maddox, S. J., Ivison, R. J., et al. 2009, MNRAS, 394, 1307

Dwek, E. 1998, ApJ, 501, 643

Dwek, E. & Cherchneff, I. 2011, ApJ, 727, 63

Dwek, E., Galliano, F., & Jones, A. P. 2007, ApJ, 662, 927

Dwek, E. & Scalo, J. M. 1980, ApJ, 239, 193

Eales, S., Dunne, L., Clements, D., et al. 2010, PASP, 122, 499

Eales, S. A. & Edmunds, M. G. 1996, MNRAS, 280, 1167

Edge, A. & Sutherland, W. 2013, VIKING (VISTA Kilo-degree Infrared Galaxy Survey Data Release 1, Tech. rep., ESO

Edmunds, M. G. 1990, MNRAS, 246, 678

Edmunds, M. G. 2001, MNRAS, 328, 223

Efstathiou, G. 2000, MNRAS, 317, 697

Ellis, R. S., McLure, R. J., Dunlop, J. S., et al. 2013, ApJ, 763, L7

Elmegreen, B. G. 1989, ApJ, 338, 178

Eskew, M., Zaritsky, D., & Meidt, S. 2012, AJ, 143, 139

Fabbri, J., Otsuka, M., Barlow, M. J., et al. 2011, MNRAS, 418, 1285

Fabello, S., Catinella, B., Giovanelli, R., et al. 2011a, MNRAS, 411, 993

Fabello, S., Kauffmann, G., Catinella, B., et al. 2011b, ArXiv e-prints

Fabello, S., Kauffmann, G., Catinella, B., et al. 2012, MNRAS, 427, 2841

Fall, S. M. & Efstathiou, G. 1980, MNRAS, 193, 189

Feldmann, R. 2015, MNRAS, 449, 3274

Fernández, X., Gim, H. B., van Gorkom, J. H., et al. 2016, ApJ, 824, L1

Ferrara, A., Viti, S., & Ceccarelli, C. 2016, MNRAS, 463, L112

Ferrarotti, A. S. & Gail, H.-P. 2006, A&A, 447, 553

Ferreras, I. & Silk, J. 2000, ApJ, 532, 193

Finkelstein, S. L., Ryan, Jr., R. E., Papovich, C., et al. 2015, ApJ, 810, 71

Finlator, K. & Davé, R. 2008, MNRAS, 385, 2181

Fischera, J. & Dopita, M. 2005, ApJ, 619, 340

Fisher, D. B., Bolatto, A. D., Herrera-Camus, R., et al. 2014, Nature, 505, 186

Fitzpatrick, E. L. & Massa, D. 2007, ApJ, 663, 320

Fixsen, D. J., Cheng, E. S., Gales, J. M., et al. 1996, ApJ, 473, 576

Ford, G. P., Gear, W. K., Smith, M. W. L., et al. 2013, ApJ, 769, 55

Foyle, K., Natale, G., Wilson, C. D., et al. 2013, MNRAS, 432, 2182

Freudling, W., Staveley-Smith, L., Catinella, B., et al. 2011, ApJ, 727, 40

Gall, C., Andersen, A. C., & Hjorth, J. 2011a, A&A, 528, A14

Gall, C., Hjorth, J., & Andersen, A. C. 2011b, A&A Rev, 19, 43

Gall, C., Hjorth, J., Watson, D., et al. 2014, Nature, 511, 326

Galliano, F., Hony, S., Bernard, J.-P., et al. 2011, A&A, 536, A88

Gao, Y. & Solomon, P. M. 2004, ApJ, 606, 271

Garnett, D. R. 1992, AJ, 103, 1330

Gavazzi, G., Fumagalli, M., Fossati, M., et al. 2013, A&A, 553, A89

Gavazzi, G. & Scodeggio, M. 1996, A&A, 312, L29

Giovanelli, R., Haynes, M. P., Kent, B. R., et al. 2005, AJ, 130, 2598

Glazebrook, K. 2013, Publications of the Astronomical Society of Australia, 30, 56

Gomez, H. L., Clark, C. J. R., Nozawa, T., et al. 2012a, MNRAS, 420, 3557

Gomez, H. L., Krause, O., Barlow, M. J., et al. 2012b, ApJ, 760, 96

Gordon, Y. A., Owers, M. S., Pimbblet, K. A., et al. 2016, MNRAS e-prints

Gould, R. J. & Salpeter, E. E. 1963, ApJ, 138, 393

Griffin, M. J., Abergel, A., Abreu, A., et al. 2010, A&A, 518, L3

Grootes, M. W., Tuffs, R. J., Popescu, C. C., et al. 2013, ApJ, 766, 59

Groves, B., Krause, O., Sandstrom, K., et al. 2012, MNRAS, 426, 892

Guseva, N. G., Izotov, Y. I., Fricke, K. J., & Henkel, C. 2012, A&A, 541, A115

Guseva, N. G., Izotov, Y. I., Papaderos, P., & Fricke, K. J. 2007, A&A, 464, 885

Guseva, N. G., Izotov, Y. I., & Thuan, T. X. 2000, ApJ, 531, 776

Guseva, N. G., Papaderos, P., Izotov, Y. I., et al. 2003, A&A, 407, 91

Hao, C.-N., Kennicutt, R. C., Johnson, B. D., et al. 2011, ApJ, 741, 124

Hauser, M. G. & Dwek, E. 2001, ARA&A, 39, 249

Haynes, M. P., Giovanelli, R., & Chincarini, G. L. 1984, ARA&A, 22, 445

Haynes, M. P., Giovanelli, R., Martin, A. M., et al. 2011, AJ, 142, 170

Hayward, C. C. & Smith, D. J. B. 2015, MNRAS, 446, 1512

Herrera-Camus, R., Fisher, D. B., Bolatto, A. D., et al. 2012, ApJ, 752, 112

Hirashita, H., Buat, V., & Inoue, A. K. 2003, A&A, 410, 83

Hirashita, H. & Ferrara, A. 2002, MNRAS, 337, 921

Holland, W. S., Bintley, D., Chapin, E. L., et al. 2013, MNRAS, 430, 2513

Holland, W. S., Robson, E. I., Gear, W. K., et al. 1999, MNRAS, 303, 659

Holwerda, B. W., Bianchi, S., Böker, T., et al. 2012, A&A, 541, L5

Hopkins, A. M., Driver, S. P., Brough, S., et al. 2013, MNRAS, 430, 2047

Huang, S., Haynes, M. P., Giovanelli, R., & Brinchmann, J. 2012, ApJ, 756, 113

Hughes, T. M., Baes, M., Fritz, J., et al. 2014, A&A, 565, A4

Hughes, T. M., Cortese, L., Boselli, A., Gavazzi, G., & Davies, J. I. 2013, A&A, 550, A115

Hunter, D. A., Ficut-Vicas, D., Ashley, T., et al. 2012, AJ, 144, 134

Indebetouw, R., Matsuura, M., Dwek, E., et al. 2014, ApJ, 782, L2

Inoue, A. K. 2003, PASJ, 55, 901

Irwin, M. 2010, "UKIRT Newsletter", 26, 14

Issa, M. R., MacLaren, I., & Wolfendale, A. W. 1990, A&A, 236, 237

Izotov, Y. I., Stasińska, G., Meynet, G., Guseva, N. G., & Thuan, T. X. 2006, A&A, 448, 955

Izotov, Y. I. & Thuan, T. X. 1998, ApJ, 500, 188

Izotov, Y. I. & Thuan, T. X. 2004, ApJ, 602, 200

Izotov, Y. I., Thuan, T. X., & Lipovetsky, V. A. 1994, ApJ, 435, 647

Izotov, Y. I., Thuan, T. X., & Lipovetsky, V. A. 1997, ApJS, 108, 1

Izotov, Y. I., Thuan, T. X., & Stasińska, G. 2007, ApJ, 662, 15

James, A., Dunne, L., Eales, S., & Edmunds, M. G. 2002, MNRAS, 335, 753

Jarrett, T. H., Masci, F., Tsai, C. W., et al. 2013, AJ, 145, 6

Jaskot, A. E., Oey, M. S., Salzer, J. J., et al. 2015, ApJ, 808, 66

Jenkins, E. 2013, in Proceedings of The Life Cycle of Dust in the Universe: Observations, Theory, and Laboratory Experiments (LCDU2013). 18-22 November, 2013. Taipei, Taiwan.

Jenkins, E. B. 2009, ApJ, 700, 1299

Jones, A. P. 2004, in Astronomical Society of the Pacific Conference Series, Vol. 309, Astrophysics of Dust, ed. A. N. Witt, G. C. Clayton, & B. T. Draine, 347

Jones, A. P. & Nuth, J. A. 2011, A&A, 530, A44

Jones, A. P., Tielens, A. G. G. M., & Hollenbach, D. J. 1996, ApJ, 469, 740

Jones, A. P., Tielens, A. G. G. M., Hollenbach, D. J., & McKee, C. F. 1994, ApJ, 433, 797

Kauffmann, G., Heckman, T. M., Tremonti, C., et al. 2003, MNRAS, 346, 1055

Kaviraj, S., Peirani, S., Khochfar, S., Silk, J., & Kay, S. 2009, MNRAS, 394, 1713

Kaviraj, S., Rowlands, K., Alpaslan, M., et al. 2013, MNRAS, 435, 1463

Kaviraj, S., Tan, K.-M., Ellis, R. S., & Silk, J. 2011, MNRAS, 411, 2148

Kaviraj, S., Ting, Y.-S., Bureau, M., et al. 2012, MNRAS, 423, 49

Kennicutt, R. C., Calzetti, D., Aniano, G., et al. 2011, PASP, 123, 1347

Kennicutt, Jr., R. C. 1992, ApJ, 388, 310

Kennicutt, Jr., R. C. 1998, ApJ, 498, 541

Kennicutt, Jr., R. C., Hao, C.-N., Calzetti, D., et al. 2009, ApJ, 703, 1672

Kessler, M. F., Steinz, J. A., Anderegg, M. E., et al. 1996, A&A, 315, L27

Kewley, L. J. & Dopita, M. A. 2002, ApJS, 142, 35

Kewley, L. J., Dopita, M. A., Sutherland, R. S., Heisler, C. A., & Trevena, J. 2001, ApJ, 556, 121

Kewley, L. J. & Ellison, S. L. 2008, ApJ, 681, 1183

Kim, S.-H., Martin, P. G., & Hendry, P. D. 1994, ApJ, 422, 164

Kirkpatrick, A., Calzetti, D., Kennicutt, R., et al. 2014, ApJ, 789, 130

Kobulnicky, H. A., Kennicutt, Jr., R. C., & Pizagno, J. L. 1999, ApJ, 514, 544

Kobulnicky, H. A. & Kewley, L. J. 2004, ApJ, 617, 240

Kobulnicky, H. A. & Skillman, E. D. 1997, ApJ, 489, 636

Kong, X., Charlot, S., Brinchmann, J., & Fall, S. M. 2004, MNRAS, 349, 769

Kong, X. & Cheng, F. Z. 2002, A&A, 389, 845

Kotak, R., Meikle, W. P. S., Farrah, D., et al. 2009, ApJ, 704, 306

Kott, P. S. 2001, Journal of Official Statistics, 17, 521

Kroupa, P. 2001, MNRAS, 322, 231

Lah, P., Chengalur, J. N., Briggs, F. H., et al. 2007, MNRAS, 376, 1357

Lara-López, M. A., Cepa, J., Bongiovanni, A., et al. 2010, A&A, 521, L53

Lara-López, M. A., Hopkins, A. M., López-Sánchez, A. R., et al. 2013, MNRAS, 434, 451

Law, K.-H., Gordon, K. D., & Misselt, K. A. 2011, ApJ, 738, 124

Lee, H. & Skillman, E. D. 2004, ApJ, 614, 698

Lee, J. C., Gil de Paz, A., Tremonti, C., et al. 2009, ApJ, 706, 599

Lee, S.-K., Ferguson, H. C., Somerville, R. S., Wiklind, T., & Giavalisco, M. 2010, ApJ, 725, 1644

Leroy, A. K., Walter, F., Brinks, E., et al. 2008, AJ, 136, 2782

Liang, Y. C., Yin, S. Y., Hammer, F., et al. 2006, ApJ, 652, 257

Liddle, A. 2003, An Introduction to Modern Cosmology, Second Edition

Linde, A. D. 1982, Physics Letters B, 108, 389

Lisenfeld, U. & Ferrara, A. 1998, ApJ, 496, 145

Liske, J., Baldry, I. K., Driver, S. P., et al. 2015, MNRAS, 452, 2087

López-Sánchez, Á. R., Esteban, C., & Rodríguez, M. 2004, ApJS, 153, 243

Madau, P. & Dickinson, M. 2014a, ARA&A, 52, 415

Madau, P. & Dickinson, M. 2014b, ARA&A, 52, 415

Madden, S. C., Rémy-Ruyer, A., Galametz, M., et al. 2013, PASP, 125, 600

Maeder, A. 1992, A&A, 264, 105

Magrini, L. & Gonçalves, D. R. 2009, MNRAS, 398, 280

Mancini, M., Schneider, R., Graziani, L., et al. 2015, MNRAS, 451, L70

Mannucci, F., Cresci, G., Maiolino, R., Marconi, A., & Gnerucci, A. 2010, MNRAS, 408, 2115

Mao, Y.-W., Kennicutt, Jr., R. C., Hao, C.-N., Kong, X., & Zhou, X. 2012, ApJ, 757, 52

Marino, R. A., Rosales-Ortega, F. F., Sánchez, S. F., et al. 2013, A&A, 559, A114

Masegosa, J., Moles, M., & Campos-Aguilar, A. 1994, ApJ, 420, 576

Matsuura, M., Barlow, M. J., Zijlstra, A. A., et al. 2009, MNRAS, 396, 918

Matsuura, M., Dwek, E., Barlow, M. J., et al. 2015, ApJ, 800, 50

Matsuura, M., Dwek, E., Meixner, M., et al. 2011, Science, 333, 1258

Mattsson, L., Andersen, A. C., & Munkhammar, J. D. 2012, MNRAS, 423, 26

Mattsson, L., Gomez, H. L., Andersen, A. C., et al. 2014, MNRAS, 444, 797

McKinnon, R., Torrey, P., & Vogelsberger, M. 2016, MNRAS, 457, 3775

McLure, R. J., Dunlop, J. S., Bowler, R. A. A., et al. 2013, MNRAS, 432, 2696

Meurer, G. R., Heckman, T. M., & Calzetti, D. 1999, ApJ, 521, 64

Meyer, M. J., Zwaan, M. A., Webster, R. L., et al. 2004, MNRAS, 350, 1195

Michałowski, M. J. 2015, A&A, 577, A80

Michałowski, M. J., Gentile, G., Hjorth, J., et al. 2015, A&A, 582, A78

Michałowski, M. J., Hayward, C. C., Dunlop, J. S., et al. 2014, A&A, 571, A75

Michałowski, M. J., Watson, D., & Hjorth, J. 2010, ApJ, 712, 942

Mihos, J. C. & Hernquist, L. 1994, ApJ, 431, L9

Mihos, J. C. & Hernquist, L. 1996, ApJ, 464, 641

Moffett, A. J., Ingarfield, S. A., Driver, S. P., et al. 2016, MNRAS, 457, 1308

Moorwood, A. F. M. 1996, Space Science Reviews, 77, 303

Morales-Luis, A. B., Pérez-Montero, E., Sánchez Almeida, J., & Muñoz-Tuñón, C. 2014, ApJ, 797, 81

Morgan, H. L. & Edmunds, M. G. 2003, MNRAS, 343, 427

Morrissey, P., Conrow, T., Barlow, T. A., et al. 2007, ApJS, 173, 682

Moustakas, J. & Kennicutt, Jr., R. C. 2006, ApJS, 164, 81

Moustakas, J., Kennicutt, Jr., R. C., Tremonti, C. A., et al. 2010, ApJS, 190, 233

Neugebauer, G., Habing, H. J., van Duinen, R., et al. 1984, ApJ, 278, L1

Noeske, K. G., Weiner, B. J., Faber, S. M., et al. 2007, ApJ, 660, L43

Nozawa, T., Asano, R. S., Hirashita, H., & Takeuchi, T. T. 2015, MNRAS, 447, L16

Oesch, P. A., Bouwens, R. J., Illingworth, G. D., et al. 2013, ApJ, 773, 75

Oesch, P. A., Bouwens, R. J., Illingworth, G. D., et al. 2014, ApJ, 786, 108

Oesch, P. A., Brammer, G., van Dokkum, P. G., et al. 2016, ApJ, 819, 129

Offringa, A. R. 2010, AOFlagger: RFI Software, Astrophysics Source Code Library

Offringa, A. R., van de Gronde, J. J., & Roerdink, J. B. T. M. 2012, A&A, 539, A95

Oliver, S. J., Bock, J., Altieri, B., et al. 2012, MNRAS, 424, 1614

Osterbrock, D. E. 1989, Astrophysics of gaseous nebulae and active galactic nuclei

Overcast, W. C. 2010, Master's thesis, University of Tennessee, Knoxville

Pagel, B. E. J., Edmunds, M. G., Blackwell, D. E., Chun, M. S., & Smith, G. 1979, MNRAS, 189, 95

Papadopoulos, P. P., van der Werf, P. P., Xilouris, E. M., et al. 2012, MNRAS, 426, 2601

Paturel, G., Petit, C., Prugniel, P., et al. 2003, A&A, 412, 45

Peimbert, A., Peimbert, M., & Ruiz, M. T. 2005, ApJ, 634, 1056

Pettini, M. & Pagel, B. E. J. 2004, MNRAS, 348, L59

Pilbratt, G. L., Riedinger, J. R., Passvogel, T., et al. 2010, A&A, 518, L1

Pilyugin, L. S. & Grebel, E. K. 2016, MNRAS, 457, 3678

Pilyugin, L. S. & Thuan, T. X. 2005, ApJ, 631, 231

Pilyugin, L. S., Vílchez, J. M., & Thuan, T. X. 2010, ApJ, 720, 1738

Planck Collaboration, Ade, P. A. R., Aghanim, N., et al. 2011a, A&A, 536, A1

Planck Collaboration, Ade, P. A. R., Aghanim, N., et al. 2011b, A&A, 536, A19

Poglitsch, A., Waelkens, C., Geis, N., et al. 2010, A&A, 518, L2

Popescu, C. C. & Hopp, U. 2000, A&AS, 142, 247

Popescu, C. C., Tuffs, R. J., Dopita, M. A., et al. 2011, A&A, 527, A109

Popping, G., Somerville, R. S., & Trager, S. C. 2014, MNRAS, 442, 2398

Prochaska, J. X., Herbert-Fort, S., & Wolfe, A. M. 2005, ApJ, 635, 123

Prochaska, J. X. & Wolfe, A. M. 2009, ApJ, 696, 1543

Pustilnik, S. A., Kniazev, A. Y., Pramskij, A. G., & Ugryumov, A. V. 2003, Ap&SS, 284, 795

Rao, S. M., Turnshek, D. A., & Nestor, D. B. 2006, ApJ, 636, 610

Rémy-Ruyer, A., Madden, S. C., Galliano, F., et al. 2014, A&A, 563, A31

Rémy-Ruyer, A., Madden, S. C., Galliano, F., et al. 2013, A&A, 557, A95

Rémy-Ruyer, A., Madden, S. C., Galliano, F., et al. 2015, A&A, 582, A121

Rhee, J., Zwaan, M. A., Briggs, F. H., et al. 2013, MNRAS, 435, 2693

Riess, A. G., Macri, L., Casertano, S., et al. 2011, ApJ, 730, 119

Romano, D., Karakas, A. I., Tosi, M., & Matteucci, F. 2010, A&A, 522, A32

Roussel, H. 2013, PASP, 125, 1126

Rowlands, K., Dunne, L., Dye, S., et al. 2014a, MNRAS, 441, 1017

Rowlands, K., Gomez, H. L., Dunne, L., et al. 2014b, MNRAS, 441, 1040

Saintonge, A., Kauffmann, G., Kramer, C., et al. 2011, MNRAS, 415, 32

Salpeter, E. E. 1955, ApJ, 121, 161

Sánchez, S. F., García-Lorenzo, B., Jahnke, K., et al. 2006, New Astr. Rev., 49, 501

Sánchez, S. F., Rosales-Ortega, F. F., Iglesias-Páramo, J., et al. 2014, A&A, 563, A49

Sanders, D. B., Mazzarella, J. M., Kim, D.-C., Surace, J. A., & Soifer, B. T. 2003, AJ, 126, 1607

Sanders, D. B., Scoville, N. Z., & Soifer, B. T. 1991, ApJ, 370, 158

Sandstrom, K. M., Leroy, A. K., Walter, F., et al. 2013, ApJ, 777, 5

Santini, P., Maiolino, R., Magnelli, B., et al. 2014, A&A, 562, A30

Sargent, B. A., Srinivasan, S., Meixner, M., et al. 2010, ApJ, 716, 878

Sarzi, M., Falcón-Barroso, J., Davies, R. L., et al. 2006, MNRAS, 366, 1151

Sauvage, M. 2011, Experiments in photometric measurements of extended sources, Tech. rep., CEA, Laboratoire AIM

Schaller, G., Schaerer, D., Meynet, G., & Maeder, A. 1992, A&AS, 96, 269

Schaye, J., Crain, R. A., Bower, R. G., et al. 2015, MNRAS, 446, 521

Schiminovich, D., Wyder, T. K., Martin, D. C., et al. 2007, ApJS, 173, 315

Schmidt, K. B., Treu, T., Trenti, M., et al. 2014, ApJ, 786, 57

Schruba, A., Leroy, A. K., Walter, F., et al. 2011, AJ, 142, 37

Schruba, A., Leroy, A. K., Walter, F., et al. 2012, AJ, 143, 138

Scoville, N., Aussel, H., Sheth, K., et al. 2014, ApJ, 783, 84

Seibert, M., Wyder, T., Neill, J., et al. 2012, in American Astronomical Society Meeting Abstracts, Vol. 219, American Astronomical Society Meeting Abstracts #219, 340.01

Sheth, K., Regan, M., Hinz, J. L., et al. 2010, PASP, 122, 1397

Shibuya, T., Kashikawa, N., Ota, K., et al. 2012, ApJ, 752, 114

Siringo, G., Kreysa, E., Kovács, A., et al. 2009, A&A, 497, 945

Skillman, E. D., Côté, S., & Miller, B. W. 2003, AJ, 125, 610

Skillman, E. D. & Kennicutt, Jr., R. C. 1993, ApJ, 411, 655

Skrutskie, M. F., Cutri, R. M., Stiening, R., et al. 2006, AJ, 131, 1163

Smith, D. J. B., Dunne, L., da Cunha, E., et al. 2012, MNRAS, 427, 703

Smith, D. J. B., Dunne, L., Maddox, S. J., et al. 2011, MNRAS, 416, 857

Smith, D. J. B., Hardcastle, M. J., Jarvis, M. J., et al. 2013, MNRAS, 436, 2435

Smith, D. J. B. & Hayward, C. C. 2015, MNRAS, 453, 1597

Smith, M. W. L., Eales, S. A., De Looze, I., et al. 2016, MNRAS, 462, 331

Springel, V., Di Matteo, T., & Hernquist, L. 2005, MNRAS, 361, 776

Starobinskii, A. A. 1978, Soviet Astronomy Letters, 4, 82

Stasińska, G. 2005, A&A, 434, 507

Steinacker, J., Baes, M., & Gordon, K. D. 2013, ARA&A, 51, 63

Storchi-Bergmann, T., Calzetti, D., & Kinney, A. L. 1994, ApJ, 429, 572

Stroe, A., Oosterloo, T., Röttgering, H. J. A., et al. 2015, MNRAS, 452, 2731

Sugerman, B. E. K., Ercolano, B., Barlow, M. J., et al. 2006, Science, 313, 196

Sutherland, W. 2012, in Science from the Next Generation Imaging and Spectroscopic Surveys

Taylor, E. N., Hopkins, A. M., Baldry, I. K., et al. 2011, MNRAS, 418, 1587

Thielemann, F.-K., Brachwitz, F., Freiburghaus, C., et al. 2001, Progress in Particle and Nuclear Physics, 46, 5

Thomas, D., Steele, O., Maraston, C., et al. 2013, MNRAS, 431, 1383

Tinsley, B. M. 1980, Fundamentals Cosmic Phys., 5, 287

Todini, P. & Ferrara, A. 2001, MNRAS, 325, 726

Tonry, J. L., Blakeslee, J. P., Ajhar, E. A., & Dressler, A. 2000, ApJ, 530, 625

Tremonti, C. A., Heckman, T. M., Kauffmann, G., et al. 2004, ApJ, 613, 898

Valiante, E., Lutz, D., Sturm, E., Genzel, R., & Chapin, E. L. 2009, ApJ, 701, 1814

Valiante, E., Smith, M. W. L., Eales, S., et al. 2016, ArXiv e-prints

van den Hoek, L. B. & Groenewegen, M. A. T. 1997, A&AS, 123, 305

van Zee, L., Haynes, M. P., Salzer, J. J., & Broeils, A. H. 1996, AJ, 112, 129

Ventura, P., Criscienzo, M. D., Schneider, R., et al. 2012, MNRAS, 424, 2345

Viaene, S., Baes, M., Bendo, G., et al. 2016, A&A, 586, A13

Viaene, S., Fritz, J., Baes, M., et al. 2014, A&A, 567, A71

Vlahakis, C., Dunne, L., & Eales, S. 2005, MNRAS, 364, 1253

Vogelsberger, M., Genel, S., Springel, V., et al. 2014, MNRAS, 444, 1518

Walker, T. P., Steigman, G., Kang, H.-S., Schramm, D. M., & Olive, K. A. 1991, ApJ, 376, 51

Walter, F., Brinks, E., de Blok, W. J. G., et al. 2008, AJ, 136, 2563

Werner, M. W., Roellig, T. L., Low, F. J., et al. 2004, ApJS, 154, 1

Whitaker, K. E., van Dokkum, P. G., Brammer, G., & Franx, M. 2012, ApJ, 754, L29

Whittet, D. C. B. 1992, Dust in the galactic environment

Wijesinghe, D. B., Hopkins, A. M., Sharp, R., et al. 2011, MNRAS, 410, 2291

Wirth, G. D., Koo, D. C., & Kron, R. G. 1994, ApJ, 435, L105

Wong, O. I., Ryan-Weber, E. V., Garcia-Appadoo, D. A., et al. 2006, MNRAS, 371, 1855

Wong, T. & Blitz, L. 2002, ApJ, 569, 157

Woosley, S. E. & Weaver, T. A. 1995, ApJS, 101, 181

Wright, A. H., Robotham, A. S. G., Bourne, N., et al. 2016, MNRAS, 460, 765

Wright, E. L., Eisenhardt, P. R. M., Mainzer, A. K., et al. 2010, AJ, 140, 1868

Yin, J., Hou, J. L., Prantzos, N., et al. 2009, A&A, 505, 497

Yin, S. Y., Liang, Y. C., Hammer, F., et al. 2007, A&A, 462, 535

York, D. G., Adelman, J., Anderson, Jr., J. E., et al. 2000, AJ, 120, 1579

Zhukovska, S. 2014, A&A, 562, A76

Zhukovska, S., Gail, H.-P., & Trieloff, M. 2008, A&A, 479, 453

Zibetti, S., Charlot, S., & Rix, H.-W. 2009, MNRAS, 400, 1181

Zitrin, A., Labbé, I., Belli, S., et al. 2015, ApJ, 810, L12

Zwaan, M. A. 2000, PhD thesis, PhD Thesis, Groningen: Rijksuniversiteit, 2000 152 p. Proefschrift, Rijksuniversiteit Groningen, 2000

Zwaan, M. A., Meyer, M. J., Staveley-Smith, L., & Webster, R. L. 2005, MNRAS, 359, L30

Zwaan, M. A., Meyer, M. J., Webster, R. L., et al. 2004, MNRAS, 350, 1210